DNA-BASED MIMICS OF MEMBRANE PROTEINS

LIPID-DNA INTERACTIONS DETERMINE FUNCTION

Diana Kornelia Morzy

Department of Physics
University of Cambridge

This dissertation is submitted for the degree of *Doctor of Philosophy.*

Trinity College March 2021

DECLARATION

This dissertation is the result of my own work and includes nothing which is the outcome of work done in collaboration except as specified in the text. It is not substantially the same as any that I have submitted, or, is being concurrently submitted for a degree or diploma or other qualification at the University of Cambridge or any other University or similar institution except as specified in the text. I further state that no substantial part of my thesis has already been submitted, or, is being concurrently submitted for any such degree, diploma or other qualification at the University of Cambridge or any other University or similar institution except as specified in the text. This thesis does not exceed the word limit of 60,000 words set by the Physics and Chemistry Degree Committee, including abstract, tables, footnotes and appendices.

Diana Morzy
21 March 2021

DNA-BASED MIMICS OF MEMBRANE PROTEINS

LIPID-DNA INTERACTIONS DETERMINE FUNCTION

Diana Kornelia Morzy

ABSTRACT

Nucleic acids, particularly DNA, are used as a nanoscale building material, due to their unique controllability *via* complementarity of base pairing. One of the potential applications of DNA nanotechnology is creating synthetic constructs mimicking function of membrane proteins. These natural molecular machines function embedded in the lipid bilayer. Similar membrane attachment of DNA-based structures is achieved by modifying the nucleic acid with hydrophobic anchors, most commonly cholesterol. Aiming at developing a fully functional and controllable synthetic membrane construct, the first step I undertook was to understand and utilize fundamental interactions between molecules: DNA, cholesterol and lipids.

Instead of starting with a complicated DNA-based model mimicking protein architecture, here I have created a set of simple systems that allowed me to examine the major interactions between involved molecules. This work describes four aspects of the DNA-lipid systems that I have built and studied experimentally. Firstly, I have analysed the effects of membrane-spanning DNA duplex on the lipids' arrangement in the pore and presented how this arrangement can be remodelled depending on the hydrophilicity of the DNA design. Secondly, I have looked at the same system from the opposite perspective - studied and prevented the distortion of the transmembrane DNA construct induced by the surrounding lipids. Thirdly, I have evaluated the importance of ions in mediating DNA-lipid interactions, reporting analysis of two electrostatic phenomena: screening and bridging. Finally, utilizing a nanoengineered four-helix structure, I discussed surfactant's influence on DNA membrane insertion efficiency, showing that aggregation of the nanostructures is one of the major factors determining their spontaneous membrane-spanning. While the understanding of phenomena in minimalistic systems is crucial for further development of complex pore-forming constructs, here I showed that even simple DNA nanostructures, when rationally designed, can mimic functionality of natural membrane proteins.

Dla moich rodziców

ACKNOWLEDGEMENTS

As a molecular system is a sum of interactions between chemical species, so is a PhD thesis a sum of interactions with people around the author. None of this work would be possible without them - thank you.

I cannot imagine making it to the end of this journey without a guide: the role undertaken by my supervisor, Prof. Ulrich Keyser. Working with him, I was given an opportunity to enthusiastically explore science on my own, knowing that somebody will correct my route when I start to get lost.

Obtaining a scientific degree is also a learning process and here, teaching was kindly provided by my groupmates. I am convinced that at some point each of the group members shared their knowledge with me, and for that I am truly grateful. In particular, Silvia Hernandez-Ainsa and Alex Ohmann introduced me to the laboratory work and in many ways shaped me as a researcher. Along with Alex, Jinbo Zhu, Kareem Al Nahas and Michael Schaich showed me lab techniques that became an experimental core of this thesis. Finally, my officemates taught me patience, while being infinitely patient with me; it is to Michael, Niklas, Jinbo, Marcus and Karolis that I owe the feeling of belonging with the academic community.

Large portion of the discoveries described here would never be made, if it was not for people who shared passion and worked with me, hand in hand. Roger Rubio-Sánchez from Lorenzo Di Michele's group and Himanshu Joshi from Aleksei Aksimentiev's group joined my endeavours with their impressive skills and hard work. Additionally, I particularly enjoyed working together with Michael Schaich, Kevin Baumann and Sarah Sandler. Here, I also want to thank the people who revised my written works (including this thesis): Niklas, Sarah, Sara, Kareem, Alex, Roger, Alice and Jędrek.

Apart from the scientific challenge, pursuing a doctoral degree was often a mental strain as well. I was lucky to be surrounded with kind people, always offering their help and support: Maciek, Agata and Józek with their calmness and warmth, Jana and Josh with their passion, big hearts and energy, Jackie and John with their smiles and creativity, Tom and Vasilis with their brilliance and good nature.

I do not have and do not expect to ever have a way to express my gratitude to Jędrek Morzy, who helped me so much more than I can describe in words.

Finally, the driving force of this work are people whom I want to make proud. My parents always saw someone amazing in me and for this (sometimes irrational) belief, I wish to dedicate this thesis to them.

LIST OF PUBLICATIONS

peer-reviewed publications

D. Morzy et al. Cations regulate membrane-attachment and functionality of DNA nanostructures, *Journal of American Chemical Society* 2021, published online

D. Sobota et al. Tailoring interleaflet lipid transfer with a DNA-based synthetic enzyme, *Nano Letters* 2020, 20(6)

K. Baumann, (…), **D. Sobota** et al. Clathrin-Inspired Coating and Stabilization of Liposomes by DNA Self-Assembly, *ACS Nano* 2020, 14(2)

M. Schaich, **D. Sobota** et al. Biophysical characterization reveals the similarities of liposomes produced using microfluidics and electroformation, *Biochimica et Biophysica Acta* 2020, 1862(9)

A. Ohmann, (…), **D. Sobota** et al. Controlling aggregation of cholesterol-modified DNA nanostructures, *Nucleic Acids Research* 2019, 47(21)

M. Schaich, (…), **D. Sobota** et al. An Integrated Microfluidic Platform for Quantifying Drug Permeation across Biomimetic Vesicle Membranes, *Molecular Pharmaceutics* 2019, 16(6)

conference papers

D. Sobota et al. Controlling the Rate and the Level of Interleaflet Lipid Transport with Switchable DNA Nanostructure, *Biophysical Journal* 2019, 118(3)

submitted

D. Morzy et al. Stabilization of base pairs improves membrane activity of a DNA-based synthetic ion channel, *submitted*.

LIST OF ABBREVIATIONS

0C	DNA nanostructures with 0 cholesterol tags
1C	DNA nanostructures with 1 cholesterol tag
2C	DNA nanostructures with 2 cholesterol tags
4H	4-helix pore
bp	base pairs
BSA	bovine serum albumin
cmc	critical micelle concentration
DLS	dynamic light scattering
DNA	deoxyribonucleic acid
DPhPC	1,2-diphytanoyl-sn-glycero-3-phosphatidylcholine
DPhPE	1,2-diphytanoyl-sn-glycero-3-phosphatidylethanolamine
DPPC	1,2-dihexadecanoyl-*sn*-glycero-3-phosphocholine
DPPE	1,2-dipalmitoyl-sn-glycero-3-phosphoethanolamine
dsDNA	double-stranded DNA
EDTA	ethylenediaminetetraacetic acid
ELS	electrophoretic light scattering
FRAP	fluorescence recovery after photobleaching
GUVs	giant unilamellar vesicles
HEPES	4-(2-hydroxyethyl)-1-piperazineethanesulfonic acid
HPLC	high performance liquid chromatography
ITO	indium tin oxide
LUVs	large unilamellar vesicles
MD	molecular dynamics
NBD	nitrobenzoxadiazole
nt	nucleotide
oPOE	n-octylpolyoxyethylene
PAGE	polyacrylamide gel electrophoresis
POPC	1-palmitoyl-2-oleoyl-sn-glycero-3-phosphocholine
SDS	sodium dodecyl sulfate
ssDNA	single-stranded DNA
TE	Tris-EDTA
TBE	Tris-Borate-EDTA
TEG	Triethylene glycol
TEMED	N,N,N',N'-Tetramethylethylenediamine
UV-vis	ultraviolet-visible

TABLE OF CONTENTS

CHAPTER 1

Introduction

As an interface between a cell and its environment, the lipid membrane is responsible for a vast range of activities in every cell of every organism. To create a platform that can interact with this interface and take active part in cell-environment signalling, is an idea as appealing as it is challenging. It would be a huge step towards building a functional synthetic cell. It would provide a whole new class of cytotoxic drugs, targeting and manipulating membranes of microbes or cancer cells. It would push the boundaries of our understanding of cell's functioning. It would allow us to design new therapeutics for numerous systematic diseases.

Such platforms were provided by nature in a form of membrane proteins. Yet, they are sophisticated molecular machines, and their manipulation is not trivial. However, there is another molecule that has been thoroughly studied and can be designed into complex, nanoscale shapes: the nucleic acid. In this work I will elaborate on the idea of using DNA as a building material to create functional membrane-interacting protein mimics.

Building a complex system, at any scale, is never an easy task. It took nature thousands of years of evolution to reach the level of infallibility that proteins display today. Importantly, the evolution proceeded from simple - but working - structures, adding more and more features that in the end resulted in such efficient and complex machines. In fact, evolution is a great example of Gall's law:

A complex system that works is invariably found to have evolved from a simple system that worked. A complex system designed from scratch never works and cannot be patched up to make it work. You have to start over with a working simple system.

John Gall, *Systemantics: How Systems Really Work and How They Fail*

This statement determined how I decided to tackle the problem. Having in mind the *ultimate goal:* to create a functional membrane protein mimic, let me guide you towards the *one-person's PhD goal:* to understand the foundations of creating such a mimic, and to leave behind this book: a comprehensive guide to whoever will come next to further develop DNA-based membrane structures.

Firstly, I will collect here what we know about the chemistry and function of the relevant molecules: lipids - because we need to know the targeted environment, membrane proteins - because we can (and should) learn from what we know is working, and DNA - because we need to know our building material. Only then I will look closer into the interactions between nucleic acids and lipids, as well as previous attempts to design membrane-interacting structures.

In the following chapters I will introduce four aspects of the DNA-lipid systems that I studied experimentally. Instead of building a complicated DNA-based model of a fully functional membrane protein, I focused on building a set of simple systems that will allow me to understand thoroughly the interactions between involved molecules. More specifically, I looked at the effects of membrane-spanning DNA on the lipids' arrangement in the pore (Chapter 4) and *vice versa*: the effects of the lipids on the stability of transmembrane DNA constructs (Chapter 5). I also evaluated the importance of ions in the system (Chapter 6) and the details of surfactant's influence on insertion efficiency (Chapter 7). Finally, I will talk more about further ideas and the future of these studies (Chapter 8).

You will soon see that this book is scaffolded on questions budding from one another, which is a very accurate illustration of the three years of PhD work that it describes. Having so many to come, let us start by asking the first one.

CHAPTER 2

Of molecules and interactions

Why are cells enveloped in lipid membranes? While providing a barrier from the environment, the membrane ensures that each cell has an ability to communicate and controllably exchange molecules with the world beyond its boundaries. In other words, each membrane represents a controllable interface, through which the cells can gather information of their environment, adapt their state and signal their response.

Even though the exact structure of membranes varies between species, it can always be described as a lipid scaffolding with proteins and other molecules embedded in it. To fulfil its functions, membrane needs *both* these components, with lipids acting as a barrier and proteins providing controllable signalling and transport through it. Both are intertwined in a complex relationship of interactions, mediated by the environment. Still, before these interactions can be studied, it is important to understand the nature of the two main components, namely lipids and transmembrane proteins, separately.

2.1. Cell membrane components: lipids

The previous paragraph requires some clarification, as it belittled lipids' contribution to the organism's functioning, calling it a mere scaffold for the "significant" molecules. In fact, lipids are an important energy storage medium[1–3] and can themselves also act as signalling platforms[4–7] – I will touch upon this in further chapters. Here, I will discuss mainly their structural application, focusing on the formation of a cell membrane, driven by a simple (and yet conserved across taxonomic kingdoms) mechanism.

Lipids are defined by their solubility: they are biomolecules soluble in non-polar solvents. This definition already suggests what a vast field of biochemistry we are stepping into in this chapter. In order to make the task of describing membrane-forming lipids feasible, I will limit the discussion to one of the eight lipid categories*, namely glycerophospholipids (also referred to as phospholipids, here PLs)[8].

*The other seven being: fatty acyls, glycerolipids, sphingolipids, sterol lipids, prenol lipids, sacharrolipids and polyketides[8].

Phospholipids are without exception amphiphilic molecules, having both hydro- and lipophilic groups. Cell membrane, the bilayer, forms in aqueous solutions, where PLs arrange themselves with the hydrophilic groups facing the water and the hydrophobic ones aggregating together (Figure 2.1a). We distinguish these two domains of a lipid as a headgroup with an affinity to water and a tail repelled by it (Figure 2.1b). The names, even though colloquial, describe accurately the molecular structure of a PL (Figure 2.1c). Glycerol and negatively charged phosphate form a hydrophilic "head", and long fatty acids (FAs) - non-polar chains of carbon atoms - are like "tails" tucked between each other in their pursuit of a water-free environment[3,8–10].

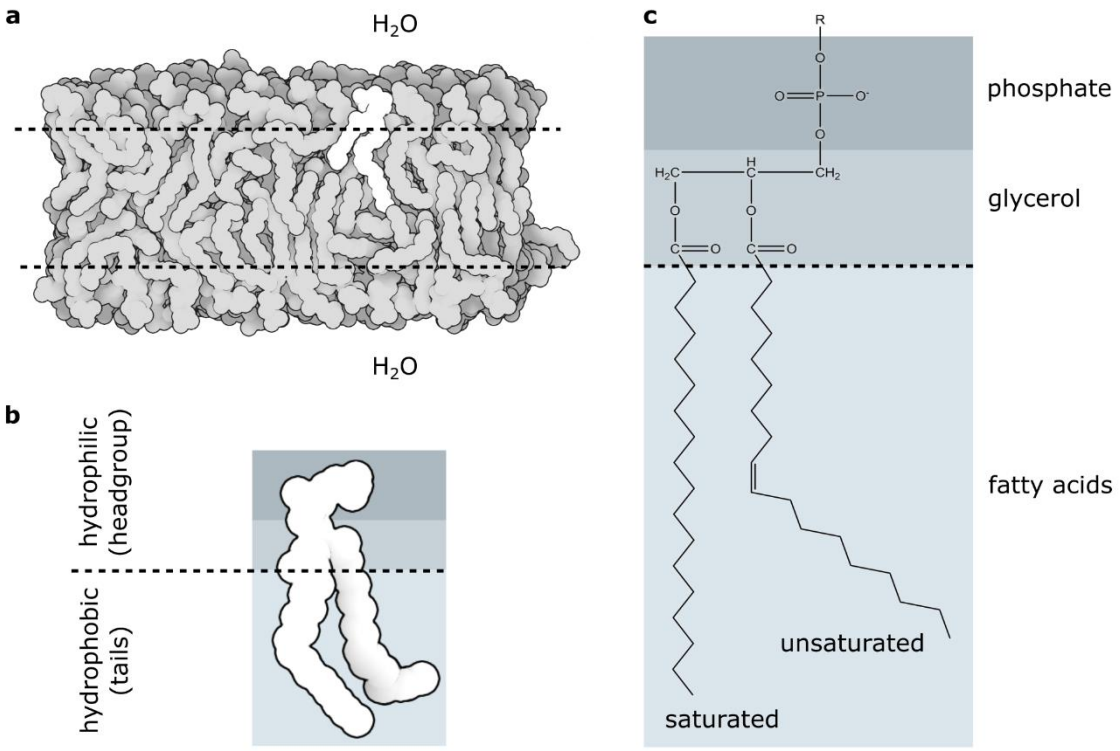

Figure 2.1 *Amphiphilic structure of phospholipids is driving bilayer formation. (a) All-atom model of a POPC lipid bilayer (simulated model adapted from Heller et al.,1993), where black dashed lines separate hydro- and lipophilic parts of a membrane. (b) Illustration of a single lipid showing its two parts: hydrophilic headgroup and hydrophobic tails. (c) Molecular structure of a glycerophospholipid with black dashed line separating the headgroup from the tails.*

Held in a membrane by hydrophobic interactions rather than strong covalent bonds, no single phospholipid will be immobilized in the bilayer's structure. Due to the thermal fluctuations of fairly flexible lipid molecules, the membrane has a liquid-like 2D structure. In fact, this model is even referred to as a fluid-mosaic, with the proteins freely diffusing in the "sea" of phospholipids.

The latter exhibit a whole range of their own movements: rotation, flexion, continuous lateral diffusion, as well as rare interleaflet flip-flop transfer[8–10], sketched in Figure 2.2.

This freedom of movement in the bilayer depends strongly on the membrane hydration, pressure and especially - temperature. Below a certain, lipid-specific temperature called transition temperature (T_t) the bilayer undergoes a phase transition (Figure 2.2). The thermal energy is then not enough to overcome hydrocarbons' ordering tendency, resulting from van der Waals attraction between FAs. In such conditions the bilayer will exhibit less mobility and behave more like a gel[11]. The transition temperature of a membrane depends on its lipid composition. Although most biological bilayer-forming lipid mixtures tend to be in the liquid phase, with FAs freely mobile and taking up more space, the presence of a rigid phase has also been reported[12–15] .

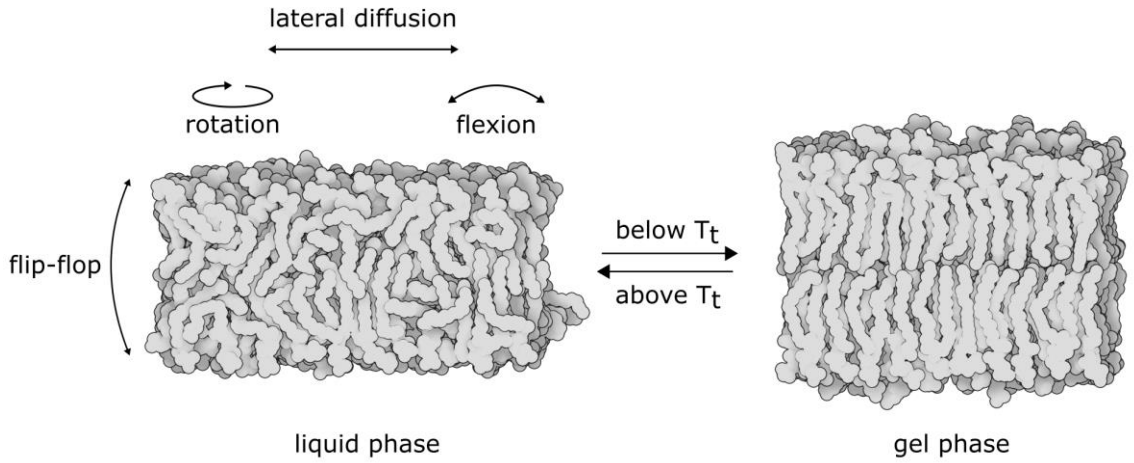

Figure 2.2 *Lipid bilayer is a 2D fluid. All-atom models of the POPC lipid bilayer in liquid and gel phase, above and below transition temperature respectively (simulated models adapted from Heller et al., 1993). Possible phospholipid movements are sketched on the liquid phase model.*

The fact that various lipid phases coexist in cell membranes is of great importance for the functioning of an organism. The concept of lateral compartmentalization of the membrane with "lipid raft" structures is an excellent example. These lipid patches with a composition enriched in sterols, saturated lipids and sphingolipids give rise to spontaneous separation of the bilayer into coexisting domains of distinct physical properties. The rafts provide an enclosed platform for populations of proteins coupled in specific localized processes, as well as take part in cell's signalling[16–18]. Another interesting concept of phase-dependency in biological membranes points out the fact that T_t of many cellular bilayers can be only 10 °C lower than the body temperature[19],

which lead to the development of a theory attributing the neural impulse to the local changes in bilayer phase - solitary density pulses* - travelling along the axon[19–22].

As mentioned above, membrane structure and properties depend strongly on the lipid composition. Although all phospholipids can be described by the head-tail model, each type of PL will differ in further chemical nuances: (I) the length and (II) the saturation of fatty acid chains, and (III) the group attached to the glycerol by the phosphate bond (R in Figure 2.1c). Since each of these features has an impact on the formed bilayer, the next part of this chapter will be dedicated to understanding the aspects of molecular structure of phospholipids.

(I) The length of the fatty acid chain. FAs containing from 2 to >30 carbon atoms have been reported. However, 12-22 is the most common range for naturally occurring PLs, with most of the animal FAs being unbranched, 16- or 18-carbon long chains[8–10].

Naturally, the length of a FA will influence the thickness of the membrane. Furthermore, it also influences the T_t: the more "points of contact" there are between the neighbouring lipid tails, the stronger the van der Waals attraction that keeps them in the ordered (gel) phase, thus the higher thermal energy is required to cause a transition into a liquid state[3,11]. This has been schematically illustrated in Figure 2.3a.

(II) A saturation of the fatty acid chain. Saturation of the FA is particularly important, as it is the main feature determining transition temperature and thus, the phase of cell membranes, where lipid tails are more or less of the same length. A saturated FA chain has solely single bonds, while an unsaturated chain has at least one double bond between two carbon molecules. Two parts of the chain separated by the double bond can either be on the same side (*cis*) or the opposite sides (*trans*) of it. For both isomers, an extra bond changes the way the molecule orients itself in space, introducing a kink in its linear structure. Furthermore, even though single bonds can rotate freely, the rotation around the double bond is restricted. This results in unsaturated lipids exhibiting considerably different interactions between lipid tails compared with the saturated ones. Similar as in the case of chain length, the saturation will determine the number of "points of contact" between neighbouring lipid tails and through that the transition temperature of the corresponding bilayer, as shown in Figure 2.3b. Chains' asymmetry will also have an analogous effect[8,9,11].

*So-called *soliton* model in neuroscience is proposed as an alternative to the generally-accepted Hodgkin-Huxley model.

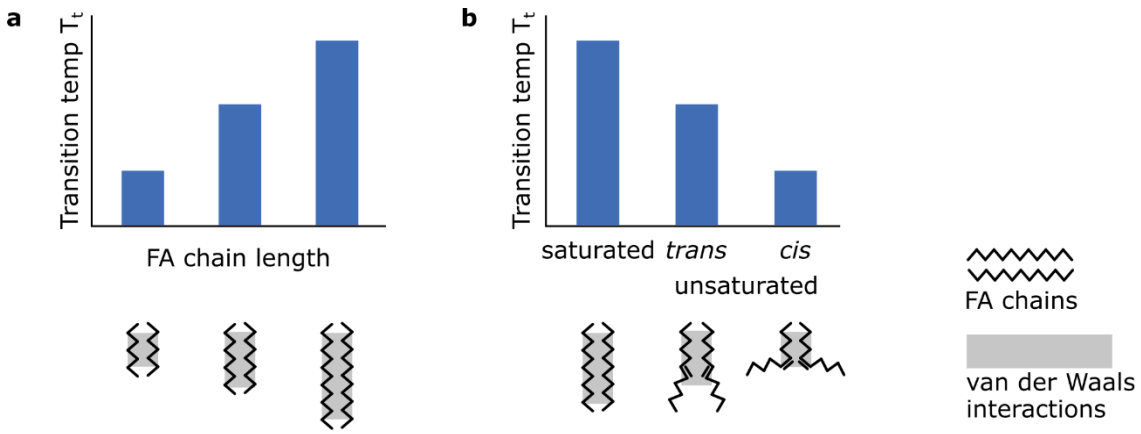

Figure 2.3 *The effect of (a) fatty acid chain length and (b) fatty acid chain unsaturation on the transition temperature of the bilayer. The sketches at the bottom illustrate the origin of the plotted dependency, with the number of "points of contact" - number of van der Waals interactions - changing with length and saturation of the FA.*

Here, I need to digress from the topic of phospholipids. While discussing the factors that determine the mechanical properties of a bilayer, it is important to mention another type of lipid - or rather a single very specific molecular specie: cholesterol. It is the most familiar example of steroid lipids, which are group of molecules derived from sterol: tetracyclic carbon ring[8], called steroid nucleus. The chemical formula of cholesterol, $C_{27}H_{46}O$, as well as careful analysis of its structure presented in Figure 2.4a, make one realize that the molecule consists almost entirely of carbon and hydrogen atoms - exactly like fatty acid chains. Indeed, it is this abundance of carbon atoms, or rather lack of polar functional groups that makes these molecules strongly hydrophobic. The sole oxygen atom is present on a hydroxyl group on one end of the molecule. With its -1 charge when deprotonated, in the membrane the hydroxyl group faces the aqueous environment, determining the direction of cholesterol in a bilayer. On the other end, the sterol group and the hydrocarbon chain will be tucked in between lipid tails and change bilayer packing. By wedging itself between FA chains, cholesterol limits the freedom of movement of liquid disordered (L_d) lipids and forces them into a less fluid, liquid ordered (L_o) phase[23–25]. An illustration of this effect is shown in Figure 2.4b.

The presence of a L_o phase is especially significant for animal cells. The membrane in a gel phase is very rigid (making it prone to breaking) and non-diffusive (preventing movement of membrane proteins, which disrupts their activity), while in liquid disordered phase the membrane is so fluid that it may not hold the proper shape of a cell. And while the latter may not be of such importance for bacterial or plant cells featuring a cell wall, for animals the plasma membrane is what determines

the cell structure and often also its mobility. For that reason, animal membranes have a 40% content of cholesterol[26], which ensures stability of the shape, while preserving the flexibility and diffusivity of a liquid bilayer[27]. Besides, when fitting in spaces between phospholipid tails, cholesterol additionally seals the membrane against any water-soluble molecules, reducing its permeability[28–30].

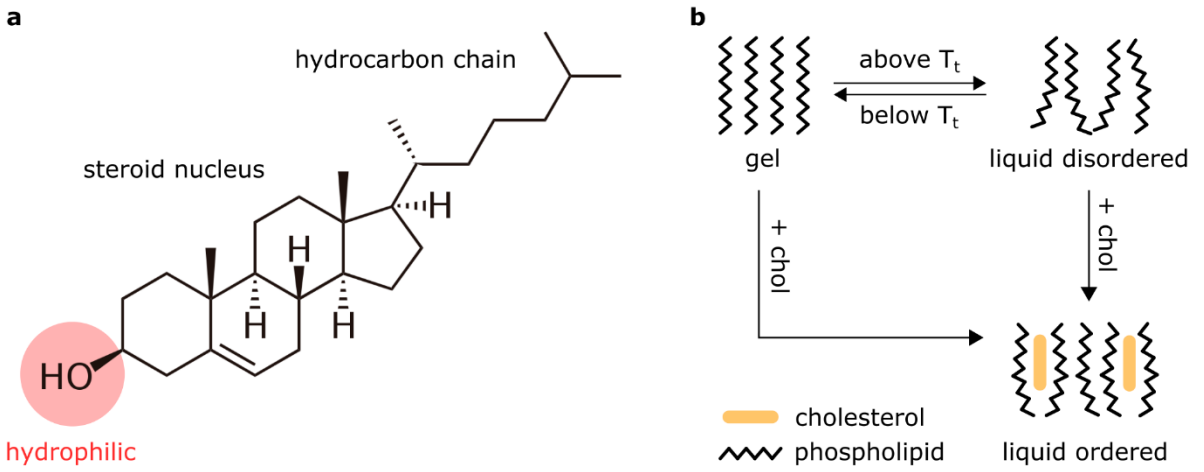

Figure 2.4 *Structure and membrane function of cholesterol. (a) Chemical structure of a cholesterol molecule. The only hydrophilic moiety - hydroxyl group - is highlighted in red. (b) The effect of cholesterol on the structure of lipid bilayers; with an addition of cholesterol, membranes transition to liquid ordered phase.*

(III) A chemical structure of the headgroup. As presented in Figure 2.1c, the headgroup of PLs consists of glycerol, a branched group providing an attachment site for lipid tails, and a phosphate bond, connecting glycerol with a lipid-specific group. There are six such groups commonly present in cell membranes, corresponding to six categories of phospholipids differing in chemistry and electrostatic properties. First five can be generally found in mammalian cells (Figure 2.5a), while PG lipids are typical components of bacterial membranes[3,8]. The molecular structure of each listed phospholipid is shown in Figure 2.5b.

1. Phosphatidic acid (PA): The simplest of PLs headgroups, with no additional functional groups attached to the phosphate. It serves as a precursor in biosynthesis of other phospholipids, but also plays a signalling role in a cell membrane. In physiological conditions phosphate is partially protonated, resulting in a -1 charge on a PA lipid[31].

2. Phosphatidyl**choline** (PC): The most abundant of mammalian phospholipids, can comprise up to 50% of PLs in a cell membrane. Choline consists of alkyl groups centred around a nitrogen atom, which carries a positive charge +1. Along with the phosphate (-1), the PC lipid has no net charge and is one of the most common examples of zwitterionic lipids[32].

3. Phosphatidyl**ethanolamine** (PE): While PC lipids are localized mainly in the outer leaflet, the majority of PE lipids - the second most plentiful PL type in mammalian cells - can be found in the inner leaflet. Its chemical structure is somewhat similar to the PC: it is a zwitterionic lipid, with an additional positively charged nitrogen atom. However, ethanolamine is a much smaller molecule than choline, resulting in a conical, rather than cylindrical shape of the lipid, which plays a role in shaping the membrane[33].

4. Phosphatidyl**inositol** (PI): Inositol is a cyclohexane, with a unique property: three of its six carbon atoms can be enzymatically phosphorylated, resulting in a headgroup with a relatively strong charge of -4. PIs comprise a small percentage of the total lipid composition and nearly all of them are located in the inner leaflet, taking part in cell signalling and protein interactions[34].

5. Phosphatidyl**serine** (PS): Serine is an amino acid, attached with its hydroxyl group to the phosphate of the headgroup. That makes the headgroup consist of amine (NH_3^+) and carboxyl (COO^-) groups, which alongside the phosphate (PO_4^-) results in a lipid carrying a net charge of -1[35,36].

6. Phosphatidyl**glycerol** (PG): This headgroup is really two glycerol molecules linked with a phosphate bond. Abundant in bacterial membranes, it is rarely found in human cells[8,37,38]. The exception being pulmonary surfactants, where it plays a signalling, rather than a structural role[39].

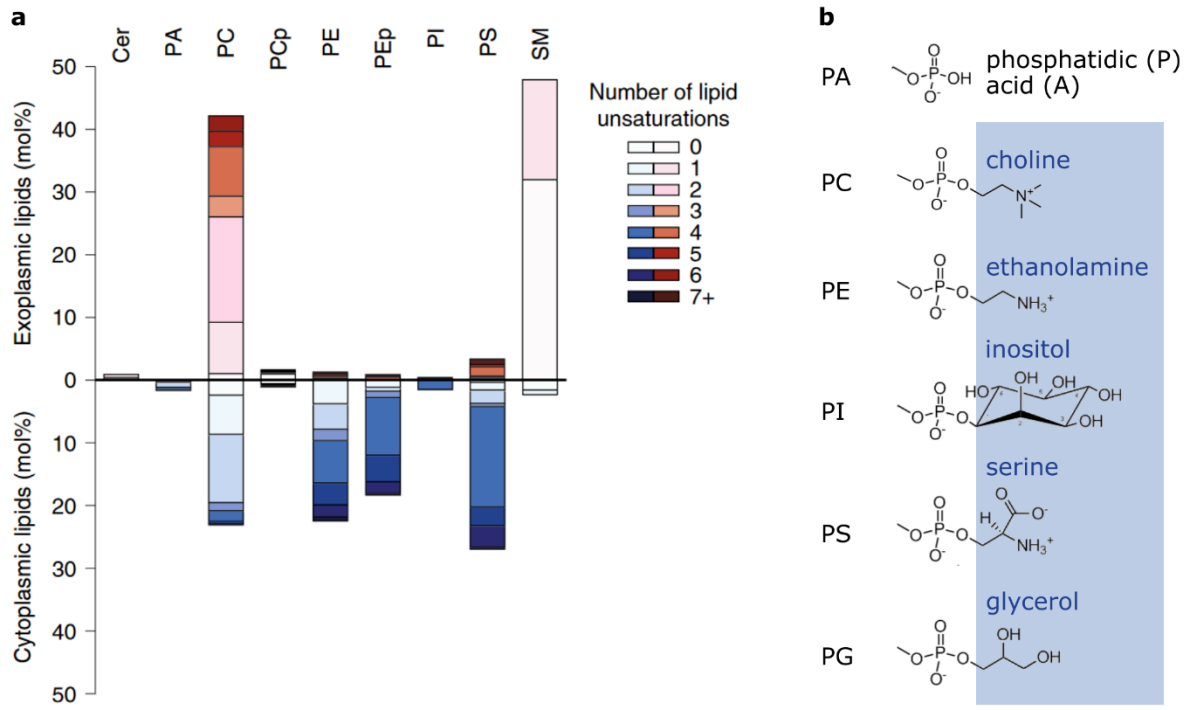

Figure 2.5 *The chemistry of headgroups of cell membrane lipids. (a) The lipid composition of an erythrocyte membrane, adapted with permission from Lorent et al., 2020*. Alongside with phospholipids (P), the membrane contains ceramide (Cer) and sphingomyelin (SM). The cholesterol content of the membrane has not been shown (≈ 40%)[26]. (b) The chemical structure of six most common types of phospholipid headgroups. The part of a molecule that is varied for each phospholipid is highlighted in blue.*

A few additional notes on the chemical structure of a PL's headgroup: Firstly, the charge of a lipid, as for any other organic molecule, depends on pH. Functional groups can be described by their pKa value: pH below which they get protonated in an aqueous solution. The amine group (NH_3^+) has pKa above neutral one and is protonated in physiological condition, making it most often responsible for the presence of a positive charge. On the other hand, phosphate groups are deprotonated and carry a negative charge in physiological conditions, as their pKa is relatively low[40,41]. (In fact, phosphate can even be further deprotonated above pH 12, allowing the lipid to carry a net charge of -2.)[31] When working in extreme conditions, either below pKa of the phosphate groups or above pKa of the amine group, the effects of pH on the structure and functionality of headgroups cannot be neglected[42,43].

*Marked panel has been reused from the cited article (https://www.nature.com/articles/s41589-020-0529-6?proof=t) with permission. Further permissions related to this material should be directed to the copyrights' owner.

Secondly, the phosphate group results in a negative charge *always* being present on the molecule (in physiological conditions). Therefore, in nature we can find zwitterionic and negatively charged PLs, but no purely positively charged ones. There is, however, a growing library of cationic phospholipids, obtained through chemical modification of natural lipids, where an additional ethyl group caps the negatively charged oxygen on a phosphate. These cationic analogues of phospholipids are used as transfecting or gene-delivery agents, as an alternative to synthetic cationic detergents[44,45].

Furthermore, the orientation of a zwitterionic lipid's headgroup is not fixed but will vary with salt and pH conditions. Depending on the surface charge, the N(+) component of a P-N dipole that forms a zwitterionic headgroup will be oriented either towards or away from the water[46]. Interestingly, in a neutral environment the P-N dipole is either nearly parallel to the surface of a bilayer[46] or even have the phosphate exposed more[47,48].

There is another interesting observation one can make about zwitterionic lipids: even though they are chemically comparable, there is a strong preference towards outer or inner leaflet for PC and PE lipids, respectively[26,49,50]. Hence, the three neutral methyl groups carried by PC and absent in PE lipid are identified by the organism as an important structural difference. Indeed, on a molecular scale these extra groups change the geometry of a lipid entirely: the smaller headgroup of a PE results in a conical shape of the molecule, while PC is cylindrical. In fact, we could approximate all lipid species as building blocks of different geometries, and based on their shape assemble them into membranes of certain packing and curvature[33,51] (Figure 2.6).

This seemingly straightforward task (picture building with Lego) gets far less trivial when the target membrane contains not only lipid building blocks, but also a vast library of sophisticated protein structures. Furthermore, these structures not only need to be present in a membrane – they need to be present in a *specific part* of it. The huge number of lipid variations exist partly as an answer to the variety and complexity of protein architectures.

Considering the graph in Figure 2.5a, note also the membrane asymmetry in unsaturation, with inner leaflet having roughly twice as many double bonds as the outer one. As we discussed a few paragraphs before, unsaturation changes lipid arrangement, and therefore an unsaturation asymmetry will lead to a difference in lipid packing between two leaflets. This is yet another example of how lipid scaffold is compatible with the transmembrane structures embedded in it;

the asymmetry in the lipid packing of a membrane correlates with the asymmetric structures of proteins spanning it[26].

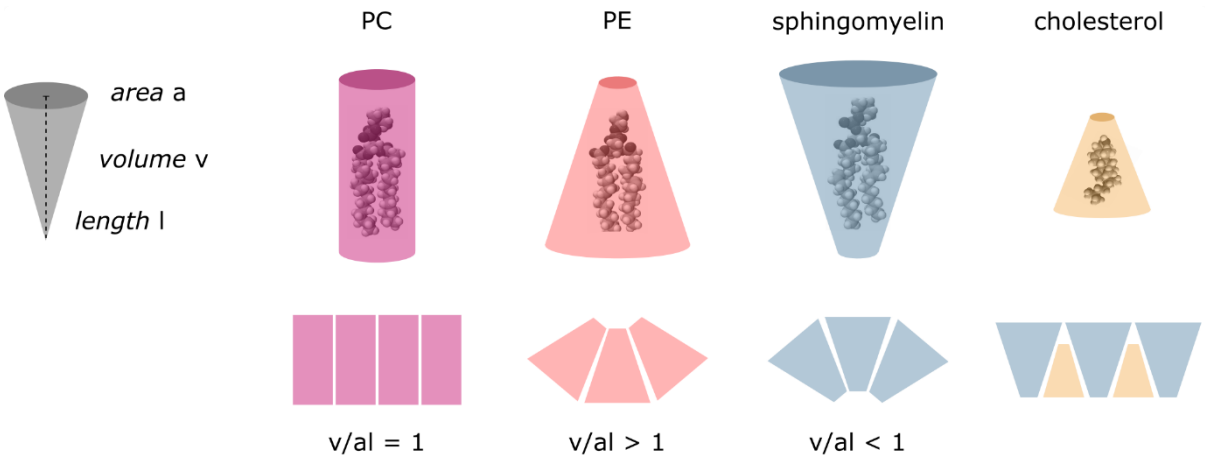

Figure 2.6 *Geometry of a lipid affects membrane curvature and packing. Lipid structures can be described using three dimensions: its headgroup area (a), length of the tail (l) and volume (v). Depending on the relation between these three parameters, each lipid can be approximated as a membrane-building block facilitating certain curvature. All-atom lipid models adapted from the website of a lipid provider: Avanti® Polar Lipids [avantilipids.com].*

In summary, the molecular structure of a lipid corresponds strongly with the properties of a bilayer it forms. Lipophilic tails of PLs are what determines the bilayer's mechanical properties: its thickness, lipid density, diffusivity, rigidity, and provide structure to the scaffold of a membrane. Lipid headgroups, as the aqueous-facing domains, are responsible for the active response of the membrane to signals from both inside and outside of the cell. Note, that this division of tasks between the two parts of the molecule is only a rough approximation. Still, it is sufficient to grasp the basics of lipids' nature and allows understanding of what is presented in next paragraphs: the origin of the structure of membrane proteins.

2.2. Cell membrane components: proteins

As mentioned previously, lipid membranes evolved as a barrier between the environment and the balanced network of cellular components. Cell's machineries are intricate and their working conditions - precisely determined. Their variation with each small change in the environment would disturb their functioning, and such complex metabolisms as ours could never have emerged. Therefore, one of the roles of a cell membrane is control over what ions and organic molecules

will the cellular components be exposed to. Figure 2.7 schematically presents bilayer's selective permeability to various molecular species found in the solution. We can form a conclusion that the larger and more charged the molecule is, the less likely it is to cross the membrane by diffusion[52].

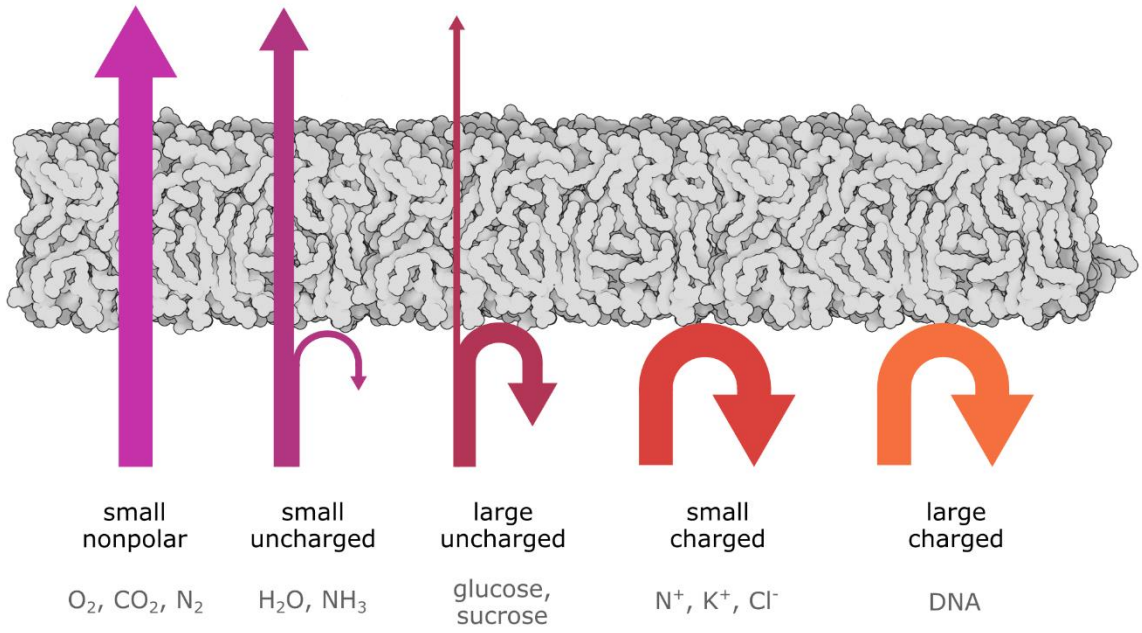

Figure 2.7 *Sketch illustrating membrane permeability to various molecules*[52]*. Simulated POPC bilayer model adapted from Heller et al., 1993.*

Yet, a cell cannot develop in a complete isolation from the environment, not to mention other cells forming the organism. It needs nutrients and it needs information. Ions are of particular importance, as they act as messengers in many signalling pathways, are responsible for membrane potential, driving neuronal and muscular response, and as proteins' cofactors are required for their functioning. Therefore, their concentration in a cell must not only be precisely controlled, but also constantly *changed*, in order to maintain homeostasis in the organism[53–55].

This notion lead to the development of transmembrane proteins*, responsible for transport of crucial molecules through the bilayer. The importance of their role makes them indispensable for sustaining life, as very well known in the medical field, where channelopathies - diseases caused by

*Actually, the evolution of lipid bilayers and membrane proteins was coupled, as none could play its role without the other[335]. Here, I simplify this co-evolution process by only describing it from one end: proteins evolving with respect to bilayers. This is not an account of the evolutionary origins of molecular structure of membrane proteins, but an illustration of contextual architecture in biology.

the disruption in functioning of membrane channels - are numerous and affect nearly every system in a body[56]. This is hardly surprising, as transmembrane proteins are present in a membrane of every cell.

The analysis of lipid membranes presented in the previous paragraphs provides foundations for understanding the nature of transmembrane constructs. *All of the membrane proteins evolved with respect to the membrane's features*. When analysing why do natural transmembrane proteins have a particular molecular structure, and which of their properties are crucial for building a pore, the answer is invariably given in the context of the lipid membrane. In this subchapter I will discuss these questions, starting from the general structure of proteins.

Proteins are polymers, long chains of similar building blocks, connected together *via* a particular type of bond, known as the peptide bond. The building blocks are called amino acids, having two parts: the amino part (NH_2) and the acidic part (COOH). The bond between nitrogen (N) and carbon (C) atoms of these two parts forms the peptide bond ((O)C-N(H))[9,10].

Proteins are not just chains of amino acids – they are *particularly folded* chains of amino acids. Complexity is one of the most prominent features of these molecules. Interestingly, due to the nature of the amino acids, proteins can only be linear. Even though amino acids will differ in their side chains, the essential backbone of the molecule remains a single thread of peptide bonds. This means that their complicated architecture is a result of folding the linear strand of amino acids (**primary** structure) into particular domains (**secondary** structure: helices, sheets, etc.), that further arrange into a complex biological platform (**tertiary** structure) with geometry defined by its function[9].

What then are membrane proteins? Simply put, these are all of the proteins located at the membrane. We distinguish integral proteins (interacting with the hydrophobic core of the bilayer), as well as peripheral ones (not anchored in the hydrophobic core). Integral proteins are further divided into transmembrane and monotopic, depending on whether they span two or only one leaflet of the membrane[10,57,58]. Figure 2.8 illustrates these classes of proteins, showing their interactions with the bilayer.

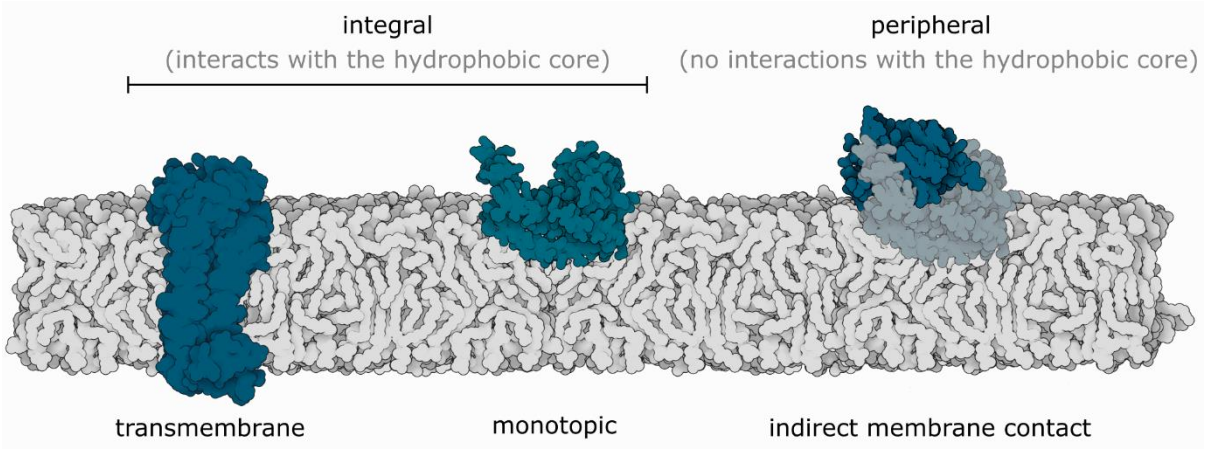

Figure 2.8 *Models of membrane-interacting proteins, schematically representing classes of molecules based on the degree to which they interact with the bilayer (simulated POPC bilayer model adapted from Heller et al., 1993). The structures of proteins were adapted from the PDB entries (left to right): 2m6b*[59]*, 5w7l*[60]*, 4bvm*[61]*.*

Membrane proteins on the extracellular side are often responsible for the cell-to-cell interactions and signalling, while the ones facing the inside of the cell provide an anchoring point for cytoskeleton and trigger intracellular signalling. The transmembrane molecules are most importantly responsible for the membrane transport. Amongst many other functions of the membrane proteins, the catalytic one needs to be mentioned; enzymatic proteins can be found bound to the membrane surface, as well as spanning the bilayer[9,10].

Molecular structures of the three classes of proteins will differ considerably, as each will be adapted to its function. In this work I focus on membrane-spanning molecules, and therefore I will analyse them more closely. The term "transmembrane" is attributed to proteins that are stably incorporated within the bilayer. The details contained in the first part of this introduction (How does the lipid bilayer look like?) combined with chemistry knowledge (How does the chemical structure result in particular properties?) paint the image of the evolution of these constructs. We have already appreciated the simplicity behind the bilayer formation: amphiphilic lipid molecules arrange into membranes with hydrophilic surfaces facing aqueous environment and a hydrophobic core hidden inside. Hence, each membrane is essentially a sandwich of hydrophilic-hydrophobic-hydrophilic layers. The structure stably incorporated within these layers should have a similar composition, in order to minimize the energetic costs of forming such systems. We will discuss this further taking as an example glycophorin, a transmembrane protein present in the bilayer of human red blood cells[62,63].

Since peptide bonds are polar, in aqueous solution they face the water molecules. In turn, when embedded in lipids, peptide bonds turn towards each other and link with hydrogen bonds, "hiding" their polarity. Otherwise, their position in a membrane would be an unstable one, their orientation not so well-defined, and as a result – their function disturbed. The formation of the hydrogen bonds within the amino acid chain is maximized in a conformation of an α helix. Therefore, most of the transmembrane proteins cross the bilayer in a helical form[9].

This is exceptionally illustrative in the architecture of glycophorin: the atomic representation in Figure 2.9a shows that the membrane-spanning domain does not have nitrogen or oxygen atoms exposed, suggesting that the functional groups that can carry the charge in a solution (amine NH_3^+ and carboxyl COO^-) are hidden. This is enabled by the formation of a helical section in the hydrophobic region, as shown by the ribbon representation in Figure 2.9b. The α helix is stabilized by the hydrogen bonds between the atoms forming a peptide bond within a single amino acid chain, schematically sketched in Figure 2.9c.

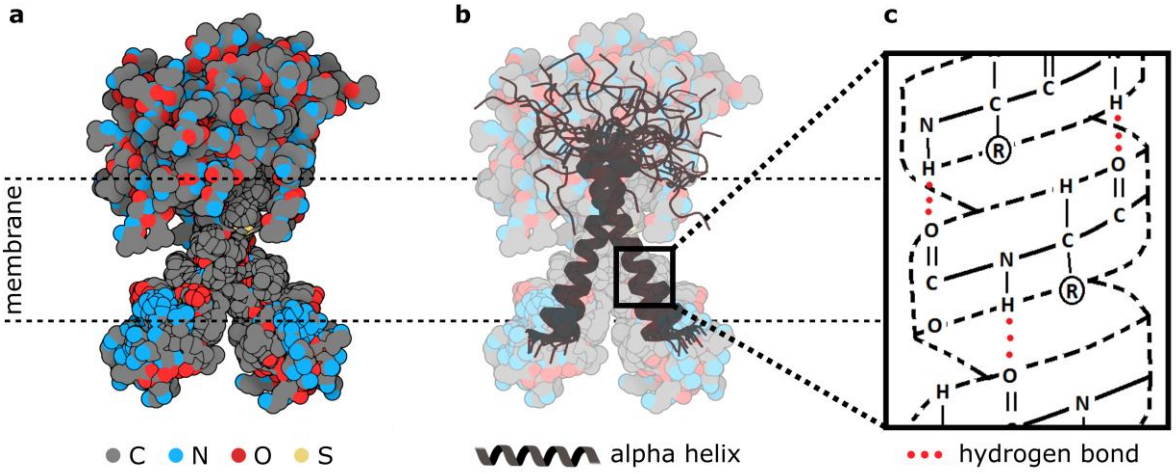

Figure 2.9 *Structure of the membrane-spanning proteins: glycophorin A (GpA). (a) All-atom model of a representative transmembrane protein glycophorin A. Hydrogen atoms not shown for clarity. Most of the visible red and blue atoms represent polar carbonyl (C=O) and amino (NH) groups exposed to aqueous environment, and "hidden" in the membrane spanning domain. The molecular structure was adapted from the PDB entry: 1afo[64]. (b) The membrane-spanning domain is formed of two alpha-helices, as shown by the ribbon representation (1afo[64]). (c) Schematic chemical structure of an alpha helix showing hydrogen bonds between polar amino and carbonyl groups. Adapted from B. A. Russel, 2017*.*

*Marked panel has been reused from the cited doctoral thesis (DOI: 10.13140/RG.2.2.36594.40645) with permission. Further permissions related to this material should be directed to the copyrights' owner.

Alpha helices are capped from both sides with polar domains, preventing the construct from slipping through the membrane, stabilizing its position. In the case of glycophorin, note the relatively massive "fringe" of polar residues facing the extracellular side of the membrane (Figure 2.9b). It forms a highly charged coating of the cells, preventing them from adhering to other parts of an organism, which facilitates circulation in the blood stream. Glycophorin is a perfect example illustrating how the structure of the transmembrane proteins always follows their functionality. Note that the same ideas can be extrapolated to other structures: only one hydrophobic part of monotopic proteins exhibits membrane affinity, while peripheral proteins have no hydrophobic domains, since they do not interact with the core of the bilayer[10].

To realize how the molecular structure of membrane proteins looks like is what I consider one of the most important points of this introduction. Firstly, it illustrates the idea that I will stress repeatedly in the course of this work: a molecule is never designed in isolation, but always in the context of its surroundings. The architecture of natural structures evolved with respect to their function, as well as their environment. What is more, by observing the natural constructs we know what solutions *work* in the system. Evolution was kind enough to run statistical simulations for us.

Seeing their significance and the overwhelming control they exert over living life forms, membrane proteins are often mimicked[65], with an aim of substituting a damaged natural analogue, creating a synthetic cell or to understand the molecular details of cell's activity. Nucleic acid nanotechnology is one of the promising pathways towards synthetic membrane structures, offering a unique ability of controlling the shape at the nanoscale.

However, looking again at Figure 2.7, we realize that what makes these membrane-spanning structures in demand - bilayer's selective permeability - is a source of issues in their use: DNA and lipids are not made to function in close proximity. Nevertheless, unique features of DNA drive researchers, including myself, to find modifications necessary to overcome the unfavourable interactions, while preserving the structural controllability.

With this in mind, I aim at creating a hierarchy of interactions in DNA-lipid system, learning about each by opposing it with another. I will give an account of this approach in Chapters 4-7. First, however, I will introduce one more topic: the properties of DNA.

2.3. Synthetic cell membrane components: DNA

At the end of this part, you will realize that building *something* with DNA is extremely easy. There are simple rules that one has to follow, and the rest is left to logical thinking. As a matter of fact, no knowledge above what was introduced in high school biology classes seems to be required.

Unless one wants to invent something new. DNA nanotechnology is a field still packed with potential new solutions, waiting to be developed. For that, one will need creativity, an understanding of the building material (Section 2.3.1), as well as the library of previously reported concepts and ideas (Section 2.3.2).

In this subchapter I will focus on key details concerning this thesis, rather than attempt to present a full account of DNA nanotechnology. Still, some of the notions described here may spark an idea, and what better reason for writing a scientific text can one have?

2.3.1. DNA as a building material

Alongside lipids and proteins, nucleic acids make one of the most important group of biomolecules. Like proteins, they are unbranched polymers, long strands of analogous domains called nucleotides (Figure 2.10a), that fold in a characteristic way, ensuring their functionality[3,66,67].

The acidity of nucleic acids comes from their phosphate group PO_4^{2-}, very similar to phosphatidic acid described earlier. This group provides a linkage between neighbouring monomers, with one of the oxygen atoms (O^-) used to form a phosphodiester bond. The remaining oxygen is responsible for the acidity of the molecule, introducing hydrogen ions (H^+) upon its deprotonation in aqueous solution. Phosphate links together pentose sugars of two monomers (Figure 2.10b). Such five-carbon sugars are called riboses: the unmodified ribose is a component of the ribonucleic acid (RNA), while its structural analogue, deoxyribose, gives name to the deoxyribonucleic acid (DNA). These sugars are cyclic "stems" of the molecule, a central group of carbon atoms linked together with phosphodiester bonds, forming a sugar-phosphate backbone of the polymer: the single-stranded (ss) nucleic acid[3,9,10].

Unlike proteins, a single thread of nucleotides (most often) does not form secondary structures, but remains flexible and disordered in a solution. The well-known twisted structure of DNA forms

only when two matching single strands come together, forming a double-stranded (ds) DNA - a **double helix.**

Ultimately, we aim at using DNA as a building material to design constructs at the nanoscale. Understanding its ability to self-assemble into a double helix is the key to achieve self-assembly into whatever-shape-one-can-imagine. Therefore, let us analyse *how* does the dsDNA structure spontaneously form, splitting the process into two steps: (1) connecting two ssDNA molecules and (2) twisting into a helix.

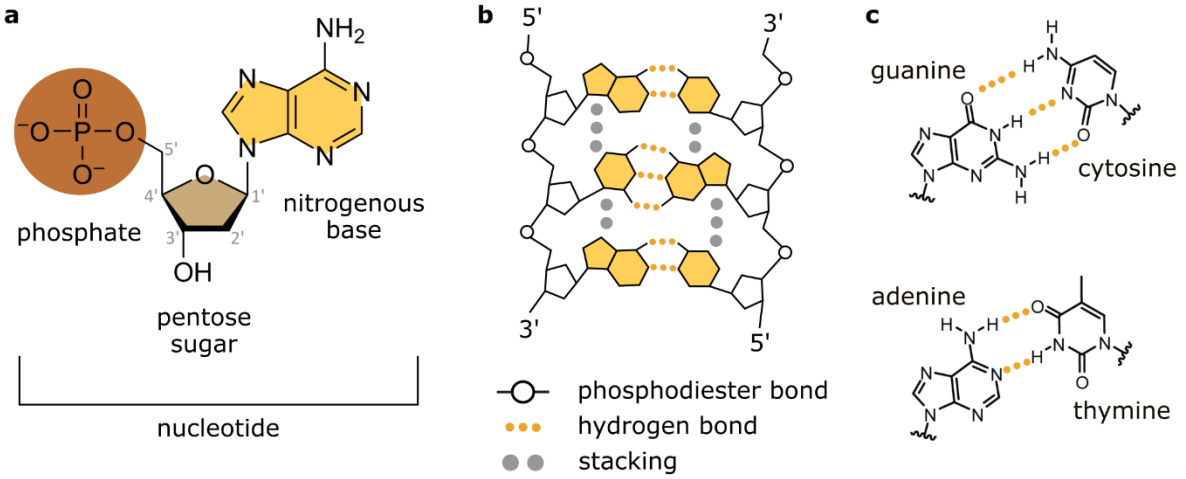

Figure 2.10 *Formation of a connection between two complementary ssDNA. (a) The chemical structure of a DNA nucleotide. Symbols written in grey are a conventional numbering of carbons in a pentameric ring of a sugar. (b) A sketch highlighting the interactions in dsDNA. The covalent phosphodiester bonds between sugars form the backbone of each strand. Formation of a connection between matching oligonucleotides is ensured by the hydrogen bonds between complementary bases, as well as stacking between the adjacent ones. Note the antiparallel direction of the two connected strands, with each end labelled after the unbound carbon: either 3' or 5'. (c) The basis of the complementarity between G-C and A-T bases, with respective base pairs formed with either three or two hydrogen bonds.*

1) The variable domain of a nucleotide - the nitrogenous base - typically occurs in DNA either as a single-ring pyrimidine (thymine (T) or cytosine (C)) or a double-ring purine (adenine (A) or guanine (G)). These four nucleobases, presented in Figure 2.10c, provide chemical groups through which they can be linked together in pairs; the connection between two ssDNA comprises of hydrogen bonds between bases of the opposite strands (Figure 2.10b).

Note, that every single strand has two ends with different terminal functional groups, indicated by the chemical convention of naming carbon atoms in the nucleotide's sugar: the 5' end has a terminal phosphate group, while the 3' end terminates with a hydroxyl group (Figure 2.10a). This is especially important, since a connection forms only between strands going in *opposite* directions, making the double helix an **antiparallel** construct.

Most importantly, **base pairing** in DNA strands is highly selective and occurs only between AT and GC bases. This specific bond formation, known as the Watson-Crick base pairing, is responsible for the most common DNA structure, mainly due to the steric hindrance preventing other combinations*. Simplifying, AT pair takes up as much space as GC pair, therefore these specific combinations are favourable, because they do not introduce any distortion into the helix. The chemical structures of the two types of base pairs are shown in Figure 2.10c, where one can also notice the different number of formed hydrogen bonds: three and two for GC and AT pairs, respectively[3,9].

The hydrogen bonds are commonly considered a factor determining the double-helix folding, which is seemingly confirmed by higher thermal stability of GC-rich duplexes (more H-bonds) than that of AT-rich structures (less H-bonds)**. Yet, thermodynamic analysis combined with calorimetric studies show that hydrogen bonds do not contribute to the maintaining of the double strand as much as another interaction - **base stacking**[68,69].

Aromatic rings of bases are oriented perpendicularly to the strand, parallel to each other. These flat, apolar groups pack tightly in the core of a helix, linked with non-covalent bonds. Additionally, the clouds of π electrons of adjacent bases merge, giving rise to the so-called π-stacking interactions. Even though H-bonds are considered the determinant of the duplex structure, stacking was shown to contribute to its stability more significantly[68].

Both base pairing and base stacking are intertwined in the process of DNA folding. They are mutually dependent on their spatial orientation determined by one another, and are crucial for the proper helix structure[68]. I will discuss the thermodynamics of a duplex formation in detail in Chapter 5. For now, we will focus on the specificity of connection between two oligonucleotides,

*Other combinations are possible and do actually provide a huge field for manipulating the structure. For example, there are Hoogsteen pairs enabling a formation of triple helices[336] or Wobble pairs between the nucleotides of RNA[337].
**In fact, this difference in thermal stability is strongly determined by the water molecules immobilized by AT pairs. For a detailed analysis of the duplex formation see Chapter 5.

regardless of its driving factor. Only the strands with matching sequences of A, T, C, G bases - **complementary** strands (running in opposite directions) - will come together and form a double-helix.

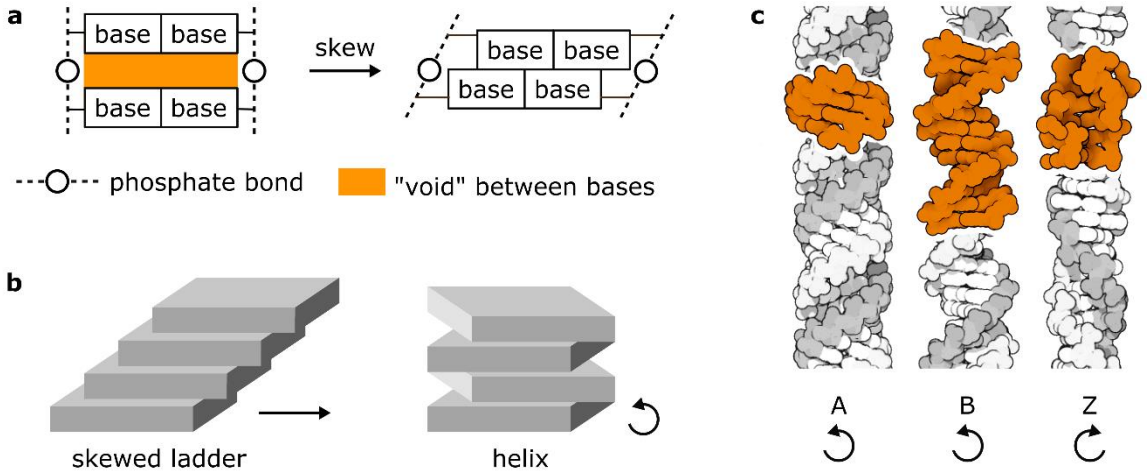

Figure 2.11 *Formation of a twisted DNA double-helix. (a) A schematic representation of an emergence of a "void" between bases hindering dsDNA from adapting a stretched, non-twisted structure, and a possible solution in skewing the bond. (b) A conceptual sketch showing how twisting into a helix allows to "fill the voids" similarly to single-directional skewing. (c) Molecular structures of A-, B- and Z-DNA. The crystallographic data were adapted from PDB entries 1ana*[70]*, 1bna*[71]*, 2dcg*[72] *for the three respective forms, while the grey image is adapted from David S. Goodsell (RCSB PDB, Molecule of the Month series). The directionality of the twist (right-handed for A and B forms, left-handed for Z form) is schematically shown with an arrow.*

2) Having determined the interactions responsible for establishing a connection between two strands of DNA, we should now understand what drives the twist of such duplex. How is the *helical* structure formed?

The distance between adjacent base pairs is 2.7 Å*, which results in a significant space for water molecules to nestle near the bases. However, the bases, and therefore the core of the dsDNA, are hydrophobic - presence of water within the centre is strongly unfavourable. One way of arranging the strands to remove the "voids" between base pairs is to skew the bonds, as shown in Figure 2.11a. In order to avoid certain steric hindrance issues coming from this arrangement, a twist is introduced into such skewed ladder model, resulting in the known double-helix structure (Figure 2.11b)[67].

*Centre-to-centre it is 3.4 Å[9], while 2.7 Å is the distance between the bases' edges.

We can twist the ladder in two directions, however, the commonly-occurring DNA is twisted to the right, with 10-10.5 bp per twist[73]. This form, called B-helix, is adapted by DNA in conditions typically found in living cells. The other right-handed structure, A-DNA with a "tighter" twist of 11 bp, forms under dehydrating conditions. RNA, unstable in a B form due to an extra hydroxyl group causing a steric hindrance, also adopts an A structure. In high salt concentrations DNA with alternating guanine and cytosine nucleotides can also twist to the left in a Z form with 12 bp per twist[74]. Models of these three DNA architectures are presented in Figure 2.11c.

In the two-step process of double-helix formation, nature allows for variation on both pairing and twisting. Yet, most commonly, Watson-Crick base pairing (A=T, G≡C) leads to the formation of a right-handed B-DNA structure, and this is the structure we will discuss by default. We know that when two single strands with complementary bases are mixed they form base pairs and twist together into a helix of a dsDNA molecule. In nature these entwine a set of globular proteins, and are tightly folded into bundles - chromosomes - comprising the genetic material of a cell. The specificity of interactions between complementary bases of nucleic acids is the foundation under encoding information in a linear structure of a double helix.

However, there is nothing that limits a DNA construct to just two components. Knowing the principle behind the nucleic acid hybridization, one can take DNA structures to the next level of complexity: instead of using them to carry genetic information, think of it as a building material to fold into any desired shape. Designing the oligonucleotide sequences that bind more than one strand allows to program the shape of the structure, leading to the development of a vast library of such DNA-based constructs (Figure 2.12a).

In short, spontaneous double-helix formation is the basis of DNA nanotechnology. However, it mainly explores possibilities related to the first "step" of the process: complementarity of nucleotides. The second "step", the twist, remains mostly unharnessed in DNA nanoengineering (although it must be mentioned that B-DNA to Z-DNA transition has been utilized to build mechanical molecular machines out of nucleic acids[75,76]). Looking at Figure 2.11c and comparing the structures of A-DNA and B-DNA, there is a potential for introducing an additional fine-tuning mechanism, where the distances between modifications along the long axis of the strands can be changed by over- and untwisting of the double-helix. In fact, while exploring its biological significance, scientists have studied B↔A, as well as right- to left-handed transitions thoroughly[77-79]. However, the microscopic level of changes, combined with many

problems still to be faced when controlling the structure at a larger scale, make it a largely unexplored pathway in DNA nanotechnology. I will discuss the helical twist more in Chapter 5, as well as in the outlook in Chapter 8. Here, I will focus on describing what can be considered the very foundation of DNA nanotechnology: how complementarity of the nucleotides is used to build desired shapes at the nanoscale.

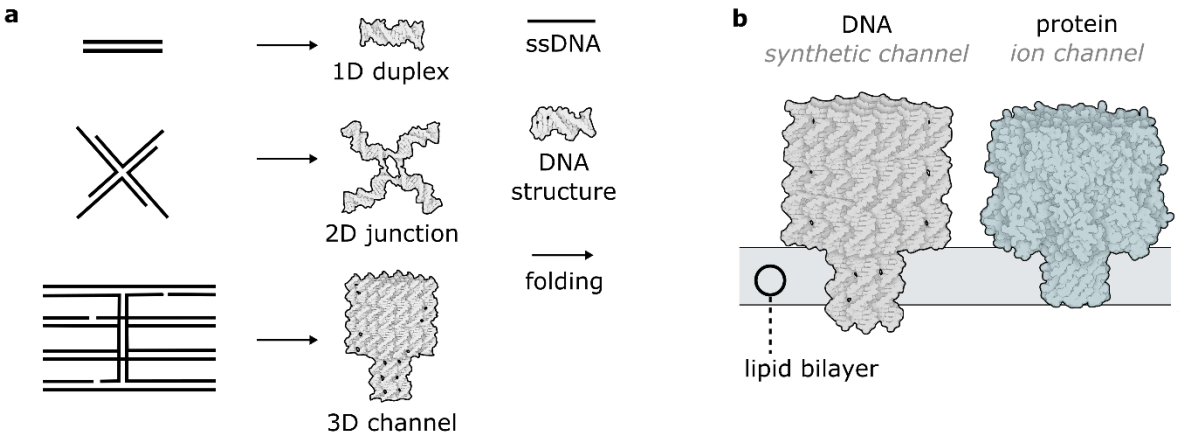

Figure 2.12 *Folding DNA into complex shapes. (a) Sketch showing the concept behind building with DNA. The crystallographic data for the DNA dodecamer and Holliday junction were adapted from PDB entries 1bna*[71] *and 2crx*[80]*, respectively. (b) Sketch comparing a DNA-based synthetic channel with a natural membrane spanning protein, α-hemolysin. The crystallographic data for the protein was adapted from PDB entry 7ahl*[81]*.*

As mentioned earlier, in biological systems DNA forms a linear, double-stranded structure, yet no physical hindrance limits the design to just two strands. Taking it just one step further: a few strands, each complementary to parts of two others, can be designed to form a branched motif[82-84]. The schematic design of an exemplary four-way (Holliday) junction construct is featured in Figure 2.12a - note the elongated ssDNA at the end of each arm. These so called **sticky ends**, as opposed to **blunt ends**, allow to program 2D DNA tiles into a bigger lattice[85,86]. A network that could be spatially controlled through programming the sequences of branched DNA motifs was in fact an inspiration that gave rise to the whole field of DNA nanotechnology*.

Many new ideas formed since nucleic acid engineering emerged for the first time. Here, I distinguish three approaches used to create DNA-based constructs: (I) Both in 2D, as well as 3D,

*Nadrian Seeman invented the field of DNA nanotechnology inspired by an arrangement of fish flying in the eerie artwork *Depth* by Maurits Escher[300].

branched junctions can be used to form bigger, modular constructs[87–89]. (II) A single long strand of DNA - "scaffold" - can be arranged in a desired shape by binding it in various places with short DNA "staples". This so-called **DNA origami** technique[90] is used for building relatively large structures, with a typical scaffold strand being a bacteriophage m13 of more than 6k nucleotides. (III) Smaller designs do not feature a single strand as a scaffold for the whole structure, but rather consist of a set of oligonucleotides that form the desired shape when bound together; DNA nanoengineering uses shorter strands of similar lengths to build simple shapes like DNA duplexes or multi-helix bundles.

As emphasized in the previous sections, membrane proteins have complex molecular structures, with a lot of functionality incorporated within a small space. Building with DNA carries two unique advantages: ease of chemical modification and a high level of control over the structure's geometry. Therefore, it is a powerful tool for synthesising nature-inspired molecular machines like ion channels (Figure 2.12b) or other membrane proteins.

2.3.2. DNA-based synthetic membrane structures

Similar to proteins, DNA constructs can interact with membranes in different ways; we distinguish between the transmembrane (spanning the bilayer) and monotopic (attached on one side) structures. I will briefly summarize reported constructs of both types, focusing, however, on the membrane-spanning ones, as they relate to the topic of this work more.

2.3.2.1. Transmembrane DNA structures

Knowing the important role of natural membrane proteins, scientists embarked on a quest to build their artificial analogues. The idea of building a synthetic transmembrane construct is by no means attributed to DNA nanoengineers. The work of Alan Hodgkin and Andrew Huxley on the ionic basis of nerve impulses (Nobel Prize in Physiology and Medicine, 1963[91]) seems to have given rise to the emergence of synthetic ion channels. Amongst many published examples[92], let me briefly describe three that in one way or another carry an insight that I consider important.

The first attempt to form synthetic channels was made with the use of beta-cyclodextrin, reported in 1982. The design was mimicking what was believed to be the regulatory mechanism of peptidic gramicidin - two subunits diffusing within opposite leaflets of a cell membrane, only forming a pore

when aligned[93]. This very first pore was directly **inspired by the mechanism of natural proteins**. Ten years later, still in the times of the first synthetic ion channels, it was shown that ionic transport may be obtained without using tube-shaped constructs, simply by inserting an ion pair (ether(-)/alkyl(+) tails) into the membrane[94]. This work proved that **structures with a cavity are not required** to observe a stable transmembrane ion flow. Finally, the idea of using crown ethers was evolving for years, spanning a few reports on consecutive generations of ion channels[65,95–97]. Crown ethers are cyclic oligomers of ethylene oxide, with a repeating $–CH_2CH_2O-$ unit. The arrangement of oxygen atoms in a crown spatially mimics oxygen from H_2O molecules of a hydration shell around monovalent ions. Therefore, crown ethers are known to coordinate cations in a very selective way: tetrameric, pentameric and hexameric crown ether will coordinate Li^+, Na^+, K^+ respectively. Thus, crown ethers can provide foundation for ion selectivity of synthetic channels.

After MacKinnon was awarded the Nobel Prize in 2003 for his studies on the selectivity of potassium channels[98], synthetic transmembrane structures became a hot-topic in the field of biomimetics. New approaches to pore formation were appearing continuously throughout the 21st century. In 2012, 30 years after the first synthetic ion channel, the difficulty of reliable design at the nanoscale was addressed using a state-of-the-art technique - building with DNA[99].

The first nucleic acid-based ion channel was folded using DNA origami method, measured nearly 50 nm in height and had a pore-forming domain of a diameter Ø = 6 nm. Importantly, it was the first attempt of overcoming unfavourable interactions between hydrophilic DNA and lipid membranes by introducing strongly hydrophobic anchors - cholesterol molecules. At the time of writing such anchors, whether cholesterol or other hydrophobic moieties, are still the most common way of ensuring the structure's affinity towards membranes.

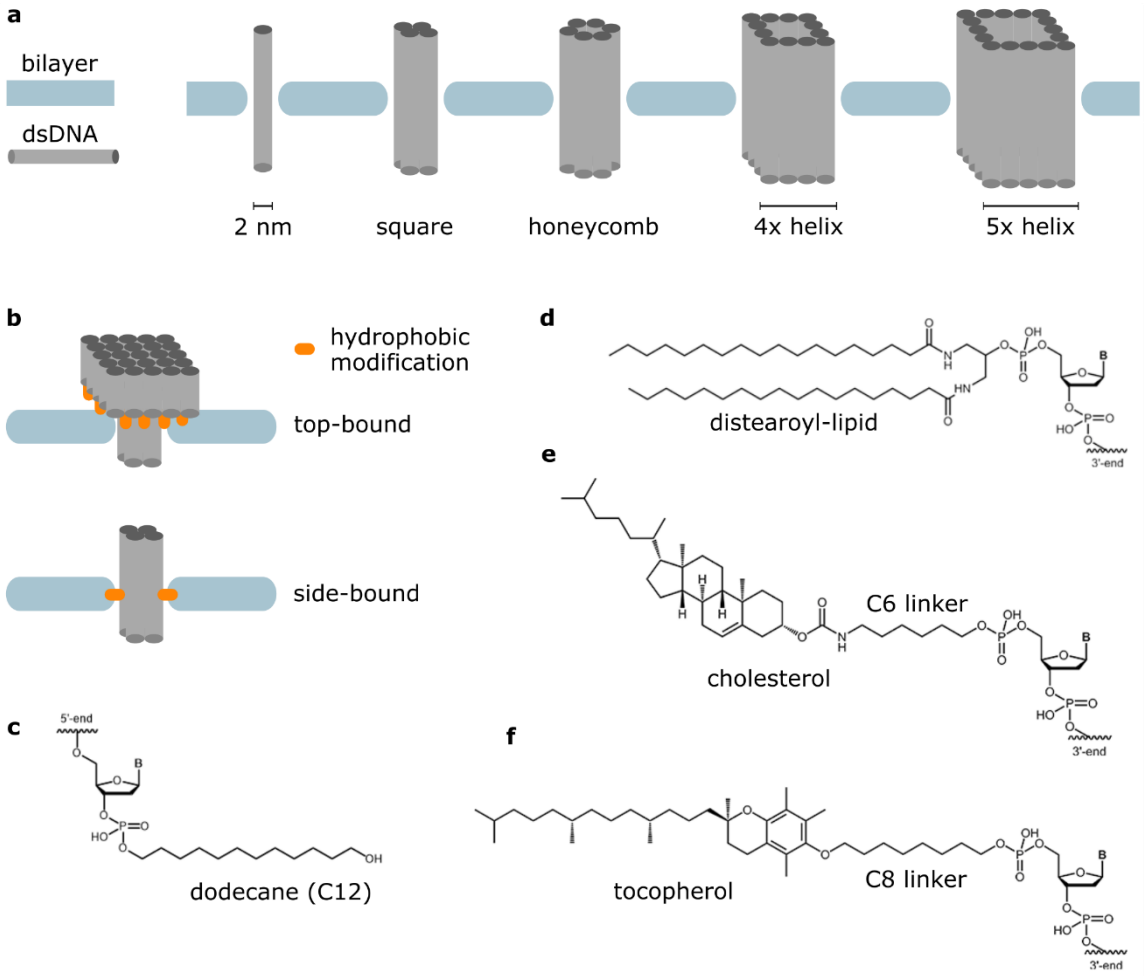

Figure 2.13 *Structure and chemistry of DNA-based pores. (a) Geometries of reported membrane-spanning domains of DNA-based channels. (b) Two modes of binding to the membrane: top-bound structures have hydrophobic anchors on an additional platform, while side-bound are attached within the membrane-spanning part. Chemical structures of some of the hydrophobic modifications: (c) alkyl chains like dodecane (d) distearoyl-lipid, (e) cholesterol, (f) tocopherol. Note that modifications are often attached to the DNA backbone through an additional linker (C6/C8/TEG).*

Many new constructs have been designed after the first DNA ion channel was published, but none went too far from this leading idea: DNA helices are arranged in various number, from a single helix of 2 nm in width[100], to a structure of almost 15 nm in diameter[101] (Figure 2.13a). Nearly all of them rely on hydrophobic modifications to ensure membrane attachment. However, structures can be anchored in a bilayer in two different ways: from the top, featuring an additional DNA platform[99,101], or from the inside of the pore[102,103] (Figure 2.13b). The library of hydrophobic modifications includes various lipophilic molecules (Figure 2.13c-f): fatty acid chains[104],

tocopherol[105], alkyl chains[106] and cholesterol[102]. The latter is still the most popular choice in DNA designs. As a matter of fact, when one looks at Figure 2.13, which sums up the general design principles of membrane-spanning DNA constructs, it seems that even though the shape, size and chemistry were varied, the basic idea remains unchanged since the first report in 2012.

However, seemingly small variations in the design often lead to a deeper understanding of the system. Studies made on the membrane-spanning DNA duplex[100] were especially insightful. They revealed the lipids' arrangement within the pore, as well as the hydrophilic environment at the DNA-lipid interface, which results in an ion transport even in the absence of a cavity. As in the case of the simple ether(-)/alkyl(+) ion pair from the early 1990s[94] mentioned before, researchers realized that an ion channel does not necessarily need to feature a tunnel through which the ions flow. The DNA-lipid interface in a pore was further studied with a bigger 4-helix bundle, which showed that not only the ion transport, but also an interleaflet lipid movement is induced upon pore formation[102]. Both these studies laid foundations for Chapter 4 of this thesis and will be discussed more thoroughly there.

These "side effects" of building a transmembrane domain with DNA prevent us from creating a reliable active structure, e.g. any gating mechanisms that block the cavity are futile, if ions can simply bypass them using the pore's interface. Therefore, another design seems very compelling: a 6-helix pore with a modified DNA backbone[107]. The membrane-spanning part of the pore's structure features charge-neutral phosphorothioate-ethyl groups instead of phosphates. Eliminating negative charges from the DNA-lipid interface is a considerable step towards a controllable bilayer pore and could significantly improve pore-forming activity of all nucleic acid membrane designs. Especially since, as we have seen in previous section, a hydrophobic membrane-spanning domain is already a "standard" in the transmembrane proteins' architecture.

Apart from multi-helix bundles, big origami structures (similar to the first one from 2012) were also shown to induce membrane transport[101,108,109]. Their large cavities evoke antimicrobial peptides and perhaps may be applied in a similar, cytotoxic manner. Note, that typical, m13-based origami constructs are twice larger (6 kbp $\approx$ 4 MDa)* than even the biggest natural ion channel (RyR, m $\approx$ 2 MDa)[110].

*An average mass of a base pair 660 Da[338] and 6407 nt-long m13 bacteriophage scaffold[339] make it a construct weighting 4.23 MDa.

2.3.2.2. Monotopic DNA structures

Inserting nucleic acids into a lipid membrane is intrinsically difficult. It is far easier to achieve DNA structures simply attached on one side of the bilayer. Therefore, the reports on monotopic DNA constructs are numerous and varied.

Every cell membrane is a crucial sensing platform and from viral units[111] to immune systems[112] the functionality of many molecules is based on their interactions with membrane receptors. Often the same receptor is present on a range of cells but in varying concentrations and distances. Monovalent binding would not discriminate between these different cells. However, if a protein binds to many receptors simultaneously, and its structure favours certain distances between them, super-selectivity can be achieved[113–115].

Such multivalent binding is a concept using pattern recognition to enhance the selectivity of interactions. Taking advantage of the most prominent asset of DNA engineering - nanoscale design precision - researchers have built constructs with well-defined spacing between ligands, to mimic proteins' enhanced selectivity and sensing efficiency[116,117]. However, an important thing to notice is that this binding is truly effective only when the distances between the receptors are approximately known. The more knowledge is gathered on the spacing between receptors, the more one can benefit from the idea of multivalent targeting. Therefore, DNA domains were also used to measure the distances between receptors[118,119] - an application to which DNA nanotechnology seems to be a perfect candidate.

Nucleic acids were also used to exert a more profound effect on the structural properties of the membrane: remodelling proteins have inspired many designs of DNA structures, and soon they could potentially enable controllable liposome division - an important step towards building a synthetic cell[120]. Arched BAR protein domains have been mimicked by curved DNA origamis[121]. The straight DNA filaments have also induced bilayer deformation[122]. Not only reshaping but also self-assembly and templating of liposomes were achieved by nucleic acid-based constructs[123–126]. 24-helix nanosprings that can tubulate membranes resemble spiral-like dynamin and ESCRT proteins[127].

Interestingly, tubulation was also induced by smaller 6-helix pores[103], as well as 4-helix DNA-tile structures[128]. However, for the purpose of controlled reshaping of the membrane, big DNA

origami constructs are usually a more obvious choice. The reason these structures have such a prominent effect on the shape of cell-sized vesicles is a combination between a rational design of membrane-anchoring modifications and the stiffness of nucleic acid's double-stranded form. Upon DNA binding to the lipids, the flexible membrane is forced to follow the structure's shape. Therefore, the scale of the constructs will determine the scale of the deformation, which justifies why DNA origami is a popular design choice but leads to a troublesome conclusion: there is a high chance that *all* of the hydrophobically-modified DNA structures of a well-defined shape will cause membrane deformation. The distortion may not be visible on a scale that is easily detected with standard imaging techniques, yet it may have an effect on bilayer's behaviour that should not be neglected.

Another protein - clathrin - is also known to deform membranes, as well as facilitate endocytosis[129]. DNA nanoengineering is a perfect tool to mimic its rather unique structure of triskelion monomers polymerizing into a cage-like scaffold around a cell. Wide DNA origamis[130], as well as simple three-arm junctions[131], were employed to build a synthetic clathrin monomer, which upon their polymerisation create a cage-like coating of vesicles. The former are reported to be "20 times more massive than their natural counterparts", making them presumably very stiff, while simple three-arms junctions are known to be flexible[84]. We can hypothesize on their effects on the liposomes: the DNA origamis will probably have a more profound deforming effect, while the smaller junctions will coat the vesicle in a more accurate manner. This is, of course, difficult to predict. Therefore, in mimicking clathrin, the choice of DNA nanotechnology is not trivial, and comparative studies could bring a lot of insight.

Apart from deforming liposomes and moving towards their division, the antagonistic, fusion-mediating protein system - SNARE - was also mimicked; membrane-bound DNA was used to induce vesicle fusion[132–135] as well as coupling[136]. A key to fusion is bringing two membrane patches in a close proximity, which is achieved by anchoring complementary oligonucleotides in respective liposomes. The formation of a favourable double helix drives vesicle contact and consequently - fusion.

Mimicking SNARE system is a particular favourite of mine because it illustrates the main design principle in DNA-membrane nanotechnology: balancing the forces in a complex system. The task is to overcome the repulsive hydration forces between lipid headgroups by applying a stronger stimulus - DNA duplex formation (which in turn is driven by unfavourable exposure of

hydrophobic nitrogenous bases to water). Effectively, researchers are playing tug-of-war with molecules: trying to assess the strength on one side and then either balance or surpass it on the other. If the anchor is too weak, the duplex will fall out of the membrane instead of bringing them closer. If the duplex is too short, the force will not be strong enough to exert any influence over the membranes. Figure 2.14 illustrates the fusion problem in a simplified sketch.

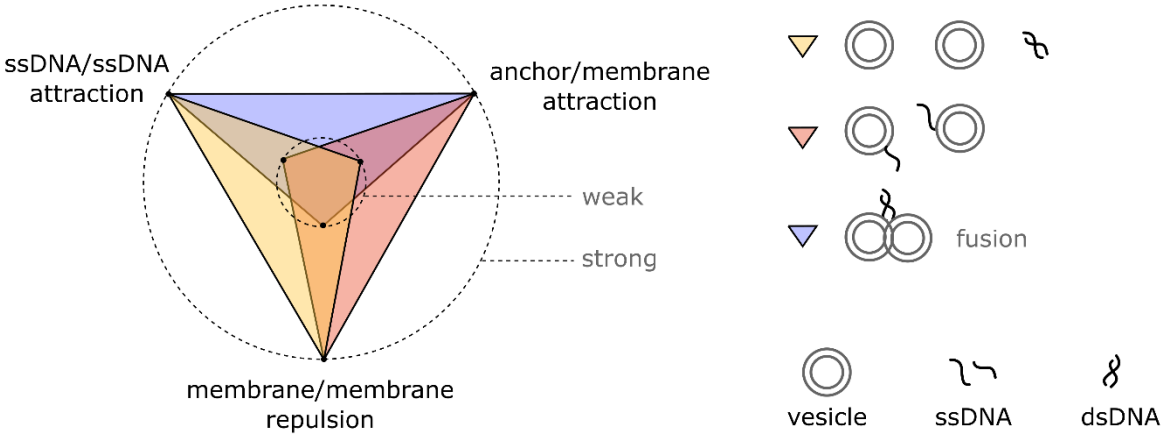

Figure 2.14 *Balancing forces in DNA-mediated vesicles fusion. By changing the length of a DNA duplex (strength of the double helix formation) and the number/strength of the membrane anchor one can facilitate fusion of vesicles, by overcoming repulsion between their membranes.*

Principles analogous to those followed and studied in pursuit of the DNA-mediated fusion are guiding the structure of this thesis, which aims at describing and balancing interactions in a molecular system. No complex origami-based constructs appear here - a simple, well-designed, membrane-tethered oligonucleotide is sometimes effective enough. Still, even in a seemingly simple arrangement there are many interactions that have not yet been studied, and that can uncover some fascinating new possibilities.

2.4. Interactions in DNA-lipid systems

For years now the idea of membrane protein-mimicking DNA constructs has been present in the scientific community. It is an appealing one indeed. Sharing an enthusiasm for such prospect, I have asked myself what steps should we, as researchers, take that will bring us closer to this goal. And even though I too, praise an ease with which DNA can be folded into sophisticated nanostructures, I decided that first of all one needs to understand the foundations: interactions between molecules comprising the studied system.

Here, I turn away from complex constructs with elaborate control mechanisms and ask questions about the simplest membrane-spanning nucleic acid there is: cholesterol-modified dsDNA (Figure 2.15a). The three components of such system: lipids, cholesterol and DNA, are intertwined in a network of relationships. Each can be affected by changes in the environment, each has intrinsic phenomena attributed to it. In this thesis, I will guide you through this interplay of molecules, using *the triangle of interactions* from Figure 2.15b as a graphical table of content.

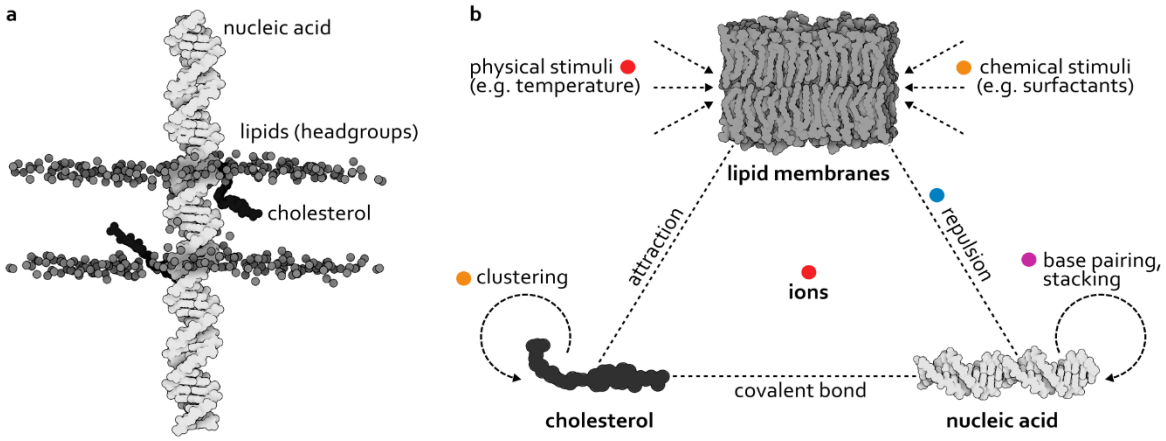

Figure 2.15 *Schematic overview of the model DNA-lipid system and interactions within. (a) Molecular structure of the system studied: cholesterol-labelled DNA embedded in a lipid bilayer (all-atom simulation built by Himanshu Joshi, PhD from Aleksei Aksimentiev's group (University of Illinois)). Lipid tails, water and ions are omitted in the sketch for clarity. (b) Three components of the system from (a) in the triangle of interactions. Colour-coded points refer to four chapters of this work. All-atom model of the POPC bilayer adapted from Heller et al., 1993.*

The work described here is mainly hands-on research, therefore in the next chapter, **Chapter 3**, I will sum up all the techniques and methods used in the experiments.

- In **Chapter 4** I will look at the direct consequences of DNA's hydrophilicity, resulting in a repulsion from lipid membranes. This hydrophilicity affects the arrangement of lipids in DNA-induced pores, causing ion flow and lipid transfer at the interface. By introducing modifications in the membrane-spanning domain, I tailor both these transport phenomena, illustrating the importance and use of protein-inspired insight into the details of the molecular design of synthetic structures.

- In **Chapter 5** I will elaborate on the hierarchy of forces in the system presented in Figure 2.15a. The struggle between cholesterol pulling towards and nucleotides pulling away from the membrane

results in a distorted DNA structure, different than the one designed. Especially the relatively weak bonds keeping the two ssDNA strands together in a helix get affected or even broken. I show how a careful design can prevent it and allow the formation of effective pores.

- **Chapter 6** discusses the role of cations in DNA-lipid systems. The dual importance of DNA's interactions with the ions is shown in mediating membrane attachment through bridging, as well as regulating it *via* screening of negatively charged DNA phosphates. Additionally, I discuss the dependency of ion-mediated interactions on the mechanical properties of bilayers - influenced by the temperature and lipid composition.

- In **Chapter 7** I will introduce a more complicated DNA design: a 4-helix pore, that carries up to four cholesterol moieties. I will use this design to study the insertion efficiency of DNA constructs, and how it is aided by surfactants. Additionally, I will discuss the influence of cholesterol-mediated clustering on the pore-forming activity of these DNA structures.

There certainly are many more questions and issues that have to be addressed before we ever see DNA-based constructs applied in biomedicine. I will discuss them in more detail in **Chapter 8**, which contains a summary of this work and presents a more extensive outlook.

CHAPTER 3

Experimental design

While the previous chapter provides knowledge about molecules comprising the DNA-lipid system, this one gives an overview of methods used for their characterization and studying. All of the experiments described here were employed to realize the findings discussed in the four consecutive chapters (Chapters 4 - 7); here is where you can find all the details of measurements and analysis*, while the discoveries themselves are presented in the next part of the thesis.

I structured this chapter on three main sections: (Section 3.1) creating DNA nanoconstructs, (Section 3.2) forming lipid structures, and (Sections 3.3 - 3.5) experimental techniques used to study their interactions.

3.1. DNA structures

In this work, two types of design were used: DNA duplexes (D) and 4-helix bundles (4H). Even though there are some differences in their design and handling, the general protocol for all will look similar: design > fold > characterize.

3.1.1. DNA design

The design of the DNA structure needs to be determined by its function. Firstly, one needs to decide what size should the construct be: a massive DNA origami, multi-helix bundle or maybe a simple DNA duplex? In Table 3.1 I collected a number of details important for making this decision with respect to membrane-interacting structures.

*All, apart from details of methods used by collaborators: descriptions of all-atom MD simulations performed by H. Joshi and DSC measurements performed by R. Rubio-Sánchez can be found in the Appendix, Sections A1 and A2, respectively.

Table 3.1 *A compatibility ranking of the three types of DNA nanotechnology designs in biological applications. If the listed property can be achieved by the particular design, it has been rated with the number of "+". Otherwise it is marked with a "–".*

	Duplex	*Bundle*	*Origami*
Physiological conditions	+++	++	+
Cell work	+++	++	+
Cavity	-	+	++
Number of modifications	+	++	+++
Studying DNA-lipid interface	++	+	+
Studying basic structural details	+++	++	+
Pore orientation well-determined	+	++	++
Stability of insertion	+	++	++
Complex shape	-	+	++
Single molecule optical assay/AFM	+	+	+++

You may have noticed that DNA origami seems to be quite a good choice in many cases. However, bear in mind two things: DNA origamis are least likely to be employed in physiological conditions, their stability in cell media still remaining an issue[137]. Additionally, their size is a disadvantage that we have not fully assessed yet – in the end, DNA origamis are a huge entanglement of a very strong charge. However, there are many research projects focusing on ensuring DNA origami's stability and biocompatibility in physiological conditions[137,138], which identify these issues and work towards resolving them.

DNA duplex is a preferable option if you are, similar to myself, interested in the very basic questions about the system. How does DNA-lipid interface look like? How does the molecular structure of the nucleic acid change when subject to forces in the membrane? How will ions affect its interactions with lipids? Duplexes are the least sensitive to changes in the environment, easy to handle, do not introduce as much charge, and most importantly, their simplicity allows to pinpoint the causes and effects of various phenomena much better than in the case of more complex constructs. Nevertheless, their membrane insertion efficiency, as well as the orientation and stability of the pore they form, do not show as much promise as the bigger structures. Geometry of a helix suggest that it is very difficult to create a duplex structure that will be forced to insert and remain in the bilayer. What is more, duplexes do not feature cavities. Although they do give rise to ion flow at the DNA-lipid interface, it is significantly more difficult to control than the ion flow

through the physical channel. Figure 3.1 schematically illustrates three types of DNA design distinguished above.

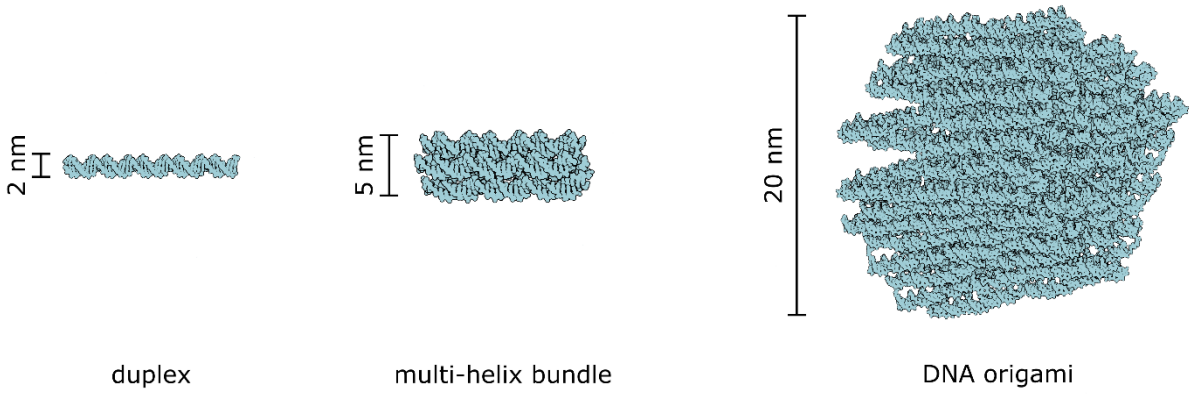

Figure 3.1 *Comparison between duplex, multi-helix bundle and DNA origami. Approximate lengths of the diagonal dimension of the structures are stated next to each model. The structure of a duplex is sketched based on all-atom simulation performed by Himanshu Joshi (University of Illinois), while DNA origami is adapted from the PDB entry 6by7*[139].

During my experiments, I have decided to work with the duplex (D) when studying specifically the ion flow at the interface – when I did *not* want the structure to have a cavity (Chapter 4). I also employed it when studying the effects lipids have on the molecular structure of a double helix, because it would be much more challenging to realize with complex constructs (Chapter 5). Finally, when assessing the importance of ions on DNA-lipid interactions duplex was an obvious choice, due to its stability in various salt concentrations (Chapter 6). However, when studying the insertion and effects that surfactants have on its efficiency, I have chosen a 4-helix bundle, designed to facilitate more stable membrane-spanning (Chapter 7).

After choosing the size of the construct, the next important design decision concerns modifications. In case of membrane-interacting DNA structures it is almost certain that some will be required. How many of them is needed for the functionality? Where should they be positioned? It is very important to ask these questions *before* one starts to design the shape.

When thinking about nucleic acid modifications, we find two parameters of a B-DNA double helix to be of crucial importance: (I) the average distance between base pairs a = 0.34 nm and (II) the number of base pairs per turn $N \approx 10$ bp[140]. The former allows to design distances between modifications, the latter should be considered when deciding where will modifications be facing in

relation to each other. A sketch of the double helix, showing the effect of these parameters on the orientation and distances of modifications is presented in Figure 3.2.

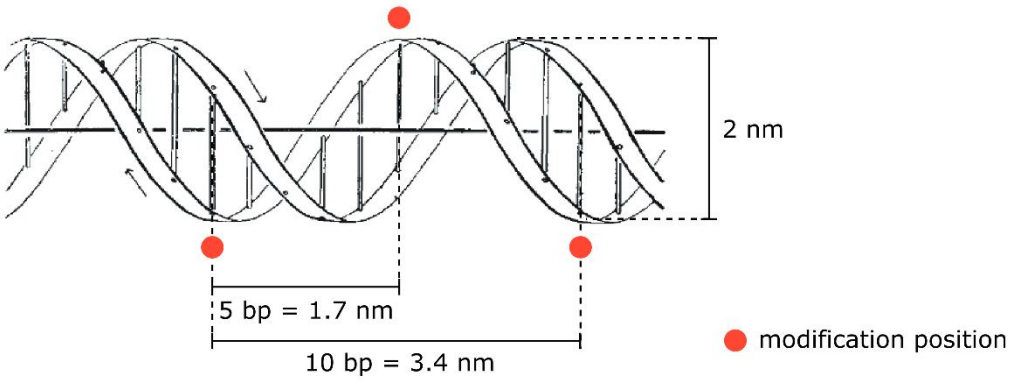

Figure 3.2 *A sketch illustrating the orientation of modifications depending on the twist. The sketch is adapted from Watson and Crick, 1953*.*

The desired angle between modified positions and the distance between them are not always compatible. For example, in the work I did on DNA duplexes the cholesterol modifications are actually positioned at 90° angle, rather than 180° which would facilitate membrane-spanning. I have decided that the distance of 4 nm (12 bp) is more important than the angle. Since my modifications were linked to the backbone *via* relatively long, flexible TEG chain ($l \approx 1.5$ nm), they have a wide range of angles they can span, wherever I introduce them. With flexible linkers, the facing angle is of much less importance than it initially seems.

As I mentioned already, the nanostructure design should be determined by its functionality. For example, when designing the 4H construct, I listed features I wanted it to have:

(I) The structure to be as small as possible.

(II) Four cholesterol modification positions, shifted towards one end, in two lines separated by 3 nm (≈ thickness of a hydrophobic core of a membrane).

(III) One strand to be modified with the dye on the end opposite to cholesterol positions.

(IV) One strand for the azide handle on the other end. Azide was used as a marker for studying structures with single-molecule Raman spectroscopy (not appearing in this work).

(V) Loops at the cholesterolized end.

*Marked panel has been reused from the cited article (https://www.nature.com/articles/171737a0) with permission. Further permissions related to this material should be directed to the copyrights' owner.

Then I used **caDNAno** software[141] to sketch a structure that fulfils as many of these requirements as possible. Figure 3.3 shows the design that I used, while in the further part of the subchapter I will introduce the architectures that were discarded in the design process.

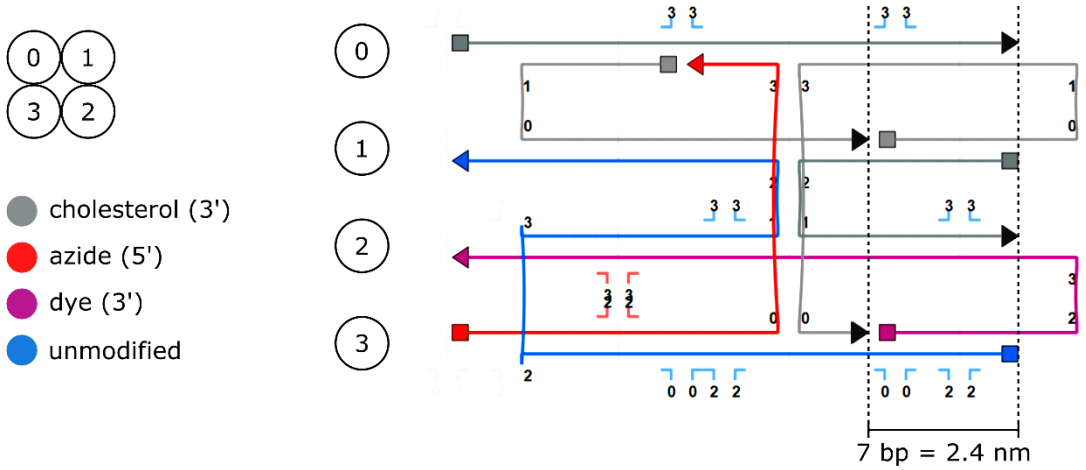

Figure 3.3. *4-helix (4H) design used in this work: screenshot from caDNAno software. Circled numbers represent the four helices. Strands were colour-coded according to the modification they were carrying. 3' ends modified with TEG-cholesterol moieties are represented by black arrows. Available connections to helix ③ are highlighted by the software.*

Using caDNAno ensures one of the most important things in the structural design: the proper connections between neighbouring helices. The connections follow the same principle as presented in Figure 3.2: the helices are properly linked when the connected bases are facing each other. In Figure 3.4 sketch of two helixes next to each other helps illustrating this notion.

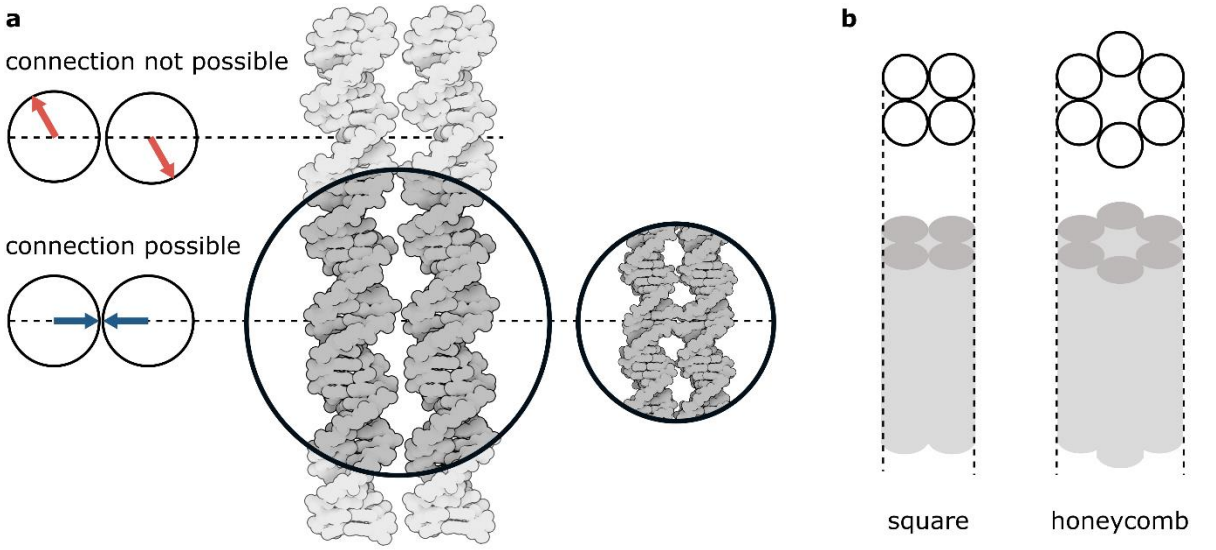

Figure 3.4 *A sketch illustrating orientation of helices with respect to each other. (a) The positions in which connection between helices can be established occurs every 10-11 bp, due to the twist. Circles represent the cross-section of the two helices, and the arrows indicate the direction in which bases are facing. (b) Illustration of two types of lattices, depending on the arrangement of the helices with respect to each other.*

To design all the connections properly would require a lot of spatial imagination, however, this is where caDNAno comes very handy. As shown in Figure 3.3, the possible connections are highlighted for each helix. Therefore, to avoid developing a strain in the structure, linkage should be introduced only in the positions indicated by the software.

Incidentally, another feature offered by caDNAno is the choice of lattice type: the helices can be arranged in squares or hexagons (honeycombs), as shown in Figure 3.4b. For DNA-based channels this usually determines the shape of the membrane-spanning domain, but also the diameter of the cavity and the minimal dimensions of the construct. In my case, the size limitation is what determined the lattice type I have built my construct on.

The first preference on the list of five features introduced earlier, the one I try to follow in any DNA-based design, is for the structure to be as small as possible. The larger the structure, the more charge it carries, and charge influences strongly how DNA interacts with membranes. In the experimental part of this work (Chapter 6) I will talk about the electrostatics in the system in detail. Here, I will only conclude by saying that charge is a problematic feature of DNA as a building block for biological applications[138]. This is why I was using the smallest bundle with a cavity possible, 4-helix one, based on the square lattice.

Since the construct was to span membranes, I had to introduce hydrophobic anchors - cholesterols. Knowing that lipid membranes are roughly 4 nm-thick, with the hydrophobic core (lipid tails) spanning around 3 nm (this differs slightly between lipid species)[142,143], I wanted the anchors to be placed at similar distance. As you can see in Figure 3.3 the distance I designed is actually smaller, taking into consideration the long TEG linkers used.

In order to facilitate insertion, cholesterols were placed on the opposite sides of the *one end* of the design. This again refers in a way to the DNA's charge: it is difficult to push a lot of charge through the membrane, so it is favourable to shorten the distance between the anchors and the end of the structure. However, that generates another issue: cholesterols at the very end of the construct are positioned in a single, exposed plane, and are therefore prone to forming clusters with other structures. In order to reduce the aggregation, I equipped my construct with overhanging loops, which shield the cholesterols and inhibit formation of bigger clusters. The effect of the loop length is presented in Figure 3.5.

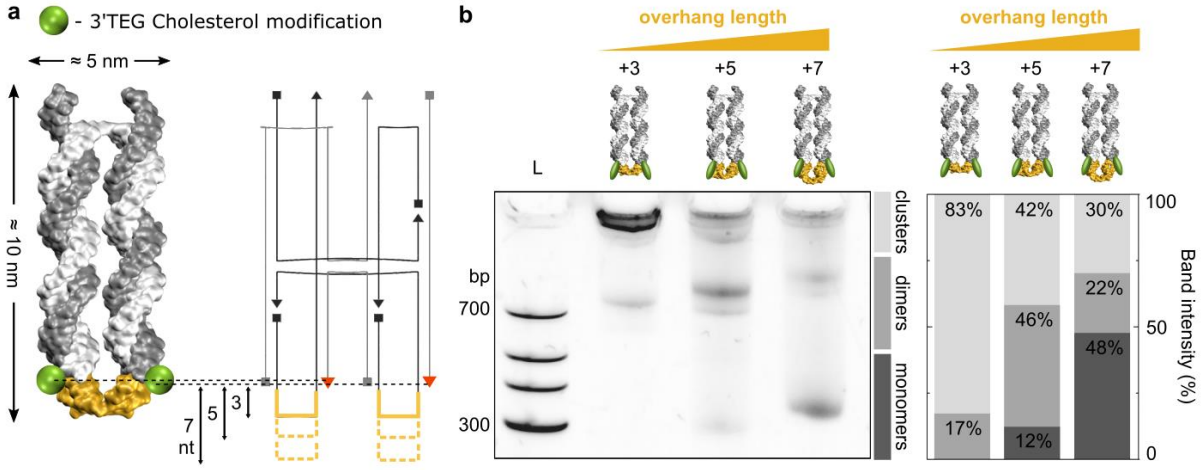

Figure 3.5 *The effect of the ssDNA loops on the cholesterol-driven clustering of nanostructures. (a) A model and a design of the 4H construct, highlighting the position of cholesterols at the end of the structure. Strands presented in yellow are additional loops, extending the structure either by 3, 5 or 7 nucleotides. (b) Gel electrophoresis results and their numerical analysis show an increased number of non-clustered (monomeric) structures in the samples with longer loops. The figure has appeared previously in Ohmann, (…), Sobota et al., 2019.*

Finally, the construct was to be used in a variety of assays, so strands that can be modified with different dyes or other markers were also included in the design.

After ensuring the proper shape of the nanostructure, it is time to build an actual molecule based on this model: design the sequences of oligonucleotides comprising the construct. In short, one has to follow two rules:

1. Keep the fraction of GC base pairs to minimum. Or more broadly, minimize the formation of secondary structures. GC-rich sequences tend to form various molecular arrangements[144], most prominent example being G-quadruplex (G4), occurring naturally in chromosomes[145].

2. Ensure no self-complementarity occurs. This could be manifested by either two identical strands binding together into a duplex, or a single strand bending and creating base pairs within the molecule, e.g. forming a hairpin. In fact, this point overlaps strongly with the first one.

Formation of inter- and intramolecular structures can be studied by analysing each single strand with an online **NUPACK** tool[146]. First put down a DNA sequence of A, T, C, G bases, remembering about minimization of GC%. After inputting the sequence in NUPACK, observe the probability of secondary structures forming, and tweak the sequences to keep it below 95%. The presence of single strands in the solution, not interacting with their identical copies but only within the nanostructure's design, improves significantly the yield of folding.

There is, of course, a number of different architectures that would fulfil the requirements I listed above. Before actually folding the structure, I have designed a few versions differing only slightly in the DNA construction, as presented in Figure 3.6a, and analysed them with **CanDo** online suite[147,148]. CanDo is an easy and powerful computational tool that allows to assess the assembly and mechanical properties of the nucleic acid construct. Therefore, I have created simulations of each of my four designs, to look at the structure and its predicted flexibility. All of the designed oligonucleotides form 4-helix bundles with more fluctuations in the loops, as expected. Additionally, one of the designs (4H1) is more flexible at the other end of the construct. Interestingly, when performing a PAGE analysis of cholesterol-modified 4H bundles, it was this version that aggregated the least; the majority of cholesterol-modified 4H1 were in a monomeric form, as highlighted in Figure 3.6b. After this realization, I decided that 4H1, with its reduced clustering, is the best choice for my design - it is this structure that I presented to you in previous paragraphs, and that I will continue to employ in experiments involving 4H construct.

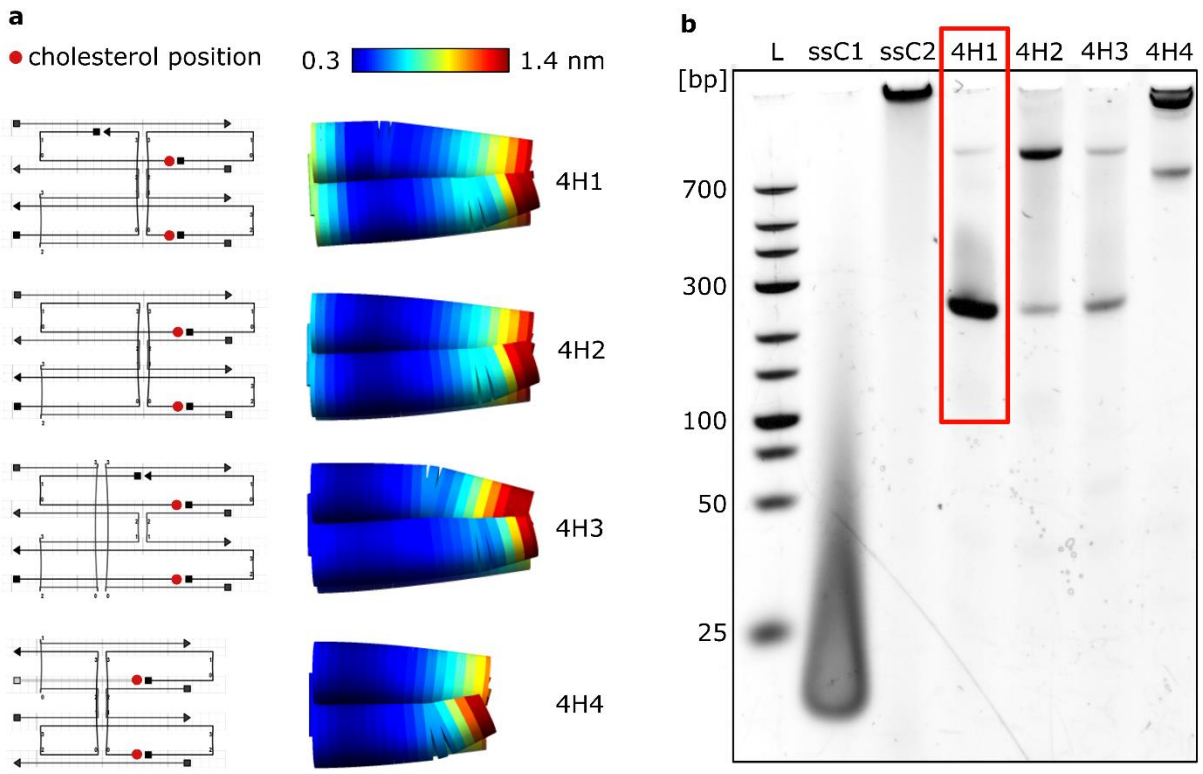

Figure 3.6 *Choosing the best variation of the design. (a) caDNAno*[141] *sketches and CanDo*[147,148] *simulations of four versions of 4H design. 2D sketches represent the design of DNA strands (square: 5', triangle: 3'), forming four helices arranged on a square lattice. The heat maps represent root mean square fluctuations (RMSF) of each structure, as visualized by CanDo online tool. (b) PAGE analysis of the four designs modified with two cholesterol molecules each (as indicated in (a)). ssDNA modified with cholesterol (ssC) were run in the first two lanes next to the ladder (L). The architecture with the majority of structures being in a monomer form (4H1) is highlighted.*

The gel also features two single strands modified with cholesterol, illustrating aggregating properties of these molecules. Note the significantly different behaviour of the two ssDNA: ssC1 produced a smear band, while ssC2 aggregated to such degree that the clusters did not migrate from the well. The gel illustrates the sequence-dependent clustering properties of cholesterol-modified DNA. In this case, the bases directly adjacent to cholesterol modifications are TAT and AGG for ssC1 and ssC2, respectively. We have shown that when guanine is a neighbouring base, cholesterol aggregation is intensified[149]. Additionally, the GC% of the two strands differ: 32% for ssC1 and 52% for ssC2, which may also play a role in driving the formation of cholesterol-mediated clustering. The details of the sequences can be found in the Appendix, Table 7.1.

A final note about the gel electrophoresis of 4H structures refers to their migration speed, as compared with the reference marker: 4H is built with 216 nt (96 bp + 24 nt), while its monomer band appears approximately at the position of a 300 bp mark. Since DNA ladder comprises of linear double strands, it is not suitable for numerical comparison with folded DNA nanostructures - apart from size, their shape also affects their mobility in a gel.

3.1.2. DNA folding

All the oligonucleotides used in this work are commercially available. Unmodified ones were obtained from Integrated DNA Technologies, Inc., which also provided cholesterol- and dye-modified strands. Oligonucleotides modified with an internal C12 spacer were initially obtained from biomers.net. However, after ordering from Eurogentec, this company was chosen as a main provider of hydrophobically-modified strands and the ones featuring two modifications. Table 3.2 summarizes purification methods and handling of the ordered strands. Importantly, all were dissolved to a final concentration of 100 μM: unmodified ones in an IDTE buffer (10 mM Tris, 0.1 mM EDTA (Ethylenediaminetetraacetic acid), pH 8.0) and the modified in Milli-Q purified water. Strands were then stored at 4 °C, except for dye-modified ones, which were frozen at -20 °C.

Table 3.2 *Summary of oligonucleotides' handling. PAGE refers to the purification from the gel, while HPLC stands for high performance liquid chromatography.*

Modification	*Purification*	*Storage medium*	*Storage temp.*	*Additional comments*
Unmodified	none (> 40 nt: PAGE)	1x TE	4 °C	-
Hydrophobic	HPLC	miliQ water	4 °C	upon suspension anneal in 70 °C for 15 min
Dye	PAGE	miliQ water	-20 °C	store and defrost as aliquots (of 10 μl or similar)

In order to fold the designed structures, the strands were mixed to a final concentration of 1 μM in TE buffer (10 mM Tris, 1 mM EDTA, pH 8.0) in a concentration of Mg^{2+} stated for each structure, but at least 4 mM $MgCl_2$ for constructs more complex than a duplex (multi-helix bundle). Cholesterol-modified strands were heated beforehand at 70 °C for 10 min.

Two annealing protocols were used in the course of this work:

1. A short one for assembling simple DNA duplexes: Strands heated to 95 °C within 5 min, and subsequently cooled to 25 °C over 30 min

2. A long one which ensured proper folding of multi-helix structures: Strands heated to 95 °C within 5 min, and subsequently cooled to 25 °C over 18 h.

In both cases the protocol consisted of two steps. First, rapid heating to temperatures above DNA melting temperature T_m (explained in section 3.1.3.2.), to ensure all of the connections are broken and single strands are independently suspended in the solution. Second, slow cooling down of the mixture allowed the strands to find their energetically-favourable conformation - the conformation of the designed nanostructure. More time is required for bigger, more complex constructs, while majority of duplexes fold properly even when incubated briefly at room temperature.

Table 3.3 *Summary of structures' design and folding.*

	Design software	*Buffer*	*Folding time*
Duplex	NUPACK	TE(1)4: 1xTE, 0-4 mM $MgCl_2$	30 min
Multi-helix construct	NUPACK, caDNAno	TE20: 1xTE, 20 mM $MgCl_2$	18 h

Folded structures were all stored at 4 °C, *never* frozen.

3.1.3. DNA characterization

3.1.3.1. Polyacrylamide gel electrophoresis (PAGE)

Gel electrophoresis is a useful tool for nucleic acid analysis, where the DNA structure is pulled through the pores of the gel by an electric field, and the observed response depends on its size, as well as its charge. Recorded **electromobility**, especially in comparison with a set of reference dsDNA samples of known length (a ladder), allows an assessment of proper folding of nanostructures, but also studying electrostatic interactions or aggregation between molecules.

The porosity of the gel needs to match the size of the studied molecules: large constructs (DNA origami) are properly examined in an agarose gel. The smaller nucleic acids (duplexes, multi-helix structures <700 bp) are analysed using a finer acrylamide, which polymerizes upon addition of

a cross-linking agent, forming a fine porous matrix. Since this work discussed solely smaller structures, only **polyacrylamide gel electrophoresis** (PAGE) technique will be described here.

Gels are hand-casted by preparing the mixture of appropriate acrylamide percentage (the higher, the finer the mesh of a gel[150]), which is poured in between two glass plates and allowed to cross-link. The gel is then placed vertically in the buffer containing ions, and the electrodes are placed on the top (negative) and the bottom (positive) of the container. DNA is introduced onto a gel from the top, which causes it to migrate through the gel towards the bottom upon applying an electric field. After imaging the gel by introducing an intercalating dye that attaches to nucleic acids, the migration of DNA can be assessed and compared with the size marker.

Here, Mini-PROTEAN® System (Bio-Rad Laboratories, Inc.) was used for the preparation and running of the gel. Gels were formed under a fume hood, at a concentration of 10% polyacrylamide, 0.5x TBE (45 mM Tris, 45 mM boric acid, 1 mM EDTA, pH 8.0) and with 11 mM $MgCl_2$, unless stated otherwise. Addition of 0.01 vol% ammonium persulfate (APS) (10%) initiates the polymerisation, while 6.7×10^{-4}% TEMED (N,N,N',N' Tetramethylethylenediamine) is used to accelerate it[151]. The exact amounts of chemicals used can be found in Table 3.4. Immediately after adding polymerisation agents the mixture was thoroughly mixed and poured in between the glass plates. Chosen comb (usually 15-teeth) was placed in the cassette, and the gel was allowed to set. The polymerization completes after 30 min, but it is recommended to wait additional 30 min (making it an hour of incubation), to ensure the reaction was performed in the whole volume of the gel.

2 μl of a 1 μM DNA sample were mixed with 0.4 μl of 6x loading dye (15% Ficoll 400, 0.9% Orange G diluted in Mili-Q water). Pipetting such small volumes makes it challenging to ensure repeatability of the protocol – every small droplet caught accidentally on the pipette tip will change the concentration of the dye drastically. To reduce this effect, I used a Kimwipe tissue (KIMTECH SCIENCE) to gently wipe the tip after drawing the dye, and only afterwards added it to the sample.

2 μl of the mixture were loaded into the well with the use of long Corning™ gel-loading tips. GeneRuler Low Range ladder (Thermo Fisher Scientific Inc.) was used as a reference. The gel was run in 0.5x TBE with 11 mM $MgCl_2$ (unless stated otherwise) at 100 mV for 90 min. After this time the gel was immersed for 10 min in GelRed (Biotium), in order to stain DNA. The imaging was performed on a GelDoc-It TM (UVP). FIJI was used to analyse gel images, usually by inverting the colour scheme to improve clarity and quantifying the intensity of appearing bands.

Table 3.4 *Quantities of chemicals used in gel and running buffer preparation. The two polymerisation catalysts are separated by the thicker line, indicating that they are added last to the mixture. *The volumes of $MgCl_2$ are for the standard protocol with the final concentration of 11 mM Mg^{2+}.*

	Gel	*Running buffer*
H_2O	8.92 ml	1484.8 ml
TBE 10x	750 µl	80 ml
$MgCl_2$ (0.5 M)*	330 µl	35.2 ml
acrylamide (30%)	5 ml	-
	= 15 ml	= 1600 ml
APS (10%)	150 µl	
TEMED	10 µl	

The standard protocol introduces 11 mM $MgCl_2$ in both the buffer and the gel itself. This was used for all the 4H (4-helix bundle, introduced above) work, as well as most of the standard controls with duplexes. However, gel electrophoresis is a powerful tool to study the folding, and sometimes also the behaviour of the structures in various media. In Chapter 6 I will look closer at the effects of ions on the DNA-lipid interactions, and there the concentration of Mg^{2+} in the gels will vary.

It may seem that it is enough to simply omit $MgCl_2$ in the gel and the running buffer to test the effects of Mg^{2+} in the folding buffer. However, there are two other things that ought to be remembered:

1. When studying the effects of specific Mg^{2+} concentration on the DNA behaviour, EDTA should be removed from the gel and buffer solutions. Otherwise, it will chelate the divalent cations in the sample's buffer, changing their concentration. In experiments presented in Chapter 6, this resulted in the running buffer consisting only of Tris. The electrophoresis will still proceed with the aid of monovalent ions in Tris (NaOH and HCl are used in commercial buffers for adjusting the pH), as well as from the deionized water – a silver lining of an otherwise troublesome fact that trace quantities of ions are *always* present in the solutions.

2. DNA is pulled through the gel by the electrostatic field, interacting with its negative charge. When positive ions are present in the solution, they too will interact with the structure – screening

its negative charge. This screening will then affect how strongly electric field "pulls" on the DNA. Therefore, the structures will be pulled stronger (= will move faster through the gel) in the absence of the Mg^{2+} ions. In practice, this comes down to samples running faster through the non-ionic gel than the ones studied in high cation concentrations. Therefore, it can happen that, in the absence of ions, after 90 min a small construct will run past the gel edge and "escape" the experiment altogether. When comparing gels in different Mg^{2+} concentrations I was running them for 60 min instead of 90 min. Figure 3.7 illustrates described differences in migration velocity, showing wells with the ladder run in four separate experiments: all for 1 hour, but each in different Mg^{2+} solution. One hour is a good compromise between all the bands being present in the gel and the bands being spread out enough to distinguish them. However, if performing a standard 11 mM $MgCl_2$ experiment, this shorter time is not recommended, as subtle differences in band positions can go unnoticed. Alternatively, the applied voltage can also be adjusted to achieve best distinction between bands in a particular experiment.

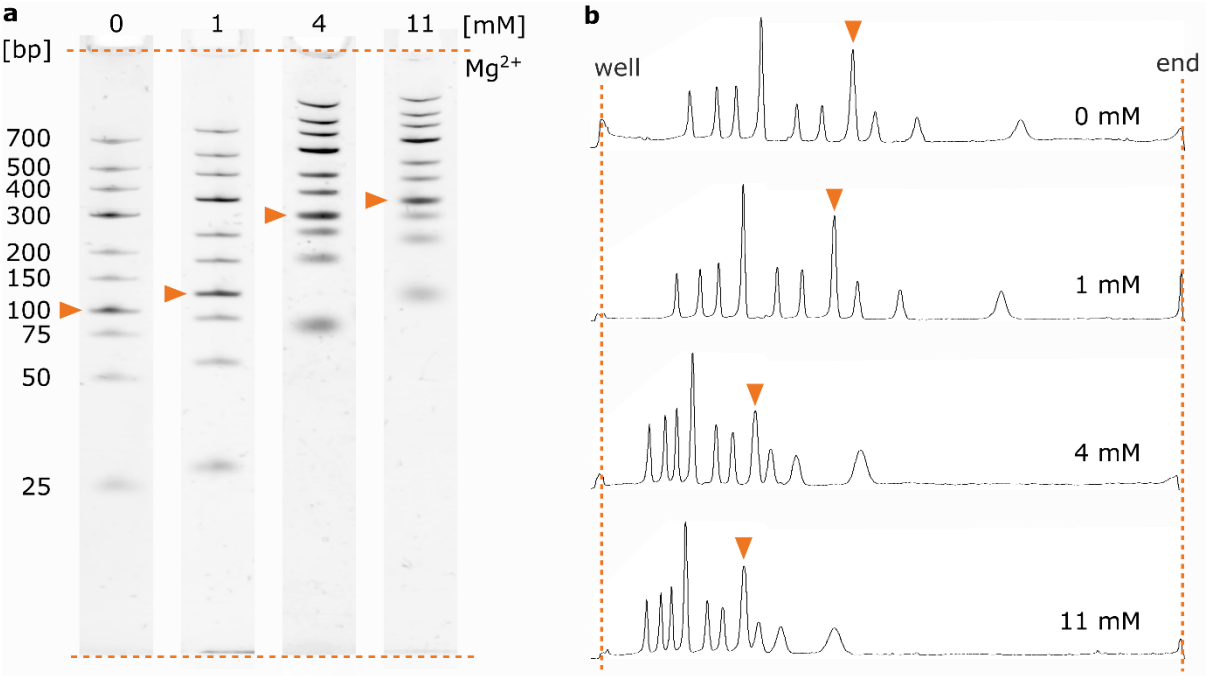

Figure 3.7 *Effects of screening on the DNA behaviour in the electric field. (a) Wells containing the ladder (GeneRuler Low Range ladder) from four separate experiments with different Mg^{2+} concentrations used: 0, 1, 4, 11 mM. The gels were all run for an hour, with 100 mV applied. Triangular markers indicate a 100 bp band. (b) Inverted intensity plots of the gel wells from (a). The triangles correspond to the markers indicating 100 bp bands. The ends of the gel are marked with dashed lines.*

3.1.3.2. Spectroscopy

Three spectroscopy setups were used in the course of this work, most of the time for characterization purposes:

1. UV-Vis spectrophotometer. Spectrophotometric thermal studies were performed in order to assess stability of the structures. Upon adding thermal energy to the system the interactions ensuring the formation of a double strand are overcome, and the helix unwinds. Depending on how strongly the two strands are held together, more or less energy is required to break them apart. We describe it by assessing duplex's **melting temperature T_m**, defined as a temperature at which half of the DNA nucleobases are unpaired.

DNA melting can be observed through UV-vis spectrophotometry: nucleobases have a specific absorbance spectrum, with a peak at 260 nm, as sketched in Figure 3.8a. During unwinding, bases are gradually unstacked, and when they are exposed, their absorbance at 260 nm increases by around 37%. This increase in the absorbance (optical density) is termed **hyperchromicity**, and results largely from unstacking, as well as disrupted hydrogen bonds which alter the aromacity of rings, limiting the resonance of nucleobases[152]. Hyperchromicity is therefore used as an indicator of dsDNA/ssDNA concentration in the sample. By recording absorbance at 260 nm as the temperature changes, **melting profiles** of nucleic acid structures are obtained. From such plot T_m is extracted, as shown in Figure 3.8b.

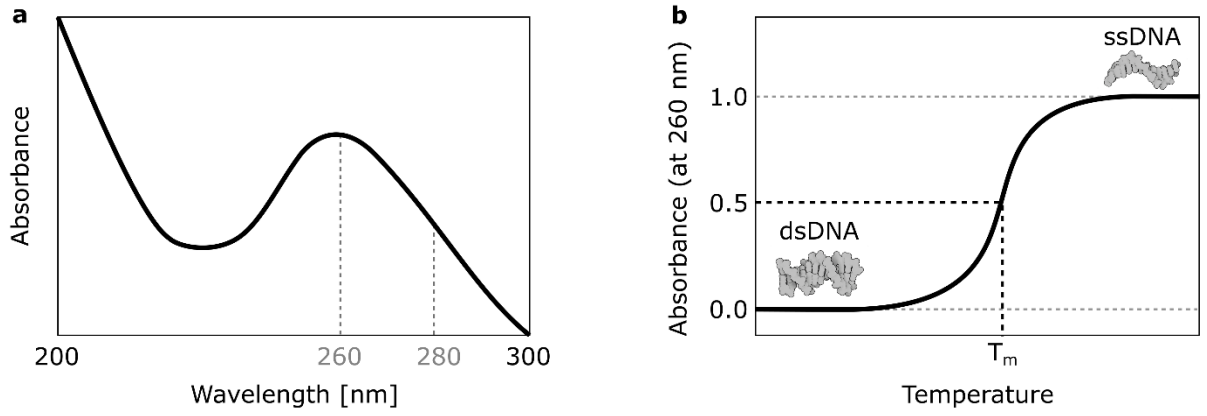

Figure 3.8 *Spectrophotometric assessment of DNA thermal stability. (a) Sketch of a typical absorbance spectrum of DNA, with a peak at 260 nm. (b) Sketch of a typical melting profile of DNA: normalized absorbance at 260 nm recorded against temperature. All-atom models of DNA are adapted from PDB entry: 1bna*[71].

Here, 100 µl of 1 µM DNA sample were added into a quartz Hellma™ cuvette and placed in a Cary 300 Bio UV-vis spectrophotometer (Agilent). The absorption spectrum was collected at 260 nm, while heating from 10 °C to 90 °C and back, with a heating rate of 1 °C/min. The melting temperature was obtained by finding the temperature corresponding to the 50% absorbance, which in turn was determined as a mean of the two linear regions (upper and lower). The data and their analysis were processed using Origin software for all measurements taken.

2. NanoDrop. Spectrophotometers can also be used to assess the concentration of DNA - the higher concentration, the more light is absorbed by the sample. Beer-Lambert law (Eq. 3.1) is applied for quantitative analysis.

$$A = \log_{10}\left(\frac{I_0}{I}\right) = \varepsilon l c \tag{3.1}$$

A - absorbance, I_0, I - intensities of light entering and exiting the sample, respectively, ε - absorptivity, l - optical path length, c – concentration[153].

Absorptivity is a property of a material that describes how easy it is for the light to pass through it. The values for nucleic acids are known: 0.020 and 0.027 $(\mu g/ml)^{-1}\ cm^{-1}$ for dsDNA and ssDNA, respectively. Note that the difference between these values (35%) corresponds to the previously described hyperchromicity effect.

For these measurements I used Thermo Scientific™ NanoDrop 2000 spectrophotometer, which is a dedicated nucleic acid quantification device, requiring only microliters of sample. Upon thorough cleaning of the sample holder with miliQ water, 1 µl of the respective buffer was used to perform a reference measurement, correcting for solution-generated absorbance and scattering. Next, 1 µl of the sample was placed on the pedestal and measured as well. The software stated concentration of measured molecules – in my case, I used it to confirm the concentration of single strands before folding the designed structures.

Less significant in my studies, but nevertheless important parameter is A_{260}/A_{280} ratio - both absorbance values are highlighted in Figure 3.8a. As DNA is often extracted from cells, residual proteins are frequently found as impurities in the nucleic acid samples. Since proteins, and especially the aromatic amino acids, absorb at 280 nm[154], the ratio between the absorbance values

is used to assess purity of DNA. A_{260}/A_{280} = 1.8 is agreed to be the ratio expected for pure DNA samples[155,156].

3. Fluorimeter. Since a number of experiments described here were based on optical assays, fluorescent labels were often placed on studied molecules. Measurements performed in bulk on these fluorescent samples were recorded on Cary Eclipse Fluorescence Spectrophotometer (Agilent), in a quartz Hellma™ cuvette. In this work, NBD dye was used to tag lipids, while DNA was labelled with Cy3 fluorophore. Despite their fluorescence spectra overlapping substantially, as can be seen in Figure 3.9, the artefacts related to this issue have been avoided by sequential imaging of the two dyes.

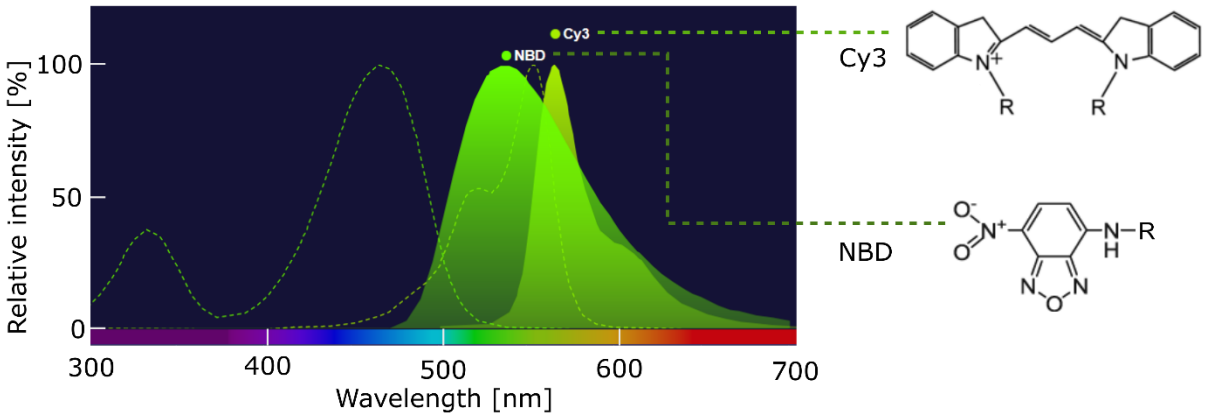

Figure 3.9 *Fluorescence spectra of NBD and Cy3 dyes, alongside their molecular structures. The spectra were sketched with the Fluorescence SpectraViewer tool (ThermoFischer Scientific).*

3.2. Lipid structures

Lipids used in this work were all PC zwitterionic lipids – their headgroups invariably consisted of phosphatidylcholine. All were obtained from Avanti® Polar Lipids (avantilipids.com). Three lipid species used in various experiments here were: POPC (16:0-18:1 PC), DPPC (16:0 PC), and DPhPC (4ME 16:0 PC). Apart from the equivalent headgroup, each lipid features a different tail chain, as illustrated by molecular structures in Figure 3.10. I have already elaborated on the effects that tail's architecture has on the properties of the bilayer, particularly its transition temperature T_t. Here we can study these effects on specific examples, as these three molecules span the wide range of thermal behaviours. POPC carries a double bond, limiting the contact between neighbouring lipids, which allows them to diffuse freely even at negative temperatures, with T_t = -2 °C. DPPC is its equivalent, but devoid of the double bond, which increases its transition temperature to

T_t = 41 °C. DPhPC, on the other hand, is a unique saturated lipid featuring eight methyl modifications spread evenly along the fatty acid chains. The presence of branches significantly decreases intramolecular interactions, preventing tight lateral packing in a vast range of temperatures; no gel-fluid transition has been detected for DPhPC lipids[157].

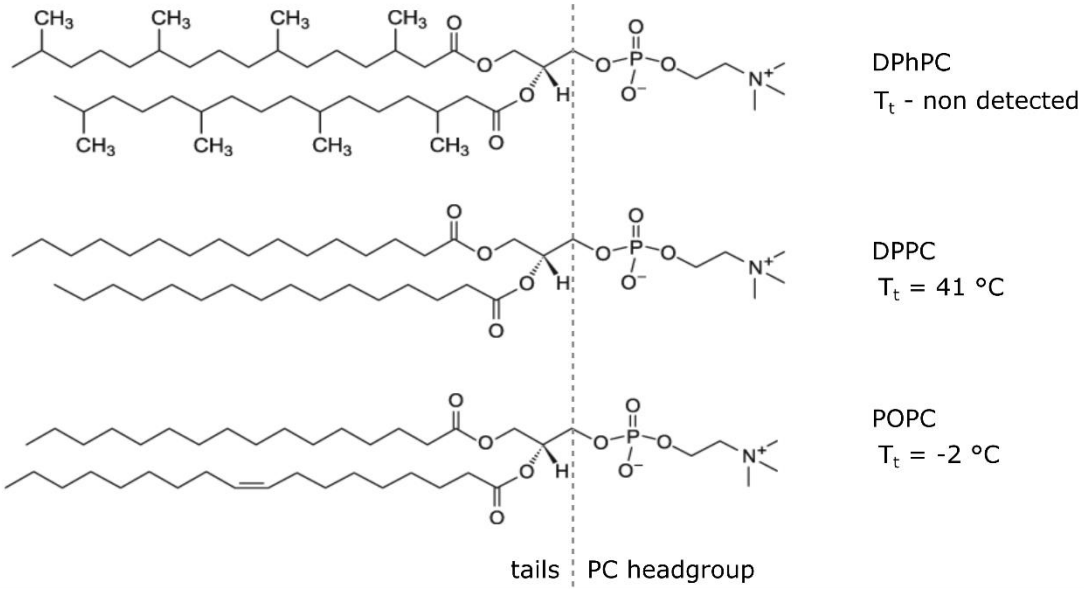

Figure 3.10 *Molecular structures of the three PC lipids used in this work: DPhPC, DPPC, POPC, alongside their T_t as stated by the provider (Avanti® Polar Lipids, avantilipids.com).*

When studying bilayers *via* optical assays, 0.5% of a fluorescently-modified PC lipid was added to the mixture. Its molecular structure can be found in Figure 3.11. The fluorophore - nitrobenzoxadiazole (NBD) – features excitation/emission maxima at 464/531 nm, as illustrated by the spectra in Figure 3.9. A small fraction of NBD-PC forming examined bilayers allows us to assume that it does not affect the transition temperature of studied membranes.

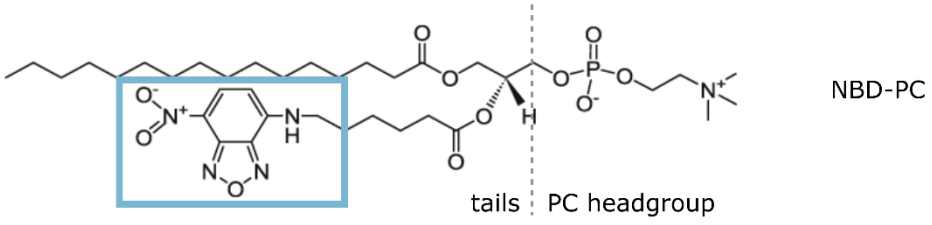

Figure 3.11 *Molecular structure of the NBD-modified PC lipid. The fluorophore has been highlighted in blue.*

These lipid species were used in various experiments as stated below, wherein DPPC-built structures were all formed and studied with the help of Roger Rubio-Sánchez (Lorenzo di Michele's group, University of Cambridge).

3.2.1. Large unilamellar vesicles (LUVs)

Large unilamellar vesicles (LUVs, < 1 μm) were prepared with extrusion, using a commercially available extruder (Avanti® Polar Lipids, Avanti Mini Extruder), following producer's protocol. Whatman® Filter Supports and Whatman® Nuclepore Track-Etched Membranes (100 nm and 200 nm) were obtained from Sigma Aldrich. The lipid layers were hydrated in 200 mM sucrose. The extrusion of DPPC vesicles was performed at 60 °C (above its T_t) to ensure bilayer fluidity.

The yield and size distribution were satisfying for performing bulk measurements and controls, though the inability to precisely assess unilamellarity and density of each batch of vesicles ruled them out for most of the membrane activity measurements. Figure 3.12 presents cryo-EM micrographs of POPC LUVs extruded through 100 nm filter.

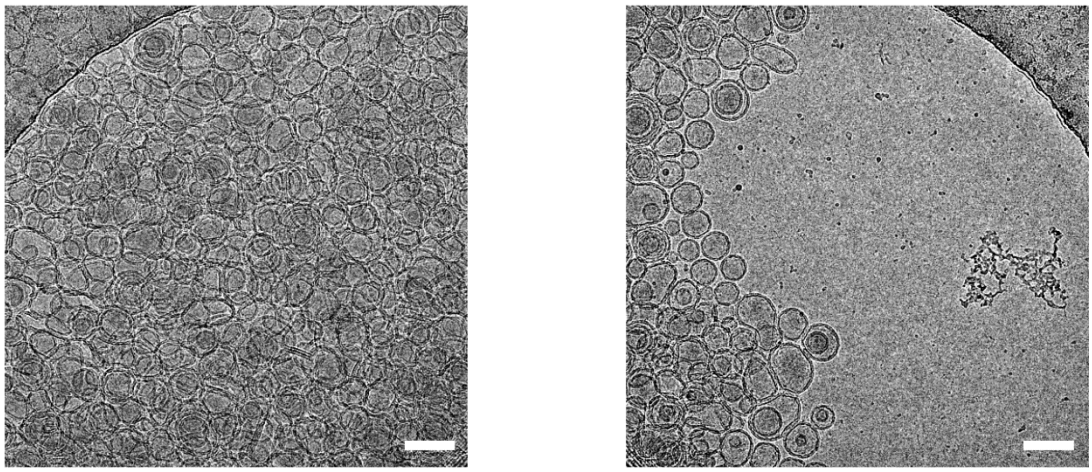

Figure 3.12 *Cryo-EM micrographs of extruded POPC large unilamellar vesicles (LUVs). Scale bars: 100 nm. The imaging was performed on FEI Titan Krios microscope, curtesy of Wolfson Electron Microscopy Suite, University of Cambridge.*

3.2.2. Giant unilamellar vesicles (GUVs)

All giant unilamellar vesicles (GUVs, > 1 μm) used here were prepared *via* electroformation. This technique is based on swelling of deposited lipid layer upon its hydration. The process occurs

spontaneously, however, an aid of external stimuli - in this case AC field - significantly improves its efficiency, and allows for more controllability. Electroformation was identified as a method yielding giant vesicles with relatively narrow size distribution and unilamellarity[158]. Figure 3.13 schematically illustrates the principle behind the technique.

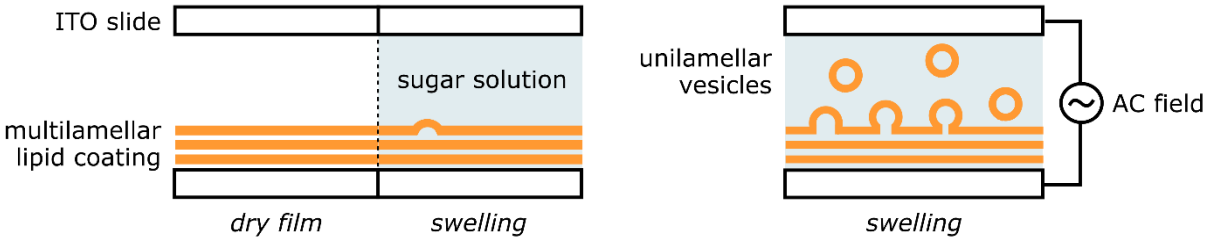

Figure 3.13 *Schematic illustration of giant unilamellar vesicles' (GUVs) preparation via electroformation.*

GUVs used in this work were either POPC or DPPC based, most often with an addition of 0.5% NBD-PC lipids, all acquired from Avanti® Polar Lipids. 80 µl of lipid mixture dissolved in chloroform to the final concentration of 5 mg/ml were deposited on a single ITO-coated glass slide using spin-coating. The slide was then placed in a desiccator for 30 min to ensure no chloroform residues remain in the lipid layer. Afterwards, the slide was moved to the electroformation chamber, a nitrile ring was placed on the lipid coating and filled with 600 µl of 1 M sorbitol in 200 mM sucrose, which was used as a buffer. Importantly, one of the biggest limits of electroformation technique is its incompatibility with charged entities in the buffer, including salts.

The osmolality of the buffers used in the experiments was oscillating around 1200 mOsm, with all the dilution buffers adjusted accordingly. Since for cell plasma the osmolality ranges between 275-325 mOsm[159], the buffers used here have far from biological osmolality. However, high osmolality buffers are less sensitive to the small changes in concentrations; a difference of a few mOsm does not affect the membrane in high-osmolality buffers, while it could result in bilayer distortion in low osmolality environment. Therefore, at a price of biological accuracy, we have ensured membrane stability in the experiments. All the buffers were adjusted to pH 7.5 (using sodium hydroxide NaOH and hydrochloride HCl solutions) - the value within the acidity range observed in natural systems[10].

A second glass slide was placed on top of the nitrile ring, ITO-coated side facing the buffer. A particular care was taken to limit number of air pockets formed in the chamber between glass slides. Then, an electroformation protocol, adapted from Kareem Al Nahas (Ulrich Keyser's group, University of Cambridge)[102], was used to swell lipid layers into GUVs. The protocol for POPC-built vesicles is illustrated on the plots in Figure 3.14. For DPPC, the experiment was conducted analogously, but ensuring that lipids and lipid-coated slide are handled above DPPC T_t = 41 °C.

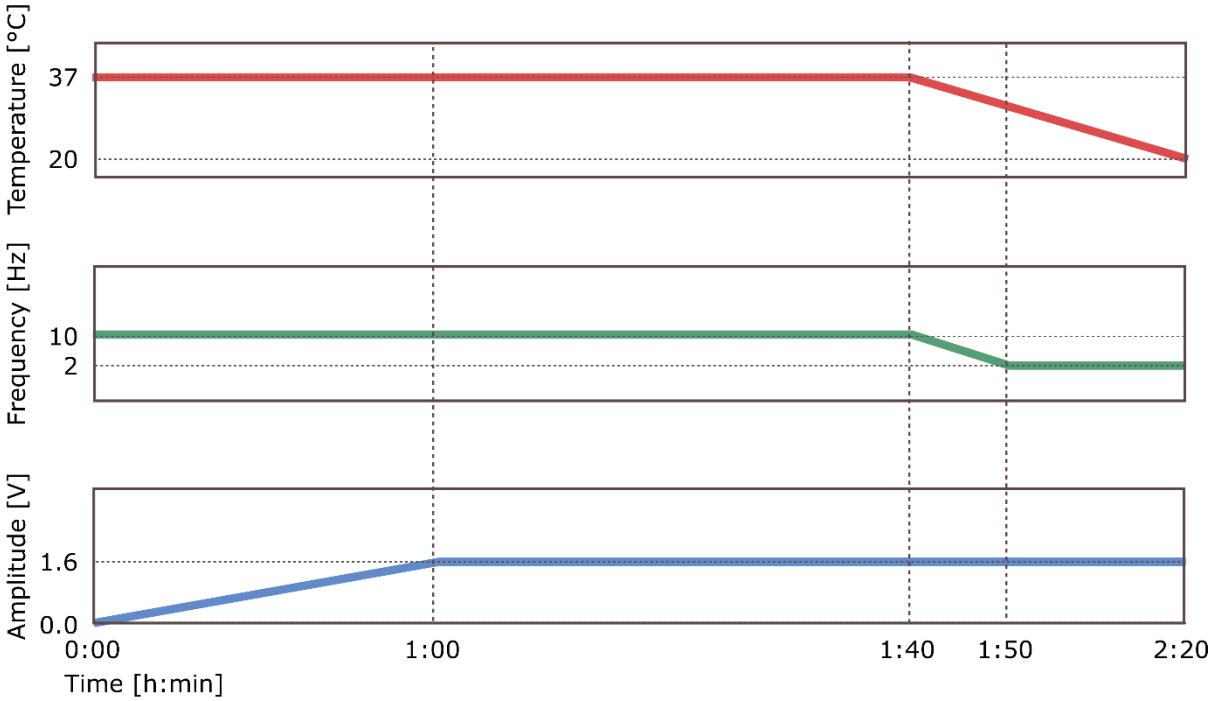

Figure 3.14 *The protocol used for electroformation of POPC GUVs. Changes in temperature as well as amplitude and frequency of the applied AC field are shown. Protocol kindly shared by Kareem Al Nahas (Ulrich Keyser's group, University of Cambridge)*[102].

After protocol finishes, sugar buffer from in between glass slides – now containing vesicles – is transferred onto a weighting boat, and from there into an Eppendorf tube. When using fluorescently-labelled lipids, the tube is covered with aluminium foil. Tubes with GUVs are stored at room temperature, in an upright position, and used within a week.

3.2.3. Suspended lipid bilayers

The bilayers used in this work were formed with Montal-Mueller method[160,161]. Such membranes are sometimes called "folded membranes", which describes the procedure used to prepare them.

Lipids in organic solvent are spread on top of aqueous buffer in each of the two chambers of a Teflon cuvette. The hole in the foil dividing them is pre-painted with an organic solvent to reduce the monolayer stress at the edges of the hole. By pipetting the solution up and down the hole is coated with a monolayer of lipids on each side – the bilayer is *folded* out of the two monolayers. I chose this method because of the exciting possibility of creating asymmetric bilayers by simply introducing different lipid mixtures into the two chambers. However, these experiments are not the scope of this thesis, and therefore only symmetrical membranes will be described.

Here, hexadecane (1 % in pentane) was added as a pre-painting on both sides of a hole (Ø = 0.15 mm) in the foil dividing *cis* and *trans* chambers of the Teflon cuvette. After 5 min of incubation, 700 µl of 0.5 M KCl, 25 mM HEPES (4-(2-hydroxyethyl)-1- piperazineethanesulfonic acid), pH 7.0 were added to each chamber. The conductance of this solution was measured to be 7.16 S/m. 5 ml of 5 mg/ml DPhPC lipids in pentane were added dropwise to each side, then the whole solution was pipetted up and down until the membrane was formed.

The membrane formation was studied by applying a triangular voltage wave with a peak-to-peak amplitude of 100 mV and a frequency of 10 Hz. In the electrolyte solution, in the absence of a membrane strong signal outside of the measured range was detected. Upon membrane formation this signal is immediately quenched, indicating that the cavity was sealed by the lipids. Figure 3.15 illustrates the respective stages of bilayer formation with sketches alongside collected data traces.

Newly-formed bilayer hinders current flow, due to its impermeability to ions. Yet, we do observe a specific membrane response: the square signal indicating membrane formation is the capacitive current, since lipid membranes can be considered electric capacitors.

If we regard the membrane as a plate capacitor, we will observe its charging with an increasing voltage, and consecutive discharging with voltage decreasing. Note, that it is the *change* in the voltage $\left(\frac{dv}{dt}\right)$ that determines the signal, rather than voltage itself. Whenever $\frac{dv}{dt}$ changes sign, the capacitive current i changes direction, following equation (Eq. 3.2). This gives rise to the square response of the bilayer, like in Figure 3.6c-d.

$$i = C\frac{dv}{dt} \tag{3.2}$$

C- capacitance of the membrane.

From the recorded traces and the known diameter of a hole Ø = 0.15 mm we can calculate the specific capacitance of membranes formed. The calculated values vary with each experiment between 1-1.2 μF/cm^2, and are of the same order of magnitude as the ones found in the literature (0.5-1 μF/cm^2)[162–164].

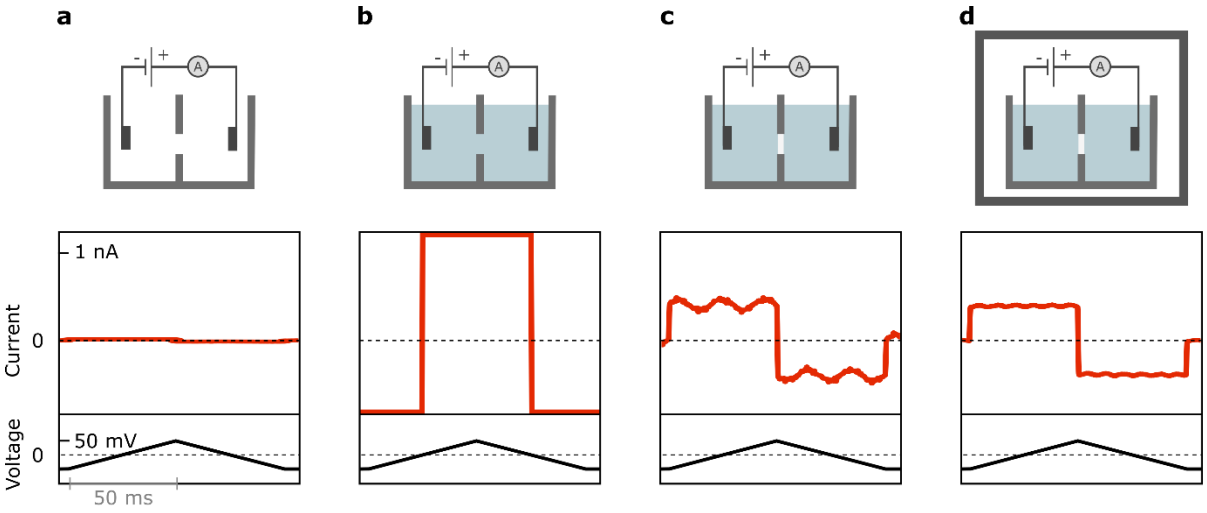

Figure 3.15 *Stages in suspended membrane formation, as indicated by current measurements. Sketches of the setup, alongside current traces collected for the applied voltage protocol. (a) In the absence of an electrolyte no current flows between the electrodes. (b) Upon addition of the KCl solution, a sharp increase in the signal above the threshold values is observed. (c) The membrane (white) formed in the cavity is impermeable to ions, no current flow is observed. The signal fluctuates noticeably. (d) The Faraday cage reduces noise significantly, which is crucial for observing subtle changes in the membrane permeability due to single molecule insertion events.*

3.3. Light scattering

3.3.1. Dynamic light scattering (DLS): size distribution

Particles suspended in a solution scatter light shone through such suspension. The schematic illustration of the dynamic light scattering (DLS) measurement setup is shown in Figure 3.16a. Each particle exhibits Brownian motion, therefore, the collected scattered signal will be fluctuating in time. Quantitative analysis is performed by measuring the intensity autocorrelation function, which compares the signal in given time increments and describes the rate of changes – degree of fluctuations (Malvern Panalytical, www.malvernpanalytical.com). Since this spontaneous

movement depends strongly on the particle's hydrodynamic radius, the detected fluctuations in the signal indicate the size distribution of a sample, as sketched in Figure 3.16b. This technique, called dynamic light scattering (DLS) is used here to assess the dimensions of LUVs, as well as DNA nanostructures.

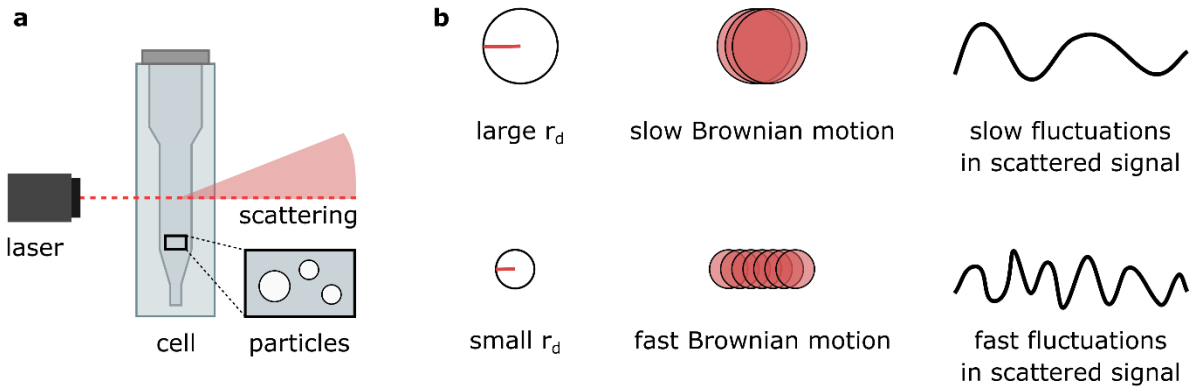

Figure 3.16 *Principle behind dynamic light scattering (DLS). (a) Schematic representation of the measurements. (b) Dependency of the scattered signal on the particle's hydrodynamic radius r_d.*

The measurements were performed on a Zetasizer Nano ZSP (Malvern Panalytical) with an excitation wavelength of 633 nm and a scattering angle fixed at 173°. For assessing hydrodynamic radius, 100 µl of either 10x diluted vesicles or 1 µM DNA were measured. 3 measurements were taken for each condition, each consisting of 12 runs.

Lognormal distribution curves were fitted to the obtained histograms of radii, following equation (Eq. 3.3):

$$y = y_0 + \frac{A}{\sqrt{2\pi}wx} e^{\frac{-\left[ln\frac{x}{x_c}\right]^2}{2w^2}} \tag{3.3}$$

y_0 – offset, x_c – center, w – log standard deviation, A – area.

The standard deviation was calculated using formula (Eq. 3.4). Both formulae, reported by Origin software, were used for plotting the data.

$$\Delta y = e^{\ln(x_c)+0.5w^2}\sqrt{e^{w^2}-1} \tag{3.4}$$

3.3.2. Electrophoretic light scattering (ELS): zeta-potential measurements

Besides spontaneous Brownian motion, any particle movement in the sample can be detected using similar principles. For example, electrophoretic mobility can easily be assessed through observation of the light scattering. This electrophoretic light scattering (ELS) allows measurements of the surface charge of the particles, and more precisely: their **zeta (ξ) potential**. In an ionic solution, charged particles are enveloped with ions interacting with it. The core particle moves together with its electric "coat", effectively having a new "surface", called a slipping plane, highlighted in Figure 3.17a. The potential at this plane is referred to as ξ potential, and is responsible for electrophoretic mobility (and electric response) of the studied particles.

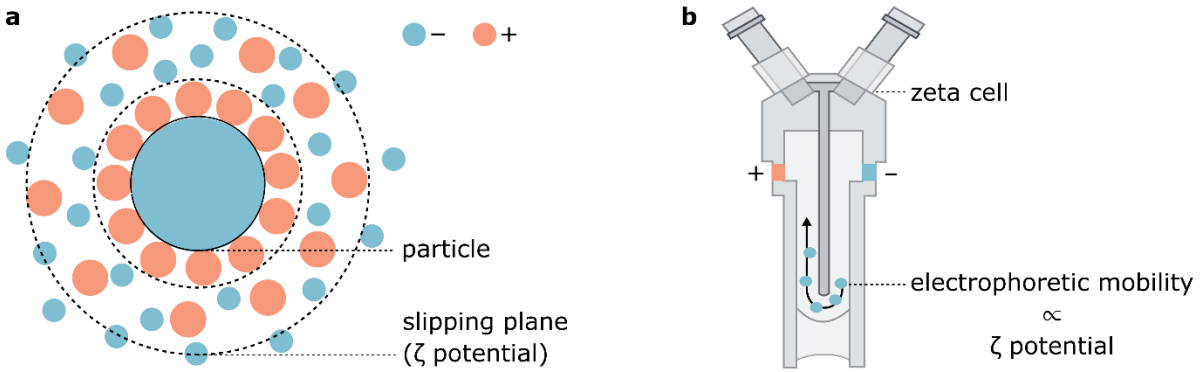

Figure 3.17 *Principle behind electrophoretic light scattering (ELS) (a) Sketch of electric layers surrounding a (negatively) charged particle with ξ potential at the slipping plane marked. (b) Schematic diagram of the zeta cell used to study electrophoretic mobility of particles.*

The ξ potential measurements were taken in a DTS1070 zeta cell, sketched in Figure 3.17b, using Zetasizer Nano ZSP (Malvern Panalytical). 800 µl of 200 mM sucrose solution with various mixtures of [DNA] = 0.1 µM, [Mg^{2+}] = 1 mM and 10x diluted LUVs is added into the zeta cell, and 3 measurements are taken for each sample, each consisting of 12 runs.

3.4. Confocal microscopy assays

The microscopy samples were imaged in silicon incubation chambers (FlexWell™, Grace Bio-Labs), attached onto a glass coverslip. To prevent vesicles from direct contact with glass, coverslips are coated with bovine serum albumin (BSA) prior to fixing chambers. For that, clean slides are incubated in 1% BSA solution in 60 °C for 1 h, afterwards thoroughly rinsed with water and placed back in 60 °C overnight, to evaporate any remaining solvents.

Sucrose-filled electroformed vesicles were suspended in an osmotically-balanced glucose buffer (≈ 1.2 M glucose, 25 mM HEPES, pH 7.5). The difference in the sugars' densities causes GUVs to sediment to the bottom of the incubation chamber, where their mobility is significantly reduced, allowing reliable imaging.

Confocal microscopy images were acquired on the Olympus FluoView filter-based FV1200F-IX83 laser scanning microscope using a 60x oil immersion objective (UPLSAPO60XO/1.35). Two studied fluorophores, NBD and Cy3, were excited using a (NBD): 25 mW 473 nm laser diode, with emission collected between 490 and 525 nm, and (Cy3): a 1.5 mW 543 nm HeNe laser, with emission collected between 560 and 590 nm. Gain was set to 1x. Laser power and the voltage applied to photomultiplier tubes (HV) were adjusted independently in each experiment to ensure lack of saturation in the studied intensity range. Images were recorded with a sampling speed of 2.0 μs/pixel, and with sequential mode of excitation, in order to prevent misrepresentations due to overlapping fluorescent spectra. FIJI was used to analyse the images[165].

When collecting the intensities of vesicles or DNA coatings on them, the sample was scanned and a number of images were taken. When comparing various samples, the imaging settings were kept identical. The only exception were samples where no DNA attachment was observed: HV of these measurements was significantly increased, to clearly show the DNA dispersed in the solution, and no visible coating on the membrane. Such change in the settings is always stated in the figure caption. Collected values were presented in a form of histograms, and the results are often reported as the peak of a Gaussian fit to the distribution. The error bars represent Gaussian RMS width.

When comparing DNA membrane coating in various salt concentrations (Chapter 6), the peaks of the distributions were plotted against [Mg^{2+}]. There, Hill function (Eq. 3.5) was used to fit curves into obtained data points.

$$I = \frac{I_{max}[c]^n}{K^n + [c]^n} \tag{3.5}$$

I - fluorescence intensity, I_{max} - maximum intensity observed, $[c]$ - ion concentration, n - Hill coefficient, K - ion concentration associated with 50% of maximum attachment ($I = 0.5$).

Dissociation constant was than calculated using formula (Eq. 3.6).

$$K_d = K^n \tag{3.6}$$

I have opted for the Hill function in order to describe empirically ion-nucleic acid interactions, as done previously[166–168]. However, it must be noted that the equation was employed here to allow an illustrative comparison of studied constructs, rather than as a mathematical model of the underlying process. Therefore, the calculated parameters do not necessarily carry the meaning most frequently ascribed to them.

3.4.1. Fluorescent recovery after photobleaching (FRAP)

The diffusion of lipids, as well as cholesterol-anchored DNA, is studied optically by tracking fluorophores attached to them. Upon bleaching of a spot of known diameter, signal intensity of this spot is recorded. After initial sharp drop, the fluorescence is gradually restored by the diffusing intact molecules, taking the place of bleached labels, as illustrated in Figure 3.18a. The rate of the signal recovery is determined by the diffusion, and by analysing the recorded intensity plots (schematically represented in Figure 3.18b), the diffusion coefficient *D* of respective samples are obtained. This technique - fluorescent recovery after photobleaching (FRAP) - was used to assess the effects of various factors on the kinetics of studied molecules, but also in confirming the lipid phase of the bilayer, as the diffusion of lipids in gel phase is strongly limited.

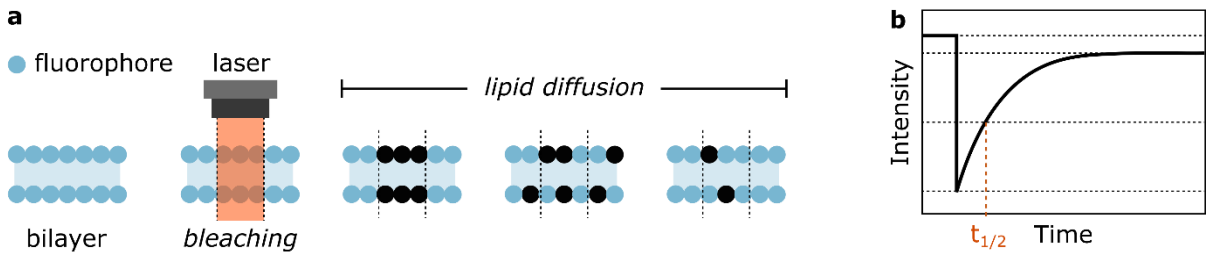

Figure 3.18 *The principle behind fluorescent recovery after photobleaching (FRAP). (a) Schematic illustration of bleaching and recovery of the fluorescent signal. (b) Sketch of a recorded curve, with the half-time $t_{1/2}$ marked on the plot.*

FRAP measurements were performed with the help of Michael Schaich (Ulrich Keyser's group, University of Cambridge). All measurements were performed at room temperature. Using the FRAP function of the FluoView software (tornado mode), a spot of Ø = 4.4 μm on the top of a GUV was bleached and the fluorescence recovery observed. 10 images were collected pre-bleaching. Bleaching was performed over 0.5 s with 99% laser power and the fluorescence recovery was recorded for 50-100 frames.

Collected recovery curves were fitted using exponential function (Eq. 3.7).

$$I_t = A\left(1 - \exp\left(-\frac{t}{\tau}\right)\right) + I \tag{3.7}$$

I_t - fluorescence intensity in time t, A - fitting parameter, I - final intensity after recovery, τ - recovery time constant.

τ was then used to calculate recovery half-time as in (Eq. 3.8).

$$t_{1/2} = \tau ln2 \tag{3.8}$$

Which in turn enabled obtaining diffusion coefficient D following the formula (Eq. 3.9)[169].

$$D = \frac{0.88r^2}{4t_{1/2}} \tag{3.9}$$

r – radius of bleached area.

3.4.2. Temperature-controlled imaging

These experiments were performed in collaboration with Roger Rubio-Sánchez (Lorenzo Di Michele's group, University of Cambridge), who also provided the following description. In order to prevent evaporation, all studies performed above room temperature (> 25 °C) were run in a sealed chamber. Here, we used borosilicate glass capillaries (CM Scientific) with internal section of 2 mm × 0.2 mm. After cleaning, capillaries were passivated by filling them with a solution of 0.1% BSA, and incubated at 60 °C for 1 h. They were subsequently cleaned with water to remove excess of BSA, and filled with vesicle samples. The sides were sealed with a two-component epoxy resin hardener onto a clean glass cover slip. The coverslip was fixed to a custom-built copper plate connected to a Peltier element using aluminium tape and coupled to a thermocouple for temperature control. Micrographs of these systems were acquired using a Leica TCS SP5 confocal microscope equipped with an HC PL APO CORR CS 40x/0.85 dry objective. Ar-ion (488 nm) and a He-Ne (543 nm) lasers were used for exciting NBD and Cy3 dyes, respectively.

Changes in DNA coating on the DPPC vesicles as a function of temperature were fitted to a reverse Hill function (Eq. 3.10). Similarly as for ion-dependent DNA membrane coating described above, Hill function serves an illustrative purpose, rather than describing a mathematical model of DNA-lipids absorption.

$$I = 1 - \frac{I_{max}[c]^n}{k^n + [c]^n} \tag{3.10}$$

3.4.3. NBD-dithionite assay

In order to observe lipid transfer between leaflets (due to the toroidal pore formation), I implemented an optical assay used in biological scramblase studies[170–172]. The assay is performed on bilayers with an NBD labels present on the lipids, and in the presence of **dithionite** ($S_2O_4^{2-}$). Dithionite plays a crucial role due to its two features: (I) it is membrane impermeable and (II) it is a strong reductant. The latter causes it to interact with NBD labels, reducing their nitro group (NO_2) to an amine (NH_2), which in turn results in loss of the fluorescent signal. The reducting activity of dithionite turns fluorescent NBD into a non-fluorescent ABD variant, as shown in Figure 3.19a.

Importantly, despite the label being attached to one of the tails, it does not nest in the hydrophobic core of the bilayer, but orients itself at the water-lipid interface, as sketched in Figure 3.19b. Therefore, the labels are exposed to the aqueous solution and by that to the externally introduced dithionite.

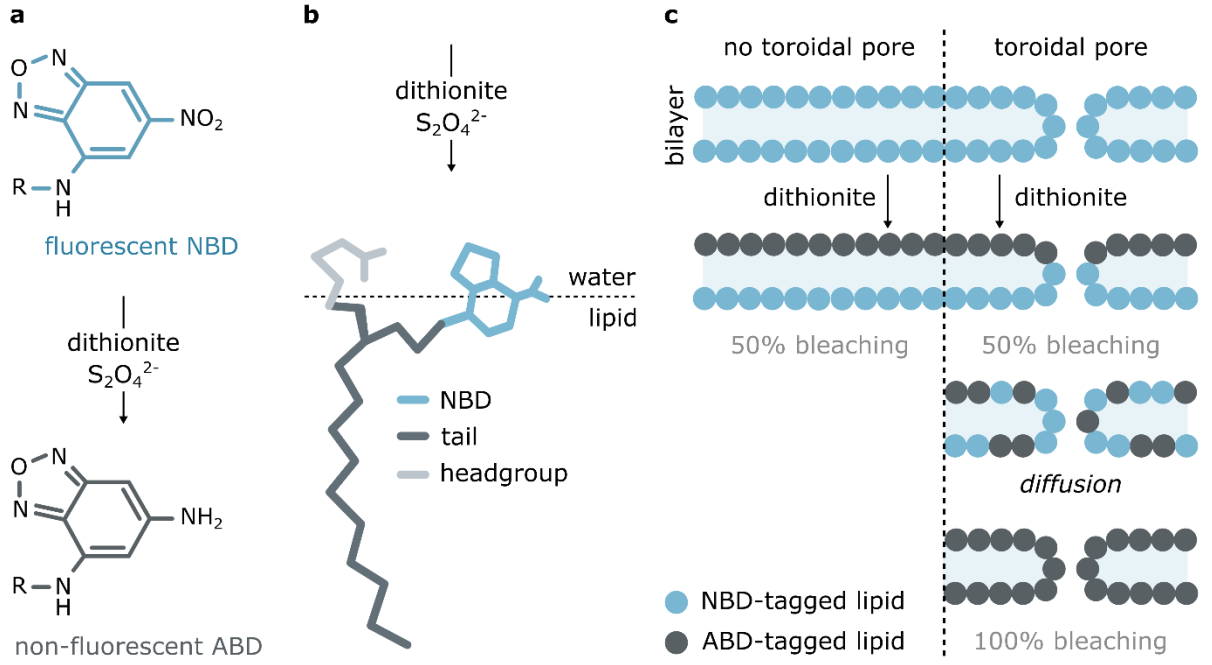

Figure 3.19 *The principle behind NBD reduction assay. (a) Molecular structure of NBD dye, turning into a non-fluorescent ABD upon reduction with dithionite ($S_2O_4^{2-}$). (b) A schematic arrangement of an NBD-PC lipid in a membrane, with NBD exposed to the aqueous environment*[173,174]*. (c) A sketch of the assay illustrating how lipid diffusion between leaflets in the toroidal pore results in a 100% signal reduction.*

Since dithionite is membrane impermeable, it reduces half of the labels of the intact bilayer - only the outer leaflet, which has fluorophores exposed to the reductant. We can track the fluorescent signal after dithionite addition, and observe a 50% loss of fluorescence. However, when toroidal pore is formed and lipids from the inner leaflet can diffuse to the outer one *via* diffusion, all of the labels will get exposed to the bleaching agent. Therefore, the fluorescent signal will be reduced by 100%, following the schematics in Figure 3.19c.

Dithionite has a third important property: (III) it is negatively charged ($S_2O_4^{2-}$). As a rather massive anion, its translocation through the membrane is limited, and transfer through DNA-induced pore is hindered completely, due to an electrostatic repulsion from DNA's phosphates. I have confirmed it experimentally, looking at the fluorescence of an internalized vesicle, which was not significantly impacted, while the external vesicle with toroidal pores was completely bleached (Figure 3.20a). The simulations run for this project by the collaborating group of Aleksei Aksimentiev compare the translocation of positive and negative ions, indicating that anions - even a small chloride Cl^- - do not go through the DNA-induced pore (Figure 3.20b).

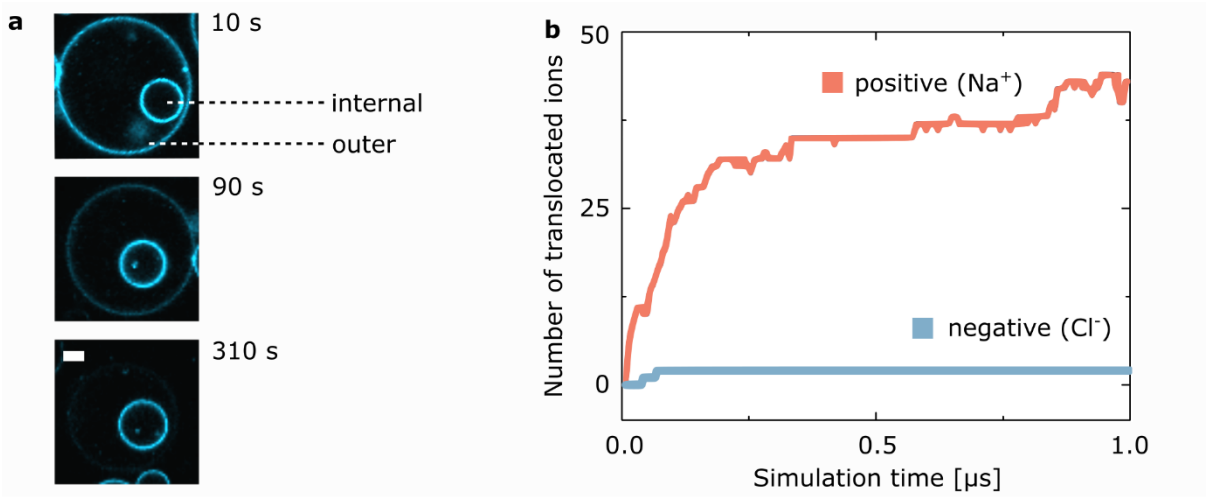

Figure 3.20 *Experimental and simulated proof of no dithionite leakage through a DNA-induced pore. (a) Micrographs of an internal vesicle, preserving its NBD fluorescence while the outer one was bleached. Scale bar: 5 μm. (b) Plot showing the number of ions translocated through a pore formed by a membrane-spanning DNA duplex in all-atom MD simulations. Simulations performed by Himanshu Joshi from Aleksei Aksimentiev group (University of Illinois).*

If dithionite does not leak inside a vesicle, the bleaching above 50% observed for pore-forming constructs is a result of leaflet merging and lipid diffusion between them. Here, I attribute the rate

of NBD bleaching to the rate of this interleaflet transfer. The assay is employed to assess the membrane activity of pore-forming DNA nanostructures.

In the experiment 20 μl of electroformed liposomes were incubated for 2 h with 50 μl of DNA structures diluted in an osmotically balanced glucose-based buffer, as described earlier. The concentration of DNA in this mixture was 0.11 μM. Immediately preceding the assay, sodium dithionite was diluted in 1 M Tris at pH 10. This solution was further diluted in osmotically balanced glucose solution, from which 30 μl were added to the chamber. The final concentrations of DNA and dithionite were 0.08 μM and 9 mM respectively (unless stated otherwise, see below). Vesicles were imaged for 30 min after dithionite addition.

For fitting all of the obtained traces, a biexponential decay equation (Eq. 3.11) was chosen to describe initial fast (dithionite acting on the outer layer of the vesicle) and then slow bleaching (further bleaching of flipped lipids)[175].

$$I = I_0 + I_1 \exp\left(-\frac{t}{\tau_1}\right) + I_2 \exp\left(-\frac{t}{\tau_2}\right) \tag{3.11}$$

I_0 – final intensity (plateau value), I_1, I_2 – coefficients describing the respective decays in signal, τ_1, τ_2 – characteristic time constants

Time constants were used to derive decay rate λ for each exponent, using (Eq. 3.12):

$$\lambda = \frac{1}{\tau} \tag{3.12}$$

The experiments were initially performed in [dithionite] = 4.5 mM. However, the dithionite-related limitations (especially its degradation in aqueous solutions *via* hydrolysis[176]) prevented me from seeing clear differences between decay rates – the timescale of dithionite activity and lipid transfer were comparable, so part of the information was lost. In order to obtain more details of the process, the experiments were performed with the concentration of dithionite doubled (final 9 mM). As a result, the initial bleaching of the outer leaflet proceeded much faster, and a clear biexponential decay trace emerged. This allowed to compare various DNA designs, as presented in Chapter 4. Plots in Figure 3.21 illustrate this effect, showing the behaviour of a representative membrane-spanning DNA duplex (2C 2D, Appendix Table A4.1). Two well-defined processes comprise signal response in 9 mM dithionite, while this is not observed in 4.5 mM.

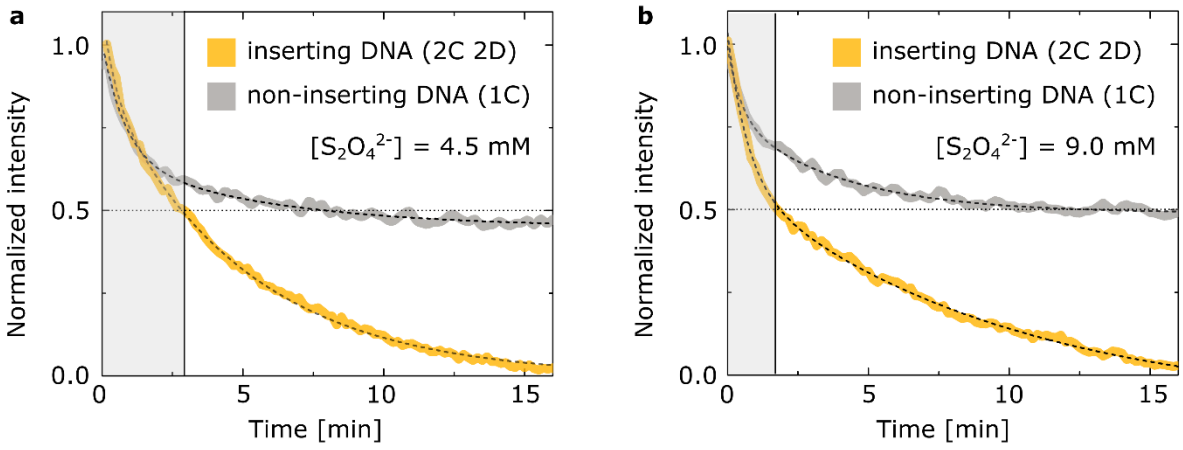

Figure 3.21 *Higher concentration of dithionite provides more informative intensity decay traces. (a) Averaged fluorescence signal traces of an inserting and non-inserting DNA, after addition of dithionite in t = 0 min. Dithionite's final concentration c = 4.5 mM. (b) Averaged decay trace for dithionite's final concentration c = 9.0 mM. The trace for a pore-forming DNA has a clearly biexponential shape, corresponding to the bleaching of the outer leaflet, and further bleaching of the lipids transferred from the inner leaflet. All traces represent at least three bleached vesicles. The initial decay (up to I = 0.5) is highlighted in grey – it is attributed to the bleaching of the outer leaflet. Further description of the design (2C 2D: 2x cholesterol, 2x dodecane, 1C: 1x cholesterol)) can be found in Chapter 4.*

3.5. Transmembrane current measurements

When studying ion channels, measuring transmembrane current in response to applied voltage provides a vast set of information about pore-forming structures. Briefly, electrodes are placed on two sides of a suspended lipid bilayer, and the current is recorded while applying voltage. As membranes are intrinsically impermeable to ions, in the absence of pores no current is flowing through the circuit. During pore formation conductance increases suddenly, as ions can then translocate freely. This increase is illustrated as a step in the current trace. Each step is attributed to the formation of a single pore, and its careful analysis provides many information about the dynamics, cooperativity and geometry of pores. For example, the bigger the pore the more ions can flow through it, and therefore the recorded conductance step is higher. Figure 3.22 illustrates the principle behind observing pore formation through transmembrane current recordings.

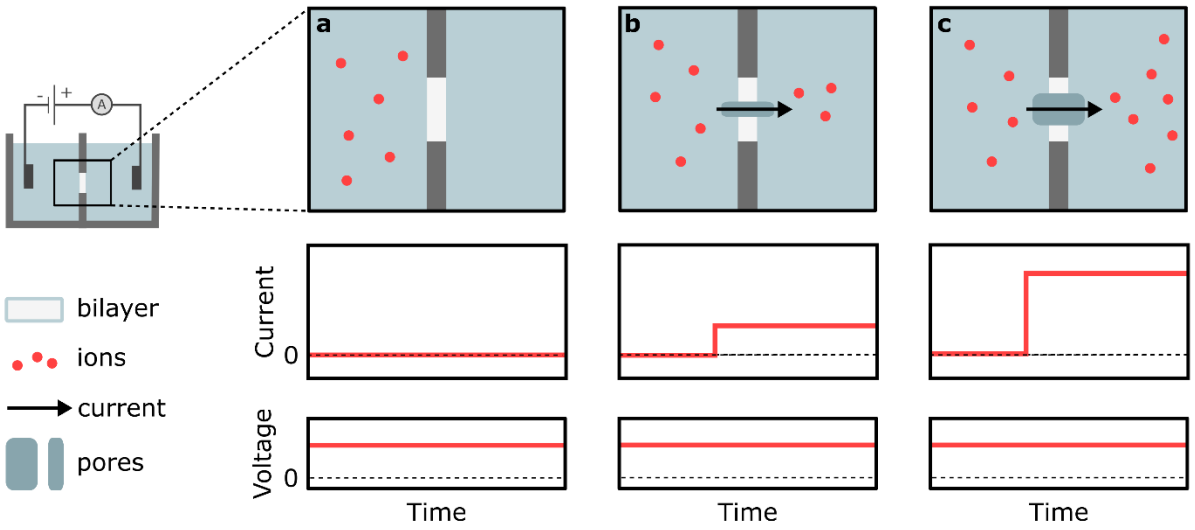

Figure 3.22 *The principle behind transmembrane current measurements and studying pore formation with it. Sketch of the setup, zoomed section showing the suspended bilayer. The respective current traces are shown for (a) an intact membrane, (b) a small, and (c) a big pore in the moment of their formation.*

Following this idea for single-molecule experiments, numerous setups and geometries have been applied to build a working system. I used bilayers formed across a hole in a Teflon cuvette, following Montel-Mueller technique described in detail above, to look at the membrane-spanning processes of single DNA-built synthetic ion channels.

Here, current data were acquired at a sampling rate of either 1 or 5 kHz using Axopatch 200B amplifier. The electrodes were Ag/AgCl, made in-house by incubating a silver wire in chlorinated bleach overnight. After membrane formation, DNA was added to the *cis* side (with the negative electrode) at the final concentration of 10 nM, and the ionic current under 50 mV voltage across the membrane was recorded. Where stated, **n-octylpolyoxyethylene (**oPOE) surfactant was added to the *cis* chamber as well, to the final concentration of 0.01%. Clampfit software was used to analyse the data, employing its "single channel search" tool, designed to study the activity of natural ion channels. The script listed the size (current level) and dwell time of all steps found by the software. Signals lasting less than 10 ms were ignored. Assuming an ohmic behaviour of the formed pores, conductance was calculated as in Eq. 3.13. Lognormal distribution curves (Eqs. 3.3, 3.4) were fitted to the obtained histograms.

$$c = \frac{I}{V} \tag{3.13}$$

c – conductance, I – current (step size), V – voltage.

Note, that in the above approach current I is attributed to the size of the step, provided for each found signal by the Clampfit analysis. The more reliable way to study the conductance of a membrane is to collect an I-V curve: current-voltage relationship. A series of voltage inputs is applied, and the current responses are measured, as shown in Figure 3.23a. The average current level is then plotted against respective voltage, and the slope of the linear fit represents measured conductance. In case of an intact membrane no signal is observed: conductance approaches 0. Examples of I-V curves obtained for membrane-spanning DNA and an intact bilayer are plotted in Figure 3.23b.

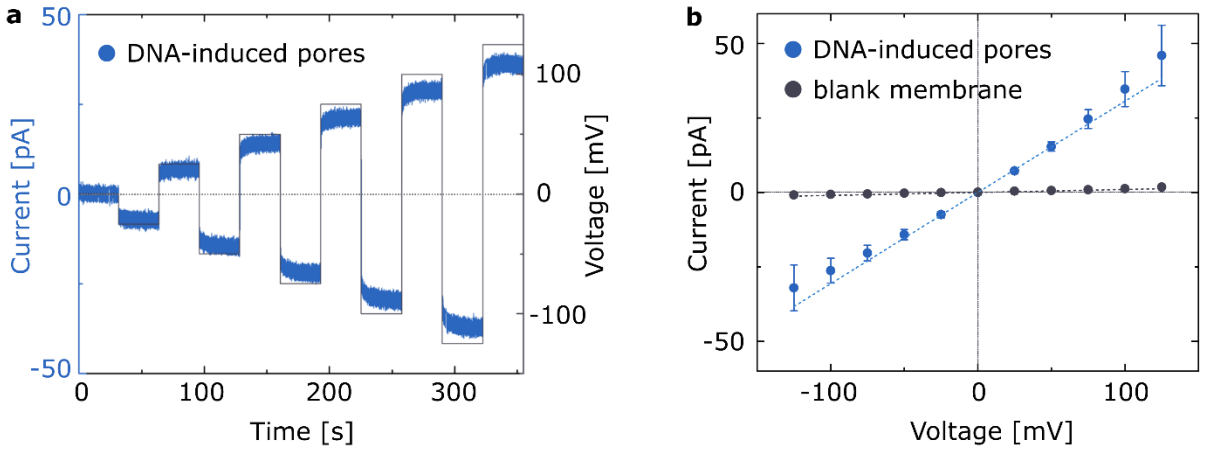

Figure 3.23 *Collecting I-V curves to assess membrane conductance. (a) Exemplary trace of voltage signal and current response recorded across bilayer in the presence of pore-forming DNA structures. (b) The I-V curve obtained from experiment shown in (a), before and after adding membrane-spanning DNA. The slope of the linear fit (dashed lines) corresponds to the conductance of the bilayer.*

In theory, the conductance values calculated for a single voltage input (in my case: 50 mV) should correspond to the slope of a whole I-V curve, and this is the assumption I make throughout this thesis. Unfortunately, what causes any discrepancies (the fluctuations and briefness of events) is also the reason why a full IV curve could not be run for all the events, which usually lasted below 1 s. The other, connected assumption, that I have already mentioned, is treating the current-voltage relation as ohmic. The exemplary curve in Figure 3.23b shows that this is only the case in

lower voltage ranges, while more and more divergence from linear relation is observed for higher values. For V = 50 mV, I have assumed that the Equation 3.12 describes the conductances correctly. I have allowed myself this approximation, because, as you will see in the next chapters, my studies are focused less on gathering the absolute values of conductances, and more on comparing them between the structures.

CHAPTER 4

Effects of membrane-spanning DNA on the arrangement of surrounding lipids

This work has previously been published in Sobota et al. *Tailoring Interleaflet Lipid Transfer with a DNA-based Synthetic Enzyme*, Nano Letters 2020, 20 (6) 4306−4311.

As DNA nanotechnology focuses on DNA, often in reported studies all other molecules seem to be playing second fiddle to the designed nucleic acid-based nanostructures, going as far as testing prospective biodevices in isolation, rather than in their targeted environment. However, this approach can be misleading. I already started to hint on this in Chapter 2, in the paragraphs discussing proteins. By looking at the membrane proteins' structure, it becomes clear that to create a functional biodevice it is crucial to design it in a *contextual* manner.

This chapter comprises the first out of four studies, in which I show that designing a synthetic membrane construct really means designing a whole DNA-lipid system - taking into account all the relevant interactions. Even though it turns the nanostructure's design into a time-consuming task, it is altogether a rather positive realisation, as it provides a number of handles one can use to increase the controllability of the constructs, without the need of complicating their architecture.

Note, that studying DNA in model lipid platforms is only a first step towards a *truly* contextual design: examining all interactions in the biological environment. Yet, starting with such a complex system would make it unfeasible to deconvolute and comprehensively describe all relationships between the molecules.

Therefore, let us start by looking at a minimalistic scenario of a DNA helix inserted into a lipid bilayer and ask a rather general question about the involved interactions: how does pore-forming DNA affect the surrounding lipids?

4.1. Hydrophilic environment at the DNA-lipid interface

Upon its insertion the membrane-spanning DNA forms a pore in the bilayer, mimicking transmembrane proteins. However, as discussed in Chapter 2, integral proteins have evolved with respect to the lipids - their membrane-spanning domain adapts a helical conformation that makes it hydrophobic, and as a result their position in the bilayer is energetically favourable.

DNA, on the other hand, has a strong negative charge on its surface making it hydrophilic - or should we say lipophobic. When pulled into the bilayer (with the aid of hydrophobic anchors), it will force the hydrophilic headgroups to face towards it. In order to arrange hydrophobic tails so that they are not in contact with the charged molecule, the headgroups from both leaflets will turn towards the DNA and cause the leaflets to merge. Therefore, membrane-spanning DNA will induce the formation of a **toroidal pore**, shaped by the merged bilayer leaflets, as shown schematically in Figure 4.1.

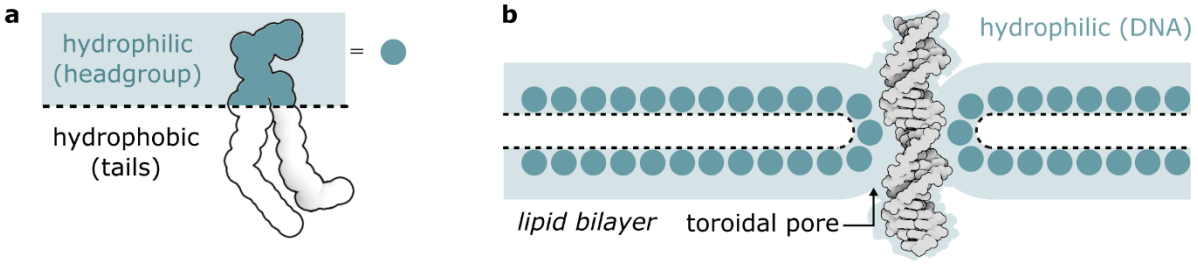

Figure 4.1 *Toroidal pore formation. (a) Model of a lipid highlighting hydrophilic and hydrophobic parts of it. (b) Schematic illustration of the arrangement of headgroups in the DNA-induced membrane pore showing the hydrophilic environment at the DNA-lipid interface. The all-atom model of DNA was built by Himanshu Joshi (Aleksei Aksimentiev's group, University of Illinois).*

Figure 4.1 highlights an important consequence of the toroidal shape of the pore, namely the hydrophilic environment at the DNA-lipid interface. This hydrophilicity has two significant implications for a synthetic transmembrane structure: (I) the presence of water in the pore facilitates the transport of ions at the interface[100] and (II) the merging of the bilayer leaflets allows lipids to move between inner and outer ones *via* diffusion[102].

The invariable ion flow (I) at the interface questions meaningfulness of designing DNA ion channels with a controllable cavity. In fact, it hints at the futility of designing *any* DNA ion channels at all. The interleaflet transport of lipids (II) too bodes ill for the protein-inspired DNA structures. Both phenomena are essentially strong, uncontrollable signals most likely to result in an immediate death of the DNA-decorated cell. As interesting as this concept may be for developing cytotoxic therapeutics, it is a significant problem for the material proposed to mimic membrane proteins.

The notion of a toroidal pore reiterates the importance of learning from nature: proteins have not developed a hydrophobic membrane-spanning domain for nothing. We can eliminate the problematic ion and lipid transport by adapting the chemical architecture of nucleic acid

constructs. The first steps in this direction have already been made with the DNA backbone of a pore-forming structure modified to remove the negative charge of the phosphates[107].

On the other hand, the previous paragraphs painted a too pessimistic picture. Ion flow and interleaflet lipid transfer are both biologically relevant phenomena, and their occurrence at the DNA-lipid interface could potentially be utilized to mimic the activity of natural proteins: ion flow is controlled by **ion channels**, while lipid flipping by transmembrane **scramblases**. Both are crucial for a proper functioning of a cell. The variety and significance of ion channels' tasks have already been mentioned in the previous chapters: they are responsible for the activity of nervous and muscular systems, and in fact, since they guard the homeostasis of every cell, each part of an organism depends on them[56,177–179]. Interleaflet lipid transfer is a less-commonly known process, yet it is also an indispensable one in ensuring the cell's survival. We have already looked at various lipid species in Chapter 2, where I emphasized how important the bilayer asymmetry is for signalling and metabolism of organisms. This causes scramblases to be involved in life-sustaining processes, like blood coagulation[35,180] or apoptosis – programmed cell death[36,181,182].

Disturbed functions of both transmembrane proteins - ion channels[177,178] and scramblases[183] - have been identified as factors responsible for many, often lethal, diseases and both are a subject of numerous research studies. Even a hint of an analogous functionality, like the one observed for DNA-induced toroidal pores, is worth better understanding and developing.

Therefore, even though we can eliminate the toroidality of the nanostructure-induced pores by turning their surface hydrophobic, here I would like to take a step in a different direction. The discovery of the toroidal pore can be utilized and will provide new functionalities to the DNA design - dependent on our ability to exert control over it. Knowing the cause of its formation we could prevent it, but we can also modify and use its activity.

4.2. Probing the shape of a lipid pore

As described in the previous paragraphs, the shape of the pore – its toroidality – results from the hydrophilicity of the pore-forming DNA. To confirm this idea, I have designed a membrane-inserting DNA duplex with four nucleotides in the central part of one of its strands replaced by a 12-carbon chain (dodecane). The membrane-spanning part of the structure is therefore half-hydrophilic and half-hydrophobic. An illustration of this construct embedded in a bilayer is shown in Figure 4.2a. The schematic was created based on the results of all-atom molecular

dynamics (MD) simulations created by Himanshu Joshi (Aleksei Aksimentiev's group, University of Illinois) and shown in Figure 4.2b (details in the Appendix, Section A1.1.). After 1 μs of simulation, the lipids were found with their headgroups predominantly pointing towards the unmodified strand, while no lipids were present within the pore on the side of the hydrophobic domain.

Realizing that the toroidality of the pore can be disrupted by modifying the membrane-spanning part, I investigated three versions of the aforementioned DNA duplex: featuring none (0D), one (1D) or two (2D) dodecane spacers placed in the central site of the structure. DNA sequences used in this work have been collected in the Appendix, Table A4.1, while the schematic representations of the designs can be found in the Appendix, Fig. A4.1.

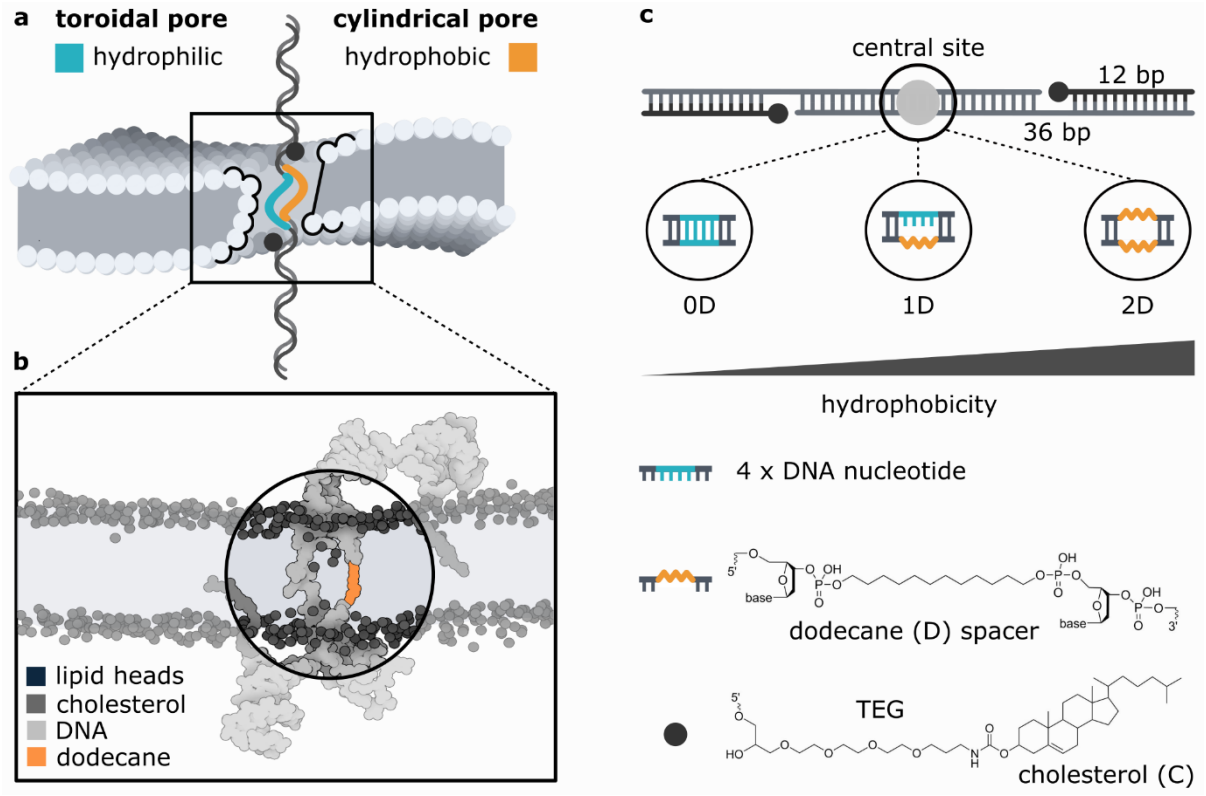

Figure 4.2 *Schematic representation of the designed DNA nanostructure. (a) The hydrophilicity of the membrane-spanning domain determines the structure of the DNA-lipid interface. (b) Snapshot from an all-atom MD simulation of the 1D construct. No lipid headgroups are present in the proximity of the dodecane spacer. (c) Schematic representation of the dsDNA construct, highlighting its membrane-anchoring (cholesterol) and internal (dodecane) modifications. Three different designs varying in hydrophobicity were used: with either none (0D), one (1D) or two (2D) dodecane spacers placed in the structure's central site.*

All tested duplexes were additionally modified with two cholesterol moieties (2C), as shown on the schematics in Figure 4.2c, which ensured membrane affinity. No attachment of unmodified DNA or caused by the presence of the C12 chain was observed, as illustrated by micrographs in Figure 4.3.

This lack of C12-driven attachment is worth elaborating on. We have established that hydrophilic DNA needs to be forced into proximity with the bilayer by hydrophobic anchors. However, as illustrated in Figure 4.3, not all hydrophobic moieties are made equal. The value I will use as a "hydrophobicity parameter" is a partition coefficient (*P*). It is the ratio of concentration of a given molecule in two immiscible liquids, in other words: the ratio of solubility values in polar (water) and apolar (octanol) solvents[184]. The measure of hydrophobicity is presented in a form of log*P*, as defined in Eq. 4.1.

$$\log P = \log\left(\frac{[solute]_{apolar}}{[solute]_{polar}}\right) \tag{4.1}$$

The log*P* values for cholesterol and dodecane are 7.11 and 2.33, respectively (Chemicalize, ChemAxon). Therefore, we can conclude that a hydrophobic anchor of log*P* = 2.33 is not enough, while anchor of log*P* = 7.11 is sufficient to ensure membrane attachment of 48 bp DNA duplex.

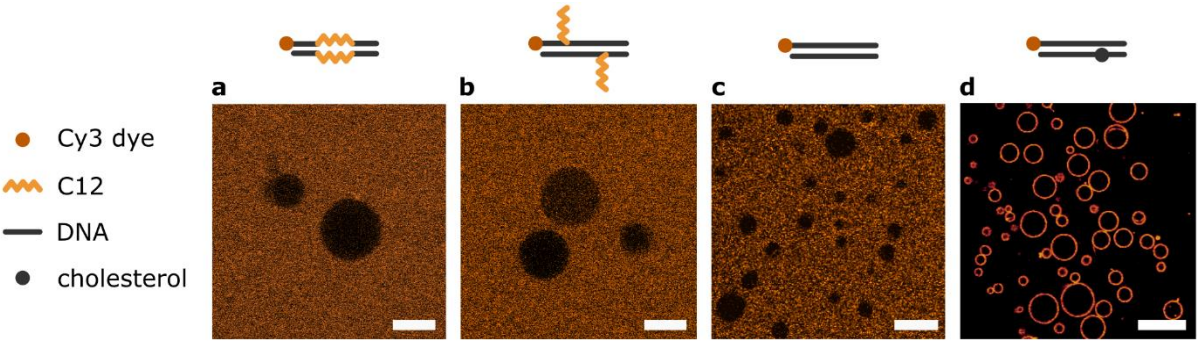

Figure 4.3 *Representative micrographs illustrating cholesterol-driven attachment. Even in the presence of the C12 domain, either placed internally (a) or overhanging (b), no attachment is observed, similarly to duplexes lacking hydrophobic modifications (c). Only cholesterol-tagged DNA was reported to coat the vesicles' membrane (d). Imaging performed in the presence of 4 mM $MgCl_2$. Scale bars: 5 µm (a-b), 20 µm (c-d).*

4.3. DNA duplex is a transient ion channel

The design of the duplexes, especially the long separation of hydrophobic anchors (24 bp ≈ 8 nm, compared with bilayer thickness ≈ 4 nm[11,143,185]), causes *transient* insertions of the structure, which has been reported earlier for a similar construct[100]. The mode of insertion can be studied by recording an ionic current across a lipid membrane in the presence of the structures. Figure 4.4a shows three representative current traces for each of the studied designs. The results indicate that: (I) the structures do not form stable pores, but induce current bursts while transiently spanning the bilayer, and (II) with an increasing number of internal dodecane modifications the total amount of ions transported across the membrane is reduced. The experimental results suggest quantitative differences in the current flow (Figure 4.4b), attributed to different sizes of water channels formed during the insertion - determined by construct's hydrophobicity as expected.

To further investigate the interactions between the inserted structures and the surrounding lipids, I continued the collaboration with Himanshu Joshi from Aleksei Aksimentiev's group (University of Illinois), who performed all-atom MD simulations. An initial examination of a 2D construct in the absence of lipids showed that, when in an aqueous solution, the dodecane modifications adapt a contracted conformation, rather than appearing fully stretched. However, after being placed in a (DPhPE) membrane, the C12 chains extend to span through the hydrophobic core, while DNA moves out from the hydrophobic region. Therefore, even though in the initial stages a toroidal pore was formed around each construct, the induced water channels differed noticeably between each system, as shown in Figure 4.4c. The number of water molecules in the pore decreased with increasing hydrophobicity of the central site, agreeing with the observed differences between experimentally obtained conductance traces. The presence of a stretched dodecane spacer affected the molecular arrangements of the created pore, resulting in a smaller number of permeated water molecules as shown on the plot in Figure 4.4d.

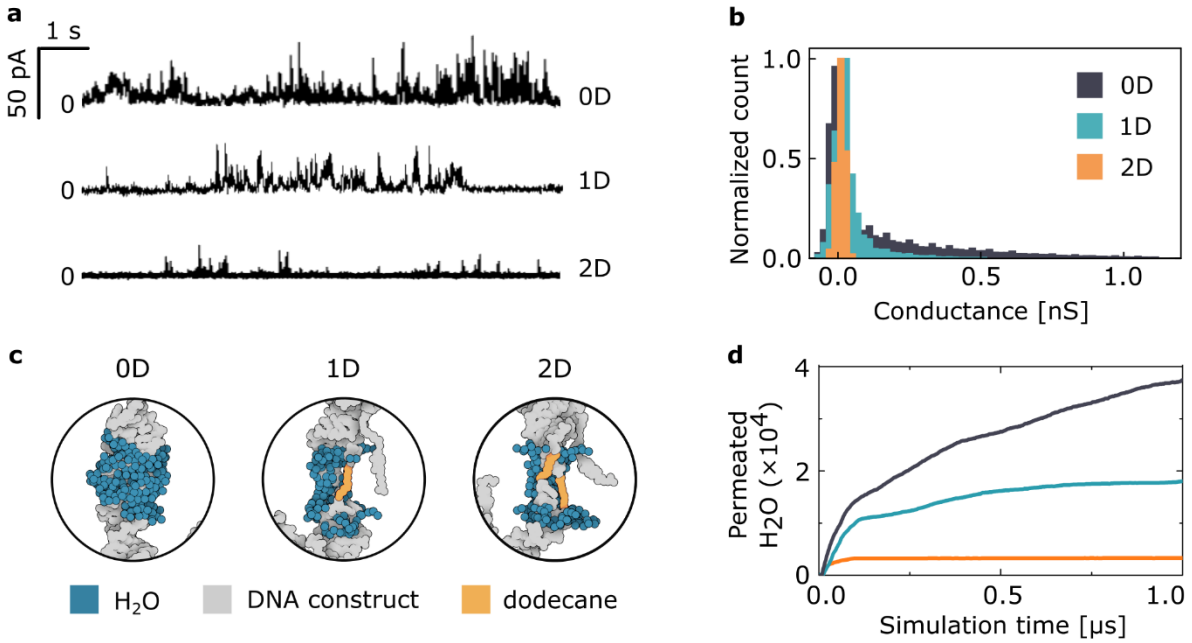

Figure 4.4 *Experiments and simulations reveal a DNA-induced transient water channel in a lipid bilayer. (a) Representative current trace for each of the three designs. (b) All-point histograms of the first 20 min of the ionic current recorded. (c) Snapshots highlighting the number of water molecules in the channel after 0.8 μs of MD simulations of DNA constructs in a DPhPE lipid bilayer. Lipids and ions are not shown for clarity. (d) Results of all-atom MD simulations showing the number of water molecules permeated through the membrane as a function of simulation time. All simulations were performed by Himanshu Joshi, PhD (Aleksei Aksimentiev's group, University of Illinois).*

The simulations showed that while in aqueous environment, dodecane domain is contracted. However, upon its membrane insertion it starts stretching. After 1 μs of simulations C12 was fully stretched, its hydrophobicity prevented the formation of the toroidal pore and subsequently hindered water, ion and lipid transfer. The C12 stretching and the resulting closure of the hydrophilic channel can be envisioned from the snapshots presented in Figure 4.5.

This observation makes the fact that duplexes span the membrane *transiently* highly significant. If the insertion would be stable, dodecane domain of the 2D constructs would prevent both the ionic current and the lipid transfer. However, due to its constant spanning of the bilayer, we can observe continuously appearing current spikes, albeit smaller than for 0D and 1D structures, because of the immediate channel disruption. This realization is crucial for understanding the functionality of the formed pores described in the next part of this chapter.

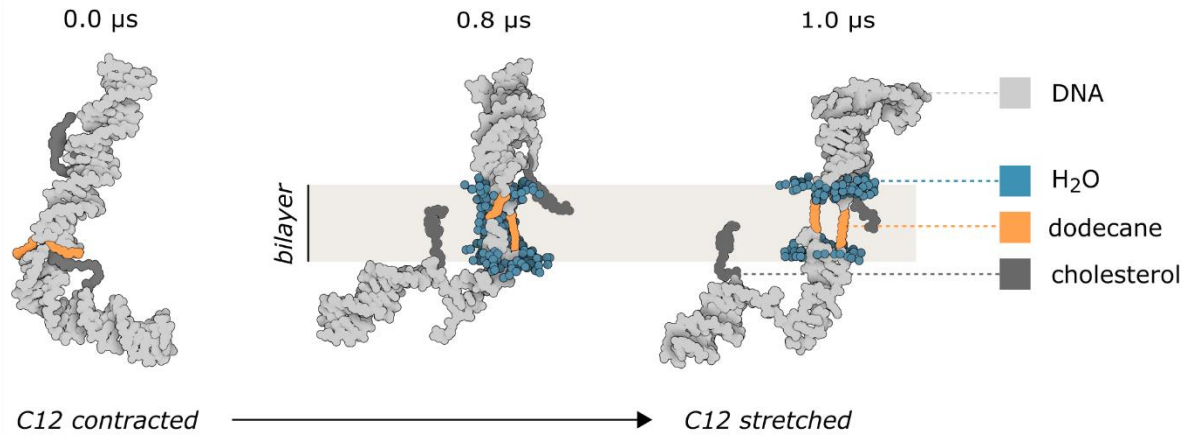

Figure 4.5 *Snapshots from MD simulations illustrating the changes in C12 domain length over time. Initially contracted, C12 stretches after being placed in the membrane, until it spans the whole thickness of the hydrophobic core. Subsequently, the water channel through the bilayer closes. All simulations were performed by Himanshu Joshi, PhD (Aleksei Aksimentiev's group, University of Illinois).*

4.4. Modulating the shape of a lipid pore

To further observe the disruption of the toroidal pore and its effects on the rate of lipid transfer, I experimentally examined the movement of lipids between the inner and outer leaflet of the bilayer. This movement is intrinsically rare due to a high energy barrier[186]. However, when the toroidal pore is formed upon DNA duplex insertion, the lipids can move unhindered between both - now merged - leaflets[102,106]. The change in the lipids' position was studied *via* an optical assay based on a redox reaction. After the DNA duplexes were incubated with giant unilamellar vesicles (GUVs), the NBD reduction assay described in Chapter 3 was performed.

In a nutshell, upon the addition of a reductant (dithionite, $[S_2O_4]^{2-}$) NBD labels on the lipids in the outer leaflet are chemically altered into their non-fluorescent analogue (bleached), while the labels in the inner leaflet remain intact[102,106,171,172]. Therefore, when no toroidal pore is formed, in the presence of the membrane-impermeable reductant, the fluorescence intensity of the vesicle decreases to around 50%, since the lipids from two leaflets do not mix and half of them have NBD labels bleached. Such loss of the signal is observed on vesicles incubated with non-inserting structures, as shown in Figure 4.6.

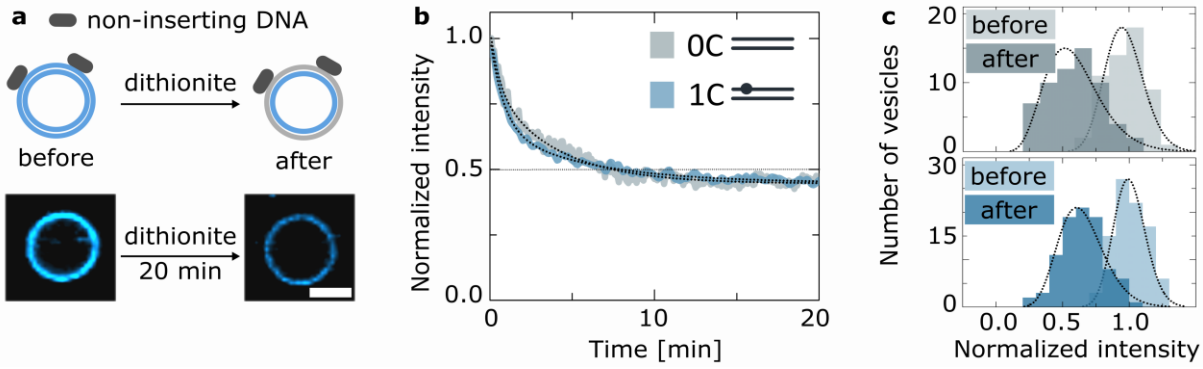

Figure 4.6 *NBD-reduction assay performed in the absence of a toroidal pore. (a) Schematic illustration of the assay performed in the presence of non-inserting DNA structures. NBD-labelled lipids are represented in blue. Micrographs from experiments with a 1C construct are shown in the bottom part of the panel. Scale bar: 5 µm. (b) Fluorescence intensity traces of non-inserting structures modified with either one (1C) or no (0C) cholesterol molecules, showing 50% loss of signal upon dithionite addition in t = 0. Each plot is an average of at least three traces (shown in the Appendix, Fig. A4.2). (c) Histograms of vesicles' fluorescence intensity collected before and 30 min after addition of dithionite. Values were normalized to the distribution peak before the experiment. Number of vesicles analysed for 0C: N_{BEFORE} = 55, N_{AFTER} = 60 and for 1C: N_{BEFORE} = 95, N_{AFTER} = 93.*

Once the toroidal pore is formed, however, NBD-lipids from the inner leaflet diffuse through the DNA-lipid interface to the outside of the vesicle, where they too are reduced. Consequently, a complete loss of the fluorescence signal is observed. In such case, I consider the rate of bleaching to be determined by two processes: dithionite bleaching the outer leaflet and the exposure of the outer leaflet lipids due to the interleaflet transfer. The analysis of the resulting biexponential decay is described in Chapter 3.

The intensity decay traces, averaged for the vesicles displaying complete bleaching, are shown in Figure 4.7a. The observed rates of bleaching (0.25 ± 0.01, 0.21 ± 0.01 and 0.09 ± 0.01 min^{-1} for 0D, 1D and 2D structures, respectively) correlate with the hydrophobicity of the central site - the more hydrophobic the membrane-spanning domain, the slower lipid transfer is observed. This suggests that the presence of the C12 spacer impedes the formation of a clear pathway for the lipids' interleaflet movement, its effect being especially noticeable when comparing vesicles incubated with 0D and 2D constructs, as illustrated by micrographs in Figure 4.7b. Note, that even the structures with an entirely hydrophobic central site (2D) cause lipid transfer across the membrane, which is an effect of the transient insertions: merging of the leaflets must occur with each membrane spanning, as was also shown through the ionic current measurements (Figure 4.4a).

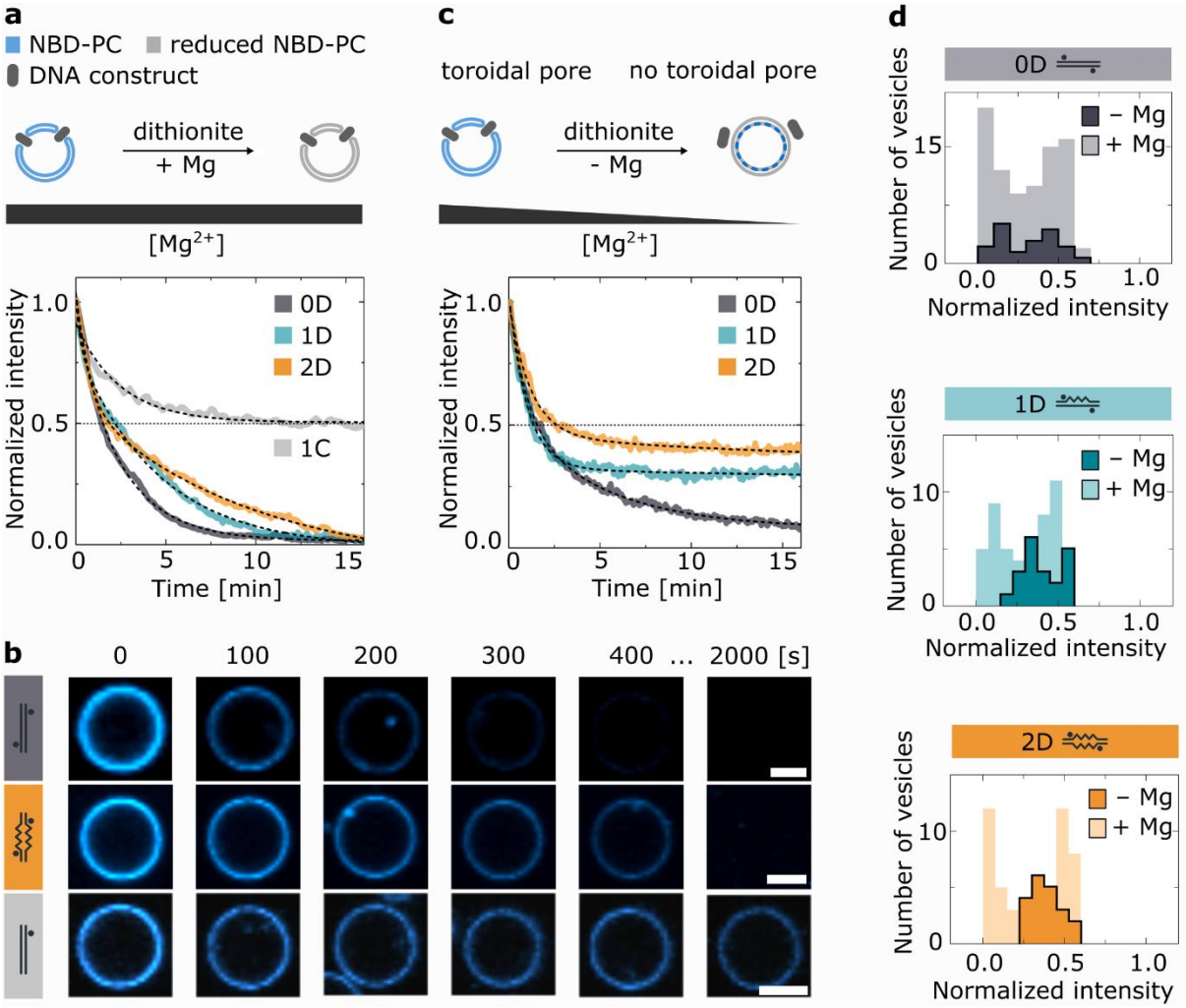

Figure 4.7 *Controlling the rate and the level of lipid flipping through DNA nanostructure's architecture and the concentration of divalent cations. (a) Experimental results from the schematically illustrated bleaching assay with magnesium concentration constant (4 mM, +Mg) throughout the experiment. The plot shows fluorescence intensity time traces collected for the three constructs and the non-inserting (1C) control upon dithionite addition at t = 0. Each plot is an average of at least three traces (shown in the Appendix, Fig. A4.3), indicative of the leaflet merging. The black dashed lines represent a biexponential fit (the obtained parameters can be found in the Appendix, Table A4.2). (b) Representative confocal microscopy image sequences at +Mg conditions, showing the difference in fluorescence decay rates of 0D and 2D structures alongside the non-inserting 1C structure. Scale bars: 5 µm. (c) Experimental results analogous to (a), with magnesium concentration decreasing by 1.5 mM (-Mg) throughout the experiment. Each plot is an average of at least three traces (shown in the Appendix, Fig. A4.4) indicated by the respective peaks in the histograms of the final intensities presented in (d). (d) Histograms of the final intensity values collected from three experiments for each DNA construct, for +Mg (N_{0D}=82, N_{1D}=49, N_{2D}=50) and -Mg (N_{0D}=24, N_{1D}=N_{2D}=20) conditions.*

4.5. Ion-responsiveness of the modified DNA structures

Due to DNA's intrinsic negative charge, cations are crucial in double helix formation and thus in ensuring the stability of DNA-based nanostructures[138,187]. Divalent cations are most often used in DNA nanotechnology, and amongst these Mg^{2+} is particularly common. The stability of duplexes was shown to decrease in lower concentration of cations[187–189], yet I did not expect the difference to be noticeable in the Mg^{2+} range used in the experiments. Indeed, the stability and yield of folding of the unmodified 0D duplexes do not seem to depend on cation concentration above 1 mM Mg^{2+}. However, internally-modified structures (1D and 2D) show higher sensitivity to changes in Mg^{2+} concentration, as presented by the results of spectroscopic measurements (Figure 4.8a) and polyacrylamide gel electrophoresis (Figure 4.8b). Duplexes prepared in various salt conditions show different behaviour during the PAGE experiment despite them being subjected to the same ionic compositions of the gel and the running buffer, additionally emphasizing the effects of folding conditions.

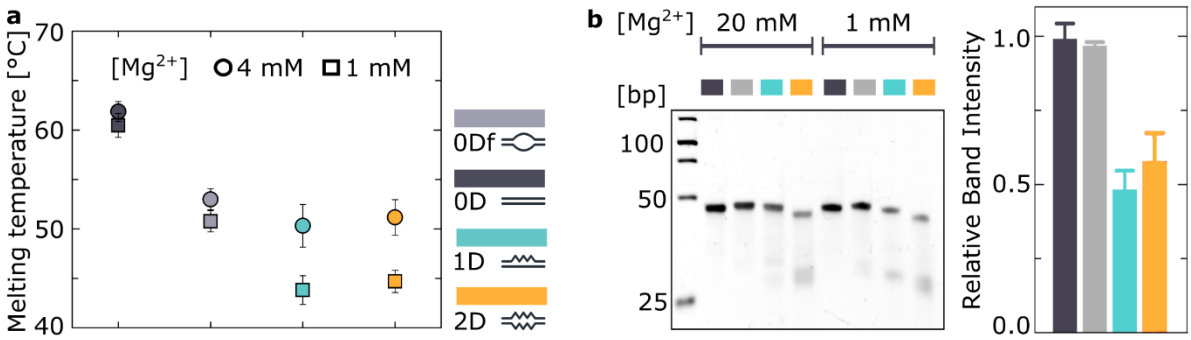

Figure 4.8 *Mg^{2+} dependency of the duplexes' stability. (a) Melting temperatures of constructs folded in either 1 or 4 mM $MgCl_2$. Exact values can be found in the Appendix, Table A4.3. (b) Polyacrylamide gel electrophoresis analysis of structures folded in either 20 or 1 mM $MgCl_2$. The column plot shows the ratio between band intensities in the two ionic concentrations: I_{1mM}/I_{20mM}. The values can be found in the Appendix, Table A4.4. The three studied duplexes were additionally compared with the 0Df structure, featuring no dodecane modifications, but with 4 nucleotides in the central site unpaired (see the Appendix, Fig. A4.1 and Table A4.1).*

Since both 1D and 2D structures have four less paired bases in their central site (which can be also determined by comparing the absolute values of T_m in Figure 4.8), it could be this mid-strand flexibility influencing the cation sensitivity of the two constructs. I have therefore introduced another structure: an analogue of the 0D without the internal C12 chains, but with four central nucleotides unpaired (0Df), mimicking the flexibility of the dodecane-modified duplexes

(sequences in the Appendix, Table A4.1). Even though, as expected, 0Df has a lower T_m than 0D, it is similarly little affected by changes in Mg^{2+}. From this I concluded that it is the presence of the dodecane in the central site that is responsible for the cation-dependency observed for 1D and 2D structures.

This notion, suggesting that internal modifications may have disrupted the well-defined helix structure, can also provide an additional way of controlling DNA-induced membrane activity. Therefore, I performed further experiments where the magnesium concentration was rapidly reduced by 1.5 mM upon the addition of dithionite, as schematically presented in Figure 4.7c. The observed effects resulted from a combination of: (I) the reducing agent bleaching the fluorophores, (II) the DNA-induced pores influencing the accessibility of fluorophores to the bleaching factor, and (III) changes in the ionic concentration affecting the stability of the DNA structure.

Histograms in Figure 4.7d present a comparison of the final intensities of the traced vesicles from the experiments previously described: with the constant (+Mg) and the decreasing (-Mg) magnesium concentration.

When there are no changes in the divalent cation concentration, all three systems exhibit similar distributions of the final fluorescence intensities. There, two populations of vesicles can clearly be distinguished: with optical signal decreased to either 50% or 0%. The first group was assigned to vesicles with no toroidal pore, indicating an absence of DNA insertions. The population of vesicles that exhibited a complete loss of fluorescence represents membranes with merged leaflets – and therefore with the DNA duplex spanning through the bilayer.

When the concentration of Mg^{2+} is reduced we can still observe a fraction of vesicles not affected by the DNA structures (bleaching ≈ 50%) and a number of them that bleach more, indicating interleaflet lipid transport. However, both 1D and 2D constructs exhibit only partial bleaching of the inner-leaflet lipids - with a distribution peak between 0% and 50% - suggesting that the DNA-induced lipid transfer was ***stopped*** during the experiment. I attribute this effect to the decreased stability of these structures in the lower Mg^{2+} concentration (Figure 4.8) and a subsequent disruption of lipid flipping occurring during the assay. As a result, only a fraction of the lipids changes their interleaflet position - reminiscent of the effects of natural scramblases, which exhibit control over the amount of transferred lipids[190]. The level on which the lipid movement is terminated depends on the number of dodecane modifications, with 0D showing the lowest level

of residual fluorescence. The change in cation concentration by 1.5 mM resulted in bleaching of around 92%, 70% and 61% of lipids, caused by the 0D, 1D and 2D structures, respectively (Figure 4.7c). The results indicate that it is possible to not only control the rate of lipid interleaflet movements using hydrophobic modifications, but also use an external stimulus to vary the level of such transfer.

Although I attributed the differences between +Mg and –Mg experiments to the duplex stability being affected by the cation concentration, I almost certainly have not painted the full picture of the phenomena occurring in this system. I showed that 0D construct does not display a significant structural sensitivity in the studied Mg^{2+} range (Figure 4.8). Yet, the plots in Figure 4.7a and c indicate a relatively small, but still noticeable change in activity. What does this change result from?

A reasonable deduction would be that this difference occurs due to the affected membrane insertion efficiency. And indeed, ions play a huge role in maintaining DNA-lipid anchoring even when they do not affect the DNA structure itself. I will elaborate on this topic in Chapter 6, entirely dedicated to the action of cations in the studied system. Here, it was the structural stability and its cation-dependency that played a more significant role in changing the DNA membrane activity, inducing differences in ion-responsiveness of the three studied designs.

4.6. Conclusions

This chapter presented synthetic DNA-based nanostructures that insert into membranes and act as both ion channels and lipid-flipping constructs. Both activities of the membrane-spanning DNA have been shown previously[100,102], even if not simultaneously for the same structure. Here, I experimentally showed that a single DNA duplex exhibits both functionalities, with ions and lipids transferred through the same pathway: DNA-lipid interface. Simulations performed by Aleksei Aksimentiev's group provided deeper understanding of the molecular phenomena and confirmed the experimental results. In nature, transmembrane scramblases are responsible for changing the bilayer asymmetry, and they too work as ion channels with the same route for both transported moieties[191].

Additionally, inspired by the hydrophobic membrane-spanning domain of transmembrane proteins, I have designed internally modified variations of the self-inserting duplex. By changing the number of hydrophobic spacers, I achieved control over the structures' interaction with the surrounding lipids. Internal modifications caused disruption of a toroidal pore and

the hydrophilic environment at the DNA-lipid interface, which in turn resulted in different rates of lipid flipping induced by the duplexes. I have also demonstrated a fundamental connection between the design of the DNA structure and its ability to transfer lipids in response to external stimuli like divalent ions. The removal of Mg^{2+} resulted in hindering the lipid flipping, which until now was a unique feature of specialized transmembrane proteins.

We can draw several conclusions from these findings. Firstly, aiming to design transmembrane protein mimics, I took a step towards a controllable membrane-active structure. Changing the hydrophobicity of the DNA surface can lead to different membrane responses. A remarkable next step would be to design a structure with "tuneable" hydrophobicity of the membrane-spanning domain. By tuneability I assume a controllable exposure of hydrophilic surfaces, rather than chemical changes in DNA structure. Incidentally, such controllable exposure is one of the proposed mechanisms of the action of natural scramblases, with lipids transported in a stimulus-gated hydrophilic groove in an otherwise hydrophobic domain of the protein[192]. When building a DNA-based mimic, I recommend protein-inspired solutions, as they have already been proven to work.

On that note, the discovered Mg^{2+}-dependency of the amount of transported lipids is especially exciting, since scramblases are known for their divalent cation-responsiveness[170,193]. However, the proposed explanation for the duplexes' sensitivity to cation concentration does not assume any ion selectivity, while in a cell it is specifically calcium ions that control the interleaflet lipid transport. The mechanisms responsible for the ion-responsiveness of proteins and DNA-based structures could not be more different. Perhaps the notion of stability/ions interplay can be more useful in less precise functionalities displayed by DNA nanoengineered devices - but useful nonetheless.

Additionally, when building synthetic biological devices, whether with DNA or any other material, one does not always need to complicate the design to achieve more controllability. The opportunity for functionality regulation can very well be present in the system already, we just need to realize how to use it. In the studies presented here, changes made to the DNA-lipid interface and the presence of ions allowed us to observe new responses. Their variation led to a relatively high control over the system, without the need of expanding the design. With this I want to stress that thorough research of all the interactions in the synthetic system is required, not only to avoid unexpected issues, but also to unlock new possibilities and creative solutions.

Finally, the presented experiments and simulations emphasize the importance of contextual design when creating new constructs. Here, I show that the architecture of the designed structures should not be treated in isolation, but rather with respect to their interactions with the surrounding environment - and in a broader sense, their prospective applications[194] – which is essential for the creation of a new generation of complex molecular machineries.

CHAPTER 5

Effects of surrounding lipids on the stability of membrane-spanning DNA

This work is submitted for publishing as Morzy et al. *Stabilization of base pairs improves membrane activity of a DNA-based synthetic ion channel.*

In the previous chapter I started the analysis of the studied three-component network (DNA-cholesterol-lipids) by assessing how the presence of inserted DNA affects the arrangement of lipids in a bilayer. Here, I will tackle the analysis from the opposite end: what is the influence of the surrounding lipids on the inserted DNA? Similarly to the previous project, I will aim at not only describing the interactions and underlying phenomena, but I will also show how these findings can unlock new functionalities of membrane-interacting DNA nanostructures.

The previous chapter has shown that repulsive DNA-lipids interactions result in a lipid pore forced to adopt a toroidal arrangement. Here, on the other hand, I will show that DNA and its architecture are not left unaltered in such a system. However, before analysing changes in the structure of the double helix, one should look at what holds it together in the first place.

5.1. Forces maintaining the double helix

I already briefly described the chemistry responsible for the double strand formation in Chapter 2: H-bonds and stacking are mutually dependent and therefore both are responsible for forming and maintaining the double helix. I also highlighted the difference in the number of hydrogen bonds between A=T and G≡C pairs. Knowing that a GC-rich DNA "melts" at higher temperatures than an AT-rich one, a simple conclusion follows: hydrogen bonds are responsible for the helix stability.

However, studying the calorimetry of DNA duplexes, an unexpected result emerges: a higher heat capacity is attributed to AT bp dissociation than GC bp. Yet, it remains true that lower temperatures are required to melt AT-rich DNA, as illustrated by the schematic heat capacity plots in Figure 5.1.

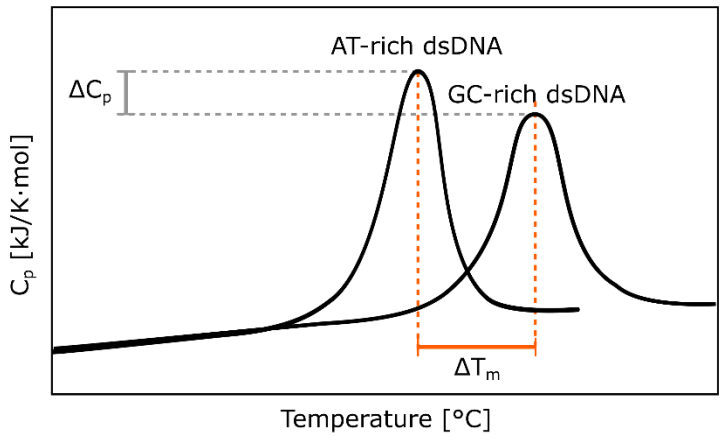

Figure 5.1 *Calorimetric measurements reveal the enthalpic and entropic contributions of base pairs to the double helix formation. Comparison of heat capacities of AT- and GC-rich DNA recorded throughout its heating. Sketched after Privalov and Robinson, 2020.*

Experiments show that GC pairs contribute more to the thermal stability of the duplex (higher melting temperature). Analysing it in terms of thermodynamics, it could be so if (I) the GC bp enthalpy was higher than AT bp. Through calorimetric measurements we now know this is not the case. Therefore, it is deduced to be an effect of (II) AT having a higher entropic contribution and by that being easier to break in the second-law-of-thermodynamics-driven world. This has been confirmed by analysing the experimentally obtained values[68], presented in Table 5.1.

Table 5.1 *Contribution of GC and AT base pairs to the thermodynamics of duplex disassociation at 298 K (25 °C). Enthalpy (ΔH) and entropy (ΔS) changes, as well as the intrinsic values (highlighted), after ignoring the contribution of the hydration spine in AT base pairs ($\Delta H_w \approx 9\ kJ/mol$ and $\Delta S_w \approx 33\ J/K \cdot mol$, respectively), were used to calculate Gibbs free energy (before (ΔG_{+w}) and after (ΔG_{-w}) taking water contribution into account) following its definition: $\Delta G = \Delta H - \Delta S \cdot T$. Values per base pair, data obtained from Privalov and Robinson, 2020.*

	ΔH [kJ/mol]	$\Delta H - \Delta H_w$ [kJ/mol]	ΔS [J/K·mol]	$\Delta S - \Delta S_w$ [J/K·mol]	ΔG_{+w} [kJ/mol]	ΔG_{-w} [kJ/mol]
GC	19.0 ± 0.2	19.0 ± 0.2	36.2 ± 0.2	36.2 ± 0.2	8.2 ± 0.2	8.2 ± 0.2
AT	28.0 ± 0.3	19.0 ± 0.3	73.5 ± 0.5	40.5 ± 0.2	6.1 ± 0.2	6.9 ± 0.4

The higher enthalpy and entropy contributed by the AT pair are found to result from water molecules which the pair immobilizes in the minor groove of the helix. Even though water is present all around the dsDNA, in minor grooves of AT-rich duplexes they adopt a stable conformation resembling the one in ice crystals, forming a so-called **spine of hydration**[195–197],

shown in Figure 5.2a. It may result from the AT duplexes having narrower minor grooves and thus restricting bound water more[198].

This water formation contributes significantly to both the enthalpy and entropy of the AT bp disassociation: approximately 9 kJ/mol and 33 J/K·mol, respectively. Upon subtracting these values from the ones measured for the AT base pair, the intrinsic values (highlighted in Table 5.1) show that the enthalpic contribution of AT and GC base pairs are practically identical, while the entropy of AT pairs is higher than GC by 4 J/K·mol.

We can attribute the differences between the intrinsic values to the additional hydrogen bond in the GC pair. Since enthalpies are the same, H-bond contributions to the enthalpy are negligible. On the other hand, assigning -4 J/K·mol entropy* to the disassociation of a single H bond results in GC pairs being responsible for a Gibbs energy of double strand unfolding of 3.6 kJ/mol, while AT contributes 2.4 kJ/mol, both around 40% of the total ΔG calculated for each pair (Table 5.1, Figure 5.2b).

This answers a part of our question: the entropy decrease resulting from H-bond formation in an aqueous environment is one of the phenomena driving the duplex formation. But what contributes to the remaining 4.5 kJ/mol of the Gibbs energy?

As we already observed, the enthalpy of DNA unfolding does not depend on the H-bonds between bases. Nevertheless, we observe a significant enthalpy of disassociation of both the AT- and GC-rich dsDNA. This enthalpy results not from hydrogen bonds between the opposite bases, but from stacking between the adjacent ones.

The flat hydrophobic surfaces of aromatic rings arrange themselves in coin-like stacks within the helix core. In fact, there are many similarities between this process and the bilayer formation, with van der Waals interactions between apolar molecules responsible for the stability of the structure formed. Additionally, a more specific process, termed π stacking[199], takes place when the parallel organization of flat nucleobases maximizes the interactions between π electron clouds of the aromatic rings, and this too plays its role in maintaining the double strand.

*Negative entropy of hydrogen bonds is an effect of water molecules arranging around the polar groups of nucleobases upon their exposure[68,340].

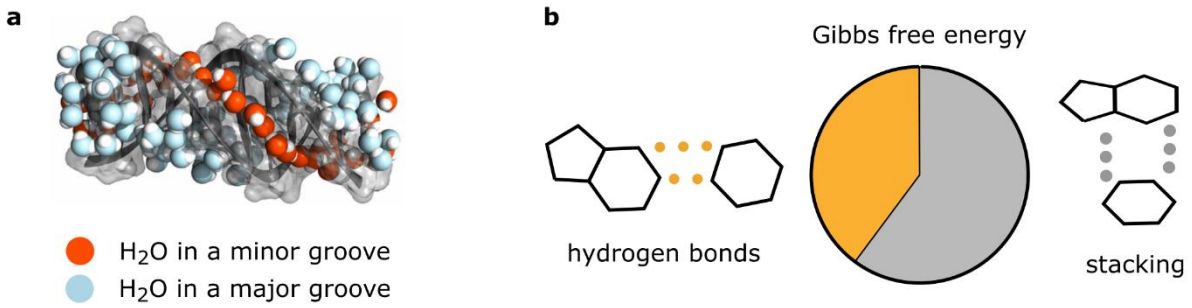

Figure 5.2 *Forces responsible for double helix stability. (a) MD simulation snapshot showing loosely bound water (blue) in the major and the spine of hydration (red) in the minor groove of a duplex. Adapted from McDermott et al., 2017*. (b) Schematic illustration showing the contribution of base pairing (hydrogen bonds) and base stacking to the Gibbs free energy of the dsDNA formation. The schematic plot was sketched based on the data from Table 5.1 and shows 40% and 60% input from the two processes, respectively.*

The parallel arrangement of the nucleobases is crucial for the formation of hydrogen bonds between the opposite strands. Formation of base pairs with no hydrogen bonds whatsoever has also been reported, hinting at the importance of stacking[200]. Still, H-bonds remain a significant force responsible for the double helix structure.

It must be noted, however, that these contributing factors are relatively weak. The free energy landscape of DNA is generally considered shallow, with thermal fluctuations and various solvent conditions able to disturb its structure. In fact, nature uses this sensitivity of DNA structures for recognition purposes[201–203]. But in DNA nanotechnology, one should be wary of taking the structure for granted and not to trust the strength of the double-stranded rope too much.

5.2. DNA insertion is a tug-of-war game.

Firstly, let us consider what happens with the molecules in the studied system: DNA modified with cholesterol approaches a lipid membrane. DNA, with its strong charge, does not want to be too close to the hydrophobic lipids. Cholesterol, on the other hand, moves towards them readily. Effectively, the two start pulling in opposite directions, playing a tug-of-war game. And just like the game, it can end in one of the three scenarios presented schematically in Figure 5.3:

*Marked panel has been reused from the cited article (https://pubs.acs.org/doi/abs/10.1021/acscentsci.7b00100) with permission. Further permissions related to this material should be directed to the copyrights' owner.

One possible outcome is **dominating cholesterol**: it pulls the dsDNA and forces it into the membrane. This is the ultimate goal of DNA membrane insertion, the result which I - the designer - am trying to ensure.

Conversely, we may observe **dominating dsDNA**. Here, it means that DNA's aversion to the hydrophobic core of a membrane prevents the structure, and with it the cholesterol, from inserting into the bilayer. Cholesterol is known to be a very strong anchor (logP = 7.11, Chemicalize, ChemAxon), therefore it is rarely identified as the weakness of the design. (Although, as you will see in the next chapter (Chapter 6), cholesterol is not unassisted in ensuring membrane anchoring. Cations are required to provide screening of the negatively charged DNA phosphates.)

Finally, the two parts of a molecule may **no longer engage in the struggle**. For the cholesterol-driven DNA insertion this signifies either linkage between DNA and cholesterol breaking or the double strand unwinding.

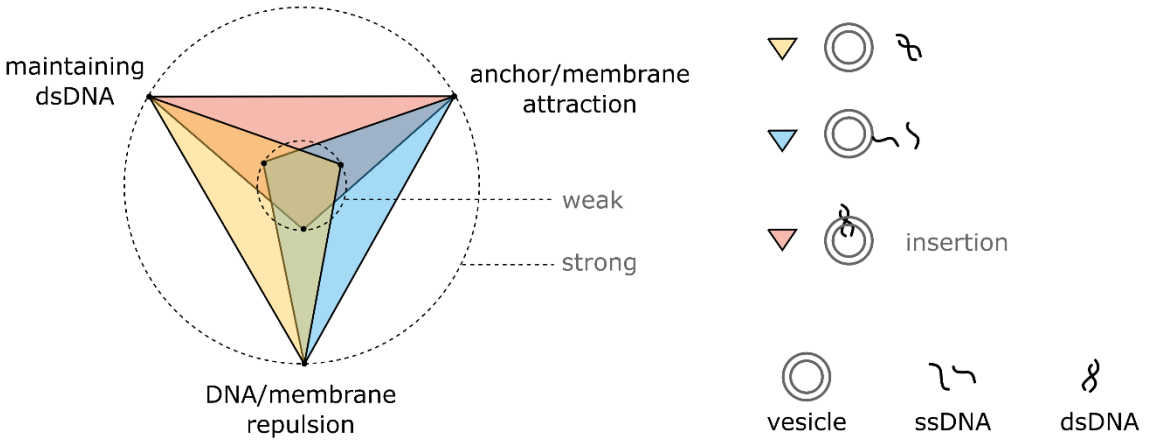

Figure 5.3 *Balancing forces in DNA membrane insertion. By changing the strength of double helix formation and the number/ strength of the membrane anchor, one can facilitate membrane insertion by overcoming the repulsion between DNA and membrane. The graphical legend corresponds to the three "tug-of-war" outcomes described in the text: DNA dominating (yellow), cholesterol dominating (red), two parts of the molecule no longer engaged in the struggle (blue).*

The third scenario is the one particularly important in this chapter, although it is the first one (dominating cholesterol) that is the aim of this whole thesis. What processes will disrupt the connection between the dsDNA and its hydrophobic modification? Firstly, the covalent bond between cholesterol and the DNA backbone is one of the strongest linkages in the chemistry world, and we assume it will not give way. However, the double strand itself is not necessarily as reliable.

If the dsDNA unwinds, cholesterol can enter the membrane, while covalently attached ssDNA can remain outside, sticking out of the bilayer, and the rest of the (hydrophilic) structure will move away from the hydrophobic environment. The unfavourable interactions will only affect apolar nucleobases, now exposed to the aqueous environment. It is important to realize that there is *always* a dominating interaction in the system. DNA and lipids were not made to interact in as close a proximity as we are trying to enforce. We can only facilitate certain outcomes and balance the forces in the system to ensure the desired effect, but no all-satisfying solutions are possible (unless we significantly alter the chemistry of the DNA backbone).

The idea of DNA unwinding completely to allow cholesterol inserting into the membrane is an extreme case. Let us take a step back and consider which base pairs specifically should not be taken for granted.

It has previously been established that terminal base pairing is weaker than in the middle of the duplex[204,205]. Therefore, the dsDNA is subject to fraying at the ends or in the position of nicks – discontinuities in the sugar-phosphate backbone of one of the strands forming the double-helix. Even though nicked secondary structures are stabilized by the stacking between the adjacent base pairs, this too is formed in a transient manner, with an equilibrium between two conformations: stacked (straight) and unstacked (kinked)[206–208]. Therefore, both effects responsible for the DNA stability, base pairing and base stacking, are affected in the position of a nick. Since the free energy of cholesterol membrane insertion is -75 kJ/mol[101,209], and the free energy contribution of single base pair dissociation ranges from around 6 (AT) to 8 (GC) kJ/mol[68], I expect that a short part of the double-strand can be misshapen if it facilitates cholesterol insertion. I hypothesize that if cholesterol is placed at a discontinuity, the combined effect of its pulling towards and DNA pulling away from the bilayer will be stronger than the less stable terminal base pairs, resulting in flexing and fraying of the nick region. Therefore, even carefully designed DNA constructs can prove inefficient as transmembrane channels, since the envisioned molecular structure will be distorted.

5.3. Probing the effects of helix stability on DNA-membrane interactions

In order to probe the effects of base pairing stability and investigate their importance in synthetic DNA-based transmembrane systems, I studied three designs of DNA duplexes carrying two cholesterol moieties, varying the distance between the modifications and the number of nicks. Two structures were comprised of four strands each, with cholesterol positioned at the nick.

Modifications were introduced symmetrically towards the centre of the construct, separated by either 24 bp (≈ 8 nm) or 12 bp (≈ 4 nm). The third structure consisted of two strands, with cholesterols introduced as internal modifications, separated by 8 nm. I will refer to these three structures using the notation: (the distance between cholesterols)-(number of nicks): *4 nm-2x, 8 nm-2x, 8 nm-0x*. Sketches in Figure 5.4 give a better understanding of the designs (a), alongside the chemical structure of the cholesterol linkage (b).

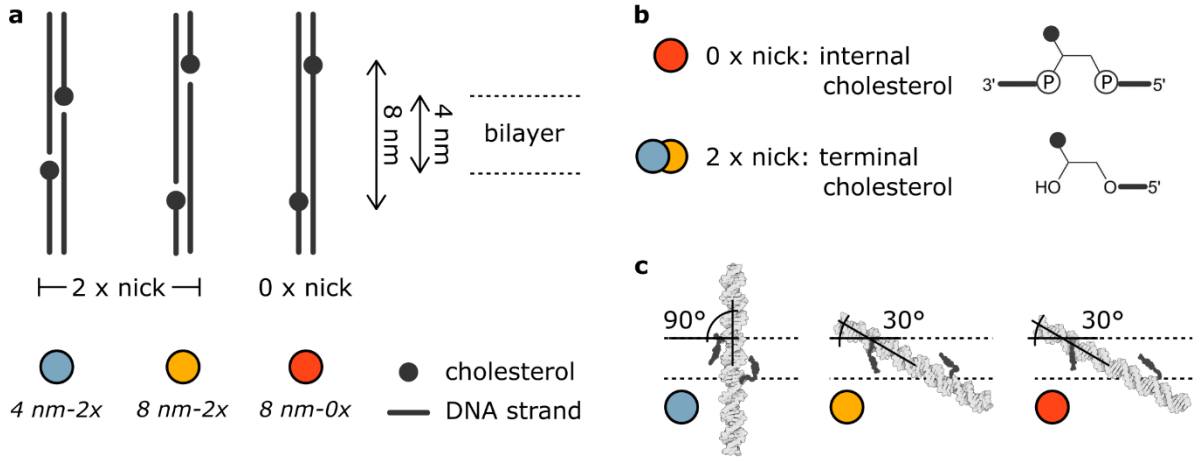

Figure 5.4 *Schematic representation of the three studied DNA duplexes. (a) Sketch illustrating the differences between the structures: distance between two cholesterol modifications and number of nicks in the modified positions. (b) Chemical linkage of the introduced modifications: cholesterol in between two phosphates of a backbone in the absence of nicks or cholesterol at the terminal end, in the position of a nick. (c) Snapshots from MD simulations performed by Himanshu Joshi, PhD (Aleksei Aksimentiev's group, University of Illinois) illustrating the initial configuration of duplexes in the bilayer (represented with dashed lines).*

The analysis of DNA sequences (Appendix, Fig. A5.1, Table A5.1) using the NUPACK suite[146] shows lower base pair formation probability for two nucleotides adjacent to each nick (40-70% probability, as compared with 100% for bases mid-strand), as presented in Figure 5.5. The figure is a suggestive illustration of the fact I stated earlier: the terminal bases, whether at the end of the duplex or at discontinuities, are less stable than the ones in the middle of the double strand. These are prone to fraying and the weakest links of the DNA nanostructure.

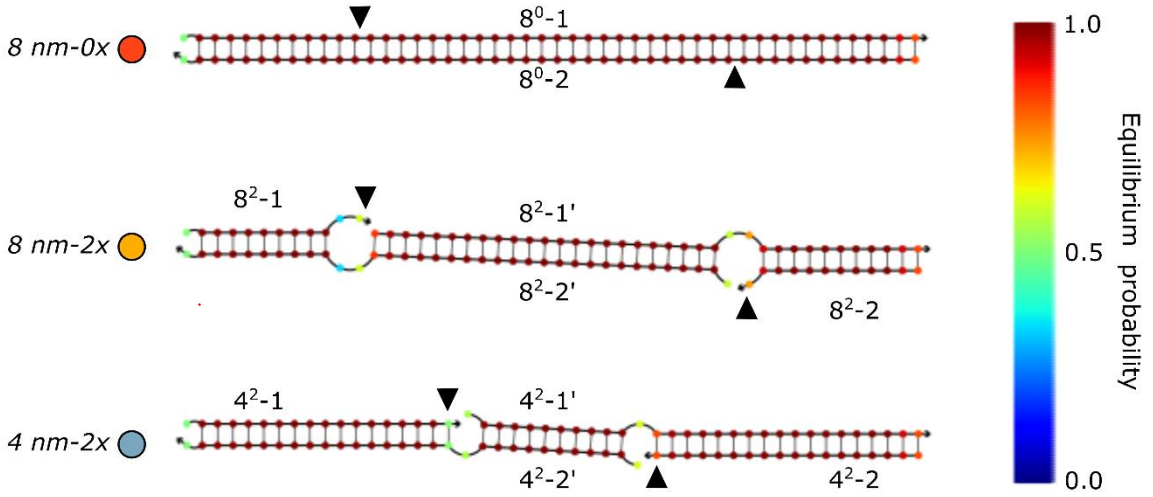

Figure 5.5 *NUPACK*[146] *analysis of the three designs used in this work. The colour coding illustrates the probability of forming base pairs. Black arrows point at the positions of cholesterol in each construct.*

The three structures were folded using commercially available strands and characterized with respect to their stability. Firstly, the non-nicked structure has the highest melting temperature T_m (Figure 5.6a), corresponding with the NUPACK-predicted base pair formation probability – the presence of nicks affects the thermal stability of dsDNA. Secondly, by observing the absorbance vs temperature curves (Figure 5.6b), we can suggest a "process of thermal unfolding" for each structure. As the temperature increases, the shortest (12 nt) strands building *8 nm-2x* are the first to disassemble, only then followed by the rest of the structure, which can be observed as a two-step melting curve. *4 nm-2x* melting, on the other hand, features only one step at the temperature in between the two steps of *8 nm-2x*. This suggests that both domains of the *4 nm* duplex, defined by the positions of nicks, are of similar stability, despite their different length. In other words, the central, 12 bp-long part of *4 nm-2x* is more stable than the 12 bp terminal part of the *8 nm-2x*. Interestingly, this may be an indirect observation of base stacking. Non-nicked *8 nm-0x* is the simplest of the three constructs to analyse: long strands with no discontinuities are the most stable, melting in a single-step manner at 76 °C.

Gel electrophoresis confirmed a proper folding of all the designed duplexes, as shown in Figure 5.6c. Structures with hydrophobic anchors move through the gel slower than unmodified ones, due to cholesterol increasing their molecular weight. Additionally, the lower intensity of bands featuring 2C duplexes is attributed to their clustering, which by reducing their mobility causes

them to either remain in the well of a gel or produce smeared bands, indicative of transiently formed aggregates[149].

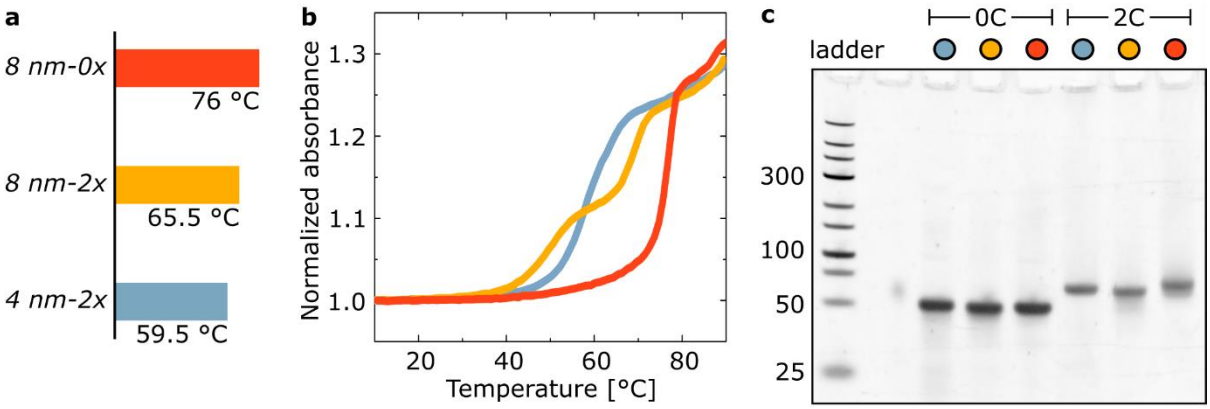

Figure 5.6 *Stability and folding yield of the constructs. (a) Melting temperatures indicating the highest thermal stability for the non-nicked duplex. Obtained from the curves from (b). (b) Absorbance profiles (at 260 nm) illustrating the thermal unfolding of studied duplexes. (c) PAGE analysis of the structures unmodified (0C) and modified with 2 cholesterol molecules (2C).*

5.4. Repulsive DNA-lipid interactions distort structure of the nicked duplex

Based on the three designs, all-atom MD systems were built by Himanshu Joshi (Aleksei Aksimentiev's group, University of Illinois), with each structure embedded in a DPhPC lipid bilayer in the presence of ions (details in the Appendix, Section A1.1.). Considering that the thickness of the membrane is around 4 nm[20-22], the structures differing in the distance between cholesterols were oriented differently to accommodate the hydrophobic modifications within the core of the bilayer, as schematically presented in Figure 5.4c. Both *8 nm* structures were inserted in a tilted conformation (at a 30° angle to the bilayer) in order to place both cholesterol anchors within the volume occupied by the lipid membrane. The *4 nm-2x* structure, with its cholesterol spacing adjusted to the bilayer thickness, was oriented perpendicularly to the bilayer. The simulations were allowed to run for 1 μs, after which we analysed the orientation and molecular structure of DNA in the bilayer. Snapshots of the conformation of duplexes are presented in Figure 5.7a.

The spacing between the cholesterols causing the tilt of the *8 nm-2x* design was forced to change upon embedding in the bilayer. Fraying of the base pairs at the nicks allows for the straightening of the tilted structure, while keeping both hydrophobic molecules anchored in the bilayer's core. On the other hand, the *8 nm-0x* design was initially oriented in the membrane in a similarly tilted

manner, yet its final conformation was much less distorted than the nicked analogue. We attribute this to the stability of base pairing in the absence of nicks: the non-nicked structure was not frayed, and therefore it does not have the additional flexibility that enabled bending of the nicked duplex. Figure 5.7b highlights the differences between base pairing in the analogous positions in *8nm-2x* and *8 nm-0x* constructs.

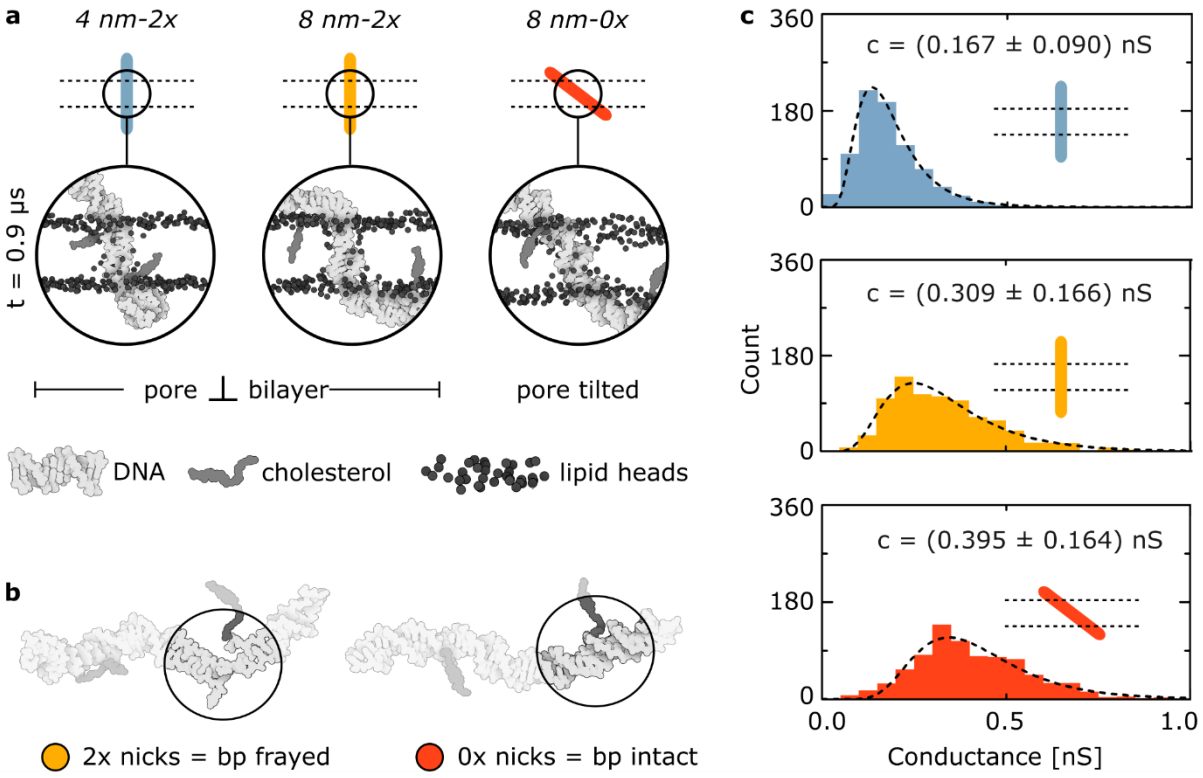

Figure 5.7 *The effects of repulsive DNA-lipid interactions on the molecular structure of the duplexes. (a) Sketches and respective frames from all-atom MD simulations at t = 0.9 µs. Lipid tails, ions and water molecules are not shown for clarity. (b) Snapshots from the MD simulations highlighting frayed base pairs in the position of one of the nicks in the 8 nm-2x structure, while the respective base pairs of 8 nm-0x stay intact. (c) All-point histograms of the simulated ionic current traces for all three structures. The dashed lines represent lognormal fits, with the conductance peak values stated on each plot. The error values represent standard deviation. MD simulations were performed by Himanshu Joshi, PhD (Aleksei Aksimentiev's group, University of Illinois).*

The *4 nm-2x* design has the minimum number of DNA nucleotides required inside the bilayer. Nevertheless, after equilibration of the system we observe unwinding of the *4 nm-2x* double helix placed within the bilayer, as shown in Figure 5.8. DNA-lipid repulsion is therefore stronger than

the forces introducing the twist to the dsDNA. As analysed in Chapter 2, the twist results from the hydrophobicity of nucleobases, seeking to ensure a tight, "water-proof" conformation. The helix unwinding in the membrane is another example of a (relative) weakness of the nucleobase-water repulsion - it seems that all the other forces playing a role in the studied system are stronger and dominate over it.

Note, that the plot in Figure 5.8b suggests that this unwinding is disrupted in the absence of nicks. The *8 nm-0x* duplex struggles to preserve the natural ≈ 3.4 Å rise[210] (distance between adjacent base pairs) and in the timescale of simulations does not seem to find a stable conformation - unlike the two nicked constructs, with their rise reaching a *plateau* around 4.5 Å.

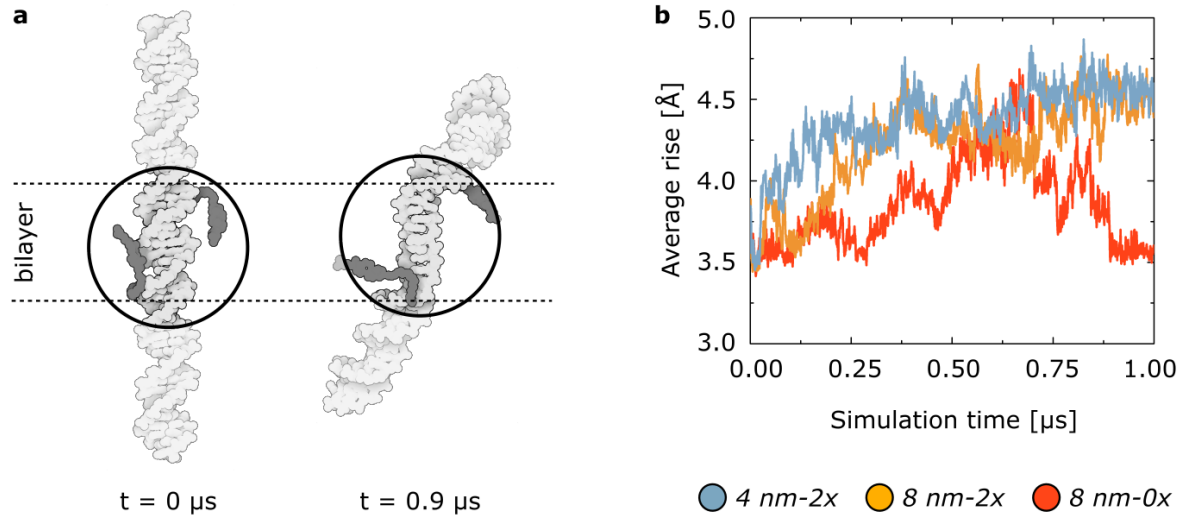

Figure 5.8 *Change to the DNA twist in the membrane-spanning domains observed via simulations. (a) The 4 nm-2x construct showing a prominent change to the double-helix conformation of the DNA in the membrane-spanning region. (b) The rise measured throughout the simulations of all three structures. MD simulations were performed by Himanshu Joshi, PhD (Aleksei Aksimentiev's group, University of Illinois).*

Summing up, in the presence of nicks membrane-interacting DNA structures can be distorted from their original design. This distortion will have an impact on the activity, which in the simulations was strongly correlated with the size of the DNA-induced pore. The smaller pore of *8 nm-2x* resulted in a smaller ionic current than in the case of the bigger pore formed by *8 nm-0x* (Figure 5.7c). Similarly, the number of water molecules permeated through the membrane was smaller for the nicked constructs (Appendix, Fig. A5.2).

Experimental results allowed further confirmation of the notions observed *via* simulations. Together with Sarah Sandler (Ulrich Keyser's group, University of Cambridge), I studied the insertion of the structures by measuring the ionic current through DPhPC membranes in a 0.5 M KCl solution, while applying a voltage of 50 mV. In the absence of membrane-spanning structures no current is recorded, while upon DNA insertion an increase in the signal is readily identified. Automatic analysis of the current traces by the Clampfit software enabled finding all single-channel signals. Assuming an ohmic behaviour, each signal was attributed to a formation of a pore of a certain conductance. Figure 5.9 shows histograms of collected signals for each structure. While the results between the constructs with two nicks are indistinguishable, suggesting similar pore size (lognormal fit peaks at (0.183 ± 0.060) nS and (0.182 ± 0.068) nS for *4 nm-2x* and *8 nm-2x* respectively), the *8 nm-0x* structure has much wider signal distribution, peaking at roughly twice the conductance value: (0.378 ± 0.152) nS, suggesting a bigger pore size.

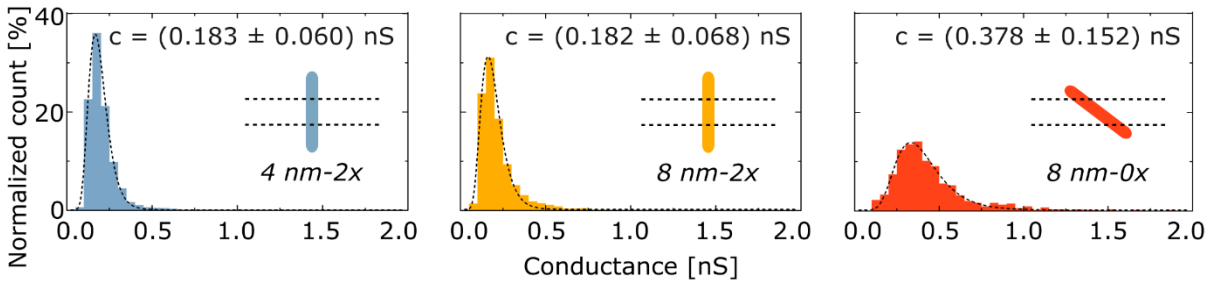

Figure 5.9 *Histograms of reported signals from the experimental ionic current measurements for all three structures.* $N_{4nm\text{-}2x}$ *= 4287,* $N_{8nm\text{-}2x}$ *= 4857,* $N_{8nm\text{-}0x}$ *= 542. The dashed lines represent lognormal fits, with the conductance peak values stated on each plot. The error values represent standard deviation. The data were collected from three independent experiments, each 2 hours long (total of 6 hours for each structure). The inset sketches illustrate hypothetical orientation of the duplexes in a bilayer, following the results of the simulations.*

The conductance values found here are higher than the ones reported previously for similar structures, yet still of the same order of magnitude (reported 0.1 nS for the solution of twice higher conductivity[100]). The difference may result from chemical variations between constructs, since the previously reported duplex was anchored in a membrane using six porphyrin modifications (logP in a range [8.9, 11.8][211]), resulting in a strongly hydrophobic environment in the pore. This in turn causes smaller ion flow, as discussed in the previous chapter (Chapter 4).

On the other hand, the conductances measured *via* simulations for *4 nm-2x* and *8 nm-0x* (0.167 nS and 0.395 nS, respectively) have a remarkable agreement with the values obtained from

the experiments (0.183 nS and 0.378 nS, respectively). The similar conductances reported from the experiments and the simulations suggest that indeed the twice higher values are a result of *8 nm-0x* forming bigger pores, rather than inserting as a dimer. The conductance recorded in the simulations for *8 nm-2x* (0.309 nS), even though smaller than for a non-nicked analogue, does not reach a value similar to the *4 nm* structure as in the experiments (0.182 nS). However, this was to be expected as the difference between timescales of simulations and experiments will play a more significant role in the case of the *8 nm-2x* construct. This structure needs time for a change in conformation – not relevant at the milliseconds scale of experiments but consisting a large part of the simulation time. Nevertheless, the experimental observations agree with the simulations and confirm our initial assumptions of the importance of base pairing stability and cholesterol linkage.

5.5. Improving insertion and pore stability by reducing structure's degrees of freedom

Collected current traces for the three duplexes show a transient ion flow, as presented in Figure 5.10a, which in turn suggests transient membrane spanning: we read each step change in the signal as the structure going in and out of the bilayer. The duplex constantly changes its orientation and shape in order to find the energetic minimum in the interplay between cholesterol pulling towards the membrane and DNA pulling away from it. By removing the nicks from the design, we effectively reduce its degrees of freedom, thus the structure has less ability to change. Therefore, for the *8 nm-0x* we observe more well-defined steps in the measured current, with two clearly distinguishable states: inserted and not inserted. Meanwhile, the nicked *8 nm-2x* constantly changes its structure by fraying bases and flexing in the nick position in order to find the most favourable conformation with respect to the bilayer. A continuous alteration of the pore results in spikes and crooked steps in the current traces.

At a glance, the traces recorded for nicked *4 nm* and *8 nm* structures seem identical. Careful analysis, however, hints at a longer duration of events observed for *8 nm-2x.* Note that most of the presented signal of *8 nm-2x* is above the baseline, despite the traces being equally noisy as for *4 nm-2x.* It is not trivial to notice this difference by looking at conductance changes, due to the troublesome determination of start and end points of the events. Therefore, the duration of events detected by the script and analysed in the previous subchapter was also recorded, and violin plots of their distribution (based on kernel density profiles) are shown in Figure 5.10b.

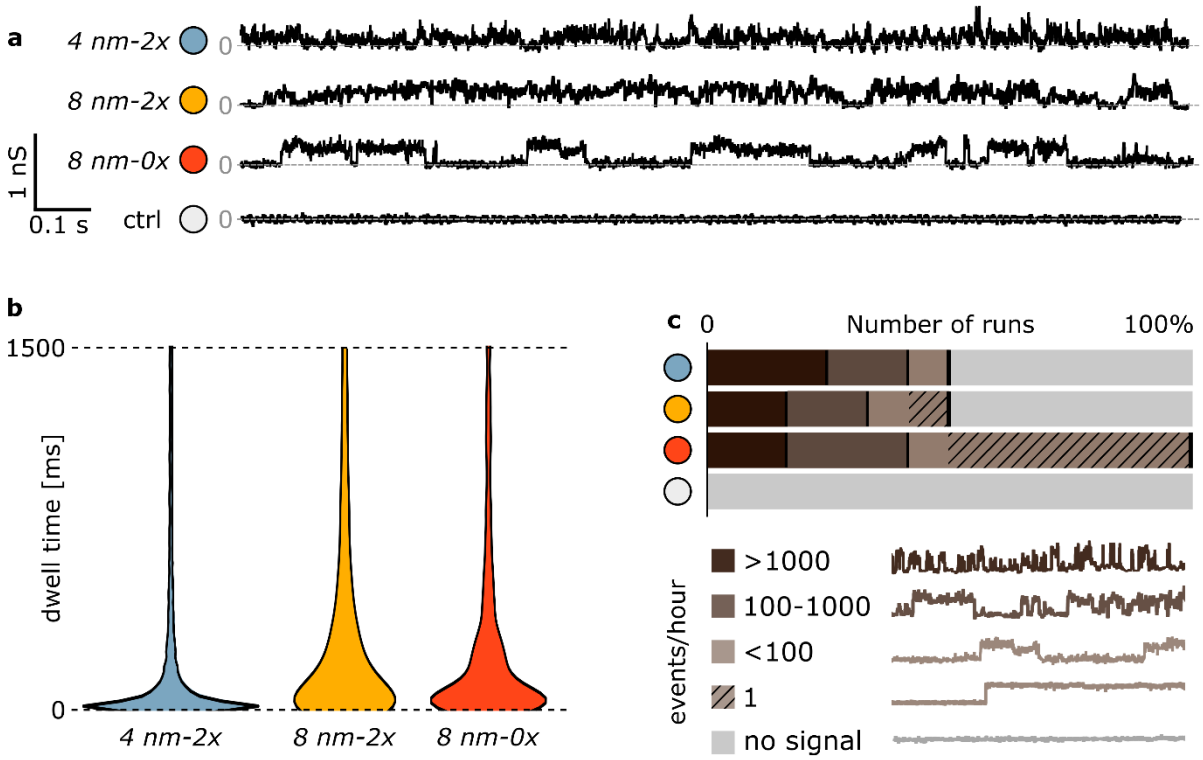

Figure 5.10 *Improving the pore stability and the insertion efficiency by removing nicks from the design. (a) Examples of current traces collected for studied constructs. The "control" structure (ctrl, white) is a non-inserting duplex with a single cholesterol modification. (b) Violin plots of the dwell time distribution for events presented in the histograms in Figure 5.9. Normalized kernel density curves, range [0,1500] ms shown for clarity. (c) Plot illustrating the insertion efficiency of the studied structures, reporting a percentage of runs with any signal above the noise threshold (± 0.05 nS). The pattern symbolizes runs with a stable, long-lasting insertion event. 12 runs per structure, each at least 0.5 h long.*

The analysis of the dwell times presents a significantly bigger challenge than that of the signal's magnitude. In this work, the deep understanding of processes at a molecular scale comes largely from the simulations. However, looking at the milliseconds timescales *via* all-atom simulations is unfeasible. Therefore, to grasp the true mechanisms behind DNA inserting into and pulling out of the membrane is not within the scope of this work. Nevertheless, I will share some observations and ideas, with a disclaimer that the latter are all speculative.

Most importantly, even though the magnitude of the signals observed for the two nicked structures are similar, their dwell times differ considerably; *4 nm* and *8 nm* nicked constructs behave differently in the membrane, despite forming pores of similar size. For *4 nm-2x* we observe narrowly distributed, short events, while durations of *8 nm-2x* events have a much wider range.

Even though the distance between the cholesterols of *4 nm-2x* is designed to ensure the most optimal orientation in the membrane, the briefness of events shows that it does not find a favourable position in a bilayer. This may suggest that, in fact, we are not observing *4 nm-2x* anchored in a membrane with both cholesterols, but that the spikes represent its ***attempts*** to span the bilayer. It starts entering the membrane but withdraws before both cholesterols can find their position in the hydrophobic core.

Why is the *4 nm* structure so different in that respect from the *8 nm* ones? Perhaps the difference results from *4 nm* having a longer part of dsDNA to push through the bilayer than the other two duplexes – more hydrophilic DNA needs to span through the membrane before the cholesterol modifications can reach it and find their preferred conformation. It seems likely that what distinguishes the design is also causing the noticeable difference in the obtained results.

Looking at the violin plots from another point of view, we can ask: why is the non-nicked construct not noticeably different from its nicked analogue? Despite it producing clearer steps, *8 nm-0x* has a broad dwell time distribution, with the majority of events being short (< 100 ms). Statistically, its dwell times are not longer than for the nicked *8 nm* duplex. *8 nm-2x* is shown to struggle while in the membrane, and perhaps its ability to adopt many conformations before it leaves the bilayer is the reason behind the distribution of duration times shifted towards higher values.

On the other hand, the ***longest*** observed signals were invariably attributed to the non-nicked duplex, yet they have not been included in the analysis in Figure 5.10b, as they are outliers observed only a handful of times. Yet they were very distinct, and a number of runs featured solely such long events. In fact, the majority of experiments with the non-nicked structure featured a single or a few steps, as seen from the plot in Figure 5.10c. Even though the nicked duplexes also produced events of a low frequency, for *8 nm-0x* we report signals of an exceptionally long duration (on a time scale of minutes), examples of which are presented in Figure 5.11.

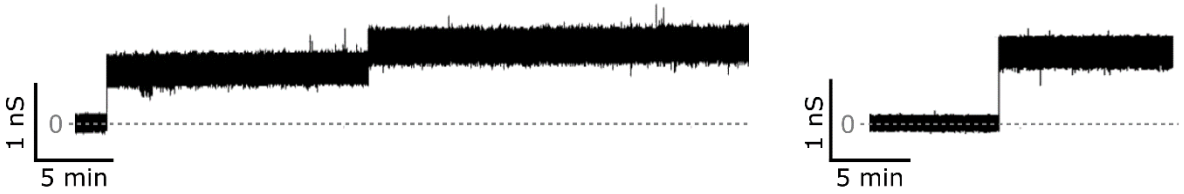

Figure 5.11 *Examples of long-lasting steps in the membrane conductance observed for the 8 nm-0x structure.*

While analysing Figure 5.10c, note that the nicked structures did not always produce observable effects on the membrane conductance. The plot presents the percentage of runs with detected signal above the noise level (> 0.05 nS), out of a set of performed measurements (12 runs at least 0.5 h long, for each structure). Three membrane-inserting duplexes were studied alongside the control - a non-inserting, single-cholesterol (1C) structure. As expected, the 1C construct did not produce any signal, as a single cholesterol is not enough to ensure entering a bilayer. More importantly, while the insertion of the nicked constructs was only reported in 50% of the experiments, the duplex without the nicks produced a signal successfully every time. This highly desired effect of removing the nicks can probably also be attributed to its lower structural variability.

Fluorescence recovery after photobleaching (FRAP) measurements performed on DNA-coated vesicles shed more light on the differences in membrane interactions that may lead to differing insertion efficiencies. The results, shown in Figure 5.12, indicate that the non-nicked construct diffuses in the membrane faster than its nicked analogue. Since the diffusion rate of cholesterol-tethered DNA has been reported to decrease with an increasing number of cholesterol anchors[26-29], the observed difference may result from the stronger anchoring of the nicked duplex. If the population of *8 nm-2x* has both cholesterols stably positioned in a membrane (due to the fraying at the nick's position, allowing the cholesterol-modified strand to twist), the anchors exert no force to overcome DNA-lipid repulsion. On the other hand, if the non-nicked structure attaches with a single cholesterol, the remaining one may pull the whole construct inside the bilayer, as this is the only way for it to embed within the hydrophobic core. Inset in Figure 5.12b schematically illustrates this hypothetical arrangement. Note, that this speculation assumes that DNA insertion rate is in both cases small enough to ignore the role of membrane-spanning units in the observed diffusion rates. More rigorous statistical experiments, as well as additional molecular simulations are required to fully uncover the mechanisms behind the DNA membrane insertion.

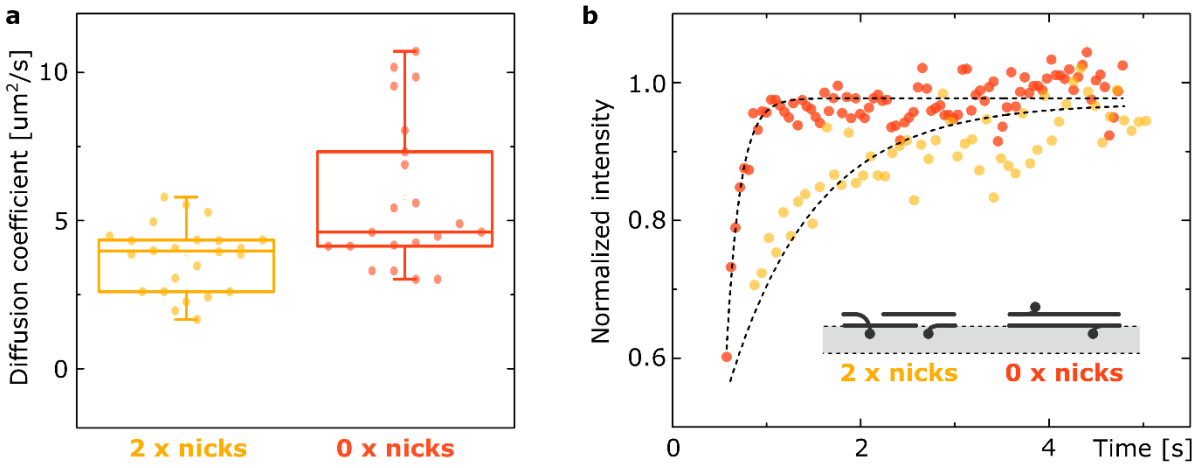

Figure 5.12 *Fluorescence recovery after photobleaching (FRAP) measurements results. Comparison of diffusion coefficients obtained for 8 nm-2x and 8 nm-0x structures in a form of box plots (a) alongside representative fluorescence recovery traces (b). Experiments were performed at room temperature. Inset schematically illustrates a hypothetical conformation of the duplexes in contact with the bilayer (grey rectangle).*

Apart from single-level changes in the current, multiple insertions were also observed for all three structures. After a certain time (tens of minutes) multiple constructs were invariably seen to affect the membrane's conductance, as shown with a representative trace and its all-point histogram in Figure 5.13a-b. With many constructs spanning the membrane in a transient manner, similarly complex traces reaching high conductance values were observed for all runs (the exception being the *8 nm-0x*, which often caused single, long-lasting steps as described earlier). Despite many inserting constructs, clear, discreet steps of multiple levels are rarely observed, due to the short dwell times - even for the non-nicked structure. Still, because of the higher stability of pores formed by the *8 nm-0x* duplex, some examples of multiple insertions could be detected (Figure 5.13c).

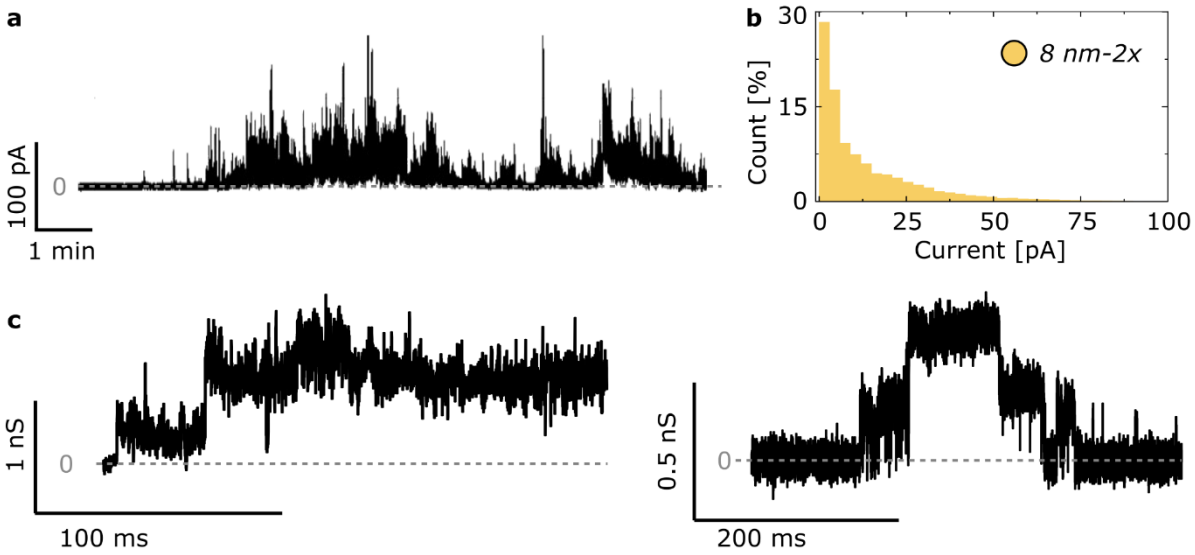

Figure 5.13 *Multiple structures span the membrane simultaneously. (a) Exemplary trace for 8 nm-2x showing representative long-term behaviour of all studied constructs alongside (b) the respective all-point histogram. (c) Well-defined steps of multiple insertions recorded for the non-nicked 8 nm-0x structure.*

All the results described above indicate what a strong effect the lack of nicks has on the activity of a membrane-spanning construct. Decreasing the degrees of freedom resulted in a higher insertion efficiency as well as a better pore stability of the non-nicked structure.

5.6. Conclusions

In this chapter, I investigated (with the help of Aksimentiev group's simulations) the effects of nicks in the DNA-built transmembrane structures on their membrane interactions. Mindful of the base pairing and base stacking instability at the terminal ends of the strands, I studied the behaviour of constructs modified with cholesterol either at the position of nicks or introduced internally, with no discontinuities present in the double strand. The repulsive DNA-lipid interactions are strong enough to distort the molecular structure of the nicked construct by causing fraying of base pairs at the nicks. This introduces flexibility of the structure not accounted for by the design. However, in the absence of nicks the base pairs do not fray and the structure at equilibrium remains as designed. More thorough analysis concluded the presence of noticeable differences between the nicked and the non-nicked structures. The insertion efficiency of the DNA-induced pores in the absence of nicks was significantly higher, as was their stability.

By considering stabilization of base pairs, and through that limiting the degrees of freedom of the DNA-built structures, we overcame the distorting DNA-lipid interactions. Careful structural design, taking into consideration influence of environmental forces, is of particular significance for building biomimicking devices, where the targeted environment features a vast range of complex chemical compositions. To that end, presented DNA duplexes are inspired by natural transmembrane proteins for which varying the tilt of helices is one of the conformational changes influencing their activity, and can depend on the hydrophobic mismatch between the protein and the bilayer[216–218].

Even though the tilt of the membrane protein's helix may vary, the helical *structure* stays unchanged in a wide range of hydrophobic mismatch arrangements[219]. In nature, the thickness of the bilayer is adjusted to proteins' membrane-spanning domain[220], and if the cost of protein embedment is too high, it does not remain incorporated within the membrane[221]. DNA duplexes, on the other hand, particularly the two nicked constructs, display significant changes to their helical structure upon membrane insertion, as we have shown through simulations. I suggest that the reported unwinding of the double strand has a potential to be utilized as a signalling pathway. For example, membrane-tethered DNA duplex can be designed to mimic the Talin mechanosensing protein[222], whose functionality is based on transitions between a stretched and an unstretched conformation. And while force sensing DNA nanodevices have been reported previously[223,224], the unwinding observed here can also potentially be used to detect structural changes occurring within the bilayer.

Similar as in the previous chapter, we can draw conclusions with respect to the advances in DNA-based membrane protein mimics. Critically, the designed DNA structure should not be taken for granted, as in biology there are many forces powerful enough to distort it. A simple idea of connecting discontinuities of the DNA strands helped preserving the designed shape, as well as improved the pore-forming activity of the transmembrane duplex. Applying even this simple observation to a more complex design will result in a molecular machine that not only efficiently self-inserts into lipid membranes but also performs in a stable and more controllable manner. Such features would be most desirable, and comprise a huge step towards building a membrane protein-mimicking structure.

The insights gathered in this chapter further strengthen the idea behind this thesis: the significance of looking at the network of interacting molecules as a whole. Careful structural design, taking into

consideration the influence of environmental forces, is necessary for building biomimicking systems, where the targeted environment features a vast range of complex chemical interactions. Since the most remarkable advantage of DNA nanoengineering is the ease of controlling the molecular structure at the nanoscale, it is especially important that this controllability of shape is not lost due to overlooked interactions.

Here, I have introduced the tug-of-war metaphor for the membrane-spanning DNA constructs. Hopefully you are ready to follow this concept, as in the next chapter we will look at it more closely, focusing on the influence that ions have over the "game's" outcome, as well as their role in mediating DNA-lipid interactions in the absence of attachment-driving cholesterol anchors.

CHAPTER 6

Effects of cations on the attachment and functionality of membrane-bound DNA

This work has previously been published in Morzy et al. *Cations regulate membrane-attachment and functionality of DNA nanostructures.* Journal of American Chemical Society 2021, online.

We have now looked at the DNA-lipid system from two angles, studying and utilising the mutual influence both molecules have on one another. However, in previously described projects there was another, mostly unnoticed, and yet powerful moiety. A real *éminence gris* of biological systems: ions.

Electrostatic forces are key to DNA-lipid interactions, in view of the strong negative charge of nucleic acid backbones[9] and the diverse charge architectures found in lipid head groups[225]. Additionally, these nanosystems function in complex solvent conditions, where ions of different valency and size are able to screen or enhance Coulomb interactions[226–229]. Medicine in particular benefits from understanding of electrostatic phenomena, with nucleic acids and lipids often coexisting in a well-defined ionic medium, for example in DNA lipoplexes for gene therapy[230,231], cell transformation[44,232,233] and for vaccine development [234,235].

But understanding of ion-dependant phenomena in DNA-lipid systems is especially significant for DNA nanotechnology, which explores architectures with novel morphologies, charge distributions, and diverse chemical modifications[106,121,236], that interact with lipid membranes in new ways. Rational harnessing of the electrostatic effects of ions - present in the system, though for now unexploited - could unlock novel, programmable functionalities in biomimetic nanodevices.

While complex DNA nanostructures are folded at standardized cation concentrations (tens of mM for divalent cations or hundreds of mM for monovalent ones)[138], the stability of dsDNA over broad ionic-strength ranges[187,194] allows us to disentangle the effects of membrane-DNA interactions from ion-dependant structural changes. Thus, in this chapter we will continue looking at DNA duplexes, employing them as probes to understand the role of cations in the system.

6.1. Cation-mediated bridging between DNA and zwitterionic membranes is dependent on lipid phase.

Even though this thesis is focused on analysing membrane-inserting, cholesterol-modified DNA, here I will simplify the system and only study an unmodified DNA duplex and its interactions with lipids. This will allow me to disentangle all the processes facilitated or influenced by ions. The findings described in this section were obtained with the help of Roger Rubio-Sánchez (phase-dependency experiments, Di Michele's group, University of Cambridge) and Himanshu Joshi, PhD (all-atom simulations, Aksimentiev's group, University of Illinois).

Here, we used a 36 bp-long dsDNA (Appendix, Fig. A6.1, Table A6.1). As mentioned, simple duplexes have a huge advantage over more complex structures when it comes to probing the effects of ions: their stability is not sensitive to cation concentration changes. I have hinted on this previously in Chapter 4, and I will elaborate on this here.

All the experiments were performed in a range of magnesium concentrations between 0 and 4 mM, spanning the physiologically-relevant values for serum (0.75 - 1.25 mM[237]). Figure 6.1 presents PAGE alongside intensity profiles of its lanes, showing the yield of folding in different Mg^{2+} concentrations. Even though a small-scale unfolded DNA can be observed in lower cation concentrations, an evident majority of the duplexes assembles properly even in the absence of divalent cations. Note, that monovalent cations are *always* present in the sample (as water impurities but also from commercially available buffers, using NaOH and HCl for pH adjustments). Interestingly, at the highest studied Mg^{2+} concentration (4 mM) we observe a slight shift towards a lower electromobility of the duplexes. It may be indirectly connected with the effect described in Chapter 3: cations screen the negative charge on the DNA backbone, making it less responsive in an electric field. We will study the screening effects thoroughly a few paragraphs further into this chapter.

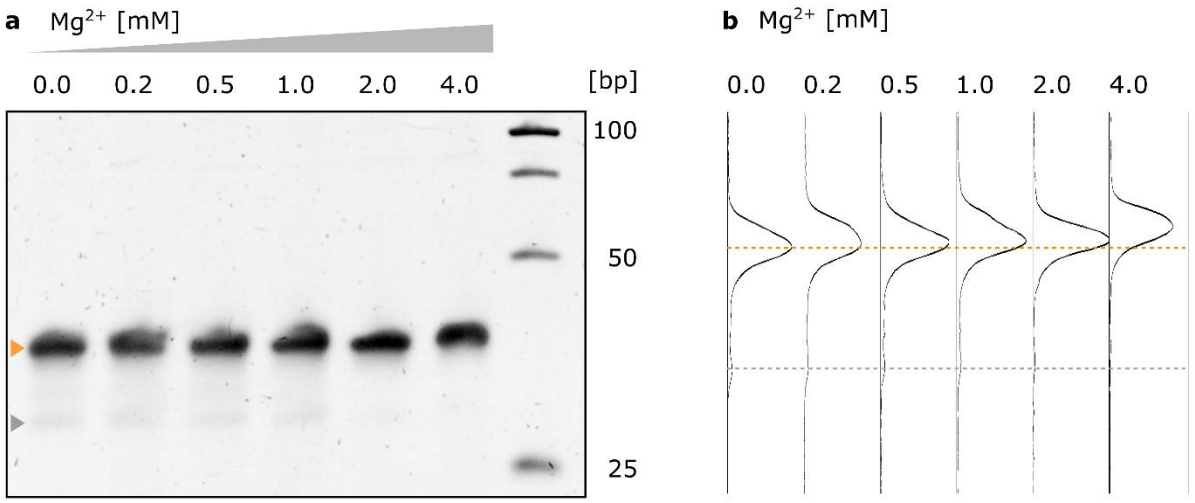

Figure 6.1 *PAGE of the 36 bp-long duplex used to probe the phase- and cation-dependant membrane attachment in various Mg^{2+} concentrations. (a) The (intensity-inverted) image of the gel highlighting the folded duplex (orange) and DNA not properly folded (grey). (b) The intensity profiles of the lanes seen in (a). Dashed lines correspond to the position of markers on the gel. Sodium ions (≈ 10 mM) were present in each sample. The gel and the buffer did not contain divalent cations.*

Confirming that in all Mg^{2+} concentrations the majority of duplexes is properly assembled, we can attribute all observations in further experiments to the ions' effects on the DNA-lipid interactions, rather than effects on the DNA itself.

Firstly, together with Roger Rubio-Sánchez (Lorenzo Di Michele's group, University of Cambridge) we have incubated the duplexes with GUVs made of DPPC lipids both in the absence and presence of 1 mM $MgCl_2$. As shown in the representative micrographs in Figure 6.2a, with Mg^{2+} ions, GUVs at room temperature (≈ 25 °C) have a bright layer of DNA attached to their surface. On the other hand, GUVs in non-ionic solutions do not display DNA attachment. This observation hints at an electrostatic origin of the observed behaviour, and is consistent with the previous reports of ion-membrane interactions[238,239] and DNA-membrane binding mediated by divalent cations[240–243].

Since the transition temperature of DPPC is T_t = 41 °C[244,245], at room temperature the GUVs are in a gel phase[246]. As summarized in Figure 6.2, no DNA attachment was observed to the GUVs prepared from POPC, which although share the same head group as DPPC, form liquid disordered bilayers (L_d) at room temperature (T_t = -2 °C). The difference in the DNA attachment between gel and liquid PC bilayers suggests the regulatory role of the lipid phase - a concept that has been

previously evoked to rationalize the partitioning of DNA structures in phase-separated membranes[247,248].

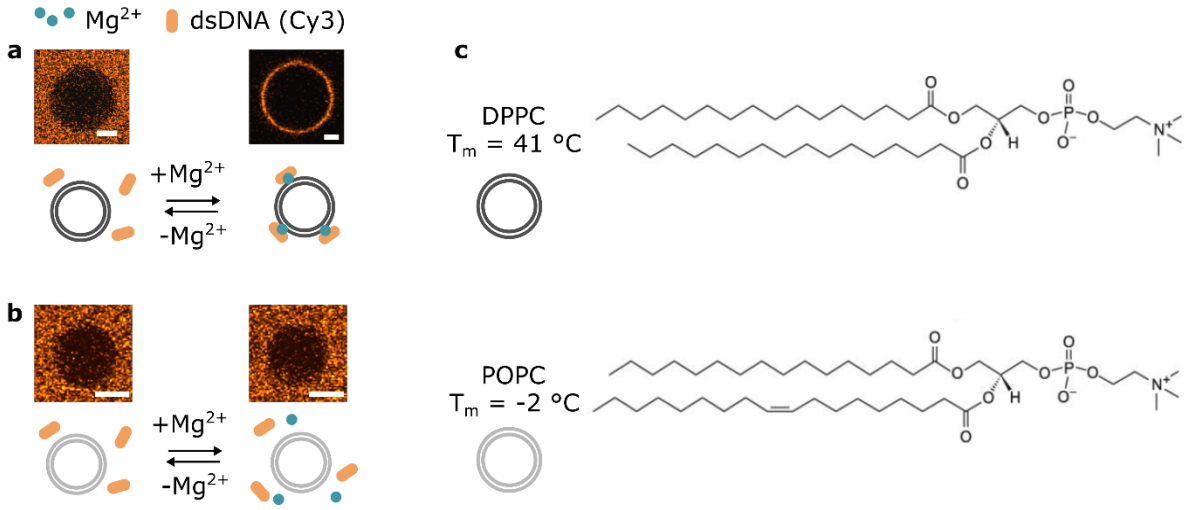

Figure 6.2 *Ion-driven attachment depends on the lipid type. (a) Representative micrographs showing an ion-induced membrane attachment of the studied duplex when incubated with DPPC vesicles. Scale bars: 5 µm. (b) Representative micrographs showing no ion-induced membrane attachment of the studied duplex when incubated with POPC vesicles. Scale bars: 5 µm. (c) Molecular structure of DPPC and POPC lipids, differing in the double bond in one of the tails. Transition temperatures (Avanti® Polar Lipids, avantilipids.com) stated next to each lipid.*

To further determine the role of the lipid phase on DNA attachment, we imaged samples of DPPC GUVs incubated with dsDNA motifs and 1 mM Mg^{2+}, while gradually heating up from room temperature to well above T_t (50 °C). The presence of a gel phase at 20 °C and a liquid phase at 50 °C was confirmed by the change in the lipid diffusion coefficient (D) as determined by fluorescence recovery after photobleaching (FRAP), the results of which are reported in Figure 6.3.

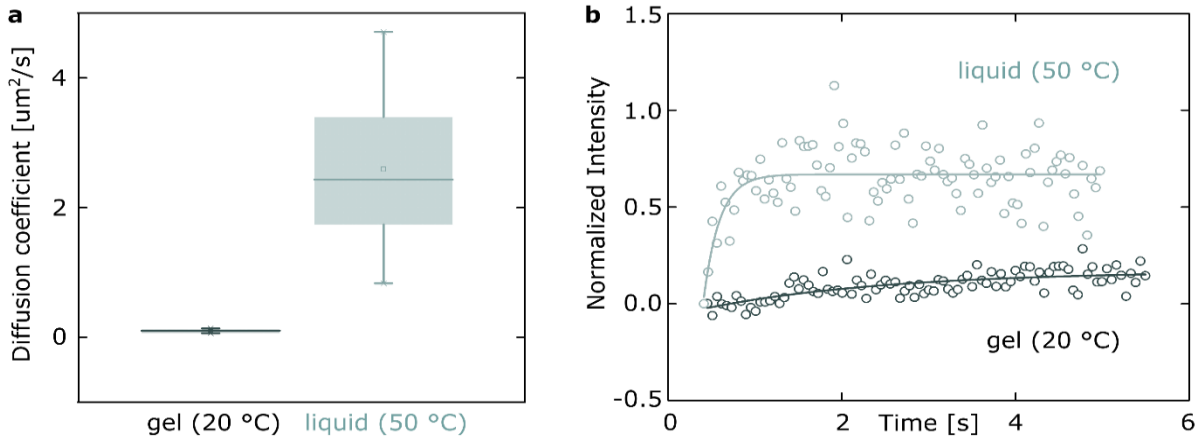

Figure 6.3 *FRAP measurements confirmed the phase of DPPC vesicles. (a) Box plots showing the diffusion coefficient (D) values for fluorescently tagged NBD-PC lipids in a DPPC gel and liquid phase membranes. (b) Representative fluorescence traces after bleaching illustrating negligible diffusion of lipids in the gel phase.*

While below the DPPC transition temperature the DNA coating remained uniform, we observed the emergence of a patchy DNA distribution as the temperature was increased above T_t, followed by a gradual detachment of the constructs (Figure 6.4a-b). Figure 6.4c quantitatively illustrates the temperature dependence of DNA attachment. The fluorescence intensity data and their comparison with the position of the DSC peak in Figure 6.4d, confirm that DNA detachment initiates at T_t and proceeds gradually, rather than sharply, as the temperature is increased. Data collected on cooling, shown in Figure 6.4c, illustrate the reversibility of the temperature-dependant DNA attachment.

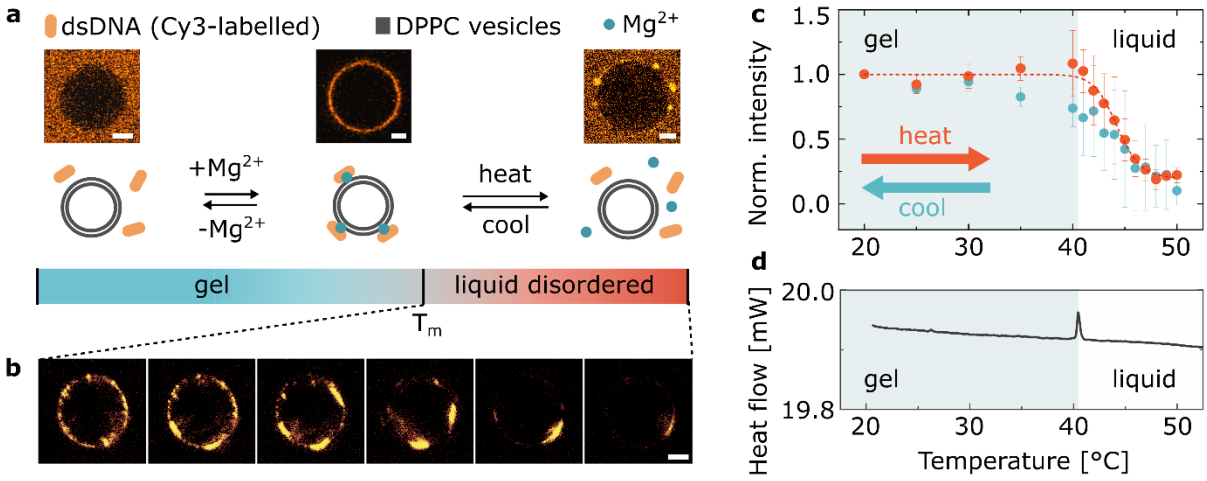

Figure 6.4 *Cations mediate bridging between DNA and gel phase PC bilayers. (a) Representative confocal micrographs and schematic representation of the interaction between DPPC GUVs and Cy3-labelled dsDNA in ionic (1 mM Mg^{2+}) and non-ionic buffers, as observed at room temperature and upon heating above the phase transition temperature (T_t) of lipids. Scale bar: 5 µm. (b) Representative confocal micrographs of DPPC GUVs showing gradual detachment of dsDNA with the temperature increasing above T_t. Scale bar: 5 µm. (c) Temperature-dependence of the attachment of DNA constructs to DPPC GUVs recorded via fluorescence upon heating (red points) and cooling (turquoise points). The dashed line represents a reverse Hill binding curve fitted to the "heating" data points – the fit is only illustrative and does not represent a mathematical model of binding. The error bars represent the standard deviation from three independent experiments. (d) DSC plot of DPPC large unilamellar vesicles (LUVs) incubated with dsDNA in the presence of Mg^{2+}. The position of the peak indicates the T_t of the membrane. DSC data of plain LUVs can be found in the Appendix, Fig. A6.2. The DSC measurements were performed by Roger Rubio-Sánchez (Lorenzo Di Michele's group, University of Cambridge).*

To exclude the possibility that kinetic factors, specifically a slow desorption of DNA, influenced the observed trend, we have incubated the GUVs at 43 °C (just above T_t) for 60 min. As shown in Figure 6.5a, we observed no time-dependant DNA detachment, indicating that the trend presented in Figure 6.4 is in fact temperature- rather than time-dependent. Furthermore, spectrophotometric measurements were used to ascertain the DNA structure stability in the tested temperature range, as presented in Figure 6.5b.

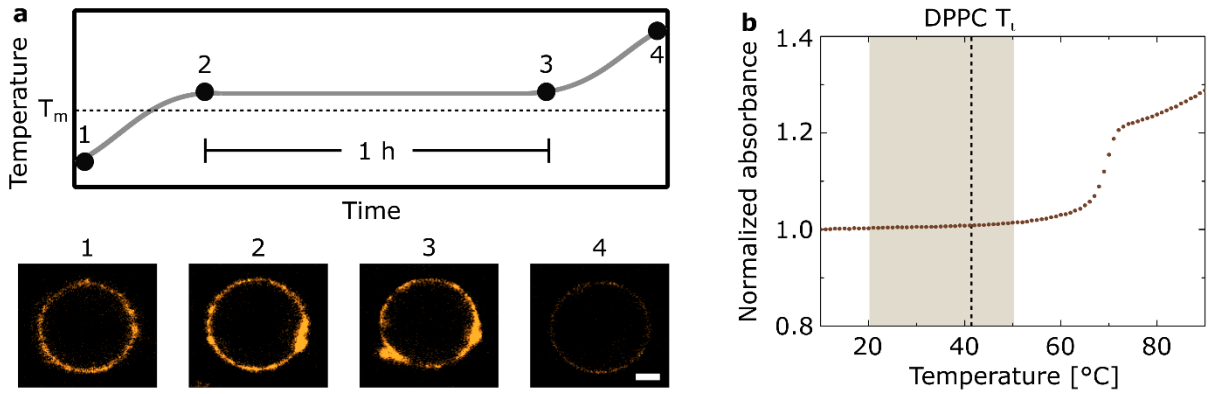

Figure 6.5 *Control experiments for temperature-dependant attachment recordings. (a) Representative confocal micrographs illustrating the absence of time-dependant detachment of DNA duplexes from DPPC GUVs if incubated just above T_t. Cy3-labelled DNA uniformly coats DPPC vesicles in the gel phase (1), while the "patches" emerge when temperature is increased to 43 °C, just above T_t = 41 °C (2). After incubating the sample for 1 h at 43 °C, no clear changes in the coverage degree are observed (3). Upon further temperature increase to 50 °C, the detachment proceeds (4). Scale bar: 5 µm. (b) Experimental absorbance at 260 nm as a function of temperature, showing the melting curve obtained for the DNA duplex in the Tris solution of 1 mM Mg^{2+}. The highlighted area represents the temperature range over which the membrane-affinity experiments were carried out, while the dashed line indicates the T_t for DPPC lipids.*

Besides changing the temperature, the phase of DPPC-based bilayers can be tuned isothermally by altering their composition with the addition of cholesterol. To help disentangle the effect of temperature and bilayer phase on membrane-DNA adhesion, we tested GUVs prepared with cholesterol/DPPC molar ratios of 0%, 5%, 15% and 25%, which at room temperature display a homogeneous gel phase (0 and 5%), co-existence of gel and liquid ordered (L_o) phases (15%), and a homogeneous L_o phase (25%)[246]. Representative micrographs of these conditions are shown in Figure 6.6a, which further confirm that the electrostatic-mediated attachment is only prevalent in the presence of membranes in a gel phase, while no attachment is observed for the L_o phase. For GUVs displaying gel-L_o phase coexistence (cholesterol/DPPC molar ratio of 15%) the DNA is localized on portions of the GUVs, which presumably correspond to the gel phase domains (see the Appendix, Fig. A6.3.). Notably, cholesterol itself does not mediate DNA attachment when embedded in a liquid bilayer, given that no DNA adhesion is observed at high cholesterol/DPPC molar fractions or if cholesterol is added to POPC membranes, as shown in Figure 6.6b.

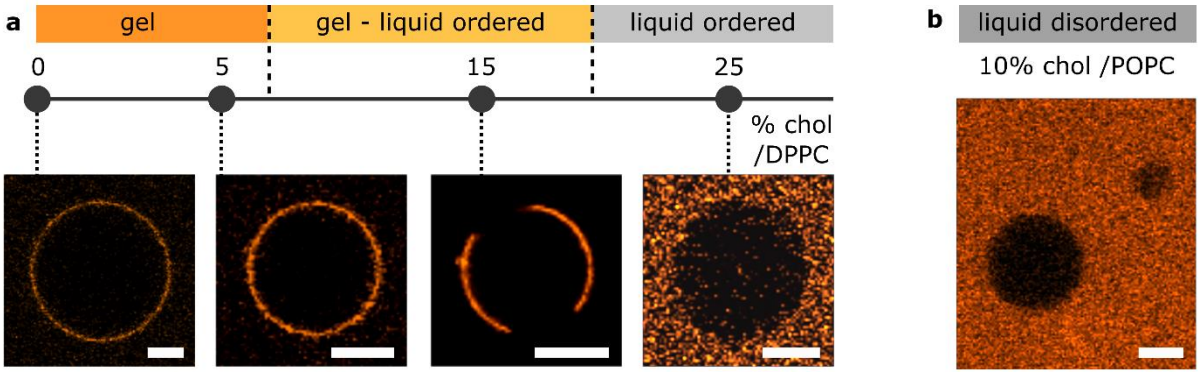

Figure 6.6 *Dependence of the DNA attachment on the bilayer phase. (a) Micrographs showing changes in attachment with the phase modulated by changing the cholesterol molar fraction in the DPPC/cholesterol binary mixtures. Scale bars: 10 µm. (b) Representative confocal micrograph demonstrating the lack of DNA attachment on liquid disordered POPC/cholesterol GUV. Scale bar: 10 µm.*

We observed no membrane attachment in the presence of solely monovalent ions (K^+ and Na^+), while divalent ones (Mg^{2+} and Ca^{2+}) caused DNA to coat the membrane. Representative micrographs in Figure 6.7 illustrate this observation, which suggests that the reported ion-dependant behaviour can be attributed to cation bridging, known to be caused by multivalent ions only[249]. The presence of divalent-ion bridging is also consistent with the previously reported decrease in DNA-membrane affinity following the addition of monovalent ions[250,251], given that bridging depends strongly on the monovalent-to-divalent ions ratio[252].

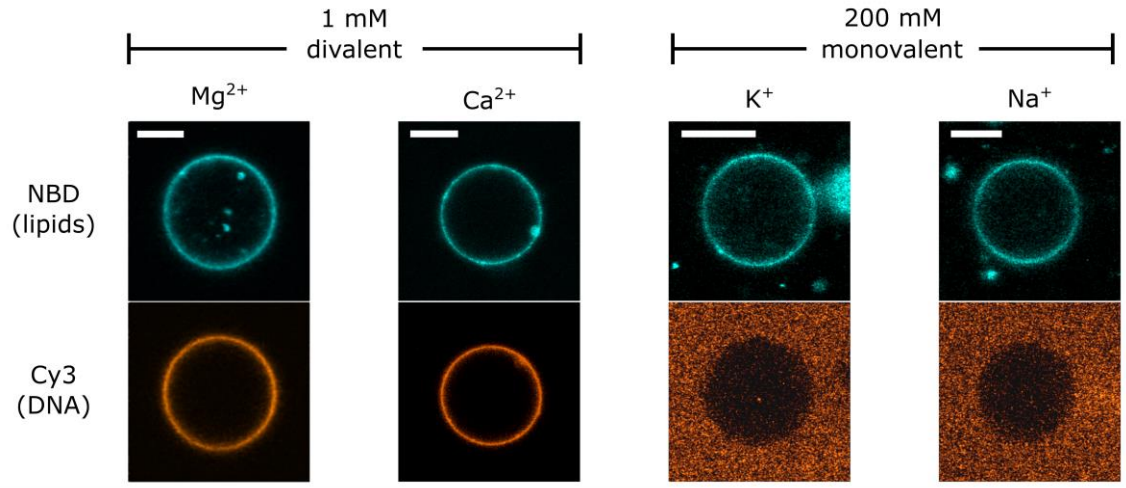

Figure 6.7 *Representative micrographs showing the attachment of unmodified DNA duplex to GUVs in solutions containing different cations. Vesicles were prepared with DPPC and 0.5% of NBD-PC. Images, acquired at room temperature with membranes in gel phase, show the selective attachment that DNA duplexes display for gel phases only in the presence of divalent cations. Scale bar: 10 µm.*

In summary, we demonstrated that divalent cations can mediate adsorption of dsDNA to zwitterionic (PC) lipid membranes. However, the effect is only detectable for gel phase bilayers, while DNA does not adhere to PC bilayers with liquid – either L_o or L_d – phases. We hypothesize that the number of cations bound to the bilayer depends on its phase, and in turn DNA attachment is strongly correlated with the number of membrane-bound cations. To test this hypothesis, we performed zeta (ξ) potential measurements on DPPC large unilamellar vesicles (LUVs, Ø = (246 ± 1) nm) above and below their phase transition temperature. The obtained values are collected in Figure 6.8, while exact values can be found in the Appendix, Table A6.2.

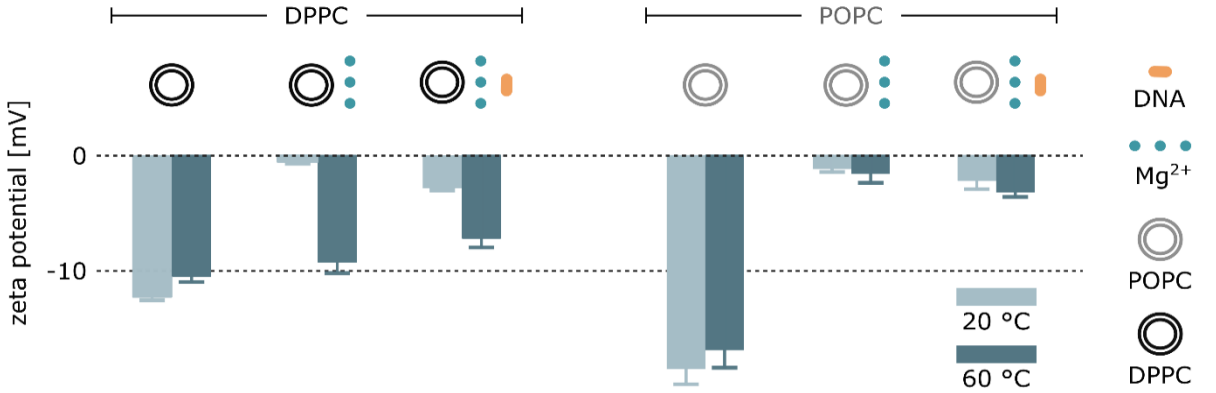

Figure 6.8 *Zeta (ξ) potential values collected for either DPPC or POPC LUVs in non-ionic solution, after addition of Mg^{2+} (1 mM) and DNA (10 nM). Values were measured below (20 °C) and above (60 °C) the DPPC phase-transition temperature. Error bars represent standard deviation from three measurements, each consisting of 12 runs. The exact values can be found in the Appendix, Table A6.2.*

We observe a negative ξ potential of -12.2 ± 0.2 mV for the LUVs in a non-ionic solution, resulting from the exposure of the phosphate on the PC headgroup. This orientation of the headgroup is reported to result from the choline's orientation towards the bilayer core[47,48]. The negative surface charge explains the lack of DNA attachment in the absence of cations[242]. After the addition of magnesium ions, the surface charge is screened (ξ potential = -0.54 ± 0.1 mV), suggesting cation adsorption to the surface, which may lead to DNA adsorption through bridging. Once the system is heated up, causing the vesicles to transition to the liquid phase, the ξ-potential drops back to -8.99 ± 1.0 mV, indicating magnesium desorption. The reversible attachment of DNA can also be observed: ξ-potential of DNA-coated vesicles reaches -2.73 ± 0.2 mV and drops to -7.07 ± 0.7 mV after heating the samples above the transition temperature of the membranes.

The ξ potential measurements performed on DPPC vesicles support our hypothesis that DNA-lipid adhesive interactions are mediated by divalent-cation *bridging*, and that the magnesium cations adsorb onto gel phase bilayers. However, measurements performed on liquid phase POPC vesicles in a non-ionic solution result in a value of ξ potential similarly negative to the one recorded for gel phase DPPC (Figure 6.8). Similarly, a screening effect of cations is reported, suggesting that factors other than the surface charge regulate adsorption of cations onto PC bilayers, and thus DNA adhesion.

To gain insights into the mechanism of the Mg^{2+}-mediated interactions between dsDNA and a lipid bilayer membrane in fluid or gel phase, I once again collaborated with Himanshu Joshi from Aleksei Aksimentiev group at the University of Illinois, who constructed all-atom systems containing a patch of either liquid or gel membranes, and used the all-atom MD method to probe the interactions of Mg^{2+} and DNA with them (details in the Appendix, Section A1.2.). Since the parameters describing affinity of water, ions and DNA towards a headgroup are well-described for PE lipids[253–255], as opposed to PC ones, DPhPE (T_t < rt) and DPPE (T_t < rt) bilayers were chosen to perform these studies. In the absence of DNA free equilibration simulations of both the membrane systems in high concentration (100-300 mM) $MgCl_2$ solutions showed accumulation of Mg^{2+} ions near the lipid head groups. Nevertheless, the local concentration of Mg^{2+} ions was found to be considerably higher near the surface of the gel phase membrane than near the surface of the fluid phase membrane, indicating a stronger affinity of Mg^{2+} to the gel phase membranes.

To quantitatively examine the affinity of Mg^{2+} ions to fluid and gel phase membranes, the potential of mean force (PMF) between one Mg^{2+} ion and either DPhPE or DPPE membrane was determined. PMF describes how the free energy changes as a function of a coordinate – in our case, the distance from the centre of the bilayer, defined by the illustrated typical simulation system in Figure 6.9a. The resulting PMF curves, presented in Figure 6.9b, show small yet clearly discernible difference in the binding affinity of Mg^{2+} to the membrane: the PMF minimum near the PE headgroups is 1.0 kcal/mol lower for the gel phase membrane than for the fluid phase one. Importantly, the difference is found to originate from a differential coordination of the Mg^{2+} ion by the lipid head groups, illustrated by plots in Figure 6.9c. At the PMF's minima, approximately four and six PE phosphates are found to surround Mg^{2+} in the fluid and gel phase, respectively. Images in Figure 6.9d illustrate the representative configurations of the lipids surrounding the ion.

The simulations confirmed observations reported in the experiments as well as gained insight into the molecular details of the role of divalent cations on the DNA interactions with lipid bilayers. Even though divalent cations bind to zwitterionic lipids in both liquid and gel phase (as we also observed experimentally in ξ potential measurements), the affinity towards gel phase membranes is higher due to the higher number of lipid headgroups coordinating the Mg^{2+} ion. The simulations shed light on the molecular phenomena responsible for the phase-dependant behaviour and confirmed that the attachment results from Mg^{2+}-mediated bridging.

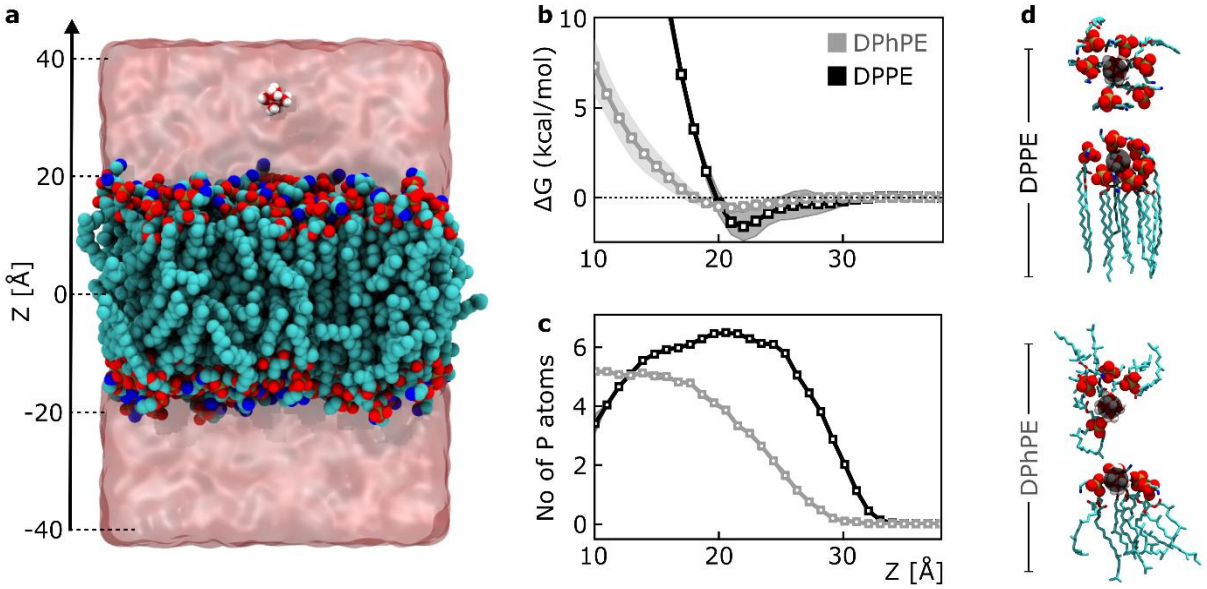

Figure 6.9 *MD simulations of Mg^{2+} binding to fluid and gel phase membranes, performed by Himanshu Joshi, PhD (Aleksei Aksimentiev's group, University of Illinois). (a) Typical system used for the simulations of the Mg^{2+} affinity to a lipid membrane. Non-hydrogen atoms of the DPhPE membrane are shown as blue (N), tan (P), red (O), and cyan (C) spheres. One magnesium ion and its first solvation shell, $Mg[H_2O]_6^{2+}$ is shown explicitly using red and white spheres; the semi-transparent surface illustrates the volume occupied by 100 mM $MgCl_2$ solution. (b) Free energy of $Mg[H_2O]_6^{2+}$ versus the distance to the midplane of the lipid membrane. Z is defined in panel (a). (c) Number of phosphorus atoms of the lipid head groups within 1 nm of a $Mg[H_2O]_6^{2+}$ ion versus its distance from the membrane midplane. Z is defined in panel (a). (d) Representative coordination of the magnesium ions by the lipid head groups at the minimum of the respective free energy curves. Mg^{2+} ion has been highlighted in black.*

6.2. Cation screening regulates membrane insertion of amphiphilic DNA constructs.

In the previous subchapter we have looked at the membrane affinity of unmodified DNA, mediated by an electrostatic phenomenon. It is important to realize that the observed behaviour indicates only the *attachment* of the duplexes to the surface of a bilayer. They are not in any way anchored, nor will they insert and span the membrane. Yet, by studying this simpler arrangement we have learnt that the cation-mediated bridging exists in the system, present and ready to be utilized. Even if in DNA-lipid-cholesterol network it is usually eclipsed by the hydrophobic modifications on the construct, which are known to produce strong affinity of the DNA for the bilayers regardless of their phase[248].

The question that emerges is, whether ions are crucial in membrane interactions of the cholesterol-modified DNA despite the bridging being, if not absent due to liquid phase of the membrane, then overshadowed by the hydrophobic moiety? In the view of the negative surface charge displayed by zwitterionic PC bilayers, I hypothesise that cations still play a regulatory screening role, modulating the DNA lipid affinity caused by another attractive force. Even if cations are not *driving* the attachment, their charge can still *enable* it.

To get an insight into the ions' part in the three-components system, I will return to using the structure known from previous chapters: dsDNA tagged with two cholesterol molecules (2C). Sequences used for folding these structures can be found in the Appendix, Table A6.1 and Fig. A6.1. I once again studied the 2C structures' ability to decorate the surface of POPC GUVs (L_d phase) for a range of magnesium concentrations between 0 and 4 mM. Firstly, the ions' effect on the structure of the duplex was studied *via* PAGE (Figure 6.10) and melting profiles (Figure 6.11), both indicating that the folding yield of the construct is not significantly affected by changes in cation concentration.

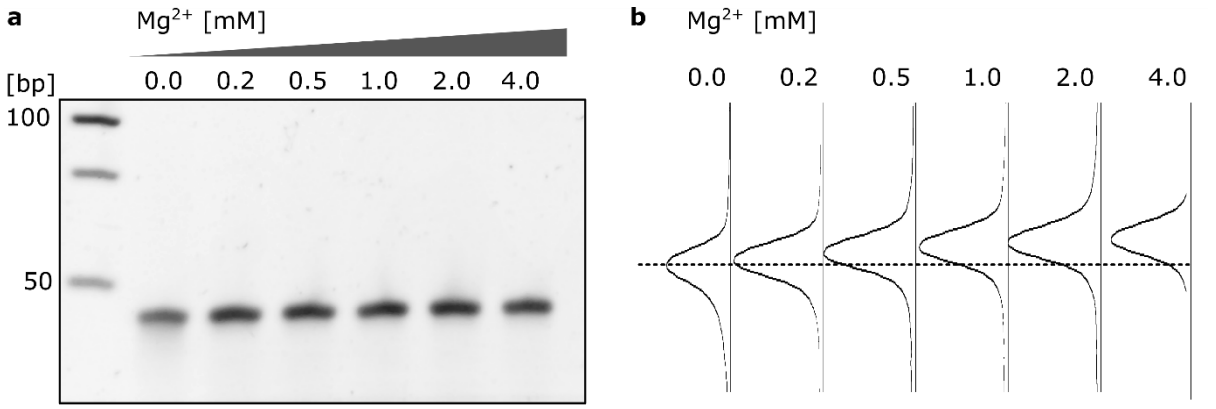

Figure 6.10 *PAGE of the unmodified (0C) DNA construct folded in different concentrations of magnesium. (a) Intensity-inverted image of the gel indicating the presence of the folded structure in each sample. (b) Intensity profiles of the lanes of the gel. The dashed line represents the position of the structures folded in the absence of magnesium. Sodium ions (≈ 10 mM) were present in all samples.*

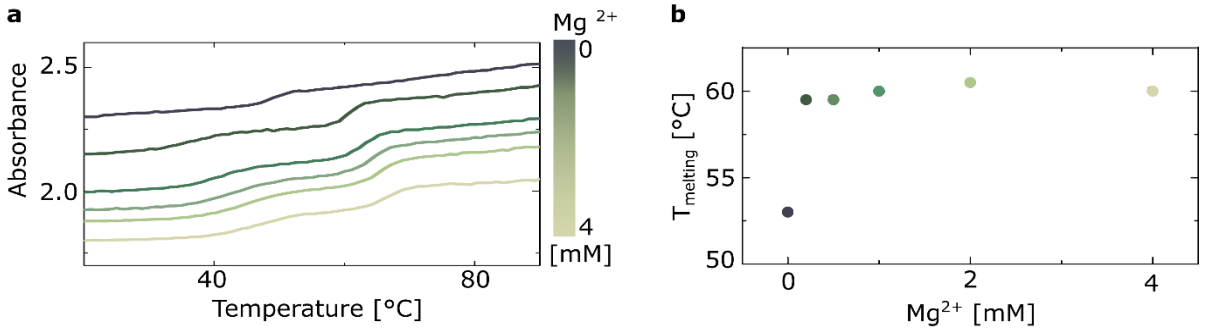

Figure 6.11 *Mg^{2+}-dependency of melting temperatures of unmodified (0C) DNA construct. (a) Collected UV-vis absorbance at 260 nm. The curves have been offset on the y axis during data processing to help illustrate the observed trend. (b) Melting temperatures plotted against concentration of Mg^{2+} in the sample. Experiments were performed in 1x TE buffer with the respective concentration of ions. Sodium ions (≈ 10 mM) were present in all samples.*

After incubating Cy3-labelled duplexes with POPC GUVs, the fluorescence intensity of the DNA membrane coating was measured. The observations are summarized in Figure 6.12. A strong dependency of the degree of DNA adsorption on magnesium concentration is noticeable, with denser DNA coatings found for higher salt concentrations, and the lack of any detectable attachment observed in the absence of salt.

I attribute this trend to the *screening* effect becoming more and more prominent with an increasing concentration of positive ions. On one side, cations can help screening the DNA-DNA repulsion, hence facilitating the formation of denser DNA coatings[227,256]. This phenomenon

is most probably taking place in the system, and may be responsible for the observed increase of the thickness of the DNA coating at high ion concentration (Figure 6.12, 4 mM), resulting from the layered organisation of charged molecules[257,258]. However, it does not explain the complete lack of DNA attachment at low ion concentrations. Therefore, I speculate that the observed behaviour results mainly from the screening of DNA-lipid repulsion.

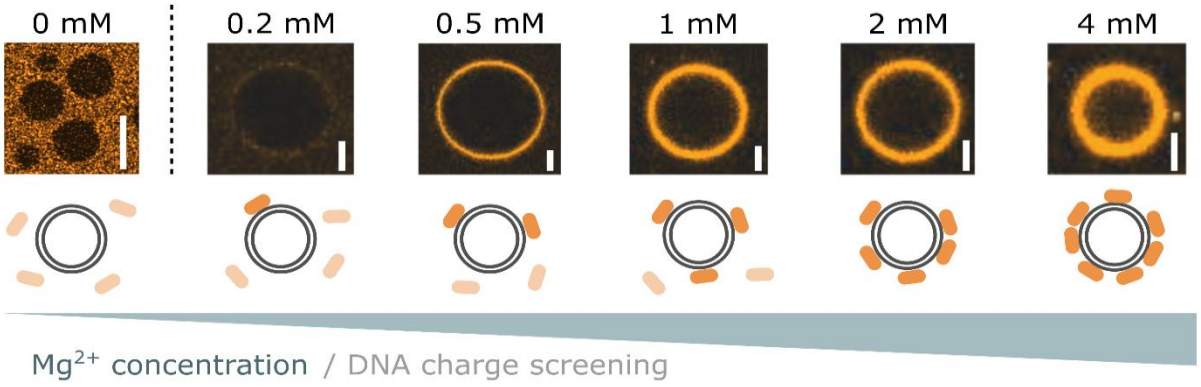

Figure 6.12 *Illustration of the screening effect of magnesium cations. Representative confocal micrographs of the Cy3-labelled 2C DNA constructs coating the surface of POPC GUVs at varying Mg^{2+} concentration. No attachment was detected in the absence of magnesium (0 mM) - the contrast of the image was increased for clarity, while no contrast adjustments are applied to the following micrographs (0.2 – 4.0 mM). Scale bars: (0 mM) 20 µm, (0.2 – 4.0 mM) 5 µm.*

Liquid phase PC bilayers do not spontaneously bind DNA nanostructures. In fact, in the absence of cations, DNA-lipid repulsion prevents nanostructures from approaching the membrane even in the presence of hydrophobic moieties. I will further unravel this phenomenon by going back to the tug-of-war metaphor introduced in the previous chapter.

As explained earlier, two competing effects regulate the interactions between amphiphilic DNA constructs and lipid bilayers: the attractive hydrophobic force between the cholesterol moieties and the bilayer core, and the electrostatic repulsion between the lipid headgroups and the DNA motifs. These two forces compete, pulling either towards the membrane (cholesterol) or away from it (DNA). Generally, cholesterol is considered a very strong hydrophobic anchor (logP = 7.11, Chemicalize, ChemAxon), and it is assumed that it will invariably cause DNA membrane attachment.

However, as shown by the results in Figure 6.12, cholesterol is not unaided in its efforts. Cations, screening the negatively charged phosphates on DNA, hinder the factor responsible for DNA

pulling away from the membrane in the first place: its charge. When cations are not present, the charge is not screened, and DNA's repulsion from POPC lipids turns out to be stronger than the cholesterol attraction towards them.

This has one extremely interesting implication. Let us try to answer the question: is there such "balance" of the opposing sides in this tug-of-war game, where ions are *not* needed? By *reductio ad absurdum,* what if we have two cholesterol molecules attached to a single nucleotide? Would we observe similar cation requirement as illustrated in Figure 6.12?

While the two previous chapters focused on showing the significance of the *contextual* design, here I want to make a point of illustrating how crucial is for the quantitative design to be *relative*. We cannot compare the efficiency of a single *vs* a double cholesterol anchor, when it is not in relation to the size of the DNA that carries it. Therefore, I classify each hydrophobically-modified DNA construct using a **tug-of-war ratio** between the number of negatively-charged nucleotides and that of cholesterol moieties (nt:chol). I hypothesize that constructs differing in this measure will exhibit different degrees of membrane affinity dependant on the ion concentration, given that cations will screen the electrostatic repulsion without affecting the cholesterol-lipid attraction.

Here, I will introduce three variations on the same structure: previously introduced 2C dsDNA alongside an analogous duplex (1C) and a 12 nt single strand (ss1C), both modified with a single cholesterol molecule. The whole library of duplexes used in this chapter is sketched in Figure 6.13.

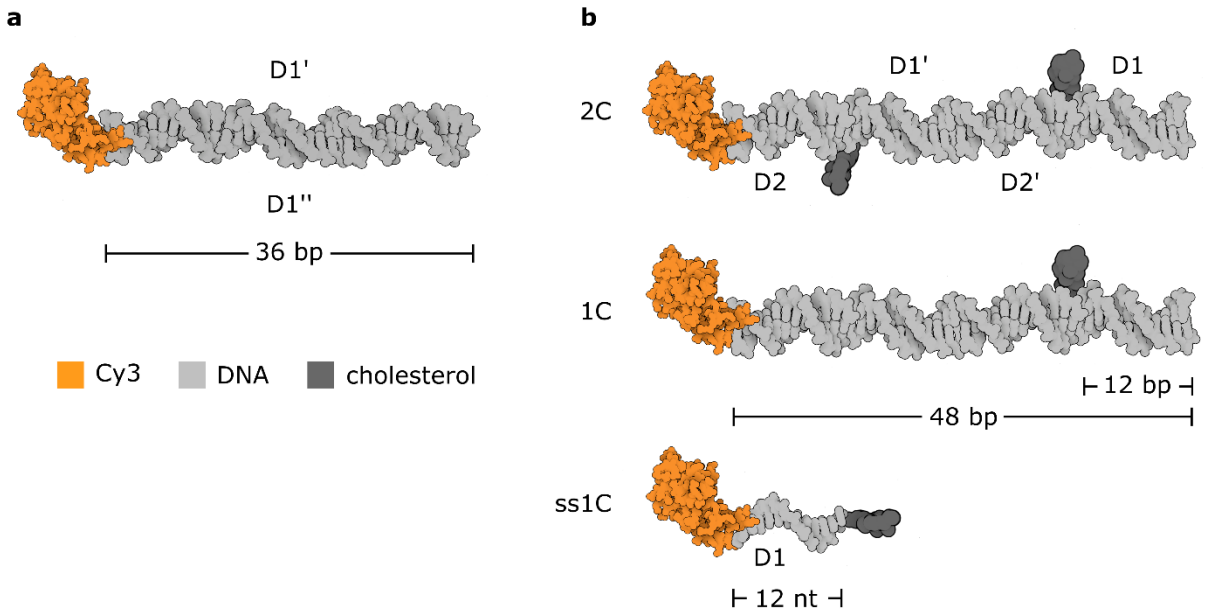

Figure 6.13 *Sketches of the DNA constructs used in this work. Sequences can be found in the Appendix, Table A6.1. (a) The 36 bp-long duplex with D1' strand modified with Cy3 molecule used for the study of phase- and cation-dependant DNA affinity towards membranes. (b) The three cholesterol-modified nanostructures used to study the effect of ionic screening on hydrophobicity-induced insertion in liquid membranes: 48 bp-long duplexes, consisting of four strands with two (2C) or one (1C) cholesterol moiety respectively, alongside a DNA strand of 12 nucleotides modified on both ends with either Cy3 or cholesterol (ss1C).*

The fluorescence intensity of vesicles' coating in Mg^{2+} range of [0, 4] mM was recorded and collected in histograms in Figure 6.14a-c. The distribution peak values for each structure are plotted against the magnesium concentration in Figure 6.14d (also collected in the Appendix, Table A6.3), together with an inset bar chart visualizing their nt:chol: 96 (1C), 48 (2C), 12 (ss1C). By fitting the data with Hill binding curves, I extracted the dissociation constant values of 0.11, 0.15 and 0.83 mM for ss1C, 2C, 1C structures respectively (for details see Appendix, Table A6.4).

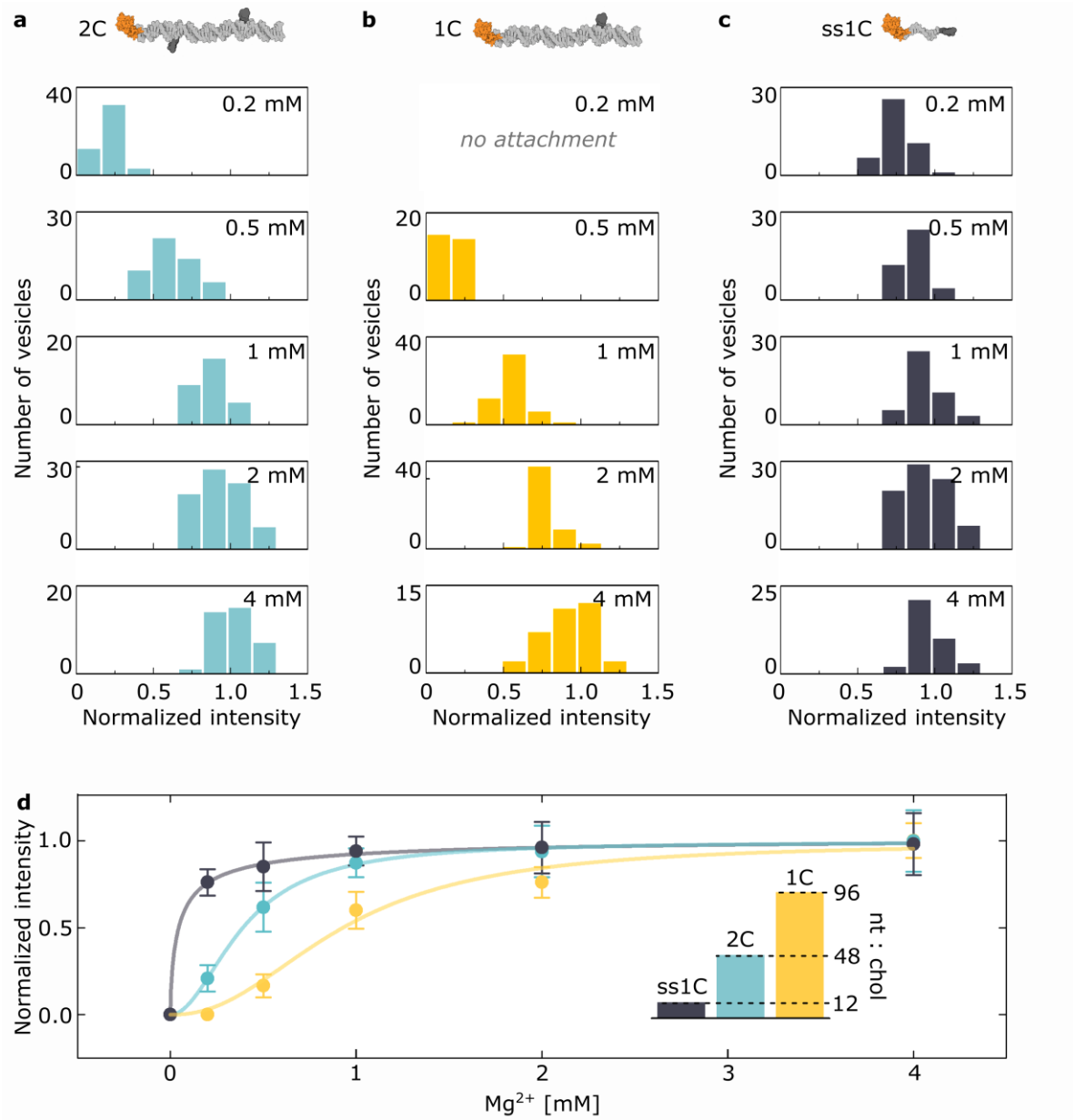

Figure 6.14 *Magnesium-dependency varies with hydrophobicity-to-charge ratio. Fluorescence intensity distributions of the Cy3-labelled DNA constructs on the surface of POPC GUVs at varying Mg^{2+} concentration collected for (a) 2C, (b) 1C, (c) ss1C structures. All data were normalized to the distribution peak value for 2C coating in 4 mM Mg^{2+}. (d) Magnesium-dependency of the peak of the intensity distributions in panels (a-c). The values, obtained upon fitting a Gaussian peak function to the respective histograms, can be found in the Appendix Table A6.3. The solid lines are best fits of a Hill function (obtained parameters in the Appendix, Table A6.4), which does not represent a mathematical model of binding but serves an illustrative purpose. The error bars represent Gaussian RMS width. The bar plot in the inset shows the differences in the ratio between the number of nucleotides and cholesterol tags (nt:chol).*

The lower nt:chol ratios, the lower the amount of screening required to achieve a given degree of attachment. This observation confirms my earlier statement: the absolute number of modifications does not reliably describe the structure in terms of its membrane interactions. What is really significant, is the *relative* number - the balance of forces competing against each other, rather than the isolated force itself.

Furthermore, the divalent ions are indispensable for the attachment of all studied constructs, even ss1C, which is a ssDNA molecule to which both the fluorophore and the cholesterol modification are covalently linked. Besides further showing the importance of charge screening, it also constitutes a control, proving that the observed effect is not a result of the structure's stability being affected by low ionic concentrations.

To once again show that the observed trend is not an effect of lower yield of folding, I have performed a set of gel electrophoreses in various salt concentrations. The results from two independent PAGE experiments, performed for 2C in either 0 mM or 4 mM Mg^{2+}, can be found in Figure 6.15. The electrophoresis shows that regardless of the magnesium content, the majority of the DNA strands are assembled into duplexes. Representative intensity profiles, as shown in Figure 6.15b, allow a more thorough analysis of the gel lanes. In the absence of salt, a small proportion of the constructs did not assemble properly, however most of the strands - 85% - formed the designed 48 bp duplex, as indicated by the size reference. Single-stranded components were not observed in samples prepared at 4 mM Mg^{2+}. However, with the higher salt concentration the duplex band was wider and smeared, which suggests that hydrophobic interactions between structures, enabling them to form dimers and multimers, are also dependant on the solution's ionic strength. The difference in the migration distance recorded in the two different gels is ascribed to the effect that the shielding of the negatively-charged phosphate has on the rate of migration[259] – yet another illustration of the nucleic acid charge screening.

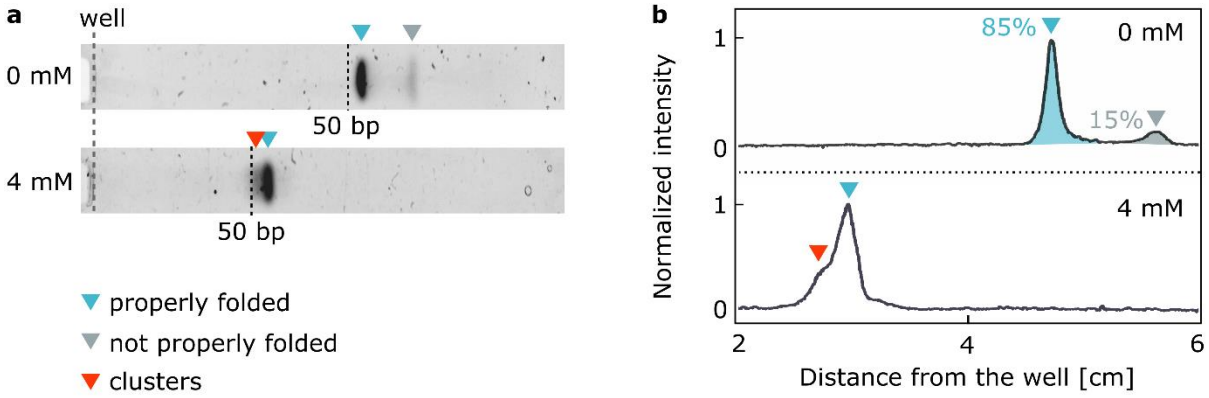

Figure 6.15 *The effects of divalent cations on the structure and electromobility of DNA constructs. (a) Inverted PAGE of 2C nanostructures containing either 0 or 4 mM $MgCl_2$ in both the gel and the buffer. The dsDNA constructs self-assemble correctly, as indicated by the blue arrow. Disassembled strands (grey arrow) and clusters (red arrow) have also been highlighted. Sodium ions (≈ 10 mM) were present in all samples. (b) Inverted intensity profiles of the gel lanes shown in (a). The differences in distance from the well illustrate the screening effect of magnesium, reducing the electromobility of structures in the 4 mM Mg^{2+} experiment.*

As discussed in the previous subchapter, the attractive interactions between unmodified DNA constructs and gel phase PC membranes are due to bridging, and therefore they emerge only with divalent cations, as monovalent ones are generally unable to bridge. The behaviour reported here is a separate, independent phenomenon, resulting from screening that facilitates the cholesterol-driven membrane binding. As screening is a process that occurs regardless of cation valency, even though more efficiently for higher valency, we expect the attachment to be induced by the addition of monovalent ions as well. Therefore, I have confirmed that the DNA attachment can also be facilitated by calcium (Ca^{2+}) and potassium ions (K^{+}), as presented in Figure 6.16. However, orders of magnitude higher concentrations of monovalent ions (100 mM) were required to match the trends observed with divalent ones (4 mM).

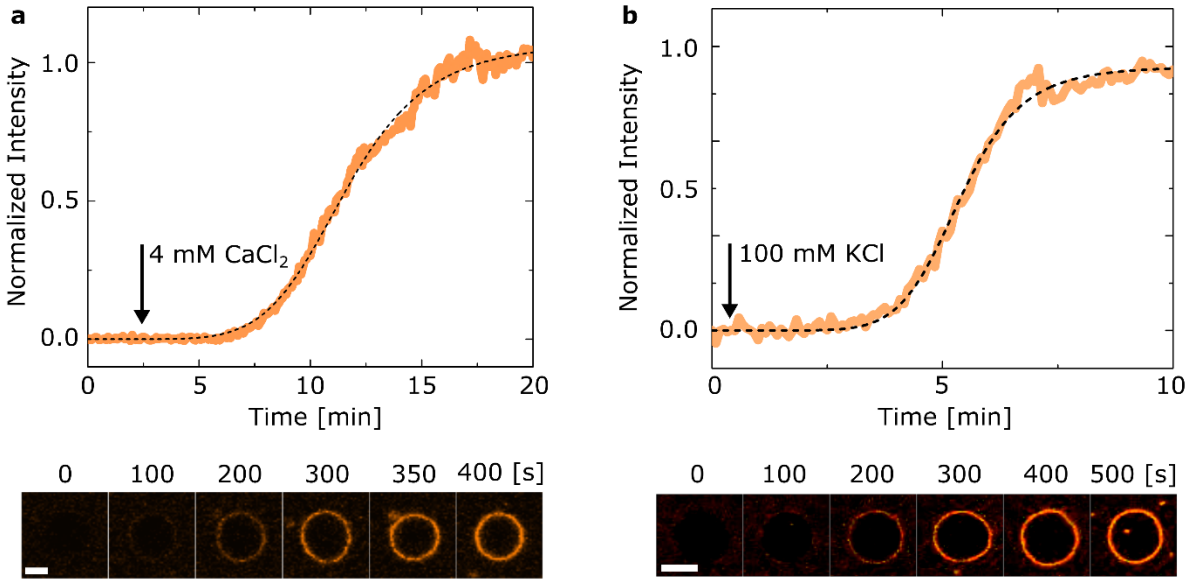

Figure 6.16 *Charge screening occurs independently of the cation's valency. Upon addition of (a) 4 mM Ca^{2+} as well as (b) 100 mM K^{+}, membrane attachment of 2C DNA structures to POPC GUVs is induced. Scale bars: 5 µm. Dashed lines represent a sigmoidal fit.*

6.3. Cation-regulated activation of a membrane-bound DNA nanomachine.

The dependency of the membrane affinity of hydrophobically-tagged DNA on salt concentration offers a route to reversibly trigger attachment and detachment by adding and removing cations. As summarized in Figure 6.17a-c, GUVs were incubated with 2C DNA nanostructures, initially in the absence of cations. Magnesium was then added, triggering the attachment of DNA. The subsequent addition of EDTA, chelating the magnesium ions, produced a drop in fluorescence to the background levels. Finally, adding further free magnesium caused the DNA to bind the membranes once again, demonstrating full reversibility of the salt-regulated attachment process.

The reversible effect of cations on the membrane attachment of cholesterol-modified DNA nanostructures is reminiscent of the cation-dependant activity seen in a number of natural transmembrane proteins[191,260]. Inspired by their biological analogues, I demonstrated that the activity of synthetic DNA nanodevices can also be regulated by cations. I have therefore considered the functionality of 2C DNA constructs, which upon membrane insertion form toroidal pores in lipid bilayers, triggering the exchange of lipids between the inner and outer leaflets, similar to scramblase enzymes[102,106]. Here I prove that the activity of such a synthetic enzyme can be triggered with cations, remarkably alike the natural scramblases[191].

I used a previously described assay based on the reduction of NBD, a dye that while fluorescent in its oxidized state, bleaches upon exposure to a strong reducing agent[102]. As summarized in Figure 6.17d-f, I have prepared GUVs in which both leaflets contained NBD-labelled lipids. The vesicles were initially incubated with the 2C DNA in the absence of ions, which as expected did not attach to the membranes and were therefore in an inactive state. I then added the reducing agent - dithionite ($S_2O_4^{2-}$) - to the outer solution, which being unable to penetrate the GUVs, caused bleaching only of the NBD molecules on the outer bilayer leaflet, resulting in approximately 50% loss of fluorescence. The addition of magnesium at this point activated the nanostructures, causing their insertion into the membranes. The functional synthetic enzymes enabled mixing of the inner and outer membrane leaflets and the exposure of previously unbleached NBD fluorophores to the reducing agent, causing a decrease of the NBD emission below the initial 50%.

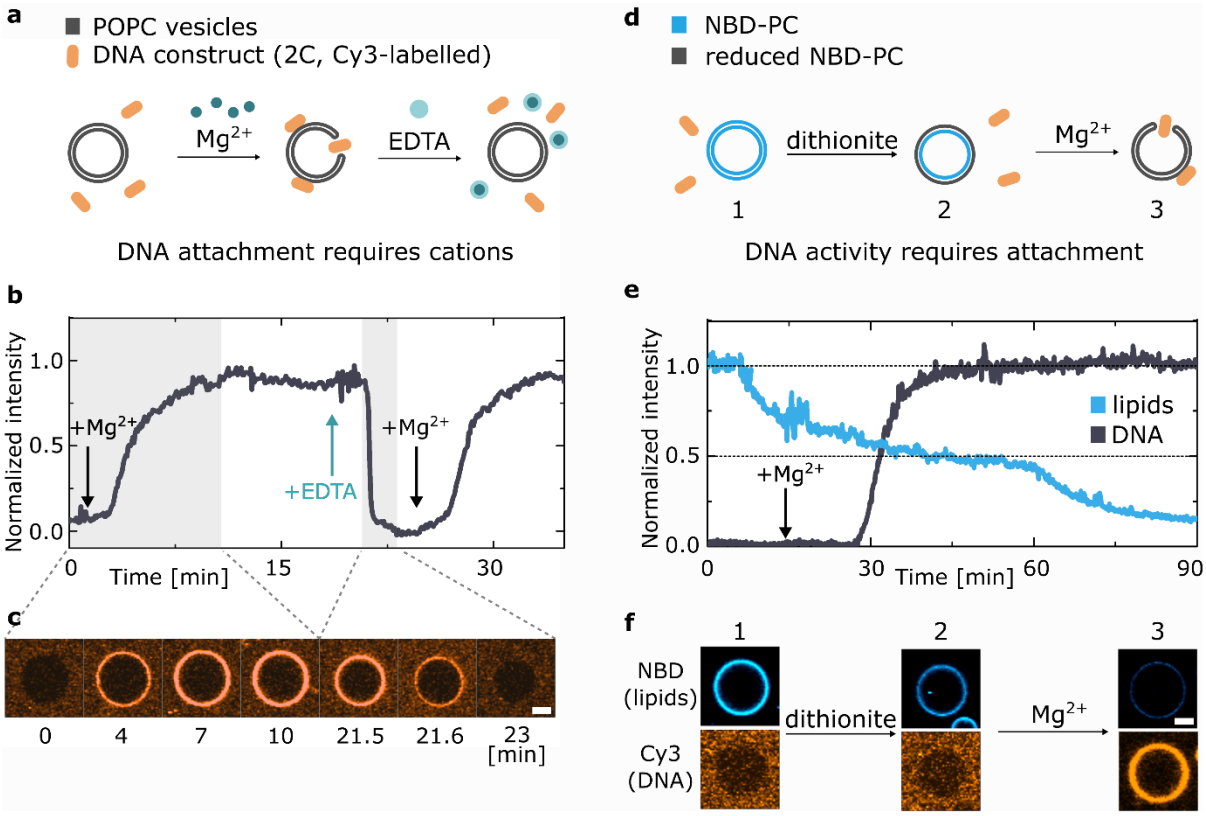

Figure 6.17 *Cation-regulated reversible DNA membrane binding and activation of a synthetic enzyme. (a) Schematic representation of the mechanism leading to a reversible DNA membrane attachment upon addition of magnesium and its removal by means of chelating agent EDTA. (b) Representative fluorescence intensity trace of Cy3-labelled DNA nanostructures (2C) as recorded from POPC GUVs. DNA attachment and detachment are triggered by the addition of magnesium chloride and EDTA respectively, as indicated by arrows. Delays associated with the diffusion of added Mg^{2+} and EDTA through the experimental chamber result in short lag times before changes in fluorescence are observed. (c) Confocal micrographs from the highlighted grey areas of the trace in (b), demonstrating the attachment and detachment transients. Scale bar: 5 µm. (d) Schematics of the NBD-dithionite reduction assay used to demonstrate cation-activated lipid scrambling. (e) Representative trace of the fluorescent intensity of NBD-labelled lipids (blue) upon addition of dithionite alongside the trace representing Cy3-labelled DNA (black), coating the vesicle after addition of magnesium (arrow). (f) Representative confocal micrographs, showing the fluorescence of both DNA and lipids at each stage of the experiment described in (d). Scale bar: 5 µm.*

As a control, the results for the pore-forming 2C were contrasted with 1C DNA, which can bind to the membranes upon the addition of magnesium, but does not create a toroidal pore (Figure 6.18). The sharp decrease of the NBD emission below 50% of the initial value was not

observed, further confirming that the behaviour detected with 2C is indeed attributed to the DNA-induced lipid scrambling, and that the addition of magnesium acted as an external stimulus for activating the enzyme.

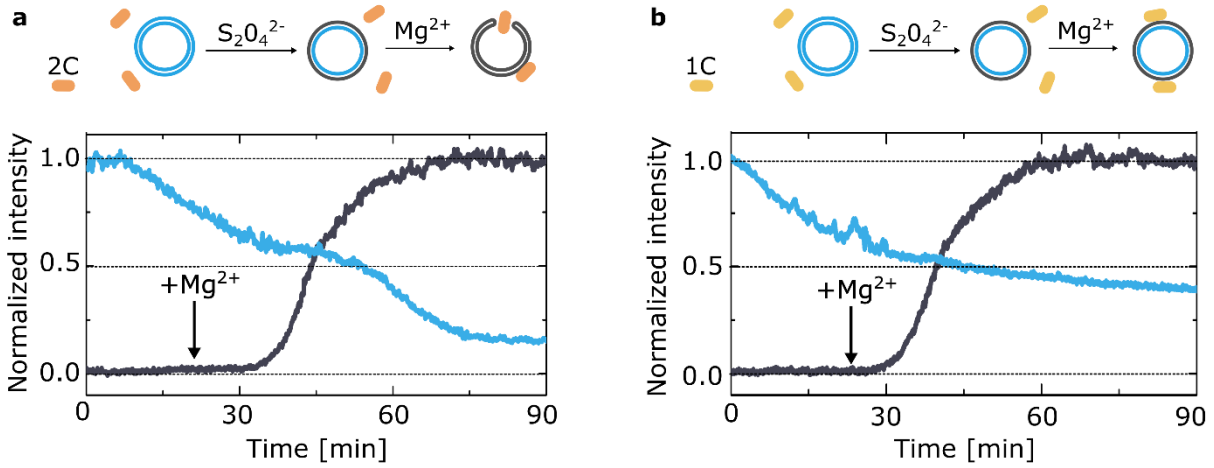

Figure 6.18 *NBD reduction assay performed in the presence of (a) an inserting 2C structure and (b) a non-inserting 1C structure. Representative trace of the fluorescent intensity of NBD-labelled lipids (blue) upon addition of dithionite alongside the trace representing Cy3-labelled DNA (black), coating the vesicle after addition of magnesium (arrow). The plot in (a) is an example of a repeated experiment from Figure 6.17e. Similar as in Fig. 6.17, the delay in the observed changes in fluorescence are a result of the diffusion of added Mg^{2+} through the experimental chamber.*

6.4. Conclusions

In summary, here I have explored the mechanisms through which cations regulate and mediate electrostatic interactions between DNA nanostructures and zwitterionic PC lipid bilayers.

First, with the help of Roger Rubio (University of Cambridge) and Himanshu Joshi (University of Illinois), we described the *bridging* phenomenon - attractive forces between unmodified DNA duplexes and lipid bilayers, occurring in the presence of divalent cations. We elucidated the origin of its phase-dependency and demonstrated how it can be exploited to program a reversible membrane attachment of the nanostructures by tuning independent physico-chemical parameters that cause liquid-gel phase transitions in the membranes, including temperature and sterol content.

Secondly, I examined the *screening* effect of cations by studying the interactions between liquid phase bilayers and DNA nanostructures modified with cholesterol moieties. Despite the presence

of highly hydrophobic tags, Coulomb repulsion between liquid membranes and the negatively charged DNA cannot be overcome by cholesterol modifications only; cations are required to screen the electrostatic forces and through that enable membrane attachment.

I would like to emphasize the importance of the experimental flow in this chapter, reflecting the approach of the whole thesis: knowing about the complexity of the ion-mediated interactions, we have deconvoluted their effects by simplifying the DNA-cholesterol-lipids system into an even simpler DNA-lipids relationship. Only after assessing ions' role in a simpler scenario, I moved towards more complicated designs. This allowed me to understand that the two described processes: *bridging* and *screening* co-exist and can equally be utilized in nanoengineering biological responses.

Bridging-related experiments are my first step towards **targeting** cells based on their membrane properties. The parallel with proteins embedded and constrained within lipid rafts [18,261,262] makes it especially exciting, since, as already stressed in previous chapters, I consider nature-inspired mechanisms the most promising for nanoengineered structures.

While studying *screening*, I returned to the previously discussed tug-of-war model of cholesterol-modified DNA and its membrane affinity. I showed that the constructs' membrane attachment varies with the salt concentration depending on the ratio between the number of nucleotides and that of hydrophobic moieties in each nanostructure: the tug-of-war ratio. This finding brings attention to the effects of the nanostructure's size. DNA origamis are certainly carrying a lot of promise, but the consequences of forming such massive (charged!) bioconstructs simply need to be taken into account in the design. While many researchers are tackling the problem of the origamis' stability in physiological conditions[137,138,194], we should also look at how is their functionality affected when moving towards *in vivo* experiments.

Finally, the modulating effect of cations can also be exploited to rationally design new responses, as in the magnesium-dependant synthetic scramblase enzyme presented here. One can envisage a range of opportunities becoming available to more complex architectures, with DNA-based membrane channels that change their shape, orientation, and activity, similar to natural membrane proteins they are designed to mimic.

CHAPTER 7

Effects of surfactants on DNA-lipid interactions

While experiments in Chapters 4 and 5 were comparing different DNA designs (either internally modified with dodecane (Chapter 4) or with various position and linkage of cholesterol (Chapter 5)), the previous chapter (Chapter 6) introduced an idea of exerting control in the system through changes applied to the lipid bilayer. Since the bridging was literally linking lipids and DNA, unsurprisingly, the process could be affected from both sides: by controlling DNA-cation or lipid-cation connection.

But similarly, efficiency of membrane-spanning can change drastically with bilayer composition or its mechanical and physical properties. This is by now a well-known phenomenon, as years of biological research developed, and is dependent on bilayer-affecting protocols[1,2]. Most significantly, the process of transfection, where a particular genetic information is introduced into an organism's genome, depends on exogenous DNA crossing the membrane. And while DNA can be taken up by cells under certain conditions, a spontaneous uptake is inefficient and rarely observed[3]. Thus, a vast range of methods have been developed in order to facilitate this process. Conveniently for the field of DNA-based transmembrane structures, forcing nucleic acids through the lipid bilayer has already been thoroughly studied for decades.

7.1. Dual role of surfactants in biological research protocols.

One of the membrane-disrupting methods in DNA transfection employs surfactants, amphiphilic surface active agents, which spontaneously insert into lipid bilayers[1]. As their molecular structure is not matching the ones of lipids forming the bilayer, they often induce a mechanical strain in the architecture of the membrane.

Surfactants that do not freely flip between leaflets cause the bilayer to curve. However, the ones that spontaneously distribute themselves uniformly on both sides of the membrane introduce a strain as well. Micelle-forming surfactants induce a curvature stress, as they do not match with the planar topology of a monolayer (Figure 7.1a). Since in a bilayer two leaflets are coupled, they cannot both curve in the same way. This results in membranes with uniformly distributed surfactant molecules becoming disordered and thinned, due to the strain that mismatched units induce

(Figure 7.1b). One of the ways this strain can be released is partitioning of surfactants to one part of the bilayer and a formation of highly-curved rims of a toroidal pore (Figure 7.1c). Both the disordering and pore-formation disrupt the membrane, facilitating bilayer spanning or crossing by larger biomolecules[4,5].

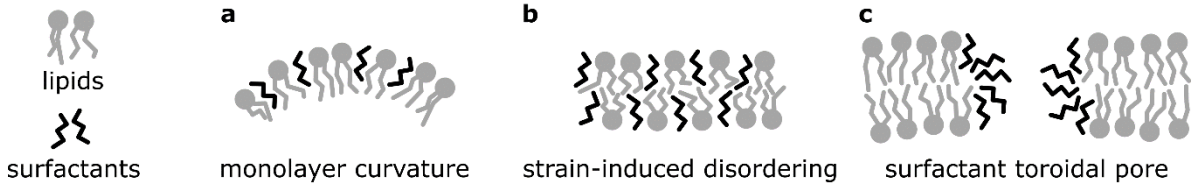

Figure 7.1 *Membrane disruption by surfactants. (a) Mismatch between the dimensions of the membrane-forming lipids and the inserted surfactants leads to a spontaneous curvature. (b) Coupled monolayers of a membrane cannot assume the curved structure, which causes membrane thinning and disordering. (c) The formation of a surfactant-rich rim – a toroidal pore – allows reduction of the curvature-related strain.*

However, another process closely related to my endeavours has also utilized surfactants to facilitate membrane interactions: insertion of an integral protein into model bilayers, performed in order to study ion channels and other transmembrane structures. Importantly, there, surfactants first directly interact with the protein of interest and only then mediate membrane interactions. Their role is to form micelles that incorporate the protein and then fuse with the studied membrane, in that way enabling insertion[6–8]. A reverse process of protein reconstitution - separation from the cell membrane while preventing denaturation in aqueous solution - also utilizes surfactants to stabilize proteins carrying hydrophobic domains[9,10].

DNA/surfactant complexes are thoroughly studied for unmodified DNA and cationic surfactants, particularly for gene delivery applications[263–265]. However, details of interactions of cholesterol-modified DNA with non-ionic surfactants have not received much attention so far. Even though detergents introduced into the sample will interact with the membrane-spanning domain encircling integral proteins[266], will the arrangement look similar around the protruding cholesterol anchors of a DNA nanostructure? What is the role of surfactants in membrane-spanning DNA interactions with the bilayer?

7.2. Cholesterol-modified DNA in the presence of a surfactant.

In order to study the effects of a surfactant on membrane-inserting DNA construct, here I introduced a structure more complex than a duplex. The aim of this project is to assess how insertion efficiency depends on DNA's interactions with a surfactant, and in turn to achieve a facilitated insertion. For that reason, I employed a multi-helix bundle: 4-helix (4H) structure, whose geometry facilitates membrane spanning better than duplex's. Additionally, it induces larger pores, meaning that the signal will be easier to detect. I have discussed the details of 4H design in the methods section (Chapter 3), while here the summary of the construct's architecture is presented in Figure 7.2. The sequences used for folding 4H structure can be found in the Appendix, Fig. A7.1 and Table A7.1.

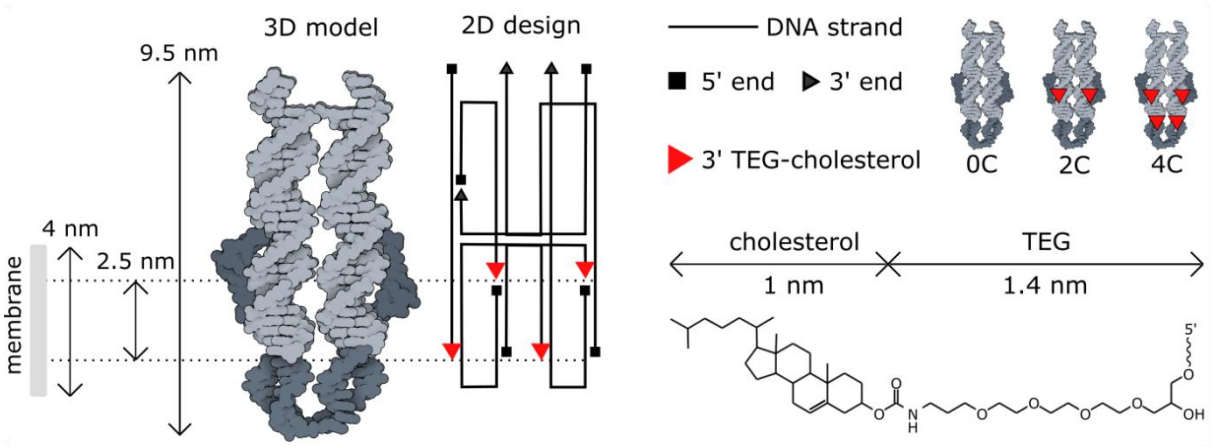

Figure 7.2 *Design of the 4-helix (4H) structure used in this project. The "shielding" DNA strands are highlighted in dark blue. The construct was modified with either two (2C) or four (4C) cholesterols, while unmodified (0C) DNA was used as a control. Further details of the design can be found in the Appendix, Fig. A7.1 and Table A7.1.*

There are two parameters that can be varied in the design: number of cholesterols and the presence of "shielding" strands. Since the first is rather self-explanatory, I will elaborate on the second. The cholesterol-modified DNA structures aggregate, due to the attraction between hydrophobic moieties. In order to prevent the aggregation, I have "shielded" hydrophobic cholesterol from the surrounding water with overhanging single strands of DNA. As nucleobases are apolar, ssDNA will readily wrap around the cholesterol modifications, protecting the constructs from clustering[149]. 4H structure has two sets of "shields": loops around cholesterols on one end and ssDNA overhangs around the two modifications in the middle of the construct. PAGE analysis in

Figure 7.3 shows a significant effect that the "shielding" has on aggregation. All the experiments presented in this chapter utilize the "shielded" constructs, unless stated otherwise.

The same gel also features 4H after it was mixed in 1:1 ratio with 1% octylpolyoxyethylene (C_8E_n*, oPOE), a non-ionic surfactant. Polyoxyethylene detergents, which have chemical formulas of the type C_xE_n, are an extensive family of surfactants employed in protein crystallization and stabilization[267]. While oPOE is standardly utilized in micelle-mediated protein reconstitution[268,269], its close derivative, dodecylpolyoxyethylene ($C_{12}E_n$), has been shown to induce membrane disordering and thinning[270] and through that facilitate electroporation of cell membranes[271]. It has been employed previously in studies on synthetic DNA ion channels[102,272] and therefore chosen here to assess its effects on DNA membrane insertion.

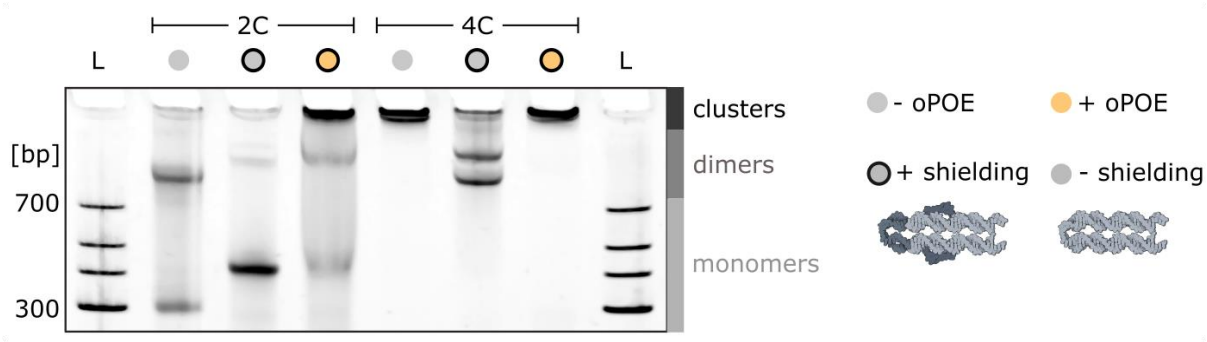

Figure 7.3 *PAGE analysis showing the effects of additional ssDNA overhangs ("+/- shielding") as well as addition of a 0.5% octylpolyoxyethylene surfactant ("+/- oPOE") on the aggregating behaviour of cholesterol-modified 4H structures.*

The analysis of the gel suggests that after the addition of the surfactant the concentration of DNA nanostructure's monomers dispersed in the solution decreases. Instead, DNA bands containing the surfactant do not migrate in the electric field from the well, which indicates the formation of large complexes.

One of the possible architectures formed in the DNA/surfactant samples are oPOE micelles (aggregation number N = 75)[273], incorporating DNA constructs. At the concentration of 0.5%, oPOE in the sample is above its critical micelle concentration (cmc_{oPOE} = 0.15%)[274], the spontaneous formation of micelles is therefore favourable. Additionally, DNA lipoplexes were previously shown to be immobile in gel electrophoresis, presumably not only due to their size but

*Octylpolyoxyethylene with a chemical formula C_8E_n was purchased as a mixture of molecules with n = [2,9] (Sigma-Aldrich).

also lack of charge[275]. Such complexes were shown to incorporate a staining dye, despite their compact form[275,276].

However, on the gel these big micellar structures cannot be clearly distinguished from cholesterol-mediated clusters, as deduced from the similarities of bands with aggregating 4C construct ran with (+) and without (-) oPOE (- shielding). Large aggregates will be immobile in the gel due to their size. Micelles, on the other hand, are smaller (75x oPOE weight < 40 kDa, while single DNA monomer weights > 60 kDa), but uncharged, therefore they too can exhibit no electromobility in PAGE analysis.

We can shed more light on the formed complexes by observing the behaviour of 4C 4H mixed with another surfactant - sodium dodecyl sulfate (SDS) - below and above its cmc concentration (cmc_{SDS} = 0.23%)[277]. Its anionic structure allows to gather more insight into complexes' behaviour in the electric field, as compared to non-ionic oPOE which cannot be observed by the means of electrophoretic measurements. I will use these experiments to speculate on the general DNA/surfactant interplay, while keeping in mind that due to the charge of SDS, its interactions with DNA may be different than oPOE's.

The gel featuring samples of 4C nanostructures mixed with various concentrations of SDS is shown in Figure 7.4. Two observations suggest that surfactant's presence mediates aggregation, *even* if it also forms DNA-incorporating micelles. Firstly, an SDS addition below its cmc resulted in an increased number of structures retained in the well, which implies higher degree of aggregation, presumably induced by the surfactant. Secondly, at high SDS concentration (2%) a band of high electromobility appears. I attribute this band to SDS micelles, featuring a negative charge allowing them to migrate in the applied electric field, unlike oPOE. The visualization of micelles may be possible due to their higher concentration when well above cmc_{SDS}. Note, that cmc is the concentration at which formation of micelles *starts*[278], which may explain why at 1% there is no analogous band detected on the gel - not enough micelles have formed yet.

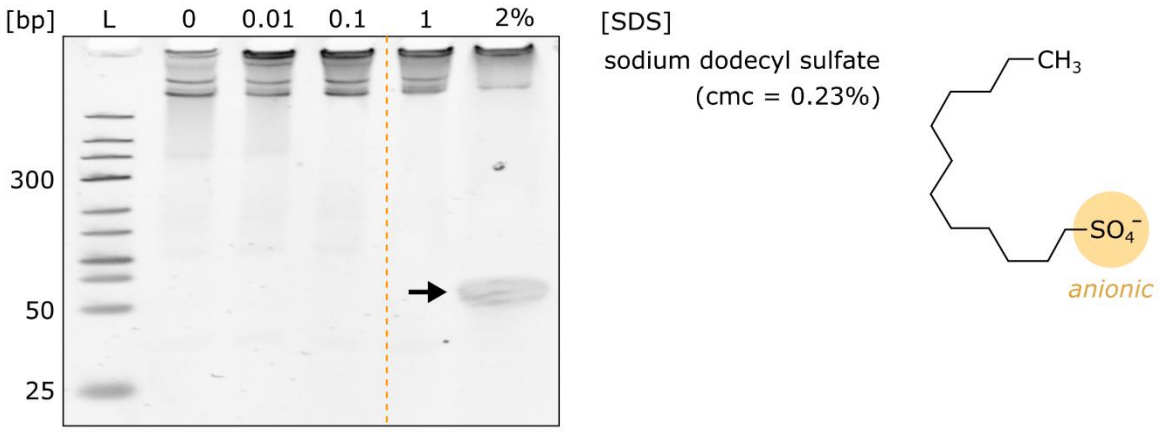

Figure 7.4 *PAGE analysis of 4C 4H construct mixed at different concentrations of SDS: below and above its cmc (0.23%)*[277]*. Dashed line separates lanes with [SDS] < cmc (left) and [SDS] > cmc (right). An additional band appearing at [SDS] = 2%, presumably containing SDS micelles, is marked with a black arrow. Molecular structure of SDS is also shown, with its anionic group highlighted in yellow.*

The results of the electrophoretic experiments suggest that surfactants can facilitate cholesterol-mediated aggregation. Yet, the measurements did not present a conclusive proof of oPOE-induced clusters, and more thorough analysis is required to fully understand DNA-cholesterol-surfactant interactions.

Similar to the gel, DLS experiments also indirectly show that oPOE associates with DNA structures. As seen in Figure 7.5, the peak attributed to 4H monomers (as compared with unmodified 0C that is not prone to aggregation) decreases after an addition of only 0.01% oPOE, while in 0.1% oPOE the DNA monomers are not detected by the setup anymore – only the peak corresponding to the surfactant alone is visible. Since at the studied concentrations oPOE is included below its cmc, and since its decreasing effect on the number of monomers is noticeable in all samples, this can signify that, in fact, oPOE induces increased clustering, rather than incorporates DNA in micelles. Still, similarly as in the gel, it is not possible to distinguish surfactant-facilitated clusters from surfactant-formed micelles with certainty.

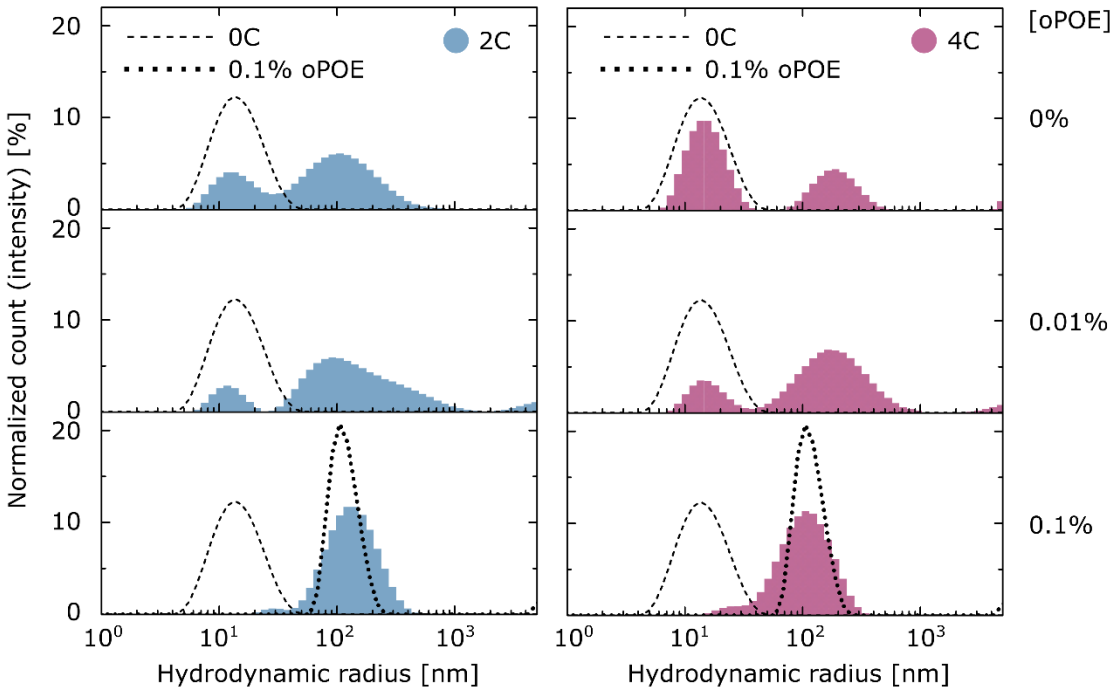

Figure 7.5 *Dynamic light scattering (DLS) size measurements of 4H: 2C and 4C structures in 0, 0.01 and 0.1% oPOE. Peaks collected for 0C (no oPOE), as well as 0.1% oPOE (no DNA) have been shown for comparison.*

On the other hand, when recording structures' diffusion by following their fluorescent labels (Cy3) *via* fluorescence recovery after photobleaching (FRAP)*, the addition of the surfactant (final [oPOE] = 0.01%) does not induce changes in the lateral dynamics of membrane attachment (Figure 7.6). The experiments did not detect differences between the diffusion of 2C and 4C structures, and as they are expected to attach with different strengths (different number of embedded cholesterol anchors)[215], I consider the technique not to be sensitive enough to clearly disentangle the effects of the surfactant, the number of anchors, and effects of DNA insertion.

A shift in the distributions of diffusion coefficients (D) of lipids tested in the presence and absence of oPOE suggests that the surfactants reduce lipids' diffusion. While PAGE and DLS show oPOE effect on the cholesterol-modified DNA, FRAP results indicate that lipids-oPOE interactions are also present in the system.

*FRAP measurements were performed by Michael Schaich, PhD (Ulrich Keyser's group, University of Cambridge).

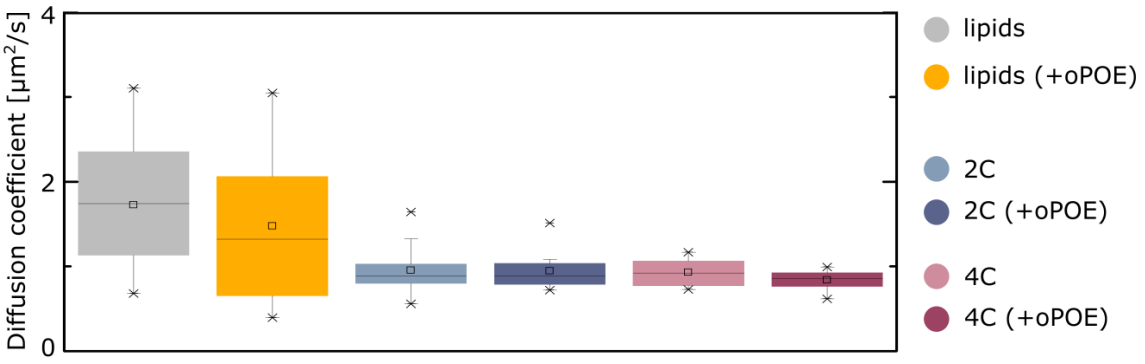

Figure 7.6 *Box plots of the diffusion coefficients collected for NBD-labelled lipids (no DNA addition), as well as Cy3-labelled DNA coating of the POPC vesicles, using fluorescence recovery after photobleaching (FRAP) method, measured at room temperature. Values after the addition of oPOE to the final concentration of 0.01% (+oPOE) were also recorded. FRAP experiments were performed by Michael Schaich, PhD (Ulrich Keyser's group, University of Cambridge).*

Studying the nanostructures' behaviour in the absence of the surfactant, both DNA characterization techniques (PAGE and DLS) show that 4H constructs are prone to aggregation. The clustering is particularly strong for the structures modified with a larger number of hydrophobic anchors and to an extent occurs even despite the "shielding". Before continuing the examination of the surfactants' effects, I would like to briefly share some discussion on the cholesterol-mediated clustering and its importance for membrane interactions.

7.3. Cholesterol membrane insertion vs aggregation.

Throughout this work, I aim at extracting a hierarchy of interactions in the DNA-cholesterol-lipid system. Knowing about the strong aggregating tendencies of cholesterol-modified structures, I want to consider which attraction is stronger: cholesterol-cholesterol or cholesterol-lipids. Is the aggregate disassembled when an opportunity for cholesterol to embed within a lipid bilayer appears?

When examining fluorescence spectra of Cy3-labelled DNA duplexes (40 bp, sequences in the Appendix, Table A7.2), one notices that the intensity of the signal is inversely proportional to the number of cholesterol moieties on the structure. Figure 7.7a shows decreasing values of fluorescence intensities for the duplex modified with 0, 1 or 2 cholesterol molecules. I attribute this trend to self-quenching of Cy3 labels[279], which causes a decrease in the fluorescence as duplexes form cholesterol-driven aggregates.

Furthermore, an addition of lipids into the sample results in an *increase* of fluorescence, as shown in Figure 7.7b. The fluorescence of a non-cholesterolized (0C) duplex increases partially, which could be caused by its decreased concentration, effectively expanding the distance between labels. By diluting the non-aggregating DNA, the fluorophores are spread further apart, which could account for the reduced self-quenching. Importantly, both cholesterol-modified structures show a fluorescence dependency on the concentration of lipids, differing from the trend observed for 0C duplex. Having more cholesterol modifications, the signal recorded for 2C structure increases quicker with the growing lipid concentration, suggesting that the trend is determined by cholesterol-lipid interactions. These observations hint that the fluorescence-hindering aggregates are disrupted as the lipids appear in the sample. This in turn indicates that cholesterol-lipid interactions are more favourable than cholesterol-cholesterol clusters. This observation is consistent with the comparison between free energies of cholesterol micellization (≈ -53 kJ/mol)[280,281] and cholesterol membrane insertion (≈ -75 kJ/mol)[101,209], although it must be noted that these values do not take into consideration the presence of covalently attached DNA.

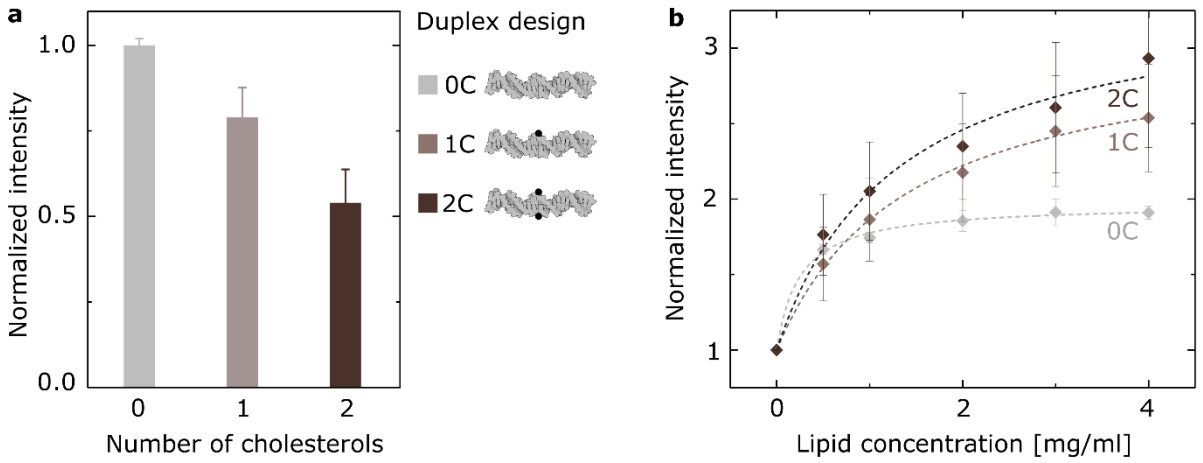

Figure 7.7 *Fluorescence measurements suggest disruption of cholesterol-mediated aggregates in the presence of lipids. (a) Fluorescence intensities of Cy3-labelled dsDNA (40 bp) depend on the number of cholesterol modifications they carry. All normalized to the intensity recorded for 0C duplex (1.0 ± 0.03, 0.79 ± 0.09, 0.54 ± 0.10 for 0C, 1C, 2C, respectively). Error bars represent standard deviation from three measurements. (b) Addition of lipids results in an increase in the fluorescence signal of DNA duplexes. Error bars represent standard deviation from three measurements.*

The results suggest that embedding cholesterol into a lipid bilayer is favoured over cholesterol clustering. Indeed, it has previously been shown that upon exposure to the membranes, cholesterol-mediated DNA aggregates disassemble, allowing monomers to interact with the bilayer[215,282]. However, with an increased number of cholesterols, the same structures formed clusters that were not spontaneously broken and coated the membrane in a non-uniform manner. Similarly, imaging fluorescently labelled 4H structures in the presence of vesicles indicates that the aggregates formed by 4C constructs are too massive to disassemble, even in the presence of a bilayer. Representative micrographs, highlighting the clusters, are presented in Figure 7.8a. Despite the self-quenching of Cy3 labels[279], aggregates are strongly fluorescent which hints at the large size of formed 4C multimers. Even though 2C features less cholesterols, it produces more prominent vesicle coating pointing towards the role played by the degree of clustering on membrane activity of DNA nanostructures. Quantitative analysis of the fluorescent intensity of the DNA rings (Figure 7.8b) clearly shows the difference in the degree of attachment, which I conclude results from the 4C forming much larger and more stable cholesterol-induced clusters.

The prominent difference in attachment observed for non-shielded structures is also noticeable for the shielded ones (Figure 7.8c), but to a lesser degree due to the aggregation being hindered by the overhanging loops. Note, however, that "shielding" is not as efficient for 4C structures as it is for 2C. This is another result of 4C forming stable clusters mediated by its four cholesterol modifications. An extreme case presented by images in Figure 7.8 serves to illustrate the significant effects that clustering has on the membrane attachment. Even though cholesterol's anchoring into the bilayer is favoured, large aggregates are linked too strongly to disassemble spontaneously.

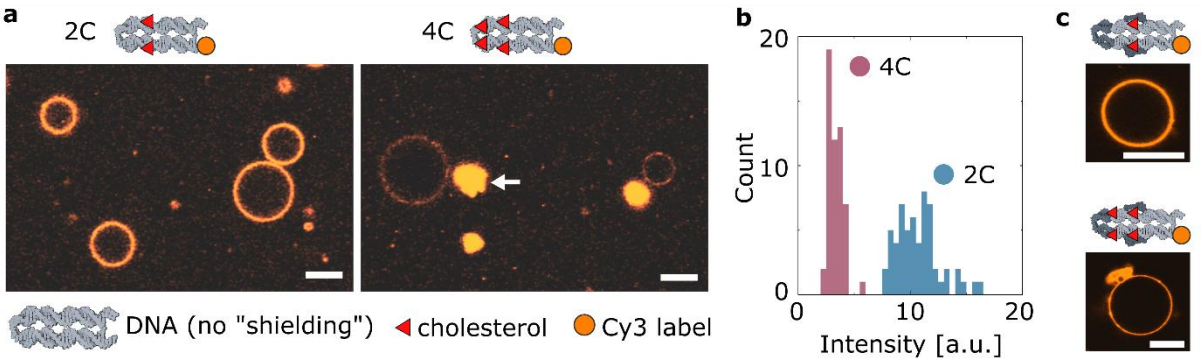

Figure 7.8 *POPC vesicle coating by Cy3-labelled 4H structures. (a) Representative micrographs showing the differences in the degree of attachment of unshielded structures. An exemplary DNA aggregate formed by 4C 4H is marked with a white arrow. Scale bars: 10 µm. (b) Histograms of coating intensity of POPC vesicles by unshielded 2C and 4C structures. Number of measured vesicles:* $N_{2C} = 58$, $N_{4C} = 54$. *(c) Micrographs presenting representative vesicles coated with Cy3-labelled shielded 4H structures, showing that despite "shields", 4C clusters are not easily disassembled in the presence of lipid bilayers. Scale bars: 10 µm.*

Results presented in this paragraph represent only a small step towards assessing the stability of cholesterol-mediated aggregates. It is worth noting how big of an impact does clustering have on the attachment, and thus on the activity of membrane-interacting structures. While I wanted to share some of the thoughts on this matter, I do not follow this line of thought, as what ultimately interests us here is the insertion efficiency of structures and its dependency on surfactant additions.

7.4. Effects of surfactant on the insertion efficiency of the pore-forming DNA.

In order to study the effects of oPOE on the membrane insertion efficiency of DNA structures, I was measuring changes in membrane conductance upon exposing it to pore-forming constructs. I have performed a set of current measurements in the presence of 2C and 4C 4H, following three protocols:

- oPOE: no surfactant was added.

+ oPOE: after adding DNA into the chamber, oPOE was separately added to a final concentration of 0.01%.

+ oPOE (premix): before adding DNA into the chamber, it was premixed (1:1 ratio) with 1% oPOE (final concentration 0.01%).

Figure 7.9a schematically illustrates the three protocols used. Each structure was tested with these three protocols, with three repeats of at least 1 h of recording membrane conductance, with 50 mV applied across it. Additionally, control experiments with only the surfactant added into the chamber at the same concentration were performed multiple times. Representative trace, as shown in Figure 7.9b, indicates that no surfactant-induced conductance changes were observed. Even if oPOE facilitated formation of the pores, these were not detected by measuring the transmembrane current.

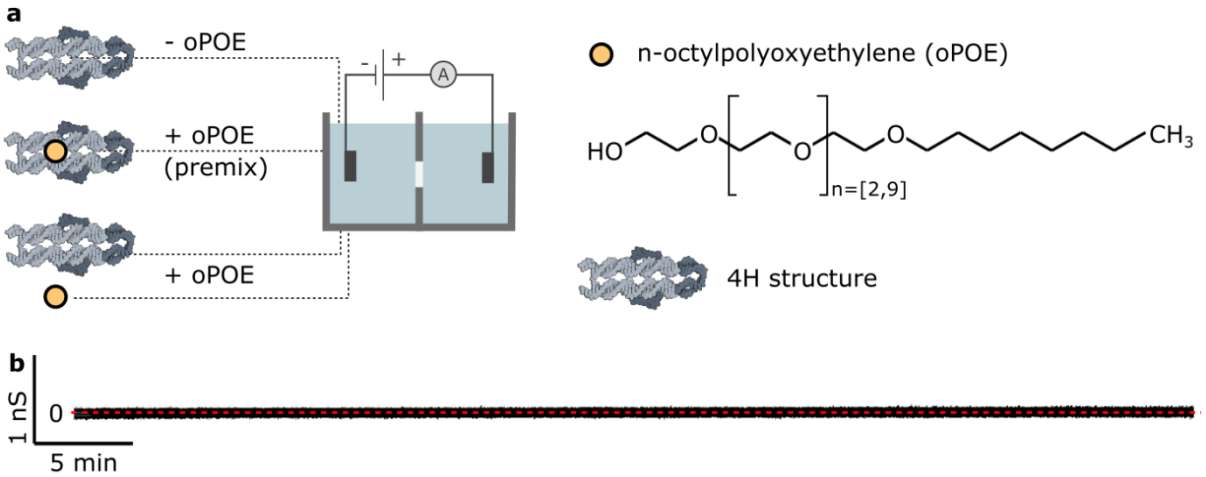

Figure 7.9 *Studying the surfactant's effects on DNA insertion via transmembrane current measurements. (a) Schematic illustration of the three oPOE mixing protocols: no oPOE added (-oPOE), oPOE premixed with the DNA before adding the mixture to the chamber (+oPOE (premix)), oPOE added separately to the chamber, after addition of DNA (+oPOE). The legend features the molecular structure of the surfactant. (b) Representative current trace obtained after addition of only oPOE into the chamber. Such control experiment was performed 10 times, recording for at least 30 minutes. No surfactant-induced changes in the membrane conductance were observed.*

The differences in the insertion of 2C construct depending on the surfactant addition are readily visible when analysing the obtained results by eye - representative traces are presented in Figure 7.10a. In the absence of a surfactant nearly no signal is detected. Faint spikes in membrane conductance ≈ 0.1 nS suggest a lack of insertion, as with the structure's diameter we expect pores of c > 0.5 nS. Nevertheless, the membrane is being affected, if even slightly, by the structure's attempts to span it.

Addition of the oPOE facilitates insertion in both protocols. However, while after premixing DNA with the surfactant the membrane conductance quickly reaches a *plateau*, when oPOE is added separately the increase is prominent and continues throughout the experiment.

The analysis of the traces with a "single channel search" script provided by the Clampfit software extracted all conductance steps which I attribute to the recorded insertion events. Histograms in Figure 7.10b show the distribution of the obtained conductance changes for runs with added surfactant. While the premixed sample features a narrow distribution of conductance changes, the traces after the separate addition of DNA and surfactant consist of diverse steps. However, the initial 35 minutes of +oPOE runs strongly resemble the distribution obtained for the "premixed" experiments. After 35 minutes the structures produced almost solely larger steps. I hypothesize that the stable increase in the step size is caused by cooperation of the inserting DNA constructs: initial insertions destabilize the membrane to a degree that facilitates consecutive insertions. Multiple insertions occurring simultaneously in the latter part of the recording are interpreted as larger conductance steps. Alternatively, proceeding insertions destabilize the membrane to a larger degree by binding with other structures already present in the membrane and, as such multimers, they disrupt the bilayer more than separate pores would.

Why the "premixed" 2C structures never insert more than up to the *plateau* value? One of the explanations would be the formation of DNA aggregates effectively reducing the structures' concentration. Consequently, only the remaining "free" constructs inserted which was facilitated by the surfactant destabilizing the membrane. In a surfactant-free environment we speculate to find more available DNA structures, but with no detergent their insertion is less favourable. Note, that these experiments are performed below the oPOE cmc (0.15%), so we do not expect micelle formation and subsequent merging with the bilayer. Nevertheless, premixing with the surfactant hindered its facilitating effect as compared with the separate addition.

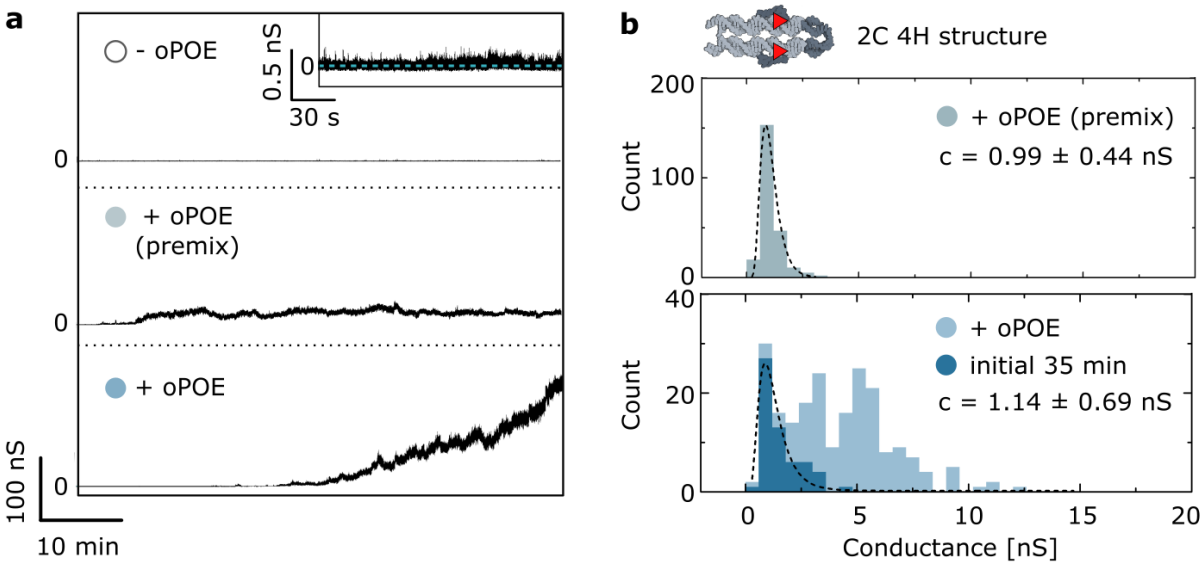

Figure 7.10 *Effects of oPOE addition on the transmembrane signal produced by 2C 4H structure. (a) Representative conductance traces recorded for 2C construct in the absence of oPOE, and after either its premixing with DNA or separate addition into the chamber. (b) Histograms of steps detected via single channel search (Clampfit) for traces obtained after the oPOE addition. Initial 35 minutes of the run with oPOE added separately has been highlighted and fitted with a lognormal distribution. Peak values of the fit are stated on each plot.*

The analogous experiments were performed for 4C constructs, as shown in Figure 7.11a, with significantly different results. Firstly, even in the absence of the surfactant, DNA pores span the membrane, increasing its conductance. Secondly, no clear facilitation of the insertion was caused by the surfactant in 4C case. Even though the traces recorded for premixed sample are noticeably noisier and the obtained conductance steps are higher, the overall effect on the membrane is not as clear as the one observed for 2C.

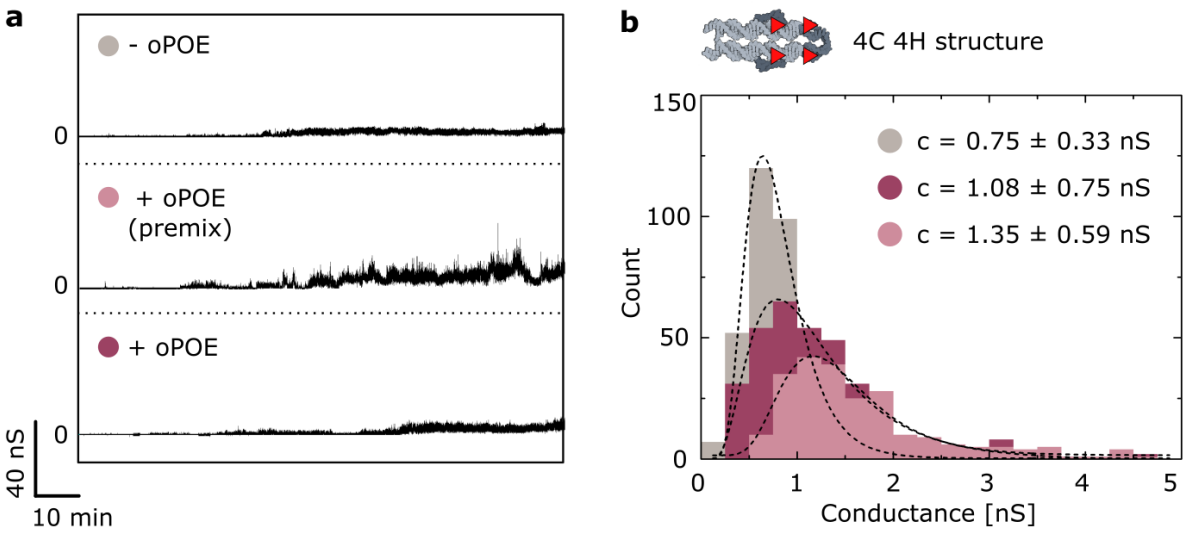

Figure 7.11 *Effects of oPOE addition on the transmembrane signal produced by 4C 4H structure. (a) Representative conductance traces recorded for 4C construct in the absence of oPOE, and after either its premixing with DNA or separate addition into the chamber. (b) Histograms of steps detected via single channel search (Clampfit) for the obtained traces. Peaks of the lognormal fits are stated on the plot.*

Histograms in Figure 7.11b indicate that in the absence of the surfactant conductance change is significantly smaller than when the oPOE is present ($c_{(-oPOE)} = 0.75$ nS, as compared with $c_{(+oPOE)} > 1$ nS). This suggests that surfactant molecules are surrounding the pore-forming DNA: either as a rim of a toroidal pore or as the structure's coat. In any case, their arrangement at the DNA-lipid interface results in an increased pore conductance, which in turn indicates that it plays a role in pore formation.

Importantly, in the absence of a surfactant 4C structure shows a significantly stronger effect on the membrane conductance than 2C (see analogous current traces (-oPOE) in Figure 7.10a and Figure 7.11a). With more cholesterols, it exhibits a stronger insertion-driving force and consequently spans the membrane, even though 2C 4H is not observed to form pores unaided. However, the fact that 4C never reaches the insertion efficiency displayed by 2C after the addition of oPOE suggests that the membrane-spanning is a complex process, influenced by multiple factors.

Here, I speculate that structures' aggregation is one of the dominant aspects influencing the insertion efficiency. While 2C exists in a solution in a monomeric state, 4C aggregates spontaneously into large clusters (the effects of which were visualized by confocal microscopy

imaging presented in Figure 7.8). Separate addition of oPOE to 2C structures resulted in a very high insertion efficiency, while in neither case did surfactant facilitate it to the same extend for 4C. The way in which surfactants modulate the interactions of cholesterol-modified DNA with bilayers is dependent on the design; the effect that the surfactant has on the structure's membrane insertion depends strongly on its mode of clustering.

7.5 DNA-induced fluctuations in the conductance traces.

Let us look closer into the recorded changes in membrane conductance, for example at a double insertion step and subsequent closure of the pores, observed for 2C 4H and presented in Figure 7.12a. One of the prominent features is a sudden increase in the noise of the trace upon insertion. I attribute it to the structure's fluctuations and continuous changes in its conformation within the membrane, resulting in constantly changing flow of ions.

Interestingly, this behaviour looks different in the further part of the trace, highlighted in Figure 7.12b. While the "regular" part of the trace fluctuates within the higher conductance level, the changes observed in the highlighted part are between the step level and (nearly) the baseline. In a way, the trace suggests numerous opening-closure events, with many "steps" of a certain duration. These rapid changes were recorded for both 2C and 4C constructs and both in the absence and presence of oPOE. Their analysis in a form of conductance vs dwell time scatter plots is presented in Figure 7.12c. While no difference is observed between the structures, the absence of oPOE results in smaller conductance levels, as discussed above. The duration of steps seems to be affected as well, as samples with the surfactant tend to produce longer events. In the absence of the surfactant there are less fluctuations in the traces, and therefore the detected events are narrowly distributed, in contrast to the samples containing oPOE, as in histograms in Figure 7.12d.

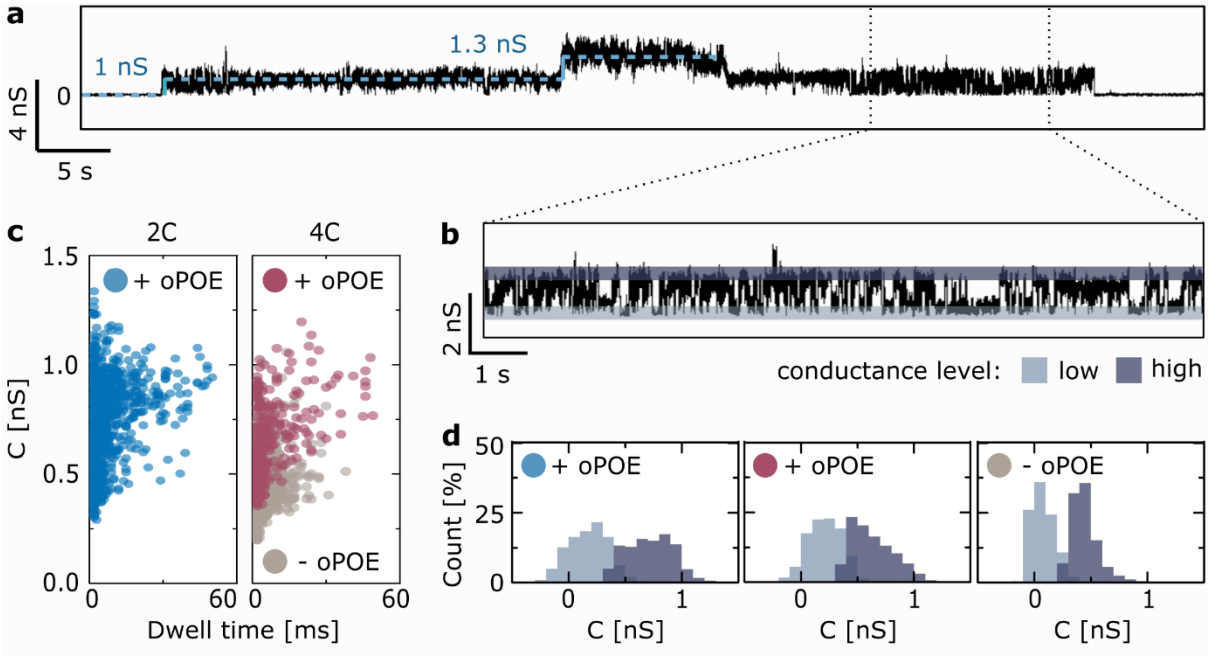

Figure 7.12 *Rapid changes in the conductance level of an inserted DNA channel. (a) Conductance trace of a 2C 4H structure, featuring two insertions and a period of rapid conductance changes ("gating"). (b) Extracted part of the trace in (a) highlighting the rapid switching between the two conductance levels: low and high. (c) Scatter plots of level vs dwell time of the changes during rapid switching, observed for both structures: 2C and 4C. (d) Histograms of conductance levels (low and high, as marked in (b)) recorded during switching.*

This rapid switching between a conductive and a non-conductive state has been reported previously for DNA structures[128,272]. Importantly, it is a recurring phenomenon observed and analysed for natural ion channels[283,284]. It is interpreted as responsive **gating** of proteins. However, DNA structures are not equipped with any mechanism that would result in such controllable behaviour. This suggests that the phenomenon observed here, as well as the similar effect reported for natural ion channels, result from a non-specific process. It may be related to lipid movements in the pore or fluctuations of the membrane-embedded biological material. Nevertheless, this phenomenon shows that not only synthetic DNA nanostructures mimic proteins, but also that processes observed for natural transmembrane molecules can be better understood through DNA models.

7.6 Conclusions

Below its cmc, surfactant addition resulted in a significant increase of insertion efficiency of 2C, which in the solution existed in a monomeric state. This indicates that oPOE inserts into the bilayer and facilitates formation of a toroidal pore, as below cmc it could not mediate insertion in a form

of micelles. As strong curvatures release the strain that surfactant insertion causes, its presence resulted in a favourable membrane-spanning of DNA nanostructures.

While assessing effects of surfactant addition on DNA insertion efficiency, I have realized the importance of another factor: aggregation. Since cholesterol provides a driving force for the insertion, I observed that the structure with more hydrophobic modifications (4C) was more successful in membrane spanning than the one with less cholesterols (2C) *in the absence of the surfactant*. However, when aided by oPOE, the less-clustering 2C was far more efficient in increasing membrane's conductance than ever observed for 4C. The effects of the surfactant on the insertion of the latter are minimal, which indicates that surfactant addition (below cmc) does not disrupt the aggregates. In turn, the results suggest that oPOE disorders the membrane, facilitating insertion of pre-existing DNA monomers.

Studies presented here indicate that the presence of a surfactant has an influence on DNA membrane activity, yet many details still remain unclear. Particularly, further experiments are required in order to fully describe the interactions between cholesterol-modified DNA and a surfactant, below and above its cmc. Additionally, this chapter showed that cholesterol-mediated clusters are an important aspect of membrane-spanning synthetic constructs. This notion also needs more thorough analysis, especially with respect to competing cholesterol-cholesterol and cholesterol-lipids affinities. A deeper understanding of processes occurring at a molecular level can be provided by simulations, which too is a next step worth taking.

The work presented in this chapter differs from three previous studies, in that here I have added a new molecule into the DNA-cholesterol-lipid triangle: the oPOE surfactant. As it interacts with both lipids and cholesterol modifications on the DNA, its effects become intertwined in the network of forces in the studied system. And despite an empirical assessment of the most efficient combination of surfactant addition and DNA structure (shielded 2C with oPOE added separately), an additional component makes the system too convoluted to paint a clear image of molecular mechanisms behind the observations. Comprehensive explanation of how surfactants aid insertion and interact with cholesterol modifications on DNA is yet to be discovered.

This last thought makes an appropriate transition to the following, last chapter of this thesis: the one that presents how many questions and studies are still awaiting in the endeavour of disentangling DNA-lipid interactions.

CHAPTER 8

Conclusions and outlook

Nucleic acid (NA) interactions with lipids are widely studied with respect to biological systems featuring unmodified nucleic acids. Contact between DNA and membranes is reported to play a role in the replication of the genetic material in cell cycles[285]. Cell transformation relies on facilitating DNA transport through the cellular membranes[44,232,233]. Biomedicine benefits from gene therapy platforms[230,231] reliant on NA-lipid formulations, while engineering NA-lipid complexes has become central in vaccine technologies[234,235].

Here, I was mostly examining interactions between hydrophobically-modified DNA and lipid bilayers. And while the results of studying DNA nanostructures in the presence of lipids can be beneficial for natural systems, they are mostly built to advance the field of bionanotechnology. Researchers aim at building sensors and measuring devices working *in vivo*[286,287], mimic remodelling proteins[121,131], induce bilayer fusion[133,134], etc., all from the membrane's surface. Finally, there is the goal of forming structures inserting into the membranes[100,102,106], which is the main subject of this work. Here, I distinguish two approaches to achieve membrane insertion of a nucleic acid:

1) Forcing: overcoming repulsion of a DNA backbone by pulling it in with strong hydrophobic anchors, e.g. cholesterols.

2) Facilitating: limiting repulsion of a DNA backbone by modifying it to reduce its charge/hydrophilicity in a membrane-spanning domain.

In this chapter I will discuss these two strategies. The work presented in this thesis focuses on cholesterol-modified DNA nanostructures, therefore, I will first summarize my findings and share some thoughts on the possible development of the "forcing" strategy. In the second part, I will elaborate on the "facilitating" approach, which involves modifying the backbone of a nucleic acid, while preserving its ability to fold at the nanoscale. Finally, I will introduce some ideas and phenomena from which DNA-based membrane structures can benefit, whatever their insertion-driving mechanisms is.

8.1. Forcing insertion with a hydrophobic anchor: summary of findings

Chapters 4-7 presented four separate case studies of different aspects of the "triangle of interactions" in the DNA-cholesterol-lipid system. The findings from these chapters are briefly described below, with next steps discussed for each. A graphical summary of the work is presented in Figure 8.1.

Chapter 4: Upon membrane insertion DNA induces a toroidal pore, with strongly curved lipid layer facing towards it. Lipids and ions can freely move on the interface of such pore. Modifying the membrane-spanning domain with an internal hydrophobic moiety influences this arrangement and can lead to the formation of a cylindrical pore, devoid of a curvature. This chapter also showed that two C12 modifications were not enough to ensure attachment of a 48 bp DNA duplex.

Next steps: By introducing a *tuneable* hydrophobicity of the membrane-spanning domain, one can harness the formation of a toroidal pore, while exhibiting control over the flow of ions and the lipid transport between leaflets. The pore formation should also be examined in various lipid mixtures, particularly asymmetric bilayers, as found in cells[26]. Since some lipids favour curvature of the membrane[288], their addition can make the formation of a toroid easier. Finally, the lack of attachment induced by (strongly hydrophobic) C12 moiety gives rise to a question: what hydrophobicity per nucleotide needs to be assured to achieve membrane affinity? This can be answered by testing attachment efficiency of different hydrophobic anchors and anchor-to-nucleotides ratios of the design.

Chapter 5: When a hydrophobic modification is linked to the terminal end of a single strand (e.g. anchor positioned in the nick) the adjacent base pairs can be broken to facilitate cholesterol embedment in the bilayer. This can result in the geometry of the structure deviating from the design. By reducing the number of nicks, the construct has less degrees of freedom, and it is easier to control and stabilize it.

Next steps: I hypothesize that the effect of internal linkage of hydrophobic modifications will be even more pronounced for complex structures, particularly the ones that can carry more anchors. By eliminating nicks from the larger designs, a new level of stability may be achieved. It will also hint on the reasons behind improved insertion efficiency of non-nicked constructs. The latter can also be studied further *via* molecular dynamics simulations, which will shed more light on the

details of the insertion. Additionally, assessing the role of the bilayer quality in insertion efficiency is one of the crucial next steps that should be undertaken.

Chapter 6: Divalent cations can lead to bridging of unmodified DNA to zwitterionic lipids, which for the duplex depends on the lipid phase. Cations are also responsible for screening the negative charge on DNA (and presumably phosphates on PC lipids as well) and are indispensable in cholesterol-driven insertion. The cation dependency varies with charge-to-hydrophobicity ratio of the DNA structure.

Next steps: As I am only reporting studies done on one type of DNA structures: relatively short duplexes, analogous experiments performed with various constructs are required to fully understand the relevant electrostatic phenomena. Of particular interest is how mechanical properties of DNA influence bridging, which can be examined with a library of structures: ssDNA, dsDNA shorter and longer than their persistence length, DNA origami platforms of various stiffness. On a similar note, deconvoluting the effects of lipid-facing surface area (number of nucleotides in contact with the membrane) and the overall size of the structures (total number of nucleotides) will provide important information for the future membrane-bound designs.

Utilizing how ion dependency varies with the nucleotides-to-hydrophobicity ratio, DNA nanostructures can be designed with respect to the targeted changes in ionic strength in cellular fluids. By further exploring different affinity of cations towards DNA, one can achieve ion selectivity in bridging and screening processes, which are particularly important for biological media. Finally, the effects of charged lipids on the DNA membrane attachment should be studied, especially in the view of variations in lipid compositions of prokaryotic and eukaryotic cell membranes.

Chapter 7: An addition of a surfactant below its cmc results in a significant improvement of insertion efficiency of 4-helix structures that existed in a solution as monomers (2C). Strongly clustered constructs (4C) were not affected by the surfactant as noticeably. Anchor-mediated aggregation is one of the major limiting factors for the insertion, but with a low number of anchors the structure's insertion needs to be aided (for example by a surfactant).

Next steps: One of the points that should be studied in detail is a comprehensive analysis of cholesterol aggregation *vs* cholesterol membrane insertion. Knowing which clusters are not disassembled spontaneously in the presence of a bilayer will help realize the balance between the number of hydrophobic anchors and the degree of aggregation.

Furthermore, molecular details of surfactant interactions with hydrophobically-modified DNA are yet to be uncovered. Of particular importance is the formation of surfactant-based micelles with incorporated DNA nanostructures, in order to test if the surfactant can chaperone membrane insertion when premixed (above its cmc) with DNA constructs, as in the case of transmembrane protein protocols.

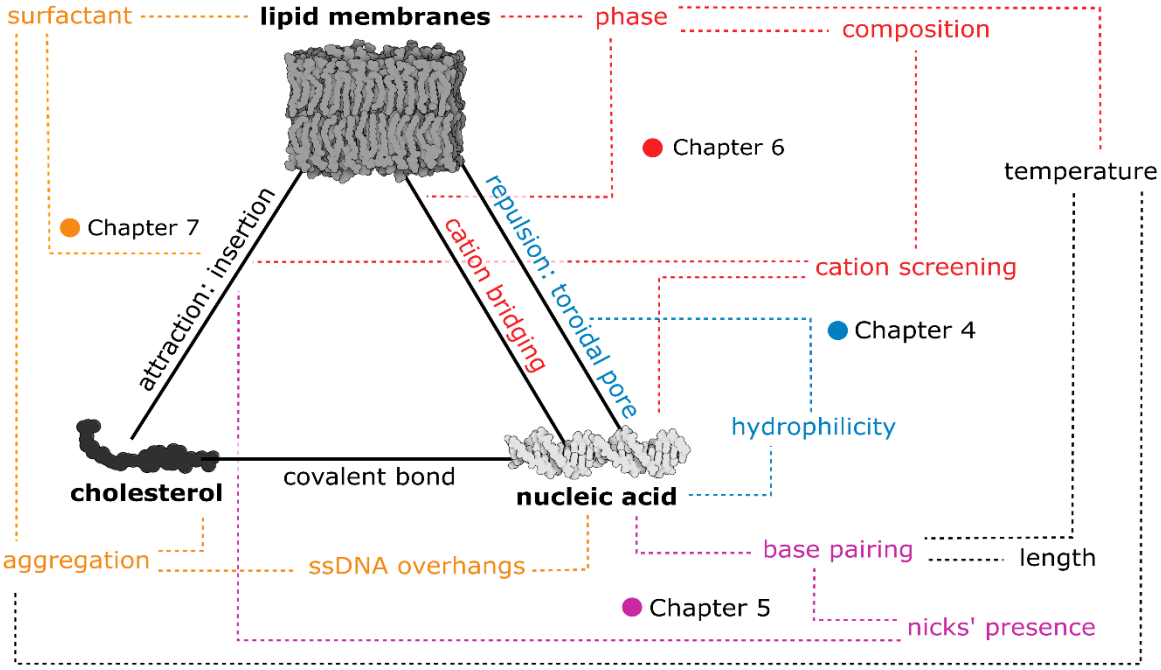

Figure 8.1 *Summary of this thesis based on the "triangle of interactions" introduced in Chapter 2. Continuous lines represent direct interactions between the three components, dashed lines show connections with their properties, relevant phenomena, and factors influencing them.*

8.2. Facilitating insertion with a modified backbone

While exploring the "triangle of interactions" it is readily visible that membrane spanning by DNA is not favourable due to its backbone charge. Even though strong hydrophobic anchors can cause membrane insertion, the continuous strain in the system makes it a non-ideal solution. In fact, while I consider hydrophobic modifications crucial for achieving efficient, spontaneous membrane insertion, I also argue that spanning bilayers with a strongly charged material has little potential for being applied in biomedicine, at least in a non-cytotoxic role. This is why I believe that the next

generation of transmembrane DNA nanostructures will feature a non-charged domain, following integral proteins' architecture.

In fact, in the field of DNA-based membrane–spanning constructs this approach has already been used to build a protein-mimicking ion channel. There, a 6-helix bundle (inspired by the six domains of many transmembrane proteins[289]) had a hydrophobic belt of an S-ethyl phosphorothioate backbone[107], a chemical modification that "caps" the negative charge of a phosphate with a neutral functional group. Other modifications (examples of which are sketched in Figure 8.2) either follow the same principle, like methylphosphonate, or substitute the phosphate altogether with another chemical linkage[290–292].

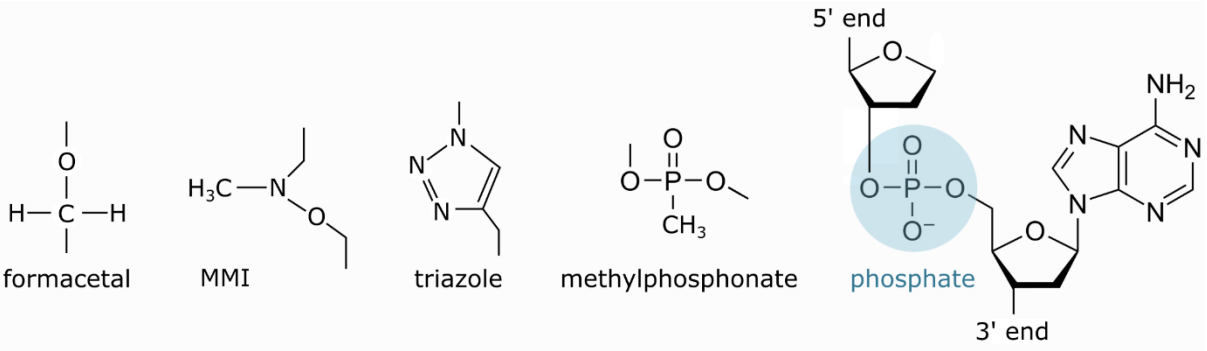

Figure 8.2 *Neutral backbone modifications, in substitution for negatively charged phosphate (highlighted in blue) forming a naturally-occurring DNA nucleotide*[290–292].

Note, that *none* of these modifications introduce a very strong hydrophobicity to the structure. If we use logP values (Chemicalize, ChemAxon) as a hydrophobicity parameter, while for cholesterol we observe strong affinity towards hydrophobic bilayer's core (logP= 7.11), most of the backbone modifications are neutral, rather than lipophilic (e.g. triazole logP = -0.1, ethyl phosphorothioate logP = 0.61). Since with dodecane modifications (logP = 2.33) I have observed no membrane attachment, I speculate that the hydrophobicity of the majority of the backbone modifications is not sufficient to ensure bilayer affinity of the DNA structure.

This thought leads to an important realization: spontaneous membrane insertion and the stability ensured by the hydrophobicity of the membrane-spanning domain are two different aspects of the design. Despite (presumably) not driving attachment in a manner observed for anchors like cholesterol, the modified backbone can still facilitate insertion. Note, that even protocols introducing natural transmembrane proteins into membranes utilize surfactants to mediate insertion[273,293].

Modifications of nucleic acids can be more extensive than substitution of the phosphate group. NA nanotechnology emerged to harness the ability to fold and reshape nucleic acid structures at the nanoscale, which is primarily ensured by the complementarity of base pairs. Therefore, synthetic nucleic acids with an entirely changed backbones but carrying designed sequences of nucleobases have also been proposed as an alternative building material.

These, so-called xeno nucleic acids (XNA) retain the ability to fold *via* the complementarity rule, but feature various modified backbones[294]. The two types of XNA that I find especially significant for DNA nanotechnology applications are: locked nucleic acids (LNA) and peptide nucleic acid (PNA). Both can be folded into a helix, as well as form double-strands with DNA or RNA oligonucleotides using Watson-Crick base pairing. Molecular structures of the two XNA, alongside a DNA nucleotide, are presented in Figure 8.3.

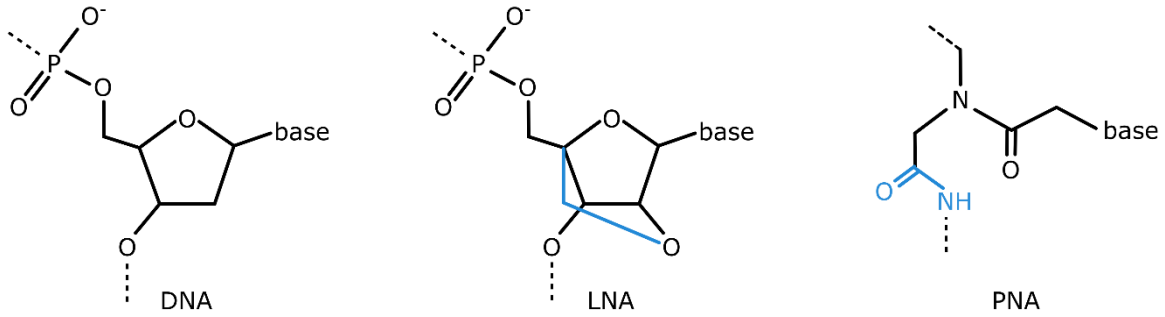

Figure 8.3 *Molecular structures of nucleotides of deoxyribonucleic acid (DNA), locked nucleic acid (LNA) and peptide nucleic acid (PNA). Additional bridge "locking" 2'O with 4'C in LNA, as well as the peptide bond in PNA have been highlighted in blue.*

LNA has the molecular structure of RNA but carries an additional chemical bridge "locking" 2' oxygen and 4' carbon, hence "locked" in the name. The phosphodiester bond, together with its negative charge, is still present in this nucleic acid's structure, therefore the modification is not facilitating membrane interactions. However, LNA has other properties that make it a promising building material for biological applications - also for building synthetic cell membrane components. Introduction of LNA into a DNA oligonucleotide results in increased affinity between the complementary strands and increases the melting temperature by several degrees[295]. Except for the general stability improvement, which helps when the structure needs to be forced into a membrane as described above, this also implicates that designed constructs can be *smaller* – less complementary nucleotides is required to ensure proper folding. For structures that can achieve their functionality with a minimalistic architecture, but are being expanded to ensure their

stability, an addition of LNA monomers can stabilize a smaller design and effectively decrease the number of negatively-charged phosphates that it carries. What is more, LNA-containing oligonucleotides exhibit nuclease resistance[295,296], which answers one of the issues faced by DNA bionanotechnology – biological stability.

In contrast, PNA deviates significantly from the molecular structure of natural nucleic acids. Unlike DNA, it does not feature a sugar, nor does it carry a phosphate bond. Its backbone is formed with N-(2-aminoethyl)-glycine units linked with peptide bonds (C(O)-NH). While having the same advantages as LNA: higher stability, stronger affinity towards complementary bases and nuclease resistance, it is also considered hydrophobic[297–299]. Lack of a negative charge in the backbone results in stronger PNA-PNA (or PNA-DNA) binding, additionally making it less dependent on the ionic composition of the solution mediating electrostatic interactions. Combining the chemistry of PNA and DNA in a rational design can lead to a perfectly balanced synthetic transmembrane construct: with DNA ensuring solubility in aqueous solutions as well as exhibiting its control over membrane transport *via* (switchable) formation of a toroidal pore, while PNA provides hydrophobicity and stability required for firm embedment of a pore-forming structure into the membrane, and nuclease-resistance for operating in biological media.

8.3. Further development of nucleic acid-based membrane structures

The family of nucleic acids is rich in variations and mechanisms that could be utilized to create a more complex relationship between molecules, ensuring better control over cellular activity, and to more accurately mimic the functionalities of membrane proteins. In fact, varying each of the structural components of a NA monomer can unlock a range of possibilities for further development of the synthetic structures.

As NA nanotechnology is still a relatively young field (40 years at the time of writing[300]), there are many features that have not been widely explored. As already mentioned in the previous chapters, the twist of a double helix is a potential parameter that could be used in the next generation of NA-based membrane devices. Tuneable unwinding of a double strand would give researchers another level of control over the structure's architecture. One potential step leading towards it is utilizing transitions between various forms of NA. The transition between right-handed B-DNA and left-handed Z-DNA has already been explored for building nanomechanical devices[75,76] and can be used for designing membrane proteins with active modulations of their molecular structure.

The transition between right-handed B-DNA and A-DNA was shown to be sequence specific[210] and reversible[79]. Additionally, it is observed to occur locally, affecting only a fragment of a long dsDNA[79]. The resulting change along the main axis (0.8 Å per base pair[210,301]) could be utilized to tune the distance between modifications in a precise manner, providing an additional feature on top of the DNA folding at the nanoscale.

Apart from varying the backbone, as described in the subchapter above, the complementarity-driving part of the double strand - base pairing - can also be utilized to ensure additional features of the nanostructure. Except for the best-recognized Watson-Crick base pairs, other complementarity mechanisms can lead to the formation of non-canonical bonds between oligonucleotides. The most prominent example are Hoogsteen base pairs formed between dsDNA and a complementary ssDNA, stabilizing a triple helix structure[302–304]. Such pairs are observed in the secondary structures of G-rich nucleic acids: G-quadruplexes, which have been reported to form *in vivo*, terminating human chromosomes in telomeric DNA[305]. Importantly, however, Hoogsteen bases formation depends strongly on pH in the solution[303,304], which means that this mechanism can be utilized to achieve pH responsiveness of the active DNA construct.

Deviation from the canonical (Watson-Crick) base pairing is also a reason why RNA nanotechnology can provide unique building blocks for nanoscale architectures. Despite similar chemistry, RNA folding exhibits more flexibility than DNA[306], with numerous possible loops and secondary motifs available in the RNA nanoengineer's toolkit[307,308]. These unique non-canonical properties of RNA reflect on its biological role: while in cells DNA mostly forms a linear double-stranded genetic material, RNA structure has many variations utilizing its secondary structures, allowing it to participate in signalling pathways and even exhibit enzymatic properties[306,309–311]. Despite DNA still dominating NA nanotechnology, RNA constructs are also emerging, including junctions[308,312], cubes[313] and RNA origami structures[314].

8.4. Concluding remarks

The vastness of possibilities in NA design makes it a promising avenue for building biological molecular machines. However, since NA nanostructures carry so much functionality, it is easy to plunge into developing their design in isolation, rather than studying them in the context of the targeted environment. The latter strategy is especially important for biological media, where complex dependencies between molecules exist on top of the complexity of synthetic structures.

Therefore, one of the important next steps, with respect to all of the projects I undertaken and described here, is to study analogous phenomena in cellular membranes and biological fluids.

The idea of contextual design of synthetic biostructures is a direct implication of protein-inspired building. Exploring solutions that nature chose in creating membrane constructs is a strategy that I consider most effective. On the other hand, I would like to briefly mention the "gating" phenomenon, described in Chapter 7, from which we can learn about natural ion channels. As an observation reported for membrane-spanning DNA, it suggests that this process does not result from complex "gating" mechanisms carried by specialized channels. Research can benefit not only from mimicking relevant natural proteins but also from a reversed approach: studying nature *through* the DNA models.

While the numerous possible pathways to explore in the field of NA nanotechnology are tempting, I would like to finish this work by once more quoting Gall's law: *A complex system that works is invariably found to have evolved from a simple system that worked.*[315] With the goal of building a structure utilizing various possible mechanisms and performing in a complex way, I advocate for starting this scientific endeavour with a simple network of interacting molecules. Understanding minimalistic nucleic acid structures builds a solid foundation under their comprehensive expansion, with many possibilities yet to be explored.

APPENDIX

A1. Simulations methods

All the simulations presented in this thesis were performed by Himanshu Joshi, PhD, as a result of collaboration with Aleksei Aksimentiev's group from University of Illinois. Below is a description of methods that were used, as reported by H. Joshi.

A1.1. Membrane-spanning DNA in Chapters 4 and 5.

All MD simulations were performed using NAMD2[316]. The all-atom models of the DNA duplexes, having the same sequences as used in experiments, were created using the NAB module of AMBERTOOLs[317]. One cholesterol molecule was covalently conjugated to each strand of dsDNA molecule using a triethylene glycol (TEG) linker, as described previously[102]. The force-field parameters of the cholesterol molecule with the linker were obtained from the CHARMM General Force Field (CGenFF) webserver[318]. To obtain the non-nicked variant of 8 nm design (*8 nm-0x*, Chapter 5), we created a custom patch using psfgen plugin of VMD[319] to make the DNA backbone continuous at the position of the cholesterol conjugation.

The dodecane spacers were introduced by replacing the four nucleotides with a dodecane molecule, as specified in Table A4.1. Two initial configurations of the 2D structure were constructed, differing by the conformation of the spacers: contracted and stretched (Figure A4.5). The initial configuration proved to have an effect on the water permeation and lipid flipping, resulting from the differences in pore formation (Figure A4.6).

Membrane-spanning DNA constructs were inserted into a pre-equilibrated patch of either 1,2-diphytanoyl-sn-glycero-3-phosphatidylethanolamine (DPhPE, Chapter 4) or 1,2-diphytanoyl-sn-glycero-3-phosphatidylcholine (DPhPC, Chapter 5) lipid bilayer, placing both cholesterol anchors within the volume occupied by the lipid membrane. All lipid molecules located within 3 Å of the DNA were removed. Mg^{2+}- hexahydrates were added near the backbone of the DNA to neutralize its negative charge, as described previously[101]. The resulting system was solvated with TIP3P water molecules[320] using the Solvate plugin of VMD[319]. Sodium and chloride ions were added to produce either a 100 mM (Chapter 4) or 500 mM (Chapter 5) solution using the Autoionize plugin of VMD.

A few additional Mg^{2+}– hexahydrates and chloride ions were added to result in the 4 mM bulk concentration of $MgCl_2$. Thus assembled systems measured 13 x 23 x 13 nm^3 and contained approximately 346,000 atoms.

The assembled systems were subjected to energy minimization using the conjugate gradient method to remove the steric clashes between the solute and solvent. Following that, we equilibrated the lipid molecules around the DNA for either 50 ns (Chapter 4) or 20 ns (Chapter 5), while harmonically restraining all the non-hydrogen atoms of DNA using a spring constant of 1 kcal/mol/$A^{\circ 2}$. Subsequently, we removed the harmonic restraints and performed 50 ns equilibration while maintaining the hydrogen bonds between the complimentary base-pairs of DNA using the extrabond utility of NAMD. Finally, we removed all the restraints and performed 1 μs long production simulations of systems using a constant number of atoms (N), pressure (P = 1 bar) and temperature (T = 298 K), the NPT ensemble.

All the MD simulation were performed using periodic boundary conditions and particle mesh Ewald (PME) method to calculate the long range electrostatic interactions[321]. The Nose-Hoover Langevin piston[322] and Langevin thermostat were used to maintain the constant pressure and temperature in the system. CHARMM36 force field parameters[323] described the bonded and non-bonded interactions between DNA, lipid bilayer, water and ions. An 8-10-12 Å cutoff scheme was used to calculate van der Waals and short range electrostatic forces. All simulations were performed using a 2 fs time step to integrate the equation of motion. SETTLE algorithm[324] was applied to keep water molecules rigid, whereas RATTLE algorithm[325] constrained all other covalent bonds involving hydrogen atoms. The coordinates of the system were saved at an interval of either 19.2 ps (Chapter 4) or 20 ps (Chapter 5). The analysis and post processing of the simulation trajectories were performed using VMD[319] and CPPTRAJ[317] and an online Fortran program Illustrator was used to visualize the structures[326].

In Chapter 5, using the SEM method[327], we computed the ionic current for the last 800 ns of the simulation trajectory.

A1.2. Magnesium affinity towards gel and liquid phase bilayers in Chapter 6.

All MD simulations were performed using program NAMD2[316], a 2 fs integration time step, 2-2-6 multiple time stepping, periodic boundary conditions, and particle mesh Ewald (PME) method over a 1 Å resolution grid to calculate the long-range electrostatic interaction[328]. The Nose-Hoover

Langevin piston[322] and Langevin thermostat were used to maintain the constant pressure and temperature in the system. An 8-10-12 Å cutoff scheme was used to calculate van der Waals and short-range electrostatic forces. SETTLE algorithm[324] was applied to keep water molecules rigid whereas RATTLE algorithm[325] constrained all other covalent bonds involving hydrogen atoms. CHARMM36 force field parameters described the bonded and non-bonded interactions among the atoms of lipid[329], water and ions[330]. Magnesium ions were modeled as magnesium hexahydrates ($Mg[H_2O]_6^{2+}$)[255]. The coordinates of the system were saved every 20 ps. The visualisation, analysis, and post-processing the simulation trajectories were performed using VMD[319] and CPPTRAJ[317].

The initial configuration of the 1,2-dipalmitoyl-sn-glycero-3-phosphoethanolamine (DPPE) lipid bilayer membrane containing 64 lipids in each leaflet was generated from the CHARMM-GUI membrane builder[331]. A pre-equilibrated patch of 1,2-diphytanoyl-sn-glycero-3-phosphoethanolamine (DPhPE) containing 64 lipids in each leaflet was obtained from a previous study[102]. Both membranes were solvated with TIP3P water molecules[320]. Magnesium hexahydrade and chloride ions were placed randomly in the solvent at 300 mM concentration. Fully assembled DPPE and DPhPE membrane systems contained 30,410 and 48,288 atoms, respectively. Each system was first subject to energy minimisation using the conjugate gradient method, which removed steric clashes between the solute and the solvent. The systems were then equilibrated without any restraints for several hundreds of nanosecond in a constant number of atoms (N), pressure (P = 1 bar) and temperature (T = 300 K) ensemble. Anisotropic pressure coupling was used to maintain the constant ratio of the system's dimension within the membrane, allowing the system's dimension normal to the membrane to adjust independently of the other dimensions. Following that, $Mg[H_2O]_6^{2+}$ ions located approximately 30 Å away from the center of the membrane were removed, producing two systems of approximately 100 mM $MgCl_2$ concentration. Each system was then in equilibration for additional 0.5 μs. Figure A6.4 presents snapshots of the simulated membranes, alongside results of their analysis.

To obtain the PMF of an $Mg[H_2O]_6^{2+}$ ion along the direction normal to the lipid bilayer (z-axis), we performed replica-exchange umbrella sampling simulations[332] using the colvar module[333] of NAMD. Starting from the state attained at the end of each 0.5 μs equilibration, a short (3 ns) steered molecular dynamics (SMD) simulation was performed to move one $Mg[H_2O]_6^{2+}$ ion along the z-axis from 40 Å to 10 Å, as measured from the center of the lipid bilayer. Each SMD trajectory was used to create 31 copies of each membrane system differing by the z-coordinate of the $Mg[H_2O]_6^{2+}$, one system for each 1 Å sampling window along the z-axis. Each replica was

simulated for 50 ns having the z-coordinate of the Mg atom restrained to the center of the sampling window with the spring constant of 2.5 kcal/mol/Å^2. During the simulation, the replicas were allowed to exchange the biasing potential between the neighbouring windows with a probability given by the Metropolis algorithm. Finally, we used WHAM[334] to subtract the contribution from the confining harmonic potential and extract the PMF of the $Mg[H_2O]_6^{2+}$ ion along the axis normal to the lipid bilayer membrane. To assess the affinity of $Mg[H_2O]_6^{2+}$ at minimal ionic concentration, we repeated the PMF calculations using a set of simulation systems containing a single $Mg[H_2O]_6^{2+}$ ion. The initial configuration of the 31 replicas (varying in the coordinate of the ion along the z-axis from 40 to 10 Å) were obtained by removing all $Mg[H_2O]_6^{2+}$ and chloride ions except one $Mg[H_2O]_6^{2+}$ and two chloride ions from the respective 100 mM of $MgCl_2$ replica systems. Each replica was simulated for approximately 67 ns while restraining the z-coordinate of the $Mg[H_2O]_6^{2+}$ ion with respect to the center of the membrane using a force constant of 2.5 kcal/mol/Å^2. The first 5 ns of the simulation was excluded, and WHAM was used to compute the PMF profile from the later part of the simulation trajectories.

A2. Differential Scanning Calorimetry

All the simulations presented in this thesis were performed by Roger Rubio-Sánchez, as a result of collaboration with Lorenzo Di Michele's group from University of Cambridge. Below is a description of methods that were used, as reported by R. Rubio-Sánchez.

Differential Scanning Calorimetry (DSC) was performed on DPPC lipid vesicles using standard aluminum DSC pans in a PerkinElmer DSC 4000 instrument. Samples were heated from 20 °C to 60 °C at 1 °C/min, equilibrated at 60 °C for two minutes, and then cooled down to 20 °C at the same rate. Throughout the ramp, heat flow (mW) was recorded for vesicles in both the presence and absence of dsDNA and Mg^{2+} ions (Figure A6.2).

A3. Figures

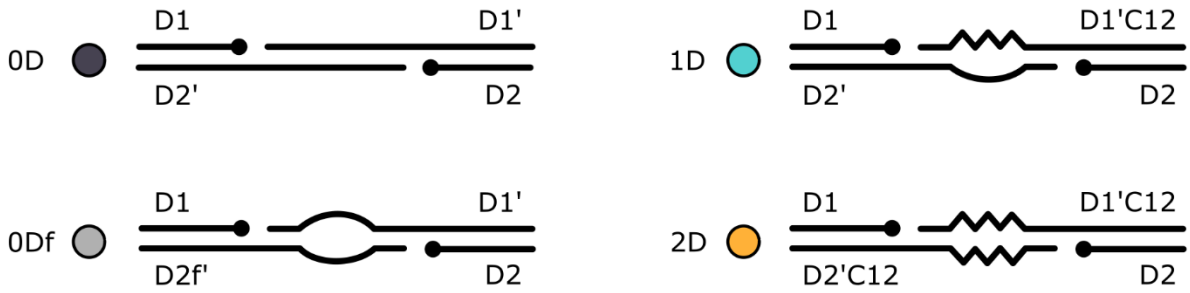

Figure A4.1 *Schematic illustration of the DNA designs featured in Chapter 4. Black circles represent cholesterol modifications. Presented structures are modified with two cholesterols each (2C), while alternative, control structures with one (1C) or no (0C) cholesterols were also used. The sequences of oligonucleotides can be found in Table A4.1.*

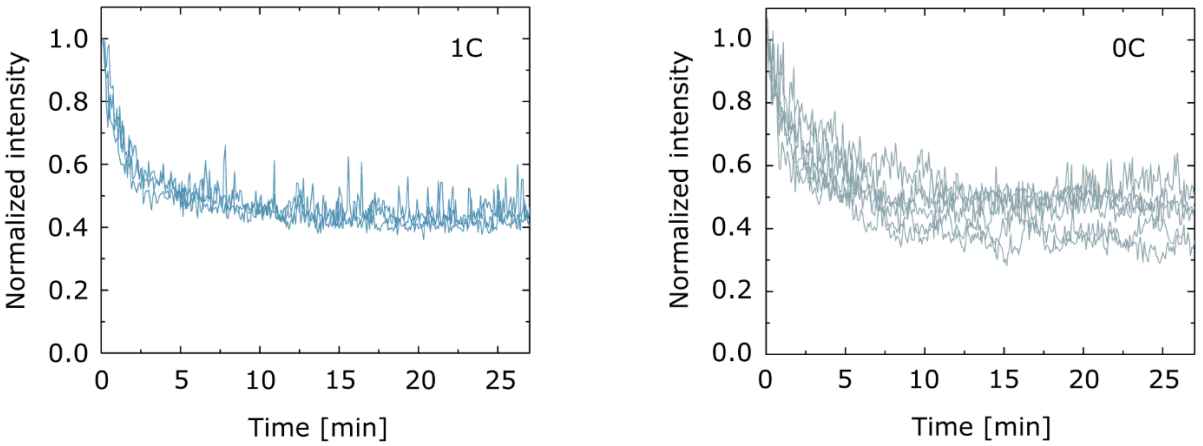

Figure A4.2 *Representative traces of fluorescence decay of control structures (0C and 1C), averaged for the traces from Fig. 4.6b. The data on each plot were collected from at least two separate experiments*

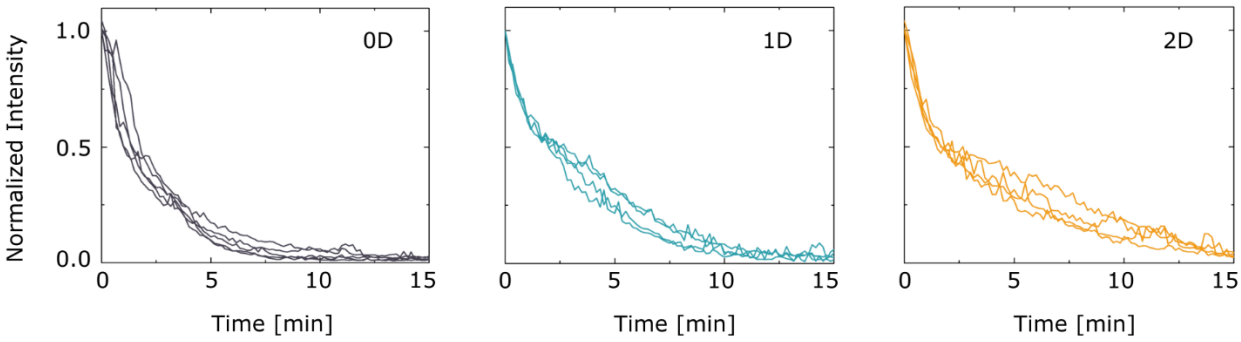

Figure A4.3 *Representative traces of fluorescence decay, averaged for the traces from Fig. 4.7a; single vesicles' fluorescence decay from the + Mg experiments, with dithionite final concentration = 9 mM. The data on each plot were collected from at least two separate experiments.*

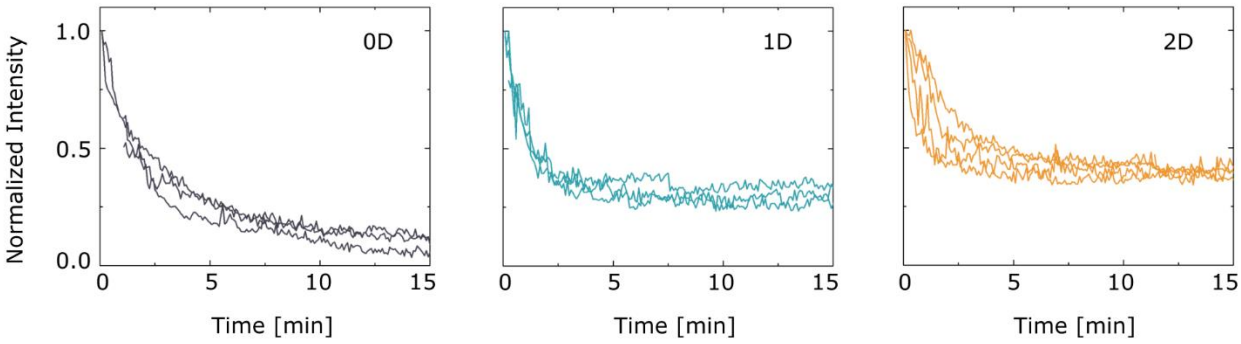

Figure A4.4 *Representative traces of fluorescence decay, averaged for the traces from Fig. 4.7c. The data on each plot were collected from at least two separate experiments.*

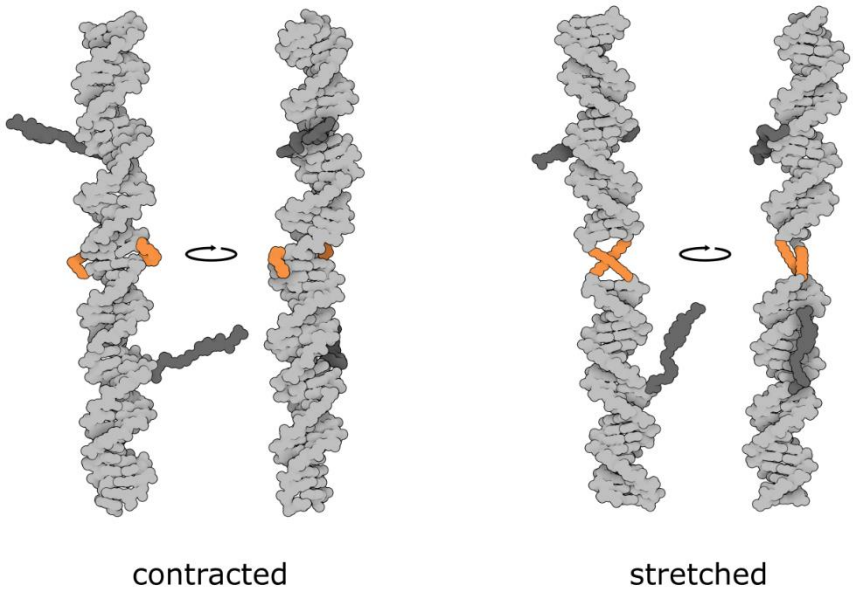

Figure A4.5 *Snapshots from the simulations of the 2D structure (Chapter 4) in its initial configuration either (a) contracted or (b) stretched.*

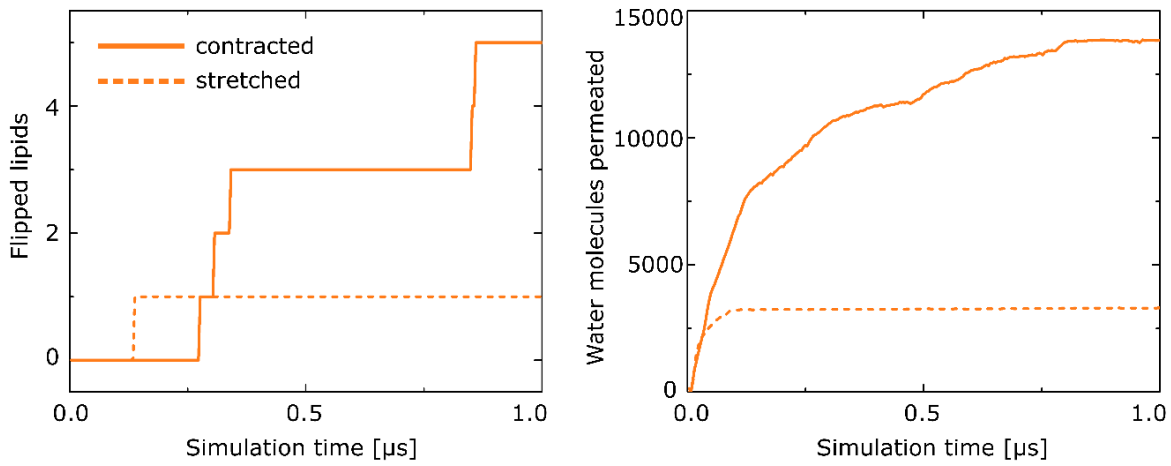

Figure A4.6 *Comparison between 2D structure simulated in the membrane in two different initial conformations: contracted and stretched (as shown in Figure A4.5). Contracted conformation of C12 chains is preferred in the solution, while they extend in the hydrophobic core of a bilayer.*

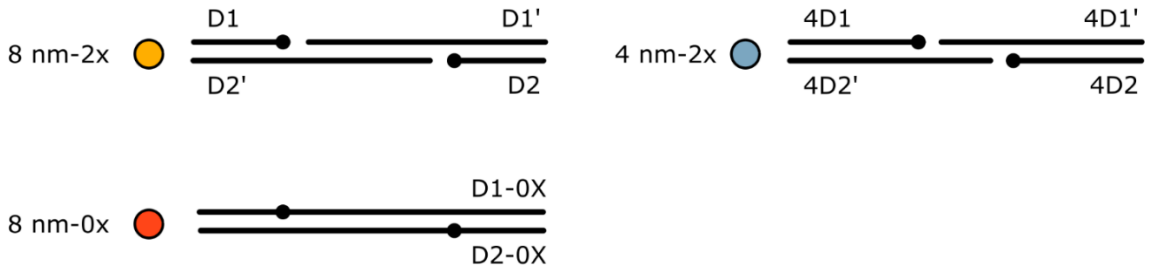

Figure A5.1 *Schematic illustration of the DNA designs featured in Chapter 5. Black circles represent cholesterol modifications. Presented structures are modified with two cholesterols each (2C), while alternative, control structures with one (1C) or no (0C) cholesterols were also used. The sequences of oligonucleotides can be found in Table A5.1.*

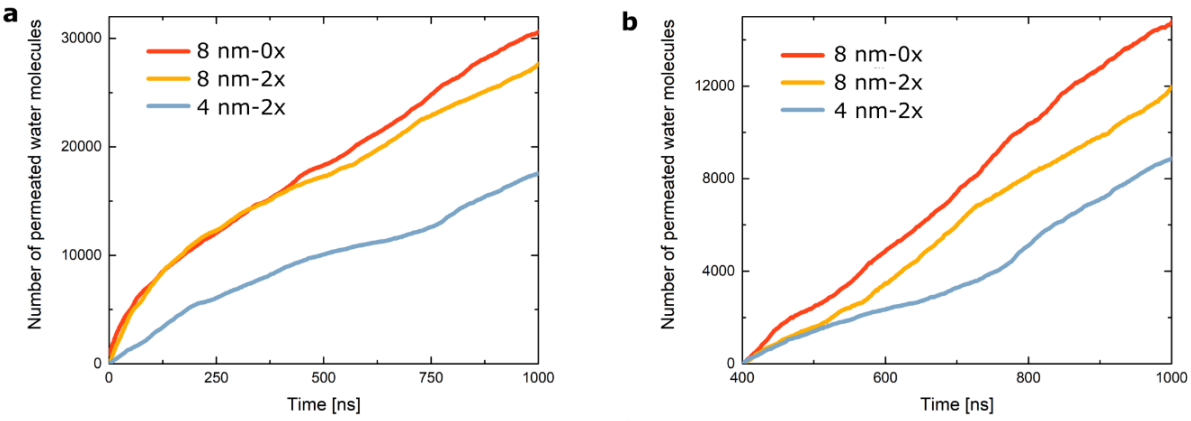

Figure A5.2 *Number of permeated water molecules observed via simulations in the systems considered in Chapter 5: throughout the whole simulation (a), and normalized change after first 400 ns (b).*

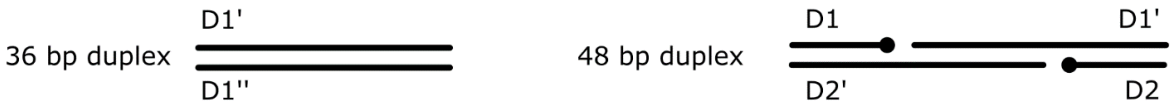

Figure A6.1 *Schematic illustration of the DNA designs featured in Chapter 5. Black circles represent cholesterol modifications. Presented structures are modified with two cholesterols each (2C), while alternative, control structures with one (1C) or no (0C) cholesterols were also used. The sequences of oligonucleotides can be found in Table A6.1.*

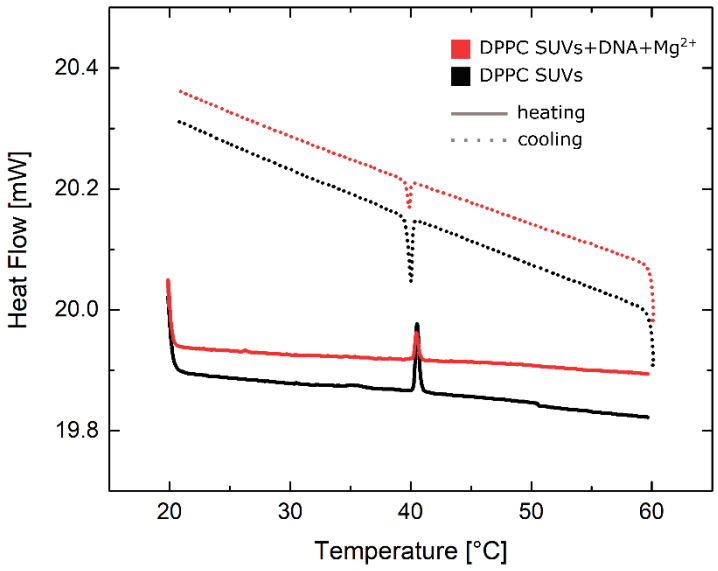

Figure A6.2 *Differential scanning calorimetry (DSC) measurements confirming DPPC phase transition temperature (41 °C [244]). Experiments were performed with LUVs in solution without added salt, as well as in the presence of Mg^{2+} and DNA, as for the experiments on DNA-membrane attachment in Chapter 6, Fig 6.4d.*

Figure A6.3 *Co-localization of DNA nanostructures and NBD-PC in de-mixed 15% cholesterol/DPPC vesicles. Representative micrographs, alongside average intensity values of the two phases (liquid ordered and gel) stated in arbitrary units, illustrate the lateral partitioning of NBD-PC lipids. The co-localization of the fluorescent signals from the DNA and NBD suggests that they both tag the gel-phased domains of the membrane. Scale bar represents 5 µm.*

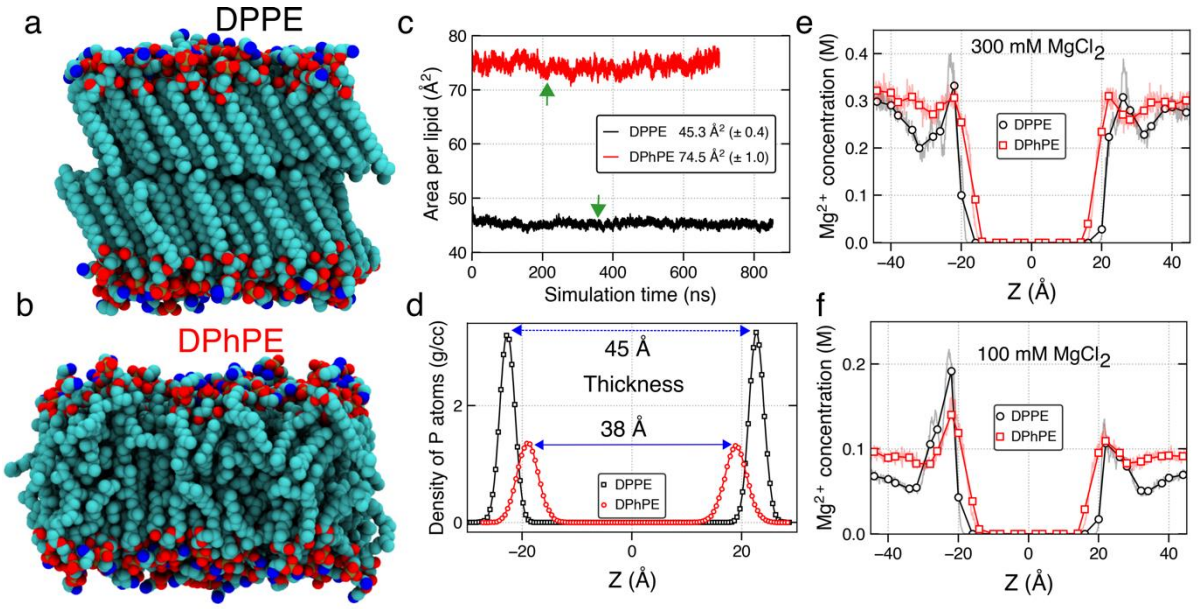

Figure A6.4 *Free-equilibration simulation of fluid and gel-phase PE membranes. Representative conformation of the (a) gel-phase (DPPE) (b) fluid-phase (DPhPE) lipid bilayer membranes containing 64 lipid molecules in each leaflet. The non-hydrogen atoms of the lipid bilayer membrane are shown as blue (N), tan (P), red (O), and cyan (C) spheres. (b) The area per head group of the DPhPE and DPPE membranes simulated first in 300 mM (up to the green arrow) and later in 100 mM solution of $MgCl_2$. (c) Local density of the P atoms of the lipid headgroups along the bilayer normal averaged over the last 0.5 µs of the equilibrium MD simulations. Local concentration of Mg^{2+} ions along the lipid bilayer normal averaged over the respective MD trajectory (excluding the first 50 ns) for the simulations performed at (d) 300 mM and (f) 100 mM concentration of $MgCl_2$. Symbols show local concentration data averaged in 3 Å bins, faded lines show 0.1 Å bin data.*

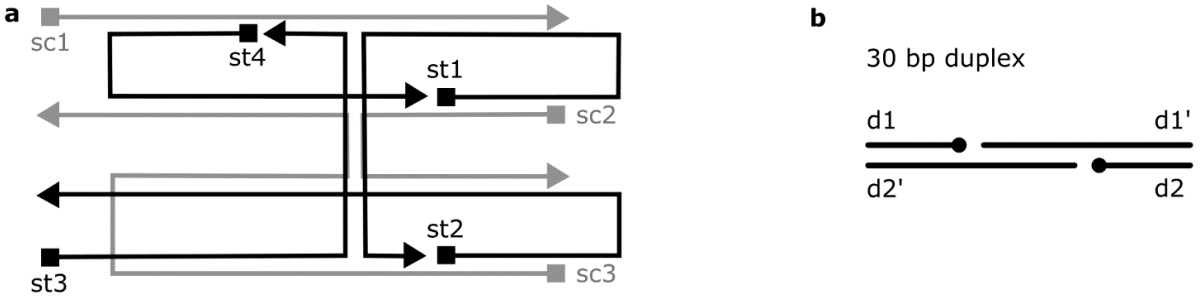

Figure A7.1 *Schematic illustration of the structures used in experiments described in Chapter 7. (a) 4-helix bundle (4H) DNA design, following caDNAno convention (square 5', triangle 3'). Strands forming double helices were grouped into "sc" and "st" for convenience. The sequences of oligonucleotides are presented in Table A7.1. (b) 30 bp-long DNA duplex. The sequences of oligonucleotides are presented in Table A7.2.*

A4. Tables

Table A4.1 *Sequences of DNA strands forming structures featured in Chapter 4. Illustration of the designs can be found in Figure A4.1. "Modif." stands for "Modification". • represents the position of cholesterol.*

Strand	*Sequence (5' > 3')*	*Length [nt]*	*Modif.*
D1	AGTAGTATCCAT●	12	3' chol
D1'	CATCGTAGCTAAAAAAGTCATACATAGATTAGAGAG	36	5' Cy3
D1'C12	CATCGTAGCT(C12)AAGTCATACATAGATTAGAGAG	32	internal C12
D2	CTCTCTAATCTA●	12	3' chol
D2f'	TGTATGACTTAAAAAGCTACGATGATGGATACTACT	36	
D2'	TGTATGACTTTTTTAGCTACGATGATGGATACTACT	36	
D2'C12	TGTATGACTT(C12)AGCTACGATGATGGATACTACT	32	internal C12

Table A4.2 *Parameters obtained by fitting double exponential equation to averaged traces of NBD bleaching, featured in Chapter 4.*

$[Mg^{2+}]$ const?	*$[S_2O_4^{2-}]$ [mM]*	Construct	I_0	*τ_1 [min]*	*λ_1 [min^{-1}]*	*τ_2 [min]*	*λ_2 [min^{-1}]*
+	4.5	0C	0.450 ± 0.001	3.01 ± 0.07	0.33 ± 0.02	-	-
+	4.5	1C	0.458 ± 0.001	3.13 ± 0.06	0.32 ± 0.01	-	-
+	4.5	2C 0D	0.005 ± 0.001	0.94 ± 0.03	1.06 ± 0.03	3.63 ± 0.04	0.28 ± 0.00
+	4.5	2C 1D	0.025 ± 0.004	0.68 ± 0.08	1.47 ± 0.17	4.19 ± 0.19	0.24 ± 0.01
+	4.5	2C 2D	- 0.076 ± 0.008	2.31 ± 0.10	0.43 ± 0.02	9.04 ± 0.30	0.11 ± 0.00
+	9	1C	0.456 ± 0.005	3.31 ± 0.16	0.30 ± 0.01	-	-
+	9	2C 0D	0.012 ± 0.007	1.63 ± 0.29	0.61 ± 0.11	3.89 ± 1.37	0.25 ± 0.01
+	9	2C 1D	-0.014 ± 0.006	0.29 ± 0.06	3.45 ± 0.71	4.66 ± 0.15	0.21 ± 0.01
+	9	2C 2D	-0.164 ± 0.03	0.72 ± 0.05	1.39 ± 0.10	11.66 ± 1.01	0.09 ± 0.01
-	4.5	2C 0D	0.076 ± 0.003	0.91 ± 0.04	1.10 ± 0.05	5.03 ± 0.17	0.20 ± 0.01
-	4.5	2C 1D	0.296 ± 0.003	0.89 ± 0.06	1.12 ± 0.08	3.84 ± 1.39	0.26 ± 0.09
-	4.5	2C 2D	0.388 ± 0.003	1.00 ± 0.06	1.00 ± 0.06	4.92 ± 0.84	0.20 ± 0.03

Table A4.3 *Melting temperatures of DNA constructs, presented in Chapter 4, Fig. 4.8a.*

Construct	T_m *[°C] (4 mM* Mg^{2+}*)*	T_m *[°C] (1 mM* Mg^{2+}*)*	ΔT_m *[°C]*
0D	60.47 ± 1.20	61.87 ± 1.01	1.40 ± 1.57
0Df	52.99 ± 1.07	50.78 ± 1.07	2.21 ± 1.51
1D	50.31 ± 2.15	43.82 ± 1.45	6.49 ± 2.59
2D	51.16 ± 1.79	44.69 ± 1.12	6.47 ± 2.11

Table A4.4 *Relative band intensities of structures folded in 1 mM* Mg^{2+}*, normalized to the respective 20 mM* Mg^{2+} *band, obtained from two independent experiments.*

Construct	*Normalized intensity (I)*	*ΔI*
0D	0.991	0.053
0Df	0.968	0.012
1D	0.483	0.064
2D	0.578	0.096

Table A5.1 *Sequences of DNA strands forming structures featured in Chapter 5. Illustration of the designs can be found in Figure A5.1. "Modif." stands for "Modification", "int." for "internal". • represents the position of cholesterol.*

Structure	*Strand*	*Sequence (5' > 3')*	*Length [nt]*	*Modif.*
4 nm-2x	D1	AGTAGTATCCATCATCGT●	18	3' chol
	D1'	AGCTTTTTAAGTCATACATAGATTAGAGAG	30	5' Cy3
	D2	CTCTCTAATCTATGTATG●	18	3' chol
	D2'	ACTTAAAAAGCTACGATGATGGATACTACT	30	
8 nm-2x	4D1	AGTAGTATCCAT●	12	3' chol
	4D1'	CATCGTAGCTTTTTAAGTCATACATAGATTAGAGAG	36	5' Cy3
	4D2	CTCTCTAATCTA●	12	3' chol
	4D2'	TGTATGACTTAAAAAGCTACGATGATGGATACTACT	36	
8 nm-0x	D1-0X	AGTAGTATCCAT●CATCGTAGCTTTTTAAGTCATACATAGATTAGAGAG	48	int. chol (5' Cy3)
	D2-0X	CTCTCTAATCTA●TGTATGACTTAAAAAGCTACGATGATGGATACTACT	48	int. chol

Table A6.1 *Sequences of DNA strands forming structures featured in Chapter 6. Illustration of the designs can be found in Figure A6.1. "Modif." stands for "Modification". • represents the position of cholesterol.*

Strand	*Sequence (5' > 3')*	*Length [nt]*	*Modif.*
D1	AGTAGTATCCAT●	12	3' chol, 5' Cy3
D1'	CATCGTAGCTAAAAAAGTCATACATAGATTAGAGAG	36	5' Cy3
D1''	CTCTCTAATCTATGTATGACTTTTTTAGCTACGATG	36	
D2	CTCTCTAATCTA●	12	3' chol
D2'	TGTATGACTTTTTTAGCTACGATGATGGATACTACT	36	

Table A6.2 *Zeta (ξ) potential values presented in the Chapter 6, Fig. 6.8. Standard deviation is from three measurements.*

Lipid species	*Conditions*	*Zeta (ξ) potential [mV]*		*Standard deviation [mV]*	
		20 °C	*60 °C*	*20 °C*	*60 °C*
DPPC	no added salt	-12.20	-10.44	0.22	0.49
	1 mM Mg^{2+}	-0.54	-8.99	0.11	0.99
	1 mM Mg^{2+} + 10 nM DNA	-2.73	-7.07	0.16	0.73
POPC	no added salt	-18.07	-16.5	1.45	1.64
	1 mM Mg^{2+}	-1.21	-1.63	0.38	0.88
	1 mM Mg^{2+} + 10 nM DNA	-2.20	-3.18	0.84	0.52

Table A6.3 *Peaks of Gaussian distribution fitted to histograms from Fig. 6.14a, used in the plot in Fig. 6.14b. Error bars represent full width at half maximum (FWHM) of the fitted peaks. All normalized to the value obtained for 2C at 4 mM Mg^{2+}.*

Mg^{2+} concentration	*Peak of the fluorescence distribution (normalized)*		
	2C	*1C*	*ss1*
0	-	-	-
0.2	0.21 ± 0.08	-	0.76 ± 0.08
0.5	0.62 ± 0.14	0.17 ± 0.07	0.85± 0.14
1	0.87 ± 0.08	0.60 ± 0.11	0.94 ± 0.08
2	0.94 ± 0.15	0.76 ± 0.09	0.96 ± 0.15
4	1.00 ± 0.18	1.00 ± 0.10	0.98 ± 0.17

Table A6.4 *Parameters obtained by fitting a Hill equation to the data for DNA-GUV affinity as a function of magnesium concentration, shown in Fig. 3b.*

Strand	*nt*	*nt:chol*	*n*	*K [mM]*	*K_d [mM]*
ss1C	12	12	0.72 ± 0.20	0.048 ± 0.014	0.112 ± 0.081
2C	96	48	1.99 ± 0.11	0.389 ± 0.012	0.153 ± 0.002
1C	96	96	2.26 ± 0.65	0.920 ± 0.142	0.828 ± 0.044

Table A7.1 *Sequences of DNA strands forming 4-helix (4H) structure, featured in Chapter 7. Illustration of the design can be found in Figure A7.1. "Modif." stands for "Modification". • represents the position of cholesterol. Sequences st1 and st4 are analogous to ssC1 and ssC2 from Figure 3.6, respectively.*

Strand	*Sequence (5' > 3')*	*Length [nt]*	*Modif.*
sc1	TTTAGCCTAGTCAGCCGTTAAGTGCCA●	27	3' chol
sc2	AGTCTGACCTGATTGAACGTAG●	22	3' chol
sc3	CGTCTCCATAGCTACTTAGCTACAGATAGGTCCACAACCAGATTACACACTTT	53	
st1	TCAGACTTTTTTTTGGCACTTAACCTAT●	28	3' chol
st2	GGAGACGTTTTTTCTACGTTCAATTTGTGGACCTATCTTT	40	
st3	TTTTGTAGCTAAGTAGGGCTG	21	5' Cy3
st4	ACTAGGCTGTGTGTAATCTGGCAGG●	25	3' chol

Table A7.2 *Sequences of DNA strands forming duplex structure, featured in Chapter 7. Illustration of the design can be found in Figure A7.1b. "Modif." stands for "Modification". • represents the position of cholesterol.*

Strand	*Sequence (5' > 3')*	*Length [nt]*	*Modif.*
d1	ACTCTAATCTATGTA●	15	3' chol
d2	TAGTATCCATCAATC●	15	3' chol
d1'	TCGTTCGGCATACATAGATTAGAGT	25	3' Cy3
d2'	TGCCGAACGAGATTGATGGATACTA	25	

REFERENCES

1. Rosen, E. D. & Spiegelman, B. M. Adipocytes as regulators of energy balance and glucose homeostasis. *Nature* **444**, 847–853 (2006).

2. Brasaemle, D. L. Thematic review series: adipocyte biology. The perilipin family of structural lipid droplet proteins: stabilization of lipid droplets and control of lipolysis. *J. Lipid Res.* **48**, (2007).

3. Berg, J., Tymoczko, J. & Stryer, L. *Biochemistry, 5th edition*. *Biochemistry* (2002).

4. Wang, X. Lipid signaling. *Curr. Opin. Plant Biol.* **7**, 329–336 (2004).

5. Malinauskas, T., Aricescu, A. R., Lu, W., Siebold, C. & Jones, E. Y. Modular mechanism of Wnt signaling inhibition by Wnt inhibitory factor 1. *Nat. Struct. Mol. Biol.* **18**, 886–893 (2011).

6. Dinasarapu, A. R., Saunders, B., Ozerlat, I., Azam, K. & Subramaniam, S. Signaling gateway molecule pages-a data model perspective. *Bioinformatics* **27**, 1736–1738 (2011).

7. Saddoughi, S. A., Song, P. & Ogretmen, B. Roles of bioactive sphingolipids in cancer biology and therapeutics. *Subcell. Biochem.* **49**, 413–440 (2008).

8. Gurr, M. I., Harwood, J. L. & Frayn, K. N. *Lipid Biochemistry*. *Lipid Biochemistry* (Springer US, 2002). doi:10.1002/9780470774366.

9. Bruce Alberts, Alexander Johnson, Julian Lewis, Martin Raff, Keith Roberts, P. W. *Molecular Biology of the Cell, 4th edition*. (Garland Science, 2002).

10. Lodish, H. *et al. Molecular Cell Biology, 4th edition*. (W. H. Freeman, 2000).

11. Rawicz, W., Olbrich, K. C., McIntosh, T., Needham, D. & Evans, E. A. Effect of chain length and unsaturation on elasticity of lipid bilayers. *Biophys. J.* **79**, 328–339 (2000).

12. Yechiel, E. & Edidin, M. Micrometer-scale domains in fibroblast plasma membranes. *J. Cell Biol.* **105**, 755–760 (1987).

13. Laude, A. J. & Prior, I. A. Plasma membrane microdomains: Organization, function and trafficking (Review). *Mol. Membr. Biol.* **21**, 193–205 (2004).

14. Metcalf, T. N., Wang, J. L. & Schindler, M. Lateral diffusion of phospholipids in the plasma membrane of soybean protoplasts: Evidence for membrane lipid domains. *Proc. Natl. Acad. Sci.* **83**, 95–99 (1986).

15. Welti, R., Rintoul, D. A., Goodsaid-Zalduondo, F., Felder, S. & Silbert, D. F. Gel phase phospholipid in the plasma membrane of sterol-depleted mouse LM cells. Analysis by fluorescence polarization and x-ray diffraction. *J. Biol. Chem.* **256**, 7528–7535 (1981).

16. Levental, I., Levental, K. R. & Heberle, F. A. Lipid Rafts: Controversies Resolved, Mysteries Remain. (2020) doi:10.1016/j.tcb.2020.01.009.

17. Levental, I. & Wang, H.-Y. Membrane domains beyond the reach of microscopy 1. *J. Lipid Res.* **61**, 2020 (2020).

18. Sezgin, E., Levental, I., Mayor, S. & Eggeling, C. The mystery of membrane organization: Composition, regulation and roles of lipid rafts. *Nat. Rev. Mol. Cell Biol.* **18**, 361–374 (2017).

19. Heimburg, T. *Thermal Biophysics of Membranes*. (Wiley, 2007).

20. Andersen, S. S. L., Jackson, A. D. & Heimburg, T. Towards a thermodynamic theory of nerve pulse propagation. *Prog. Neurobiol.* **88**, 104–113 (2009).

21. Heimburg, T. & Jackson, A. D. On soliton propagation in biomembranes and nerves. *Proc. Natl. Acad. Sci. U. S. A.* **102**, 9790–9795 (2005).

22. Heimburg, T. & Jackson, A. D. On the action potential as a propagating density pulse and the role of anesthetics. *Biophys. Rev. Lett.* **2**, 57–78 (2006).

23. De Meyer, F. & Smit, B. Effect of cholesterol on the structure of a phospholipid bilayer. *Proc. Natl. Acad. Sci. U. S. A.* **106**, 3654–3658 (2009).

24. McIntosh, T. J. The effect of cholesterol on the structure of phosphatidylcholine bilayers. *BBA - Biomembr.* **513**, 43–58 (1978).

25. Chakraborty, S. *et al.* How cholesterol stiffens unsaturated lipid membranes. *Proc. Natl. Acad. Sci. U. S. A.* **117**, 21896–21905 (2020).

26. Lorent, J. H. *et al.* Plasma membranes are asymmetric in lipid unsaturation, packing and protein shape. *Nat. Chem. Biol.* **16**, 644–652 (2020).

27. Subczynski, W. K., Pasenkiewicz-Gierula, M., Widomska, J., Mainali, L. & Raguz, M. High Cholesterol/Low Cholesterol: Effects in Biological Membranes: A Review. *Cell Biochem. Biophys.* **75**, 369–385 (2017).

28. Saito, H. & Shinoda, W. Cholesterol effect on water permeability through DPPC and PSM lipid bilayers: A molecular dynamics study. *J. Phys. Chem. B* **115**, 15241–15250 (2011).

29. Matsuoka, S. & Murata, M. Cholesterol markedly reduces ion permeability induced by membrane-bound amphotericin B. *Biochim. Biophys. Acta - Biomembr.* **1564**, 429–434 (2002).

30. Dotson, R. J., Smith, C. R., Bueche, K., Angles, G. & Pias, S. C. Influence of Cholesterol on the Oxygen Permeability of Membranes: Insight from Atomistic Simulations. *Biophys. J.* **112**, 2336–2347 (2017).

31. Kooijman, E. E. & Burger, K. N. J. Biophysics and function of phosphatidic acid: A molecular perspective. *Biochim. Biophys. Acta - Mol. Cell Biol. Lipids* **1791**, (2009).

32. Cole, L. K., Vance, J. E. & Vance, D. E. Phosphatidylcholine biosynthesis and lipoprotein metabolism. *Biochim. Biophys. Acta - Mol. Cell Biol. Lipids* **1821**, 754–761 (2012).

33. Suetsugu, S., Kurisu, S. & Takenawa, T. Dynamic shaping of cellular membranes by phospholipids and membrane-deforming proteins. *Physiol. Rev.* **94**, (2014).

34. Di Paolo, G. & De Camilli, P. Phosphoinositides in cell regulation and membrane dynamics. *Nature* **443**, 651–657 (2006).

35. Lentz, B. R. Exposure of platelet membrane phosphatidylserine regulates blood coagulation. *Prog. Lipid Res.* **42**, 423–438 (2003).

36. Leventis, P. A. & Grinstein, S. The Distribution and Function of Phosphatidylserine in Cellular Membranes. *Annu. Rev. Biophys.* **39**, (2010).

37. Vekey, K., Telekes, A. & Vertes, A. *Medical Applications of Mass Spectrometry*. (Elsevier, 2011).

38. Uphoff, A., Hermansson, M., Haimi, P. & Somerharju, P. Analysis of complex lipidomes. in *Medical Applications of Mass Spectrometry* 223–249 (Elsevier, 2008). doi:10.1016/B978-044451980-1.50013-6.

39. King, R. J. & MacBeth, M. C. Interaction of the lipid and protein components of pulmonary surfactant Role of phosphatidylglycerol and calcium. *BBA - Biomembr.* **647**, 159–168 (1981).

40. Tsui, F. C., Ojcius, D. M., Hubbell, W. L. & Stein, J. The intrinsic pKa values for phosphatidylserine and phosphatidylethanolamine in phosphatidylcholine host bilayers. *Biophys. J.* **49**, 459–468 (2009).

41. Moncelli, M. R., Becucci, L. & Guidelli, R. The Intrinsic pKa Values for Phosphatidylcholine, Phosphatidylethanolamine, and Phosphatidylserine in Monolayers Deposited on Mercury Electrodes. *Biophys. J.* **66**, 1969–1980 (1994).

42. Dickey, A. & Faller, R. Examining the contributions of lipid shape and headgroup charge on bilayer behavior. *Biophys. J.* **95**, 2636–2646 (2008).

43. Jacobsohn, M. K., Bazilian, L. S., Hardiman, J. & Jacobsohn, G. M. Effect of pH on the affinity of phospholipids for cholesterol. *Lipids* **24**, 375–382 (1989).

44. Koynova, R. & Tenchov, B. Cationic phospholipids: Structure-transfection activity relationships. *Soft Matter* **5**, 3187–3200 (2009).

45. MacDonald, R. C. *et al.* Physical and biological properties of cationic triesters of phosphatidylcholine. *Biophys. J.* **77**, 2612–2629 (1999).

46. Scherer, P. G. & Seelig, J. Electric Charge Effects on Phospholipid Headgroups. Phosphatidylcholine in Mixtures with Cationic and Anionic Amphiphilest. *Biochemistry* **28**, 7720–7728 (1989).

47. Morini, M. A. *et al.* Influence of temperature, anions and size distribution on the zeta potential of DMPC, DPPC and DMPE lipid vesicles. *Colloids Surfaces B Biointerfaces* **131**, 54–58 (2015).

48. Seelig, J. Deuterium magnetic resonance: Theory and application to lipid membranes. *Q. Rev. Biophys.* **10**, 353–418 (1977).

49. Gupta, A., Korte, T., Herrmann, A. & Wohland, T. Plasma membrane asymmetry of lipid organization: fluorescence lifetime microscopy and correlation spectroscopy analysis. *J. Lipid Res.* **61**, (2020).

50. Fujimoto, T. & Parmryd, I. Interleaflet coupling, pinning, and leaflet asymmetry-major players in plasma membrane nanodomain formation. *Front. Cell Dev. Biol.* **4**, 155 (2017).

51. Cooke, I. R. & Deserno, M. Coupling between lipid shape and membrane curvature. *Biophys. J.* **91**, 487–495 (2006).

52. Alberts, B. *et al. Essential Cell Biology 4th Edition*. (Garland Science, 2014).

53. Inorganic Ions | Types, Summary, Classification & Facts. https://alevelbiology.co.uk/notes/inorganic-ions/.

54. Bhattachar, P. K. & Samnani, P. B. *Metal Ions in Biochemistry* . (CRC Press , 2020).

55. J. Chem. Educ. Staff. Biochemical roles of some essential metal ions. *J. Chem. Educ.* **54**, 761–762 (1977).

56. Ashcroft, F. M. *Ion Channels and Disease*. (Academic Press, 1999).

57. Allen, K. N., Entova, S., Ray, L. C. & Imperiali, B. Monotopic Membrane Proteins Join the Fold. *Trends Biochem. Sci.* **44**, 7–20 (2019).

58. Seaton, B. A. & Roberts, M. F. Peripheral Membrane Proteins. in *Biological Membranes* 355–403 (Birkhäuser Boston, 1996). doi:10.1007/978-1-4684-8580-6_12.

59. Mowrey, D. D. *et al.* Open-channel structures of the human glycine receptor α1 full-length transmembrane domain. *Structure* **21**, 1897–1904 (2013).

60. Ray, L. C. *et al.* Membrane association of monotopic phosphoglycosyl transferase underpins function brief-communication. *Nat. Chem. Biol.* **14**, 528–541 (2018).

61. Ruskamo, S. *et al.* Atomic resolution view into the structure-function relationships of the human myelin peripheral membrane protein P2. *Acta Crystallogr. Sect. D Biol. Crystallogr.* **70**, 165–176 (2014).

62. Mineev, K. S. *et al.* Dimeric Structure of the Transmembrane Domain of Glycophorin A in Lipidic and Detergent Environments. *Acta Naturae* **3**, 2011 (2011).

63. Jaskiewicz, E., Jodłowska, M., Kaczmarek, R. & Zerka, A. Erythrocyte glycophorins as receptors for Plasmodium merozoites. *Parasites and Vectors* **12**, 317 (2019).

64. MacKenzie, K. R., Prestegard, J. H. & Engelman, D. M. Transmembrane helix dimer:

Structure and implications. *Science* **276**, 131–133 (1997).

65. Gokel, G. W. & Negin, S. Synthetic ion channels: From pores to biological applications. *Acc. Chem. Res.* **46**, 2824–2833 (2013).

66. Saenger, W. *Principles of Nucleic Acid Structure.* (Springer New York, 1984). doi:10.1007/978-1-4612-5190-3.

67. Calladine, C. R., Drew, H. R., Luisi, B. F. & Travers, A. A. *Understanding DNA: The Molecule and How it Works: Third Edition*. *Understanding DNA: The Molecule and How it Works: Third Edition* (Elsevier Ltd, 2004). doi:10.1016/B978-0-12-155089-9.X5000-5.

68. Privalov, P. L. & Crane-Robinson, C. Forces maintaining the DNA double helix. *Eur. Biophys. J.* **49**, 315–321 (2020).

69. Vaitiekunas, P., Crane-Robinson, C. & Privalov, P. L. The energetic basis of the DNA double helix: a combined microcalorimetric approach. *Nucleic Acids Res.* **43**, 8577–8589 (2015).

70. Conner, B. N., Yoon, C., Dickerson, J. L. & Dickerson, R. E. Helix geometry and hydration in an A-DNA tetramer: IC-C-G-G. *J. Mol. Biol.* **174**, 663–695 (1984).

71. Drew, H. R. *et al.* Structure of a B-DNA dodecamer: conformation and dynamics. *Proc. Natl. Acad. Sci. U. S. A.* **78**, 2179–2183 (1981).

72. Wang, A. H. J. *et al.* Molecular structure of a left-Handed double helical DNA fragment at atomic resolution. *Nature* **282**, 680–686 (1979).

73. Levitt, M. How many base-pairs per turn does DNA have in solution and in chromatin? Some theoretical calculations (DNA double helix/chromatin structure/energy calculations). **75**, 640–644 (1978).

74. Ussery, D. W. DNA Structure: A-, B- and Z-DNA Helix Families. in *Encyclopedia of Life Sciences* (John Wiley & Sons, Ltd, 2002). doi:10.1038/npg.els.0003122.

75. Mao, C., Sun, W., Shen, Z. & Seeman, N. C. A nanomechanical device based on the B-Z transition of DNA. *Nature* **397**, 144–146 (1999).

76. Bhanjadeo, M. M., Nayak, A. K. & Subudhi, U. Cerium chloride stimulated controlled conversion of B-to-Z DNA in self-assembled nanostructures. *Biochem. Biophys. Res.*

Commun. **482**, 916–921 (2017).

77. Vargason, J. M., Henderson, K. & Ho, P. S. A crystallographic map of the transition from B-DNA to A-DNA. *Proc. Natl. Acad. Sci. U. S. A.* **98**, 7265–7270 (2001).

78. Kannan, S., Kohlhoff, K. & Zacharias, M. B-DNA under stress: Over- and untwisting of DNA during molecular dynamics simulations. *Biophys. J.* **91**, 2956–2965 (2006).

79. Kulkarni, M. & Mukherjee, A. Understanding B-DNA to A-DNA transition in the right-handed DNA helix: Perspective from a local to global transition. *Prog. Biophys. Mol. Biol.* **128**, 63–73 (2017).

80. Gopaul, D. N., Guo, F. & Van Duyne, G. D. Structure of the Holliday junction intermediate in Cre-loxP site-specific recombination. *EMBO J.* **17**, 4175–4187 (1998).

81. Song, L. *et al.* Structure of staphylococcal α-hemolysin, a heptameric transmembrane pore. *Science* **274**, 1859–1866 (1996).

82. Wang, X. & Seeman, N. C. Assembly and characterization of 8-arm and 12-arm DNA branched junctions. *J. Am. Chem. Soc.* **129**, 8169–8176 (2007).

83. Wang, Y., Mueller, J. E., Kemper, B. & Seeman, N. C. Assembly and Characterization of Five-Arm and Six-Arm DNA Branched Junctions. *Biochemistry* **30**, 5667–5674 (1991).

84. Ma, R. I., Kallenbach, N. R., Sheardy, R. D., Petrillo, M. L. & Seeman, N. C. Three-arm nucleic acid junctions are flexible. *Nucleic Acids Res.* **14**, 9745–9753 (1986).

85. Wei, B., Dai, M. & Yin, P. Complex shapes self-assembled from single-stranded DNA tiles. *Nature* **485**, 623–626 (2012).

86. Seeman, N. C. Nucleic acid junctions and lattices. *J. Theor. Biol.* **99**, 237–247 (1982).

87. Zhang, Y. & Seeman, N. C. Construction of a DNA-Truncated Octahedron. *J. Am. Chem. Soc.* **116**, 1661–1669 (1994).

88. Brady, R. A., Brooks, N. J., Cicuta, P. & Di Michele, L. Crystallization of Amphiphilic DNA C-Stars. *Nano Lett.* **17**, 3276–3281 (2017).

89. Zheng, J. *et al.* From molecular to macroscopic via the rational design of a self-assembled 3D DNA crystal. *Nature* **461**, 74–77 (2009).

90. Rothemund, P. W. K. Folding DNA to create nanoscale shapes and patterns. *Nature* **440**, 297–302 (2006).

91. Schwiening, C. J. A brief historical perspective: Hodgkin and Huxley. *J. Physiol.* **590**, 2571–2575 (2012).

92. Sakai, N. & Matile, S. Synthetic ion channels. *Langmuir* vol. 29 9031–9040 (2013).

93. Tabushi, I., Kuroda, Y. & Yokota, K. A,B,D,F-tetrasubstituted β-cyclodextrin as artificial channel compound. *Tetrahedron Lett.* **23**, 4601–4604 (1982).

94. Kobuke, Y., Ueda, K. & Sokabe, M. Artificial Non-Peptide Single Ion Channels. *J. Am. Chem. Soc.* **114**, 7618–7622 (1992).

95. Voyer, N. & Robitaille, M. A Novel Functional Artificial Ion Channel. *J. Am. Chem. Soc.* **117**, 6599–6600 (1995).

96. Nakano, A., Xie, Q., Mallen, J. V., Echegoyen, L. & Gokel, G. W. Synthesis of a Membrane-Insertable, Sodium Cation Conducting Channel: Kinetic Analysis by Dynamic 23Na NMR. *J. Am. Chem. Soc.* **112**, 1287–1289 (1990).

97. Fang, A., Kroenlein, K., Riccardi, D. & Smolyanitsky, A. Highly mechanosensitive ion channels from graphene-embedded crown ethers. *Nat. Mater.* **18**, 76–81 (2019).

98. MacKinnon, R. Potassium channels and the atomic basis of selective ion conduction. *Biosci. Rep.* **24**, 75–100 (2004).

99. Langecker, M. *et al.* Synthetic lipid membrane channels formed by designed DNA nanostructures. *Science* **338**, 932–936 (2012).

100. Göpfrich, K. *et al.* Ion channels made from a single membrane-spanning DNA duplex. *Nano Lett.* **16**, 4665–4669 (2016).

101. Göpfrich, K. *et al.* Large-Conductance Transmembrane Porin Made from DNA Origami. *ACS Nano* **10**, 8207–8214 (2016).

102. Ohmann, A. *et al.* A synthetic enzyme built from DNA flips 107 lipids per second in biological membranes. *Nat. Commun.* **9**, (2018).

103. Birkholz, O. *et al.* Multi-functional DNA nanostructures that puncture and remodel lipid

membranes into hybrid materials. *Nat. Commun.* **9**, 1521 (2018).

104. Huo, S., Li, H., Boersma, A. J. & Herrmann, A. DNA Nanotechnology Enters Cell Membranes. *Adv. Sci.* **6**, 1900043 (2019).

105. Krishnan, S. *et al.* Molecular transport through large-diameter DNA nanopores. *Nat. Commun.* **7**, 1–7 (2016).

106. Sobota, D. *et al.* Tailoring Interleaflet Lipid Transfer with a DNA-based Synthetic Enzyme. *Nano Lett.* **20**, 4306–4311 (2020).

107. Burns, J. R., Stulz, E. & Howorka, S. Self-assembled DNA nanopores that span lipid bilayers. *Nano Lett.* **13**, 2351–2356 (2013).

108. Diederichs, T. *et al.* Synthetic protein-conductive membrane nanopores built with DNA. *Nat. Commun.* **10**, (2019).

109. Krishnan, S. *et al.* Molecular transport through large-diameter DNA nanopores. *Nat. Commun.* **7**, 12787 (2016).

110. Lanner, J. T., Georgiou, D. K., Joshi, A. D. & Hamilton, S. L. Ryanodine receptors: structure, expression, molecular details, and function in calcium release. *Cold Spring Harb. Perspect. Biol.* **2**, (2010).

111. Collins, B. E. & Paulson, J. C. Cell surface biology mediated by low affinity multivalent protein-glycan interactions. *Curr. Opin. Chem. Biol.* **8**, 617–625 (2004).

112. Boniface, J. J. *et al.* Initiation of signal transduction through the T cell receptor requires the peptide multivalent engagement of MHC ligands. *Immunity* **9**, 459–466 (1998).

113. Martinez-Veracoechea, F. J. & Frenkel, D. Designing super selectivity in multivalent nano-particle binding. *Proc. Natl. Acad. Sci. U. S. A.* **108**, 10963–10968 (2011).

114. Curk, T., Dobnikar, J. & Frenkel, D. Optimal multivalent targeting of membranes with many distinct receptors. *Proc. Natl. Acad. Sci. U. S. A.* **114**, 7210–7215 (2017).

115. Mammen, M., Choi, S. K. & Whitesides, G. M. Polyvalent interactions in biological systems: Implications for design and use of multivalent ligands and inhibitors. *Angew. Chemie - Int. Ed.* **37**, 2754–2794 (1998).

116. Rinker, S., Ke, Y., Liu, Y., Chhabra, R. & Yan, H. Self-assembled DNA nanostructures for distance-dependent multivalent ligand-protein binding. *Nat. Nanotechnol.* **3**, 418–422 (2008).

117. Li, J. *et al.* Self-assembled multivalent DNA nanostructures for noninvasive intracellular delivery of immunostimulatory CpG oligonucleotides. *ACS Nano* **5**, 8783–8789 (2011).

118. Hawkes, W. *et al.* Probing the nanoscale organisation and multivalency of cell surface receptors: DNA origami nanoarrays for cellular studies with single-molecule control. *Faraday Discuss.* **219**, 203–219 (2019).

119. Kwon, P. S. *et al.* Designer DNA architecture offers precise and multivalent spatial pattern-recognition for viral sensing and inhibition. *Nat. Chem.* **12**, 26–35 (2020).

120. Kretschmer, S., Ganzinger, K. A., Franquelim, H. G. & Schwille, P. Synthetic cell division via membrane-transforming molecular assemblies. *BMC Biol.* **17**, 1–10 (2019).

121. Franquelim, H. G., Khmelinskaia, A., Sobczak, J. P., Dietz, H. & Schwille, P. Membrane sculpting by curved DNA origami scaffolds. *Nat. Commun.* **9**, (2018).

122. Franquelim, H. G., Dietz, H. & Schwille, P. Reversible membrane deformations by straight DNA origami filaments. *Soft Matter* (2020) doi:10.1039/d0sm00150c.

123. Yang, Y. *et al.* Self-assembly of size-controlled liposomes on DNA nanotemplates. *Nat. Chem.* **8**, 476–483 (2016).

124. Dong, Y. *et al.* Cuboid Vesicles Formed by Frame-Guided Assembly on DNA Origami Scaffolds. *Angew. Chemie Int. Ed.* **56**, 1586–1589 (2017).

125. Zhang, Z., Yang, Y., Pincet, F., Llaguno, M. C. & Lin, C. Placing and shaping liposomes with reconfigurable DNA nanocages. *Nat. Chem.* **9**, 653–659 (2017).

126. Czogalla, A. *et al.* Amphipathic DNA Origami Nanoparticles to Scaffold and Deform Lipid Membrane Vesicles. *Angew. Chemie Int. Ed.* **54**, 6501–6505 (2015).

127. Grome, M. W., Zhang, Z., Pincet, F. & Lin, C. Vesicle Tubulation with Self-Assembling DNA Nanosprings. *Angew. Chemie Int. Ed.* **57**, 5330–5334 (2018).

128. Göpfrich, K. *et al.* DNA-tile structures induce ionic currents through lipid membranes. *Nano Lett.* **15**, 3134–3138 (2015).

129. Hussey, S. L. & Peterson, B. R. Efficient delivery of streptavidin to mammalian cells: Clathrin-mediated endocytosis regulated by a synthetic ligand. *J. Am. Chem. Soc.* **124**, 6265–6273 (2002).

130. Journot, C. M. A., Ramakrishna, V., Wallace, M. I. & Turberfield, A. J. Modifying Membrane Morphology and Interactions with DNA Origami Clathrin-Mimic Networks. **17**, 43 (2020).

131. Baumann, K. N. *et al.* Coating and Stabilization of Liposomes by Clathrin-Inspired DNA Self-Assembly. *ACS Nano* **14**, 2316–2323 (2020).

132. Chan, Y. H. M., Van Lengerich, B. & Boxer, S. G. Effects of linker sequences on vesicle fusion mediated by lipid-anchored DNA oligonucleotides. *Proc. Natl. Acad. Sci. U. S. A.* **106**, 979–984 (2009).

133. Stengel, G., Zahn, R. & Höök, F. DNA-induced programmable fusion of phospholipid vesicles. *J. Am. Chem. Soc.* **129**, 9584–9585 (2007).

134. Van Lengerich, B., Rawle, R. J., Bendix, P. M. & Boxer, S. G. Individual vesicle fusion events mediated by lipid-anchored DNA. *Biophys. J.* **105**, 409–419 (2013).

135. Stengel, G., Simonsson, L., Campbell, R. A. & Höök, F. Determinants for membrane fusion induced by cholesterol-modified DNA zippers. *J. Phys. Chem. B* **112**, 8264–8274 (2008).

136. Parolini, L. *et al.* Volume and porosity thermal regulation in lipid mesophases by coupling mobile ligands to soft membranes. *Nat. Commun.* **6**, (2015).

137. Bila, H., Kurisinkal, E. E. & Bastings, M. M. C. Engineering a stable future for DNA-origami as a biomaterial. *Biomater. Sci.* **7**, 532–541 (2019).

138. Kielar, C. *et al.* On the Stability of DNA Origami Nanostructures in Low-Magnesium Buffers. *Angew. Chemie - Int. Ed.* **57**, 9470–9474 (2018).

139. Dong, Y. *et al.* Folding DNA into a Lipid-Conjugated Nanobarrel for Controlled Reconstitution of Membrane Proteins. *Angew. Chemie - Int. Ed.* **57**, 2072–2076 (2018).

140. Potaman, V. N. & Sinden, R. R. DNA: Alternative Conformations and Biology. *Proc. Madame Curie Biosci. [database]* (2005).

141. Douglas, S. M. *et al.* Rapid prototyping of 3D DNA-origami shapes with caDNAno. *Nucleic Acids Res.* **37**, 5001–5006 (2009).

142. Rawicz, W., Olbrich, K. C., McIntosh, T., Needham, D. & Evans, E. A. Effect of chain length and unsaturation on elasticity of lipid bilayers. *Biophys. J.* **79**, 328–339 (2000).

143. Lewis, B. A. & Engelman, D. M. Lipid bilayer thickness varies linearly with acyl chain length in fluid phosphatidylcholine vesicles. *J. Mol. Biol.* **166**, 211–217 (1983).

144. Nguyen, H. K. & Southern, E. M. Minimising the secondary structure of DNA targets by incorporation of a modified deoxynucleoside: Implications for nucleic acid analysis by hybridisation. *Nucleic Acids Res.* **28**, 3904–3909 (2000).

145. Jansson, L. I. *et al.* Telomere DNA G-quadruplex folding within actively extending human telomerase. *Proc. Natl. Acad. Sci. U. S. A.* **116**, 9350–9359 (2019).

146. Zadeh, J. N. *et al.* NUPACK: Analysis and design of nucleic acid systems. *J. Comput. Chem.* **32**, 170–173 (2011).

147. Kim, D. N., Kilchherr, F., Dietz, H. & Bathe, M. Quantitative prediction of 3D solution shape and flexibility of nucleic acid nanostructures. *Nucleic Acids Res.* **40**, 2862–2868 (2012).

148. Castro, C. E. *et al.* A primer to scaffolded DNA origami. *Nat. Methods* **8**, 221–229 (2011).

149. Ohmann, A. *et al.* Controlling aggregation of cholesterol-modified DNA nanostructures. *Nucleic Acids Res.* **47**, 11441–11451 (2019).

150. Garfin, D. E. Chapter 29 One-Dimensional Gel Electrophoresis. in *Methods in Enzymology* vol. 463 497–513 (Academic Press Inc., 2009).

151. Pollinger, J. P. Gel Casting. in *Encyclopedia of Materials: Science and Technology* 3486–3491 (Elsevier, 2001). doi:10.1016/b0-08-043152-6/00620-3.

152. Ackerman, M. M., Ricciardi, C., Weiss, D., Chant, A. & Kraemer-Chant, C. M. Analyzing Exonuclease-Induced Hyperchromicity by UV Spectroscopy: An Undergraduate Biochemistry Laboratory Experiment. *J. Chem. Educ* **93**, 39 (2016).

153. Swinehart, D. F. The Beer-Lambert law. *J. Chem. Educ.* **39**, 333–335 (1962).

154. Sambrook, J. & Russell, D. *Molecular cloning : a laboratory manual*. (Cold Spring Harbor Laboratory Press, 2001).

155. Glasel, J. A. Validity of nucleic acid purities monitored by 260nm/280nm absorbance ratios. *Biotech.* **18**, (1995).

156. Jayasinghe, I. *et al.* True Molecular Scale Visualization of Variable Clustering Properties of Ryanodine Receptors. *Cell Rep.* **22**, 557–567 (2018).

157. Hung, W. C., Chen, F. Y. & Huang, H. W. *Order^disorder transition in bilayers of diphytanoyl phosphatidylcholine*. www.elsevier.com/locate/bba.

158. Dimitrov, D. S. & Angelova, M. I. Lipid swelling and liposome formation on solid surfaces in external electric fields. *Prog. Colloid Polym. Sci.* **73**, 48–56 (1987).

159. Gagné, F. *Biochemical Ecotoxicology: Principles and Methods*. *Biochemical Ecotoxicology: Principles and Methods* (2014). doi:10.1016/C2012-0-07586-2.

160. Montal, M. & Mueller, P. Formation of bimolecular membranes from lipid monolayers and a study of their electrical properties. *Proc. Natl. Acad. Sci. U. S. A.* **69**, 3561–3566 (1972).

161. Gutsmann, T., Heimburg, T., Keyser, U., Mahendran, K. R. & Winterhalter, M. Protein reconstitution into freestanding planar lipid membranes for electrophysiological characterization. *Nat. Protoc.* **10**, 188–198 (2015).

162. Taylor, G. J., Venkatesan, G. A., Collier, C. P. & Sarles, S. A. Direct in situ measurement of specific capacitance, monolayer tension, and bilayer tension in a droplet interface bilayer. *Soft Matter* **11**, 7592–7605 (2015).

163. Luo, K. *et al.* Investigation of membrane condensation induced by CaCO3 nanoparticles and its effect on membrane protein function. *RSC Adv.* **7**, 49858–49862 (2017).

164. Beck, V. *et al.* A new automated technique for the reconstitution of hydrophobic proteins into planar bilayer membranes. Studies of human recombinant uncoupling protein 1. *Biochim. Biophys. Acta - Bioenerg.* **1757**, 474–479 (2006).

165. Schindelin, J. *et al.* Fiji: An open-source platform for biological-image analysis. *Nat. Methods* **9**, 676–682 (2012).

166. Lipfert, J., Sim, A. Y. L., Herschlag, D. & Doniach, S. Dissecting electrostatic screening, specific ion binding, and ligand binding in an energetic model for glycine riboswitch folding. *RNA* **16**, 708–719 (2010).

167. Chu, V. B., Bai, Y., Lipfert, J., Herschlag, D. & Doniach, S. A repulsive field: advances in the electrostatics of the ion atmosphere. *Curr. Opin. Chem. Biol.* **12**, 619–625 (2008).

168. Draper, D. E. A guide to ions and RNA structure. (2004) doi:10.1261/rna.5205404.

169. Kappel, C. & Eils, R. Fluorescence recovery after photobleaching with the Leica TCS SP2. *Confocal Appl. Lett.* (2004).

170. Malvezzi, M. *et al.* Ca2+-dependent phospholipid scrambling by a reconstituted TMEM16 ion channel. *Nat. Commun.* **4**, (2013).

171. Ploier, B. & Menon, A. K. A fluorescence-based assay of phospholipid scramblase activity. *J. Vis. Exp.* **2016**, 54635 (2016).

172. Lee, B. C., Menon, A. K. & Accardi, A. The nhTMEM16 Scramblase Is Also a Nonselective Ion Channel. *Biophys. J.* **111**, 1919–1924 (2016).

173. Filipe, H. A. L., Pokorná, Š., Hof, M., Amaro, M. & Loura, L. M. S. Orientation of nitro-group governs the fluorescence lifetime of nitrobenzoxadiazole (NBD)-labeled lipids in lipid bilayers. *Phys. Chem. Chem. Phys.* **21**, 1682–1688 (2019).

174. Huster, D., Mü, P., Arnold, K. & Herrmann, A. Dynamics of Membrane Penetration of the Fluorescent 7-Nitrobenz-2-Oxa-1,3-Diazol-4-yl (NBD) Group Attached to an Acyl Chain of Phosphatidylcholine. *Biophys. J.* **80**, 822–831 (2001).

175. Malvezzi, M. *et al.* Out-of-the-groove transport of lipids by TMEM16 and GPCR scramblases. *Proc. Natl. Acad. Sci. U. S. A.* **115**, E7033–E7042 (2018).

176. Lister, M. W. & Garvie, R. C. Sodium dithionite, decomposition in aqueous solution and in the solid state. *Can. J. Chem.* **37**, 1567–1574 (1959).

177. Conte Camerino, D., Tricarico, D. & Desaphy, J. F. Ion Channel Pharmacology. *Neurotherapeutics* **4**, 184–198 (2007).

178. Camerino, D. C., Desaphy, J. F., Tricarico, D., Pierno, S. & Liantonio, A. Chapter 4 Therapeutic Approaches to Ion Channel Diseases. in *Advances in Genetics* vol. 64 81–145

(Academic Press Inc., 2008).

179. Verkman, A. S. & Galietta, L. J. V. Chloride channels as drug targets. *Nat. Rev. Drug Discov.* **8**, 153–171 (2009).

180. Kodigepalli, K. M., Bowers, K., Sharp, A. & Nanjundan, M. Roles and regulation of phospholipid scramblases. *FEBS Lett.* **589**, 3–14 (2015).

181. Segawa, K. & Nagata, S. An Apoptotic 'Eat Me' Signal: Phosphatidylserine Exposure. *Trends Cell Biol.* **25**, 639–650 (2015).

182. Sivagnanam, U., Palanirajan, S. K. & Gummadi, S. N. The role of human phospholipid scramblases in apoptosis: An overview. *Biochim. Biophys. Acta - Mol. Cell Res.* **1864**, 2261–2271 (2017).

183. Kodigepalli, K. M., Bowers, K., Sharp, A. & Nanjundan, M. Roles and regulation of phospholipid scramblases. (2014) doi:10.1016/j.febslet.2014.11.036.

184. Kwon, Y. Absorption. in *Handbook of Essential Pharmacokinetics, Pharmacodynamics and Drug Metabolism for Industrial Scientists* 35–72 (Springer US, 2002). doi:10.1007/0-306-46820-4_4.

185. Marquardt, D. *et al.* Lipid bilayer thickness determines cholesterols location in model membranes. *Soft Matter* **12**, 9417–9428 (2016).

186. Kornberg, R. D. & Mcconnell, H. M. Inside-Outside Transitions of Phospholipids in Vesicle Membranes. *Biochemistry* **10**, 1111–1120 (1971).

187. Owczarzy, R., Moreira, B. G., You, Y., Behlke, M. A. & Wälder, J. A. Predicting stability of DNA duplexes in solutions containing magnesium and monovalent cations. *Biochemistry* **47**, 5336–5353 (2008).

188. Von Ahsen, N., Wittwer, C. T. & Schütz, E. Oligonucleotide melting temperatures under PCR conditions: Nearest-neighbor corrections for MG2+, deoxynucleotide triphosphate, and dimethyl sulfoxide concentrations with comparison to alternative empirical formulas. *Clin. Chem.* **47**, 1956–1961 (2001).

189. SantaLucia, J. & Hicks, D. The Thermodynamics of DNA Structural Motifs. *Annu. Rev. Biophys. Biomol. Struct.* **33**, 415–440 (2004).

190. Sahu, S. K., Gummadi, S. N., Manoj, N. & Aradhyam, G. K. Phospholipid scramblases:

An overview. *Arch. Biochem. Biophys.* **462**, 103–114 (2007).

191. Jiang, T., Yu, K., Hartzell, H. C. & Tajkhorshid, E. Lipids and ions traverse the membrane by the same physical pathway in the nhTMEM16 scramblase. *Elife* **6**, (2017).

192. Ballesteros, A. & Swartz, K. J. Lipids surf the groove in scramblases. *Proc. Natl. Acad. Sci. U. S. A.* **115**, 7648–7650 (2018).

193. Suzuki, J., Umeda, M., Sims, P. J. & Nagata, S. Calcium-dependent phospholipid scrambling by TMEM16F. *Nature* **468**, 834–840 (2010).

194. Ramakrishnan, S., Ijäs, H., Linko, V. & Keller, A. Structural stability of DNA origami nanostructures under application-specific conditions. *Comput. Struct. Biotechnol. J.* **16**, 342–349 (2018).

195. Kopka, M. L., Fratini, A. V., Drew, H. R. & Dickerson, R. E. Ordered water structure around a B-DNA dodecamer. A quantitative study. *J. Mol. Biol.* **163**, 129–146 (1983).

196. Privé, G. G. *et al.* Helix geometry, hydration, and G·A mismatch in a B-DNA decamer. *Science* **238**, 498–504 (1987).

197. Jóhannesson, H. & Halle, B. Minor groove hydration of DNA in solution: Dependence on base composition and sequence. *J. Am. Chem. Soc.* **120**, 6859–6870 (1998).

198. McDermott, M. L., Vanselous, H., Corcelli, S. A. & Petersen, P. B. DNA's Chiral Spine of Hydration. *ACS Cent. Sci.* **3**, 708–714 (2017).

199. Martinez, C. R. & Iverson, B. L. Rethinking the term 'pi-stacking'. *Chem. Sci.* **3**, 2191–2201 (2012).

200. Matray, T. J. & Kool, E. T. Selective and stable DNA base pairing without hydrogen bonds. *J. Am. Chem. Soc.* **120**, 6191–6192 (1998).

201. Rossetti, G. *et al.* The structural impact of DNA mismatches. *Nucleic Acids Res.* **43**, 4309–4321 (2015).

202. Feng, B. *et al.* Hydrophobic catalysis and a potential biological role of DNA unstacking induced by environment effects. *Proc. Natl. Acad. Sci. U. S. A.* **116**, 17169–17174 (2019).

203. Reymer, A., Zakrzewska, K. & Lavery, R. Sequence-dependent response of DNA to

torsional stress: A potential biological regulation mechanism. *Nucleic Acids Res.* **46**, 1684–1694 (2018).

204. Ferreira, I., Amarante, T. D. & Weber, G. DNA terminal base pairs have weaker hydrogen bonds especially for at under low salt concentration. *J. Chem. Phys.* **143**, 175101 (2015).

205. Zgarbová, M., Otyepka, M., Šponer, J., Lankaš, F. & Jurečka, P. Base pair fraying in molecular dynamics simulations of DNA and RNA. *J. Chem. Theory Comput.* **10**, 3177–3189 (2014).

206. Protozanova, E., Yakovchuk, P. & Frank-Kamenetskii, M. D. Stacked-unstacked equilibrium at the nick site of DNA. *J. Mol. Biol.* **342**, 775–785 (2004).

207. Yakovchuk, P., Protozanova, E. & Frank-Kamenetskii, M. D. Base-stacking and base-pairing contributions into thermal stability of the DNA double helix. *Nucleic Acids Res.* **34**, 564–574 (2006).

208. Häse, F. & Zacharias, M. Free energy analysis and mechanism of base pair stacking in nicked DNA. *Nucleic Acids Res.* **44**, 7100–7108 (2016).

209. Bennett, W. F. D. & Tieleman, D. P. Molecular simulation of rapid translocation of cholesterol, diacylglycerol, and ceramide in model raft and nonraft membranes. *J. Lipid Res.* **53**, 421–429 (2012).

210. Waters, J. T. *et al.* Transitions of Double-Stranded DNA between the A- and B-Forms. *J. Phys. Chem. B* **120**, 8449–8456 (2016).

211. Ben-Dror, S. *et al.* On the Correlation Between Hydrophobicity, Liposome Binding and Cellular Uptake of Porphyrin Sensitizers. *Photochem. Photobiol.* **82**, 695 (2006).

212. Khmelinskaia, A., Franquelim, H. G., Petrov, E. P. & Schwille, P. Effect of anchor positioning on binding and diffusion of elongated 3D DNA nanostructures on lipid membranes. *J. Phys. D. Appl. Phys.* **49**, (2016).

213. Czogalla, A., Kauert, D. J., Seidel, R., Schwille, P. & Petrov, E. P. DNA origami nanoneedles on freestanding lipid membranes as a tool to observe isotropic-nematic transition in two dimensions. *Nano Lett.* **15**, 649–655 (2015).

214. Kocabey, S. *et al.* Membrane-Assisted Growth of DNA Origami Nanostructure Arrays.

ACS Nano **9**, 3530–3539 (2015).

215. Chidchob, P. *et al.* Spatial Presentation of Cholesterol Units on a DNA Cube as a Determinant of Membrane Protein-Mimicking Functions. *J. Am. Chem. Soc.* **141**, 19 (2019).

216. Ulmschneider, M. B., Sansom, M. S. P. & Di Nola, A. Evaluating tilt angles of membrane-associated helices: Comparison of computational and NMR techniques. *Biophys. J.* **90**, 1650–1660 (2006).

217. Sang, H. P. & Opella, S. J. Tilt angle of a trans-membrane helix is determined by hydrophobic mismatch. *J. Mol. Biol.* **350**, 310–318 (2005).

218. Holt, A. & Killian, J. A. Orientation and dynamics of transmembrane peptides: The power of simple models. *Eur. Biophys. J.* **39**, 609–621 (2010).

219. De Planque, M. R. R. *et al.* Sensitivity of single membrane-spanning α-helical peptides to hydrophobic mismatch with a lipid bilayer: Effects on backbone structure, orientation, and extent of membrane incorporation. *Biochemistry* **40**, 5000–5010 (2001).

220. Lee, A. G. Lipid-protein interactions in biological membranes: A structural perspective. *Biochim. Biophys. Acta - Biomembr.* **1612**, 1–40 (2003).

221. Richard J. Webb, J. Malcolm East, Ram P. Sharma, A. & Lee*, A. G. Hydrophobic Mismatch and the Incorporation of Peptides into Lipid Bilayers: A Possible Mechanism for Retention in the Golgi†. *Biochemistry* **37**, (1998).

222. Hu, X., Margadant, F. M., Yao, M. & Sheetz, M. P. Molecular stretching modulates mechanosensing pathways. *Protein Sci.* **26**, 1337–1351 (2017).

223. Nickels, P. C. *et al.* Molecular force spectroscopy with a DNA origami-based nanoscopic force clamp. *Science* **354**, 305–307 (2016).

224. Iwaki, M., Wickham, S. F., Ikezaki, K., Yanagida, T. & Shih, W. M. A programmable DNA origami nanospring that reveals force-induced adjacent binding of myosin VI heads. *Nat. Commun.* **7**, 1–10 (2016).

225. Dimova, R. & Marqu, C. *The Giant Vesicle Book*. (CRC Press, 2019).

226. Jacobson, D. R. & Saleh, O. A. Counting the ions surrounding nucleic acids. *Nucleic Acids Res.* **45**, 1596–1605 (2017).

227. Gebala, M., Johnson, S. L., Narlikar, G. J. & Herschlag, D. Ion counting demonstrates a high electrostatic field generated by the nucleosome. *Elife* **8**, (2019).

228. Savelyev, A. & Papoian, G. A. Electrostatic, steric, and hydration interactions favor Na+ condensation around DNA compared with K+. *J. Am. Chem. Soc.* **128**, 14506–14518 (2006).

229. Manning, G. S. Is a Small Number of Charge Neutralizations Sufficient to Bend Nucleosome Core DNA onto Its Superhelical Ramp? *J. Am. Chem. Soc.* **125**, 15087–15092 (2003).

230. Buck, J., Grossen, P., Cullis, P. R., Huwyler, J. & Witzigmann, D. Lipid-based DNA therapeutics: Hallmarks of non-viral gene delivery. *ACS Nano* **13**, 3754–3782 (2019).

231. Ewert, K. K. *et al.* A columnar phase of dendritic lipid-based cationic liposome-DNA complexes for gene delivery: Hexagonally ordered cylindrical micelles embedded in a DNA honeycomb lattice. *J. Am. Chem. Soc.* **128**, 3998–4006 (2006).

232. Felgner, P. L. *et al.* Lipofection: a highly efficient, lipid-mediated DNA-transfection procedure. *Proc. Natl. Acad. Sci. U. S. A.* **84**, 7413–7417 (1987).

233. Abbott, N. L., Jewell, C. M., Hays, M. E., Kondo, Y. & Lynn, D. M. Ferrocene-containing cationic lipids: Influence of redox state on cell transfection. *J. Am. Chem. Soc.* **127**, 11576–11577 (2005).

234. Jackson, L. A. *et al.* An mRNA Vaccine against SARS-CoV-2 — Preliminary Report. *N. Engl. J. Med.* (2020) doi:10.1056/nejmoa2022483.

235. Nanomedicine and the COVID-19 vaccines. *Nat. Nanotechnol.* **15**, 1 (2020).

236. Brady, R. A., Brooks, N. J., Foderà, V., Cicuta, P. & Di Michele, L. Amphiphilic-DNA Platform for the Design of Crystalline Frameworks with Programmable Structure and Functionality. *J. Am. Chem. Soc.* **140**, 15384–15392 (2018).

237. Mooren, F. C. *et al.* Effects of extracellular Mg2+ concentration on intracellular signalling and acid secretion in rat gastric parietal cells. *Biochim. Biophys. Acta - Mol. Cell Res.* **1358**, 279–288 (1997).

238. McManus, J. J., Rädler, J. O. & Dawson, K. A. Does Calcium Turn a Zwitterionic Lipid

Cationic? *J. Phys. Chem. B* **107**, 9869–9875 (2003).

239. Melcrová, A. *et al.* The complex nature of calcium cation interactions with phospholipid bilayers. *Sci. Rep.* **6**, (2016).

240. Gromelski, S. & Brezesinski, G. DNA condensation and interaction with zwitterionic phospholipids mediated by divalent cations. *Langmuir* **22**, 6293–6301 (2006).

241. Malghani, M. S. & Yang, J. Stable binding of DNA to zwitterionic lipid bilayers in aqueous solutions. *J. Phys. Chem. B* **102**, 8930–8933 (1998).

242. Antipina, A. Y. & Gurtovenko, A. A. Molecular-level insight into the interactions of DNA with phospholipid bilayers: Barriers and triggers. *RSC Adv.* **6**, 36425–36432 (2016).

243. Antipina, A. Y. & Gurtovenko, A. A. Molecular mechanism of calcium-induced adsorption of DNA on zwitterionic phospholipid membranes. *J. Phys. Chem. B* **119**, 6638–6645 (2015).

244. Attwood, S. J., Choi, Y. & Leonenko, Z. Preparation of DOPC and DPPC supported planar lipid bilayers for atomic force microscopy and atomic force spectroscopy. *Int. J. Mol. Sci.* **14**, 3514–3539 (2013).

245. Biltonen, R. L. & Lichtenberg, D. The use of differential scanning calorimetry as a tool to characterize liposome preparations. *Chem. Phys. Lipids* **64**, 129–142 (1993).

246. Murtola, T., Falck, E., Patra, M., Karttunen, M. & Vattulainen, I. Coarse-grained model for phospholipid/cholesterol bilayer. *J. Chem. Phys.* **121**, 9156–9165 (2004).

247. Czogalla, A. *et al.* Switchable domain partitioning and diffusion of DNA origami rods on membranes. *Faraday Discuss.* **161**, 31–43 (2012).

248. Beales, P. A. & Kyle Vanderlick, T. Partitioning of membrane-anchored DNA between coexisting lipid phases. *J. Phys. Chem. B* **113**, 13678–13686 (2009).

249. Wang, X. *et al.* Cation bridging studied by specular neutron reflection. *Langmuir* **29**, 5520–5527 (2013).

250. Langecker, M., Arnaut, V., List, J. & Simmel, F. C. DNA nanostructures interacting with lipid bilayer membranes. *Acc. Chem. Res.* **47**, 1807–1815 (2014).

251. Kempter, S. *et al.* Single Particle Tracking and Super-Resolution Imaging of Membrane-Assisted Stop-and-Go Diffusion and Lattice Assembly of DNA Origami. *ACS Nano* **13**, 996–1002 (2019).

252. Higgins, M. J., Tom, L. A. & Sobeck, D. C. Case Study I: Application of the Divalent Cation Bridging Theory to Improve Biofloc Properties and Industrial Activated Sludge System Performance-direct Addition Of Divalent Cations. *Water Environ. Res.* **76**, (2004).

253. Yoo, J. & Aksimentiev, A. New tricks for old dogs: Improving the accuracy of biomolecular force fields by pair-specific corrections to non-bonded interactions. *Phys. Chem. Chem. Phys.* **20**, 8432–8449 (2018).

254. Yoo, J. & Aksimentiev, A. Improved Parameterization of Amine-Carboxylate and Amine-Phosphate Interactions for Molecular Dynamics Simulations Using the CHARMM and AMBER Force Fields. *J. Chem. Theory Comput.* **12**, 430–443 (2016).

255. Yoo, J. & Aksimentiev, A. Improved parametrization of Li +, Na +, K +, and Mg 2+ ions for all-atom molecular dynamics simulations of nucleic acid systems. *J. Phys. Chem. Lett.* **3**, 45–50 (2012).

256. Srivastava, A. *et al.* Structure-guided DNA–DNA attraction mediated by divalent cations. *Nucleic Acids Res.* **48**, 7018–7026 (2020).

257. Lin, A. J. *et al.* Three-dimensional imaging of lipid gene-carriers: Membrane charge density controls universal transfection behavior in lamellar cationic liposome-DNA complexes. *Biophys. J.* **84**, 3307–3316 (2003).

258. Wonder, E. *et al.* Competition of charge-mediated and specific binding by peptide-tagged cationic liposome–DNA nanoparticles in vitro and in vivo. *Biomaterials* **166**, 52–63 (2018).

259. Stellwagen, E. & Stellwagen, N. C. Probing the electrostatic shielding of DNA with capillary electrophoresis. *Biophys. J.* **84**, 1855–1866 (2003).

260. Cheng, X., Zhang, X., Yu, L. & Xu, H. Calcium signaling in membrane repair. *Semin. Cell Dev. Biol.* **45**, 24–31 (2015).

261. Lin, X., Gorfe, A. A. & Levental, I. Protein Partitioning into Ordered Membrane Domains: Insights from Simulations. *Biophys. J.* **114**, 1936–1944 (2018).

262. Brown, D. A. Lipid Rafts. in *Encyclopedia of Biological Chemistry: Second Edition* 741–744 (Elsevier Inc., 2013). doi:10.1016/B978-0-12-378630-2.00185-7.

263. You, J., Kamihira, M. & Iijima, S. Surfactant-mediated gene transfer for animal cells. *Cytotechnology* **25**, 45–52 (1997).

264. Marty, R. *et al.* Structural analysis of DNA complexation with cationic lipids. *Nucleic Acids Res.* **37**, 849–857 (2009).

265. Mcmanus, J. J., Rä, J. O. & Dawson, K. A. Observation of a Rectangular Columnar Phase in a DNA-Calcium-Zwitterionic Lipid Complex. *J. Am. Chem. Soc.* **126**, 15966–15967 (2004).

266. Michel, H. Crystallization of Membrane Proteins. in *Techniques and New Developments in Photosynthesis Research* 11–15 (Springer US, 1989). doi:10.1007/978-1-4684-8571-4_2.

267. Privé, G. G. Detergents for the stabilization and crystallization of membrane proteins. *Methods* **41**, 388–397 (2007).

268. Arunmanee, W., Harris, J. R. & Lakey, J. H. Outer Membrane Protein F Stabilised with Minimal Amphipol Forms Linear Arrays and LPS-Dependent 2D Crystals. *J. Membr. Biol.* **247**, 949–956 (2014).

269. Yamashita, E., Zhalnina, M. V, Zakharov, S. D., Sharma, O. & Cramer, W. A. Crystal structures of the OmpF porin: function in a colicin translocon. *EMBO J.* **27**, 2171–2180 (2008).

270. Nazari, M., Kurdi, M. & Heerklotz, H. Classifying Surfactants with Respect to Their Effect on Lipid Membrane Order. *Biophys. J.* **102**, (2012).

271. Kandušer, M. *et al.* Effect of surfactant polyoxyethylene glycol (C12E8) on electroporation of cell line DC3F. *Colloids Surfaces A Physicochem. Eng. Asp.* **214**, 205–217 (2003).

272. Seifert, A. *et al.* Bilayer-spanning DNA nanopores with voltage-switching between open and closed state. *ACS Nano* **9**, 1117–1126 (2015).

273. Dolder, M., Engel, A. & Zulauff, M. The micelle to vesicle transition of lipids and detergents, in the presence of a membrane protein" towards a rationale for 2D crystallization. *FEBS Lett.* **382**, 203–208 (1996).

274. Zulauf, M. & Rosenbusch, J. P. Micelle clusters of octylhydroxyoligo(oxyethylenes). *J. Phys. Chem.* **87**, 856–862 (1983).

275. Gjetting, T. *et al.* In vitro and in vivo effects of polyethylene glycol (PEG)-modified lipid in DOTAP/cholesterol-mediated gene transfection. *Int. J. Nanomedicine* **5**, 371–383 (2010).

276. Murphy, E. A., Waring, A. J., Haynes, S. M. & Longmuir, K. J. Compaction of DNA in an anionic micelle environment followed by assembly into phosphatidylcholine liposomes. *Nucleic Acids Res.* **28**, 2986–2992 (2000).

277. Tummala, R., Green-Church, K. B. & Limbach, P. A. Interactions between sodium dodecyl sulfate micelles and peptides during matrix-assisted laser desorption/ionization mass spectrometry (MALDI-MS) of proteolytic digests. *J. Am. Soc. Mass Spectrom.* **16**, 1438–1446 (2005).

278. Nozière, B., Gérard, V., Baduel, C. & Ferronato, C. Extraction and characterization of surfactants from atmospheric aerosols. *J. Vis. Exp.* **2017**, (2017).

279. Berlier, J. E. *et al.* Quantitative Comparison of Long-wavelength Alexa Fluor Dyes to Cy Dyes: Fluorescence of the Dyes and Their Bioconjugates. *J. Histochem. Cytochem.* **51**, 1699–1712 (2003).

280. Baserova, V. B. & Dergunov, A. D. Interaction of lipid-free apolipoprotein A-I with cholesterol revealed by molecular modeling. *Biochim. Biophys. Acta - Proteins Proteomics* **1869**, 140614 (2021).

281. Gilbert, D. B., Tanford, C. & Reynolds, J. A. Cholesterol in Aqueous Solution. Hydrophobicity and Self-Association. *Biochemistry* **14**, 444–448 (1975).

282. List, J., Weber, M. & Simmel, F. C. Hydrophobic Actuation of a DNA Origami Bilayer Structure. *Angew. Chemie Int. Ed.* **53**, 4236–4239 (2014).

283. Mobasheri, A. *et al.* Characterization of a stretch-activated potassium channel in chondrocytes. *J. Cell. Physiol.* **223**, 511–518 (2010).

284. Saha, S. C. *et al.* Characterization of the prokaryotic sodium channel NavSp pore with a microfluidic bilayer platform. *PLoS One* **10**, (2015).

285. Budker, V. G., Godovikov, A. A., Naumova, L. P. & Slepneva, I. A. Interaction of

polynucleotides with natural and model membranes. *Nucleic Acids Res.* **8**, 2499–2516 (1980).

286. Hemmig, E. A. *et al.* Optical Voltage Sensing Using DNA Origami. *Nano Lett.* **18**, 1962–1971 (2018).

287. Bian, X., Zhang, Z., Xiong, Q., De Camilli, P. & Lin, C. A programmable DNA-origami platform for studying lipid transfer between bilayers. *Nat. Chem. Biol.* **15**, 830–837 (2019).

288. Koller, D. & Lohner, K. The role of spontaneous lipid curvature in the interaction of interfacially active peptides with membranes. *Biochim. Biophys. Acta - Biomembr.* **1838**, 2250–2259 (2014).

289. Miller, C. An overview of the potassium channel family. *Genome Biol.* **1**, reviews0004.1 (2000).

290. Micklefield, J. Backbone Modification of Nucleic Acids: Synthesis, Structure and Therapeutic Applications. *Curr. Med. Chem.* **8**, 1157–1179 (2001).

291. Sharma, V. K., Sharma, R. K. & Singh, S. K. Antisense oligonucleotides: Modifications and clinical trials. *Medchemcomm* **5**, 1454–1471 (2014).

292. Ochoa, S. & Milam, V. T. Modified nucleic acids: Expanding the capabilities of functional oligonucleotides. *Molecules* **25**, (2020).

293. Garavito, R. M. & Ferguson-Miller, S. Detergents as Tools in Membrane Biochemistry*. *J. Biol. Chem.* **276**, 32403–32406 (2001).

294. Schmidt, M. Xenobiology: A new form of life as the ultimate biosafety tool. *BioEssays* **32**, 322–331 (2010).

295. Kurreck, J., Wyszko, E., Gillen, C. & Erdmann, V. A. Design of antisense oligonucleotides stabilized by locked nucleic acids. *Nucleic Acids Res.* **30**, 1911–1918 (2002).

296. Frieden, M., Hansen, H. F. & Koch, T. Nuclease stability of LNA oligonucleotides and LNA-DNA chimeras. *Nucleosides, Nucleotides and Nucleic Acids* **22**, 1041–1043 (2003).

297. Egholm, M. *et al.* PNA hybridizes to complementary oligonucleotides obeying the Watson-Crick hydrogen-bonding rules. *Nature* **365**, 566–568 (1993).

298. Nielsen, P. E., Egholm, M., Berg, R. H. & Buchardt, O. Sequence-selective recognition of DNA by strand displacement with a thymine-substituted polyamide. *Science* **254**, 1497–1500 (1991).

299. Gupta, A., Mishra, A. & Puri, N. Peptide nucleic acids: Advanced tools for biomedical applications. *J. Biotechnol.* **259**, 148–159 (2017).

300. Seeman, N. C. DNA Nanotechnology at 40. *Nano Letters* vol. 20 1477–1478 (2020).

301. Heinemann, U. & Roske, Y. Symmetry in nucleic-acid double helices. *Symmetry (Basel).* **12**, (2020).

302. Esguerra, M., Nilsson, L. & Villa, A. Triple helical DNA in a duplex context and base pair opening. *Nucleic Acids Res.* **42**, 11329–11338 (2014).

303. Van Dongen, M. J. P., Wijmenga, S. S., Van Der Marel, G. A., Van Boom, J. H. & Hilbers, C. W. The transition from a Neutral-pH double helix to a low-pH triple helix induces a conformational switch in the CCCG tetraloop closing a Watson-Crick stem. *J. Mol. Biol.* **263**, 715–729 (1996).

304. Baumann, K. N., Fux, A. C., Joseph, J., Bohndiek, S. E. & Hernández-Ainsa, S. An active DNA-based nanoprobe for photoacoustic pH imaging. *Chem. Commun.* **54**, 10176–10178 (2018).

305. Moye, A. L. *et al.* Telomeric G-quadruplexes are a substrate and site of localization for human telomerase. *Nat. Commun.* **6**, 1–12 (2015).

306. Guo, P. The emerging field of RNA nanotechnology. *Nat. Nanotechnol.* **5**, 833–842 (2010).

307. Leontis, N. B., Lescoute, A. & Westhof, E. The building blocks and motifs of RNA architecture. *Curr. Opin. Struct. Biol.* **16**, 279–287 (2006).

308. Bindewald, E., Hayes, R., Yingling, Y. G., Kasprzak, W. & Shapiro, B. A. RNAJunction: A database of RNA junctions and kissing loops for three-dimensional structural analysis and nanodesign. *Nucleic Acids Res.* **36**, D392 (2008).

309. Ikawa, Y., Tsuda, K., Matsumura, S. & Inoue, T. De novo synthesis and development of an RNA enzyme. *Proc. Natl. Acad. Sci. U. S. A.* **101**, 13750–13755 (2004).

310. Ishikawa, J., Furuta, H. & Ikawa, Y. An in vitro-selected RNA receptor for the GAAC

loop: Modular receptor for non-GNRA-type tetraloop. *Nucleic Acids Res.* **41**, 3748–3759 (2013).

311. Jaeger, L. & Leontis, N. B. Tecto-RNA: One-dimensional self-assembly through tertiary interactions. *Angew. Chemie - Int. Ed.* **39**, 2521–2524 (2000).

312. Lescoute, A. & Westhof, E. Topology of three-way junctions in folded RNAs. *RNA* **12**, 83–93 (2006).

313. Afonin, K. A. *et al.* In vitro assembly of cubic RNA-based scaffolds designed in silico. *Nat. Nanotechnol.* **5**, 676–682 (2010).

314. Geary, C., Rothemund, P. W. K. & Andersen, E. S. A single-stranded architecture for cotranscriptional folding of RNA nanostructures. *Science* **345**, 799–804 (2014).

315. Gall, J. *Systemantics: How Systems Work and Especially how They Fail.* (Quadrangle/New York Times Book Company, 1977).

316. Phillips, J. C. *et al.* Scalable molecular dynamics on CPU and GPU architectures with NAMD. *J. Chem. Phys.* **153**, 44130 (2020).

317. Case, D. A. *et al.* AMBER14. *AMBER 14* (2014).

318. Vanommeslaeghe, K. & MacKerell, A. D. Automation of the CHARMM general force field (CGenFF) I: Bond perception and atom typing. *J. Chem. Inf. Model.* **52**, 3144–3154 (2012).

319. Humphrey, W., Dalke, A. & Schulten, K. VMD: Visual molecular dynamics. *J. Mol. Graph.* (1996) doi:10.1016/0263-7855(96)00018-5.

320. Jorgensen, W. L., Chandrasekhar, J., Madura, J. D., Impey, R. W. & Klein, M. L. Comparison of simple potential functions for simulating liquid water. *J. Chem. Phys.* **79**, 926–935 (1983).

321. Darden, T., York, D. & Pedersen, L. Particle mesh Ewald: An N·log(N) method for Ewald sums in large systems. *J. Chem. Phys.* **98**, 10089–10092 (1993).

322. Feller, S. E., Zhang, Y., Pastor, R. W. & Brooks, B. R. Constant pressure molecular dynamics simulation: The Langevin piston method. *J. Chem. Phys.* **103**, 4613–4621 (1995).

323. Hart, K. *et al.* Optimization of the CHARMM additive force field for DNA: Improved treatment of the BI/BII conformational equilibrium. *J. Chem. Theory Comput.* **8**, 348–362 (2012).

324. Miyamoto, S. & Kollman, P. A. Settle: An analytical version of the SHAKE and RATTLE algorithm for rigid water models. *J. Comput. Chem.* **13**, 952–962 (1992).

325. Andersen, H. C. Rattle: A 'velocity' version of the shake algorithm for molecular dynamics calculations. *J. Comput. Phys.* **52**, 24–34 (1983).

326. Goodsell, D. S., Autin, L. & Olson, A. J. Illustrate: Software for Biomolecular Illustration. *Structure* **27**, 1716-1720.e1 (2019).

327. Wilson, J., Sarthak, K., Si, W., Gao, L. & Aksimentiev, A. Rapid and Accurate Determination of Nanopore Ionic Current Using a Steric Exclusion Model. *ACS Sensors* **4**, 634–644 (2019).

328. Batcho, P. F., Case, D. A. & Schlick, T. Optimized particle-mesh Ewald/multiple-time step integration for molecular dynamics simulations. *J. Chem. Phys.* **115**, 4003–4018 (2001).

329. Klauda, J. B. *et al.* Update of the CHARMM All-Atom Additive Force Field for Lipids: Validation on Six Lipid Types. *J. Phys. Chem. B* **114**, 7830–7843 (2010).

330. Beglov, D. & Roux, B. Finite representation of an infinite bulk system: Solvent boundary potential for computer simulations. *J. Chem. Phys.* **100**, 9050–9063 (1994).

331. Jo, S., Lim, J. B., Klauda, J. B. & Im, W. CHARMM-GUI membrane builder for mixed bilayers and its application to yeast membranes. *Biophys. J.* **97**, 50–58 (2009).

332. Sugita, Y., Kitao, A. & Okamoto, Y. Multidimensional replica-exchange method for free-energy calculations. *J. Chem. Phys.* **113**, 6042–6051 (2000).

333. Fiorin, G., Klein, M. L. & Hénin, J. Using collective variables to drive molecular dynamics simulations. *Mol. Phys.* **111**, 3345–3362 (2013).

334. Kumar, S., Rosenberg, J. M., Bouzida, D., Swendsen, R. H. & Kollman, P. A. THE weighted histogram analysis method for free-energy calculations on biomolecules. I. The method. *J. Comput. Chem.* **13**, 1011–1021 (1992).

335. Mulkidjanian, A. Y. & Galperin, M. Y. Evolutionary origins of membrane proteins. in

Structural Bioinformatics of Membrane Proteins 1–28 (Springer Vienna, 2010). doi:10.1007/978-3-7091-0045-5_1.

336. Zhou, H. *et al.* New insights into Hoogsteen base pairs in DNA duplexes from a structure-based survey. *Nucleic Acids Res.* **43**, 3420–3433 (2015).

337. Garg, A. & Heinemann, U. A novel form of RNA double helix based on G·U and C·A+ wobble base pairing. *RNA* **24**, 209–218 (2018).

338. Stephenson, F. H. Nucleic acid quantification. in *Calculations for Molecular Biology and Biotechnology* 99–122 (Elsevier, 2010). doi:10.1016/b978-0-12-375690-9.00005-x.

339. Hill, D. F. & Petersen, G. B. Nucleotide Sequence of Bacteriophage fl DNA. *J. Vireology* **44**, 32–46 (1982).

340. Privalov, P. L. & Crane-Robinson, C. Forces maintaining the DNA double helix and its complexes with transcription factors. *Prog. Biophys. Mol. Biol.* **135**, 30–48 (2018).